

A Contribution to Transpiration Cooling for Aerospace Applications Using CMC Walls

A thesis accepted by the Faculty of Aerospace Engineering and Geodesy
of the Universität Stuttgart in partial fulfilment of the requirements for the
degree of Doctor of Engineering Sciences (Dr.-Ing.)

by

Dipl.-Ing. Tobias Langener

born in Haltern am See, Germany

Committee chair:

Committee member:

Date of defence:

Prof. Dr.-Ing. Jens von Wolfersdorf

Prof. Dr.-Ing. Stefan Schleichriem

01.07.2011

Institute of Aerospace Thermodynamics

University of Stuttgart

2011

Vitam regunt fortuna sapientiaque, non scientia.

Vorwort

Während meiner Zeit als wissenschaftlicher Mitarbeiter am Institut für Thermodynamik der Luft- und Raumfahrt hatte ich die Möglichkeit mich frei aber auch intensiv meiner wissenschaftlichen Fragestellung, der Wirkungsweise der Transpirationskühlung, zu widmen. Dieses lag vornehmlich an der sehr guten Betreuung durch meinen Doktorvater Herrn Prof. Dr.-Ing. Jens von Wolfersdorf, welcher bei Problemen immer zeitnah zum Gespräch zur Verfügung stand und auch ausreichend Freiraum für eigene Ideen gelassen hat. Außerdem möchte ich seine professionelle aber auch sehr angenehme Arbeitsweise hervorheben und auch an die gemeinsamen Dienstreisen quer durch Europa erinnern.

Des Weiteren gilt mein Dank Herrn Prof. Dr.-Ing. Stefan Schlechtriem für seine Funktion als Mitberichter bei meiner Promotion, dem der Arbeit entgegen gebrachten Interesse und dem sehr positiven Feedback nach der Prüfung.

Zu einer erfolgreichen Promotion gehören meiner Meinung nach nicht nur eine gute Betreuung, sondern auch eine positive Arbeitsumgebung. Hier gilt mein Dank Herrn Prof. Dr.-Ing. Bernhard Weigand für die sehr gute Leitung des Instituts und das Schaffen der professionellen Arbeitsbedingungen. Auch haben die vielen Kollegen, von denen einige zu guten Freunden geworden sind, die Zeit am Institut leicht gemacht. Es gab neben regem fachlichen Austausch auch zahlreiche erheiternde Diskussionen und private Vergnügungen. Einzelne Personen und Gelegenheiten möchte ich bewusst nicht nennen, das würde den Rahmen hier sprengen. Auch nicht zu vergessen ist die Hilfe der studentischen Hilfskräfte und der Studenten, die ich während ihrer Studien- und Diplomarbeit betreute.

Weiterhin ist bei einer experimentellen Arbeit eine gute Unterstützung durch die Werkstätten unabdingbar. Hier möchte ich die fachgerechte und hilfreiche Arbeit von Herrn Eberhard Mayer, Herrn Jürgen Fauser und Herrn Christian Otto von der mechanischen Werkstatt und von Herrn Uli Schwaderer und Herrn Thomas Bertnik von der elektrischen Werkstatt ganz besonders hervorheben.

Ohne die Unterstützung meiner Eltern hätte ich schon meinen Diplomstudien-gang nicht in der benötigten Zeit oder vielleicht gar nicht beendet. Auch haben sie mir meine Auslandsaufenthalte ermöglicht, durch die ich viele einzigartige Erfahrungen sammeln konnte. Während der Promotion haben Sie mich immer ermutigt, auch wenn die Experimente gerade nicht das lieferten, was sie sollten.

My girlfriend Samara is a very special person to me. She is a very calming girl, who is able to comfort me, especially in stressful situations. This was also the case during the work on this thesis. With her love, compassion, and great patience she was always able to support whatever I was doing, but in particular during the last months at ITLR and the first months in Holland.

Leiden (Niederlande), im Juli 2011

Cover Picture

The cover picture shows a temperature map obtained by infrared thermography of a transpiration cooled C/C sample at a blowing ration of $F = 0.1\%$. A velocity profile measured during the outflow characterization of a porous sample has been superposed to this.

Contents

Table of Contents	i
List of Figures	v
List of Tables	ix
Nomenclature	xi
Abstract	xv
Kurzfassung	xvii
1 Introduction	1
1.1 Hypersonic Airbreathing Propulsion	2
1.1.1 Ramjet Engines	3
1.1.1.1 Ramjet, Scramjet, and Dual-Mode Scramjet Engines	4
1.1.1.2 The Brayton Cycle	6
1.1.2 Major Technical Challenges	6
1.1.3 Selected Hypersonic Research Programs	7
1.2 Motivation and Approach	9
2 Physical Background	13
2.1 Cooling Techniques for Aerospace Applications	13
2.1.1 Film Cooling	14
2.1.2 Transpiration Cooling	17
2.2 Hot-Gas Heat Transfer without Blowing	20
2.3 Turbulent Boundary Layers Subject to Blowing	21
2.3.1 Model of Rannie	22
2.3.2 Model of Eckert and Livingood	23
2.3.3 Model of Kays et al.	24
2.4 Thermal Behavior of Porous Structures	26
2.5 Through-Flow Behavior of Porous Structures	28
2.6 Ceramic Matrix Composite (CMC) Materials	29

Contents

3	Experimental Setups and Measurement Techniques for Hot-Gas Tests	31
3.1	Experimental Facility	31
3.2	Test Setup for Supersonic Experiments	32
3.2.1	Test Channel	32
3.2.2	Sample Integration Concept	33
3.2.3	Parameter Range	34
3.3	Test Setup for Subsonic Experiments	35
3.3.1	Subsonic Flow Channel and Sample Integration Concept	36
3.3.2	Parameter Range	37
3.4	Investigated CMC Samples	39
3.5	Infrared Thermography for Quantitative Wall Temperature Measurements	40
3.6	Measurement and Data Acquisition System	43
4	Characterization of Investigated CMC Material	47
4.1	Introduction	47
4.2	Pressure Tank	47
4.3	Outflow Measurements	48
4.3.1	Introduction	48
4.3.2	Experimental Procedure	49
4.3.3	Validation	53
4.3.4	Exit-Flow Profiles of C/C Material	56
4.3.5	Conclusions	58
4.4	Through-Flow and Permeability Coefficients of C/C	59
4.4.1	Introduction	59
4.4.2	Validation of Test-Rig	60
4.4.3	Determination of Permeability Coefficients	61
5	Transpiration Cooling of C/C Wall Segments with Different Coolants	65
5.1	Pressure Distribution in the Supersonic Flow Channel	65
5.2	Surface Temperature Distribution	66
5.3	Cooling Efficiency of the Porous Wall	68
5.4	Thermal Behavior of the Porous C/C Wall in Subsonic Flow Experiments	76
5.4.1	Pressure Distribution in Subsonic Flow Regime	76
5.4.2	Wall Temperature Distribution	77
5.4.3	Wall Cooling Efficiency	79
5.4.4	Cooling Efficiency Model	82
5.4.5	Internal Temperature Profile of C/C Wall Segment	85
5.4.6	1D-Approach for Wall-Temperature Profile Prediction	87
5.5	Through-Flow Behavior of Porous Materials in Hot-Gas Tests	90
5.5.1	Modified Darcy-Forchheimer Equation for Non-Isothermal Porous Media	90
5.5.2	Prediction of the Pressure Loss Using the Wall Temperature Model for Different Coolants	94
5.6	Conclusions	98
6	Estimates for Transpiration Cooling Applied to Aerospace Structures	101

6.1 Exemplary Thermal Prediction of Application Related Combustors with Hydrogen as a Coolant	102
6.2 Application of the Transpiration Cooling Model to a Generic Combustor of Varying Geometry	106
6.3 Estimates of the Pressure Drop for Hydrogen Transpiration Cooled Porous Combustion Chambers	108
6.4 Conclusions	109
7 Summary and Outlook	111
Bibliography	113
A Uncertainty Analysis	123
B 2D Surface Temperature Maps	129
B.1 Supersonic Flow Regime	130
B.2 Subsonic Flow Regime Using the Uncooled Channel	133
C Heat Flux Components	137
D Combustion Chamber Conditions of Selected Aerospace Application	139

List of Figures

1.1	Justification for hypersonic airbreathing propulsion systems	2
1.2	Diagram of a possible scramjet propulsion system	3
1.3	Schematic of different ram propulsion systems	5
1.4	Schematic of the Brayton-cycle $h - s$ diagram	6
2.1	Schematic of film cooling configurations	15
2.2	Schematic of a transpired boundary layer over a porous wall segment	17
2.3	Temperature profile and convective heat transfer in compressible flow with a cooled wall	20
2.4	Steady thermal situation of a porous wall	26
2.5	DLR C/C and C/C-SiC manufacturing process	30
2.6	Example of C/C sample used in this study	30
3.1	ITLR supersonic combustion and hot-gas flow test bench	32
3.2	Test section with IR-thermography setup	33
3.3	Sample integration concept	34
3.4	Hot-gas channel	36
3.5	Sample integration design	37
3.6	Planck's law and Wien's law for the investigated temperature range . .	40
3.7	Radiation components recorded by the infrared camera	42
3.8	Temperature obtained from the infrared system, thermocouple mea- surements and in situ calibration versus the recorded radiation intensity	43
3.9	Test logic for a hot-gas run measuring several blowing ratios	44
4.1	Through-flow test rig	48
4.2	Experimental setup for outflow-profile measurements	50
4.3	Measurement logic of DAQ software and calibration of Pitot tube . .	51
4.4	Measurement geometry and indices	52
4.5	Contour plots of dynamic exit pressure for three different Pitot probe heights: a) $H = 0.2 \text{ mm}$, b) $H = 1 \text{ mm}$, c) $H = 3 \text{ mm}$	54
4.6	Outflow profiles of hollow sphere packings at different air mass-flow rates	55
4.7	Outflow profiles of PH1732 C/C at different air mass-flow rates	56

List of Figures

4.8	Outflow profiles of PH1606 C/C at different air mass-flow rates	57
4.9	Outflow profiles of PH1606 C/C from top (polished side) and bottom (rough side)	58
4.10	Validation of through-flow test rig	60
4.11	Through flow characteristics in the pressure tank for the PH1732 sample charge	62
4.12	Frequency of the permeability coefficients using the Monte Carlo uncertainty determination technique. PH1732-1 sample	63
5.1	Normalized pressure distribution in supersonic flow channel for $M_g = 2.1$, $p_{t,g} = 2.97 \text{ bar}$, $T_{t,g} = 1054 \text{ K}$, coolant: Air	66
5.2	Surface temperature distributions of C/C PH1732-1 sample for different blowing ratios. Top: Air as a coolant, middle: Helium as a coolant, bottom: Argon as a coolant. Main-flow conditions: $M_g = 2.1$, $p_{t,g} = 2.97 \text{ bar}$, $T_{t,g} = 1039 - 1060 \text{ K}$	67
5.3	Nondimensional temperature Θ versus coolant mass-flux \dot{m}_c/A_c for sample PH1732-1: Different coolant gases. Comparison of thermocouple to infrared data. $T_{t,g} = 1037 - 1060 \text{ K}$	69
5.4	Nondimensional temperature Θ versus coolant mass-flux \dot{m}_c/A_c for sample PH1732-2: Different total temperatures for air as coolant . . .	69
5.5	Comparison of test data versus the models of Rannie and Eckert and Livingood. Main-flow conditions: $M_g = 2.1$, $T_{t,g} = 1039 - 1060 \text{ K}$, $p_{t,g} = 2.97 \text{ bar}$	70
5.6	Comparison of test data versus the model from Kays et al. using an arbitrary hot-gas Stanton number. Main-flow conditions: $M_g = 2.1$, $T_{t,g} = 1039 - 1060 \text{ K}$, $p_{t,g} = 2.97 \text{ bar}$	71
5.7	Schematic of the heat transfer situation according to the heat balance model	71
5.8	Lateral heat conduction modified approach of Kays et al. using a realistic hot-gas Stanton number. $M_g = 2.1$, $T_{t,g} = 1039-1060 \text{ K}$, $p_{t,g} = 2.97 \text{ bar}$: Comparison to experimental results with different coolants .	73
5.9	Normalized convective heat flux from the transpiration cooling model for different coolant gases. $T_{t,g} = 1039 - 1060 \text{ K}$, PH1732-1 sample . .	74
5.10	Normalized internal and conduction heat flux from the transpiration cooling model for different coolant gases. $T_{t,g} = 1039 - 1060 \text{ K}$, PH1732-1 sample	74
5.11	Lateral heat conduction modified approach of Kays et al. $M_g = 2.1$, $T_{t,g} = 1060 \text{ K}$, $p_{t,g} = 2.97 \text{ bar}$, Air as coolant: effect of the variation of the hot-gas side heat transfer coefficient without cooling $h_{g,0}$	75
5.12	Normalized pressure distribution of subsonic flow regime in the uncooled channel for $T_{t,g} = 523 \text{ K}$, coolant: Air	76
5.13	Normalized pressure distribution of subsonic flow regime in the uncooled channel at the sample location for $T_{t,g} = 523 \text{ K}$, coolant: Air .	77
5.14	Surface temperature distributions of PH1606-1 sample ($L = 15 \text{ mm}$) for different blowing ratios. Top: Air as a coolant, middle: Helium as a coolant, bottom: Argon as a coolant. Main-flow conditions: $M_g = 0.5$, $T_{t,g} = 523 \text{ K}$	78

5.15	Cooling efficiency of C/C samples: (a) Influence of total temperature, (b) Influence of thickness, (c) Influence of sample charge, (d) Influence of coolant	80
5.16	Cooling efficiency comparing both flow regimes: $T_{t,g} = 1039 - 1060 K$ and $M_g = 2.1$ with the PH1732-1 sample versus $T_{t,g} = 523 K$ and $M_g = 0.3 - 0.7$ with the PH1606-1 porous wall material	81
5.17	Comparison of heat-balance cooling efficiency approach to experiments in subsonic flow regime. PH1606-1	82
5.18	Normalized convective heat flux from the transpiration cooling model for different hot-gas Mach number. $T_{t,g} = 520 K$, PH1606-1 sample	83
5.19	Normalized conduction and internal heat flux from the transpiration cooling model for different hot-gas Mach number. $T_{t,g} = 520 K$, PH1606-1 sample	84
5.20	Location of thermocouples on and within the porous wall samples. Dashed circles: In-sample thermocouples	85
5.21	Temperature profile of different C/C samples over nondimensional wall thickness, $T_{t,g} = 525 K$, $M_g = 0.5$. Solid symbols represent the coolant temperature in the coolant plenum	86
5.22	Temperature profile within the porous sample compared to the analytical, one-dimensional, thermal equilibrium solution (dashed lines). $T_{t,g} = 525 K$, $M_g = 0.5$. PH1606-1	89
5.23	Temperature profile within the porous sample compared to the analytical, one-dimensional, thermal equilibrium solution (dashed lines). $T_{t,g} = 525 K$, $M_g = 0.5$. PH1947-2	90
5.24	Normalized pressure loss versus superficial through-flow velocity showing the temperature effect: Comparison of through-flow model with experimental data at $M_g = 2.1$. PH1732-1, Coolant: Air	93
5.25	Normalized pressure loss versus superficial through-flow velocity showing the temperature effect: Comparison of through-flow model with experimental data at $M_g = 2.1$. PH1732-2, Coolant: Air	94
5.26	Permeability coefficients K_D and K_F from the cold flow tests for different coolants including uncertainties from Monte Carlo analysis. PH1732-1 sample	95
5.27	Permeability coefficients K_D and K_F from the cold flow tests for different coolants including uncertainties from Monte Carlo analysis. PH1606 material	95
5.28	Normalized pressure loss versus superficial through-flow velocity: experimental data compared to coupled approach for the pressure loss using the cold flow test permeability coefficients. $M_g = 0.7$, $T_{t,g} = 523 - 524 K$	96
5.29	Normalized pressure loss versus superficial through-flow velocity: Experimental data compared to coupled approach for the pressure loss using the cold flow test permeability coefficients. PH1732-1 sample. $M_g = 2.1$, $T_{t,g} = 1039 - 1054 K$	97

List of Figures

5.30	Normalized pressure loss versus superficial through-flow velocity: Experimental data compared to coupled approach for the pressure loss using the cold flow test permeability coefficients. $M_g = 0.5, T_{t,g} = 524 K$	97
6.1	Biot number of the combustion chamber heat transfer as a function of the blowing ratio for different combustion chamber conditions . .	103
6.2	Cooling efficiency using hydrogen as a coolant as a function of the coolant mass-flow rate per cooled area: LAPCAT and ATLLAS flight configurations	103
6.3	Cooling efficiency using hydrogen as a coolant as a function of the coolant mass-flow rate per cooled area: Scramjet demonstrator and generic scramjet geometry	104
6.4	Equivalence ratio of the coolant (hydrogen) for the generic combustor geometry versus the combustion chamber width. Variation of the aspect ratio W/H	107
6.5	Pressure drop for different generic wall material for the cooling situations described in Table D.1 ($M_\infty = 7$). Hot-gas conditions see Table D.2	109
B.1	Surface temperature distributions of the PH1732-1 sample ($L = 10 mm$) for different blowing ratios. Air as a coolant. Main-flow conditions: $M_g = 2.1, T_{t,g} = 1060 K$	130
B.2	Surface temperature distributions of the PH1732-1 sample ($L = 10 mm$) for different blowing ratios. Argon as a coolant. Main-flow conditions: $M_g = 2.1, T_{t,g} = 1039 K$	131
B.3	Surface temperature distributions of the PH1732-1 sample ($L = 10 mm$) for different blowing ratios. Helium as a coolant. Main-flow conditions: $M_g = 2.1, T_{t,g} = 1054 K$	132
B.4	Surface temperature distributions of the PH1606 sample ($L = 15 mm$) for different blowing ratios. Air as a coolant. Main-flow conditions: $M_g = 0.5, T_{t,g} = 521 K$	133
B.5	Surface temperature distributions of the PH1606 sample ($L = 15 mm$) for different blowing ratios. Argon as a coolant. Main-flow conditions: $M_g = 0.5, T_{t,g} = 525 K$	134
B.6	Surface temperature distributions of the PH1606 sample ($L = 15 mm$) for different blowing ratios. Helium as a coolant. Main-flow conditions: $M_g = 0.5, T_{t,g} = 525 K$	135
C.1	Normalized convective heat flux from the transpiration cooling model for different coolant gases. $T_{t,g} = 520 K$, PH1606-1 sample	137
C.2	Normalized conduction and internal heat flux from the transpiration cooling model for different coolant gases. $T_{t,g} = 520 K$, PH1606-1 sample	137

List of Tables

3.1	Supersonic channel flow and heat transfer parameters	35
3.2	Coolant parameters in supersonic flow tests	35
3.3	Subsonic channel flow and heat transfer parameters	38
3.4	Coolant parameters in subsonic flow tests	39
3.5	Investigated sample material	39
3.6	Main specifications of IR-thermography system	41
4.1	Effect of variation of readings per data point on outflow data	53
4.2	Pitot probe height variation using C/C as porous material	54
4.3	Outflow characteristics of HSP samples. $\rho_{amb} = 1.148 \text{ kg/m}^3$	56
4.4	Exit porosities of HSP samples. $\rho_{amb} = 1.148 \text{ kg/m}^3$	56
4.5	Outflow results for two different C/C samples at different air mass-flow rates. $\rho_{amb} = 1.148 \text{ kg/m}^3$	58
4.6	Exit porosities of C/C samples. $\rho_{amb} = 1.148 \text{ kg/m}^3$	59
4.7	Darcy and Forchheimer permeability coefficient and their uncertainties obtained from pressure tank test. PH1732 sample material	62
5.1	Parameters for modified Kays et al. model with heat conduction losses	73
5.2	Convective wall heat flux without blowing for several main-flow conditions. Subsonic regime all at $T_{t,g} = 523 \text{ K}$	81
5.3	Parameters for modified Kays et al. model applied to the subsonic flow transpiration cooling tests	83
5.4	Parameters for analytical calculation of temperature profile in porous wall	89
5.5	Permeability coefficients and their uncertainties for all tested materials obtained from cold flow tests with the sample integrated in the hot-gas setups	91
5.6	Reference dynamic viscosity quantities for used coolants (@ 300 K)	92
6.1	Coolant mass-flow rate, blowing ratio, and equivalence ratio for the LAPCAT scramjet at two flight Mach numbers	105
6.2	Coolant mass-flow rate, blowing ratio, and equivalence ratio for the ATLLAS ramjet	106

List of Tables

6.3	Coolant mass-flow rate, blowing ratio, and equivalence ratio for the scramjet demonstrator	106
6.4	Reference properties of hydrogen for the through-flow model obtained from <i>REFPROP</i> (@ 300 K) and generic permeability coefficients	108
A.1	Overview of the most important error sources in the measurement equipment	124
A.2	Estimated uncertainties in supersonic tests	127
A.3	Overview of uncertainties in through-flow analysis for air as a test gas	127
A.4	Estimated uncertainties in experiments using the uncooled, subsonic channel	127
D.1	Average parameters for exemplary elliptical combustion chamber calculation with hydrogen as a coolant. LAPCAT hypersonic vehicle concept with scramjet propulsion system at two flight Mach numbers	139
D.2	Assumed average parameters for exemplary circular combustion chamber calculation with hydrogen as a coolant. ATLLAS hypersonic vehicle concept with ramjet propulsion system at $M_\infty = 6$	140
D.3	Averaged parameters between inlet and outlet for rectangular combustion chamber calculation with hydrogen as a coolant. Scramjet demonstrator concept at $M_\infty = 8$. See Fuhrmann (2009)	140
D.4	Averaged parameters for generic combustion chamber calculation with hydrogen as a coolant	141

Nomenclature

Latin Symbols

a	model constant	$[-]$
A	area	$[m^2]$
B	heat-loss constant	$[W/(m^2K)]$
B	width	$[m]$
B_f	momentum transfer blowing parameter 1	$[-]$
b_f	momentum transfer blowing parameter 2	$[-]$
B_h	heat transfer blowing parameter 1	$[-]$
b_h	heat transfer blowing parameter 2	$[-]$
Bi	Biot number	$[-]$
c_0	vacuum speed of light	$[m/s]$
c_f	friction coefficient	$[-]$
c_p	specific heat capacity	$[J/(kgK)]$
C	porous wall properties constant	$[-]$
d	diameter	$[m]$
D	hydraulic diameter	$[m]$
F	blowing ratio	$[-]$
F	force	$[N]$
Gr	Grashof number	$[-]$
h	heat transfer coefficient	$[W/(m^2K)]$
h	Planck constant	$[Js]$
h	specific enthalpy	$[J/kg]$
H	(combustor) height	$[m]$
i	specific spectral radiation intensity	$[W/(m^2\mu m)]$
I	specific radiation intensity	$[W/m^2]$
k	Boltzmann constant	$[J/K]$
k	thermal conductivity	$[W/(mK)]$
K	integer value	$[-]$
K	permeability	$[m^2],[m]$
l	sample installation location	$[m]$
L	porous wall thickness	$[m]$
L	combustor length	$[m]$
M	Mach number	$[-]$

Nomenclature

\dot{m}	mass-flow rate	[kg/s]
n	exponent in viscosity-law	[–]
N	integer value	[–]
Nu	Nusselt number	[–]
p	pressure	[Pa]
Pr	Prandtl number	[–]
\dot{q}	heat-flux	[W/m^2]
\dot{Q}	heat-flow	[W]
r	radius	[m]
r	recovery factor	[–]
R	specific gas constant	[$J/(kgK)$]
R, B, F	constants for in situ calibration	[–]
Re	Reynolds number	[–]
s	specific entropy	[J/kg]
St	Stanton number	[–]
t	time	[s]
T	temperature	[K]
u	velocity component in main-stream direction	[m/s]
U	bulk velocity magnitude	[m/s]
v	velocity component in wall-normal direction	[m/s]
V	volume	[m^3]
\dot{V}	volume-flow rate	[m^3/s]
w	third cartesian velocity component	[m/s]
W	combustor width	[m]
x	distance in wall direction (porous wall)	[m]
x	distance in main-stream direction	[m]
X	non-dimensional distance in wall direction (porous wall)	[–]
y	distance in wall-normal direction	[m]
z	third cartesian co-ordinate	[m]

Greek Symbols

α	Pitot probe angle	[°]
α_1, α_2	constants	[–]
γ	isentropic exponent	[–]
Γ	density ratio	[–]
δx_i	uncertainty in variable x_i	[–]
ε	emissivity	[–]
ε	porosity	[–]
λ	wave length	[m]
θ	non-dimensional temperature ratio	[–]
Θ	cooling efficiency	[–]
μ	dynamic viscosity	[$kg/(ms)$]
ν	kinematic viscosity	[m^2/s]
ρ	density	[kg/m^3]
ϕ	equivalence ratio	[–]

Φ	blowing parameter	[–]
Ψ	temperature ratio	[–]
ξ	velocity ratio	[–]

Subscripts

0	no blowing, uncooled	
<i>aw</i>	adiabatic wall	
<i>b</i>	backside	
<i>c</i>	coolant	
<i>cal</i>	calibrated	
<i>CC</i>	combustion chamber	
<i>cu</i>	copper	
<i>D</i>	based upon hydraulic diameter	
<i>D</i>	Darcian permeability	
<i>ex</i>	exit	
<i>in</i>	inlet	
<i>fc</i>	film cooling	
<i>for</i>	foreign gas injection	
<i>F</i>	Forchheimer permeability	
<i>g</i>	hot-gas channel	
<i>m</i>	average	
<i>max</i>	maximum	
<i>n</i>	free convection	
<i>obj</i>	object	
<i>open</i>	open volume of porous material	
<i>p</i>	pore	
<i>pl</i>	coolant plenum	
<i>r</i>	recovery	
<i>rad</i>	radiation	
<i>s</i>	solid (porous wall)	
<i>s</i>	static	
<i>sink</i>	sink temperature	
<i>sp</i>	specific	
<i>stoich</i>	stoichiometric	
<i>ref</i>	reference	
<i>t</i>	total	
<i>w</i>	wall	
<i>win</i>	window	
∞	flight conditions	

Superscripts

–	averaged	
+	positive value	

Nomenclature

Abbreviations

<i>ATLLAS</i>	Aerodynamic and Thermal Load Interactions with Lightweight Advanced Materials for High Speed Flight
<i>C/C</i>	carbon/carbon
<i>C/C-SiC</i>	silicon carbide infiltrated carbon/carbon
<i>CFD</i>	computational fluid dynamics
<i>CFRP</i>	carbon fibre-reinforced plastic
<i>CMC</i>	ceramic matrix composite
<i>DARPA</i>	Defense Advanced Research Projects Agency
<i>DFG</i>	German Science Foundation
<i>DLR</i>	German Aerospace Center
<i>HSP</i>	hollow sphere packing
<i>ILSS</i>	interlaminar shear stress
<i>ITLR</i>	Institute of Aerospace Thermodynamics
<i>JAPHAR</i>	Joint Airbreathing Propulsion for Hypersonic Application Research
<i>LAPCAT</i>	Long-term Advance Propulsion Concepts and Technologies
<i>LES</i>	large eddy simulation
<i>LSI</i>	liquid silicon infiltration
<i>NASP</i>	National Aero-Space Plane Program
<i>NIST</i>	National Institute of Standards and Technology
<i>ONERA</i>	Office National d'Etudes et Recherches Aérospatiales
<i>PREPHA</i>	Research and Technology Program for Advanced Hypersonic Propulsion
<i>RBCC</i>	rocket based combined cycle
<i>RTM</i>	resin transfer moulding
<i>SFB – TRR40</i>	collaborative research center 'Technological foundations for the design of thermally and mechanically highly loaded components of future space transportation systems'
<i>SHEFEX</i>	Sharp Edge Flight Experiment
<i>SSTO</i>	single stage to orbit
<i>STS</i>	Space Shuttle Transportation System
<i>TBCC</i>	turbo based combined cycle
<i>TSTO</i>	two stage to orbit
<i>WHIPOX</i>	Wound Highly Porous Oxide composite

Abstract

For faster and more efficient air transportation systems sustained hypersonic flight offers a great potential. One possibility is to use scramjet (supersonic combustion ramjet) propelled airbreathing space planes because this propulsion system can be very efficient at very high flight Mach numbers. In the past several large-scale research programs were carried out in the USA, Europe and Russia to solve the technical difficulties, which are inherent with a novel propulsion system.

Currently, several research programs are ongoing investigating the technological foundations in this area such as aerodynamic efficiency, system level design and integration, environmental aspects and thermal efficiency, and protection systems. The last is especially addressed by the European research program ATLLAS and the German national project SFB-TRR40, in which the work of this thesis was embedded in. The work presented here focusses on the transpiration cooling technique applied to porous CMC (ceramic matrix composite) materials, which offer a great potential for the use in aerospace applications. The aim was to identify the cooling mechanisms involved and verify and extend models describing these phenomena, which can be found in literature.

For this, an experimental study was carried out using the hot-gas flow facility available at the ITLR (Institute of Aerospace Thermodynamics of the Universität Stuttgart) and several porous carbon/carbon CMC samples provided by the DLR (German Aerospace Center) were investigated with respect to their cooling efficiency. First, the material was characterized with respect to their outflow and through-flow behavior in separate test setups. Then, these samples were exposed to heated supersonic and subsonic flows generating different heat loads. The surface temperature of the porous wall segments were determined using thermocouple measurements and in situ calibrated infrared thermography. As coolants gaseous air, argon, and helium were used. Since the models available in literature were not capable of representing the specific thermal phenomena in our test setup, they had to be extended. This was verified by a number of transpiration cooling experiments at different temperature levels and heat loads. With the help of this model, transpiration cooling prediction in

aerospace (testing) application within non-adiabatic environment is possible when knowing the main-stream conditions.

Furthermore, the pressure drop over the C/C samples was recorded in the transpiration cooling tests as well as in cold-flow experiments after a detailed characterization of the samples with respect to their through-flow behavior. The influence of the non-isothermal wall, which is common in aerospace application, on the pressure loss was identified and the Darcy-Forchheimer equation was extended for non-isothermal through-flow. This approach was verified with the experimental data for different thermal situations, heat loads and coolant gases whilst only the coolant properties and the hot-gas side wall temperature had to be given to obtain a result for the pressure drop.

As a last step, the model for the cooling efficiency was coupled with the extended model for the through-flow behavior to eliminate the need to know the wall temperature. This was also verified using the available experimental data. Now, only the main-stream conditions and the coolant properties need to be known. Then, this model was used to give an estimate of the coolant mass-flow rate and the supply pressure drop for several aerospace application related combustion chambers. It was shown that it is possible to use transpiration cooling with hydrogen as a coolant in high-temperature and high-pressure environments given the availability of a suitable wall material allowing reasonable supply pressure levels at the required coolant mass-flow rates.

Kurzfassung

Wegen des starken Wachstums des Transportsektors wird auch die Nachfrage nach schnelleren und kostengünstigeren Flugzeugen oder Raumtransportsystemen immer größer. Hier bieten Flugzeuge welche im Hyperschallbereich operieren, ein großes Potenzial. Eine Möglichkeit ist es, Scramjet Antriebssysteme zu verwenden, da dieses Antriebskonzept bei hohen Machzahlen einen guten Wirkungsgrad aufweist. In der Vergangenheit wurden bereits verschiedene Technologieprogramme in den USA, Europa oder Russland durchgeführt, welche die technologischen Schwierigkeiten, die ein neues Antriebskonzept mit sich bringt, zu bewältigen versuchten.

Derzeit gibt es in Europa verschiedene Forschungsprojekte, welche sich mit den technologischen Grundlagen auf diesem Gebiet befassen. Die wichtigsten Bereiche sind hier die aerodynamische Güte des Flugzeugkonzeptes, Systemauslegung und die Integration der einzelnen Komponenten, Umweltaspekte und die Optimierung der thermischen Effizienz des Antriebes bzw. die Qualifikation und Entwicklung von Kühlmethode. Der letzte Punkt wird im Besonderen durch die Forschungsprojekte ATLLAS und den Sonderforschungsbereich SFB-TRR40 behandelt, wobei diese Arbeit als Teil dieser Projekte stattfand. Die hier diskutierte Methode, die Transpiration Kühlung mit keramischen Verbundwerkstoffen (CMC), bietet ein sehr hohes Potenzial zur Anwendung im Bereiche der Luft- und Raumfahrt. Das Ziel dieser Arbeit war die Kühlmechanismen, welche hierbei zu beachten sind, genau zu identifizieren und im Hinblick auf bereits in der Literatur vorhandene Modellansätze zu überprüfen.

Hierbei wurden mehrere Versuchreihen unter Verwendung der Heißgasversuchsanlage am Institut für Thermodynamik der Luft- und Raumfahrt (ITLR) an der Universität Stuttgart durchgeführt, wobei die porösen Carbon/Carbon-Wandmaterialproben vom Deutschen Zentrum für Luft- und Raumfahrt (DLR) bereitgestellt wurden. Zuerst wurde das Material in einem separaten Versuchsaufbau bezüglich seiner Durchströmeigenschaften und seinem Ausflussverhalten untersucht. Danach wurden diese unter Anwendung der Transpiration Kühlung in Über- und Unterschallströmungen bis zu einer Totaltemperatur von 1120 K getestet. Die Oberflächentem-

peratur des porösen Wandsegments wurde mit Hilfe von Thermoelementmessungen und quantitativer Infrarot-Thermografie bestimmt. Daraus konnte die Kühleffizienz bestimmt werden. Als Kühlgas wurden Luft, Argon und Helium verwendet.

Es wurde festgestellt, dass die Transpirationskühlungsmodelle aus der Literatur nicht ausreichend in der Lage waren, die thermische Situation in unserem Versuchsaufbau wiederzugeben. Daher wurde ein existierendes Modell im Hinblick auf die an der porösen Wand auftretende Querwärmeleitung modifiziert und durch Messungen bei verschiedenen Totaltemperaturen, Wärmelasten und bei Fremdgasausblasung validiert. Nun ist es möglich, das erweiterte Transpirationskühlungsmodell auch auf andere, nicht adiabate Versuche oder Anwendungen aus dem Bereich der Luft- und Raumfahrt anzuwenden.

Des Weiteren wurde der Druckverlust, welcher bei der Durchströmung der porösen Proben auftrat, untersucht. Diese Daten wurden sowohl im Kaltgastest als auch direkt im Transpirationskühlungsversuch gewonnen. Da die durchströmte, poröse Wand unter Wärmelast nicht isotherm ist, beeinflusst diese auch die Fluidtemperatur in der Wand was mit dem Druckverlust rückgekoppelt ist. Um diesen Effekt näher zu quantifizieren wurde die Darcy-Forchheimer-Gleichung erweitert. Dieses konnte anhand der Messergebnisse verifiziert werden, wobei verschiedene Heißgasströmungsbedingungen und Kühlfluide verwendet wurden.

Zuletzt wurde das erweiterte Modell für die Transpirationskühlung mit dem erweiterten Modell für die Durchströmung eines porösen Materials gekoppelt. Da beim letzteren immer die Kühlgastemperatur und die Wandtemperatur an der Heißgasseite gegeben sein mussten, wurde dieses so modifiziert, dass man nun nur noch die Kühlgaseigenschaften und die Hauptströmungsbedingungen kennen muss, um den Druckverlust über die poröse Wand bei Transpirationsvorgängen zu ermitteln. Das gekoppelte Modell wurde dann für verschiedene realitätsnahe Hauptströmungsbedingungen angewandt, und es konnte gezeigt werden, dass es bei Verwendung von Wasserstoff als Kühlgas in den meisten Fällen möglich ist mit wenig Kühlgaseinsatz die Brennkammerwände effizient zu kühlen. Hierbei ist es wichtig, dass geeignete Wandmaterialien zur Verfügung stehen, damit bei gegebenem Kühlgasmassenstrom ein vertretbarer Druckverlust gegeben ist.

Introduction

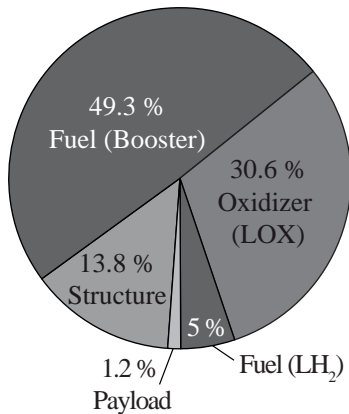
In a globalized and connected world the transportation markets grow rapidly. This is due to the worldwide interlinked design and manufacturing processes, global trade and logistics, and the increasing popularity of international vacations. The growth takes place within the sea transportation sector, where new larger vessels of greater quantity than before are demanded, but foremost within the air transportation sector. Here, not only more efficient planes, airport systems and logistics and therefore lower costs are important, but also safe travel at shorter flight duration. The market share of business travelers managing the global economy is growing steadily. Now, new plane concepts at high flight velocities offer a great potential of saving time and money by reducing the flight time between intercontinental destinations. The goal of current European research projects such as LAPCAT II (Serre and Defoort 2009) or ATLLAS (Steelant 2009a) is to develop concepts for supersonic or hypersonic space planes cruising at high altitudes and velocities to cut the flight time between, for example, Frankfurt and Sydney into a fraction of what it is now.

For space transportation basically the same motivation to develop a more cost-effective way into orbit can be found: The increasing need for communication infrastructure, either for civil or military application, but also the continuation of manned space flights demand new launcher systems, which are stressing the mostly public budgets less than today. Only a good balance between costs and benefits of human space flight ensures future missions to, for example, the moon or other planets. Therefore, new concepts have to be found.

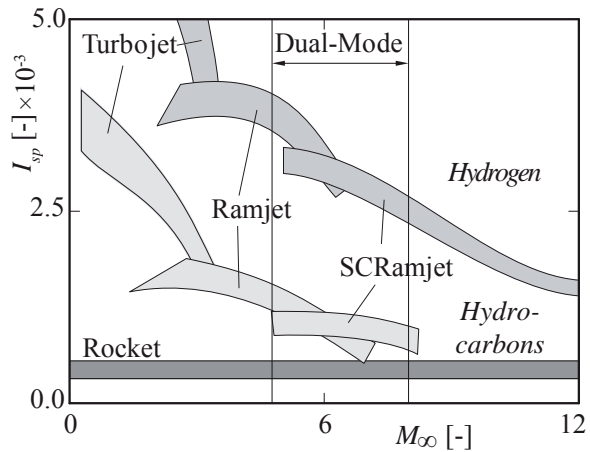
When striving for means of transportation at high supersonic or hypersonic speeds (up to flight Mach numbers of 12 or even higher), either for commercial aviation or for space flight, one has to overcome many challenges (Polezhaev 2000). New propulsion concepts at higher efficiency, the integration of the vehicle components and their aerodynamic optimization, and the exposition of some aircraft components to extremely high aerothermal loads are the most challenging topics on the way to new plane concepts. The research described in this thesis focusses on a promising cooling technique, called transpiration cooling, to cope with these high aerothermal loads whilst incorporating modern, lightweight composite materials.

1.1 Hypersonic Airbreathing Propulsion

To achieve the goal of affordable, high speed flight the payload to total aircraft mass ratio has to be significantly increased. The mass distribution of the Space Shuttle Transportation System (STS) is given in Fig. 1.1(a). One notices that the oxidizer for the main-engine (liquid oxygen) is more than 30 % of the total vehicle mass, which is 2040 tonnes. The payload into the lower earth orbit is only 1.2 %, a quite insignificant figure if one relates this to the effort made by using the STS. This clearly points out the difficulty of rocket propulsion systems, where a great part of the start mass is consumed by the oxidizer which on top of this has to be carried during the flight. In contrast, along the flight trajectory in the dense part of the atmosphere enough oxidizer in the form of gaseous air is available, which could be used. This concept has always been followed by modern turbojets or turbofans.



(a) Mass distribution of the Space Shuttle Transportation System (STS)



(b) Specific impulse of various engine types as a function of flight Mach number

Figure 1.1: Justification for hypersonic airbreathing propulsion systems

A widely used measure for the performance of propulsion systems is the specific impulse, the ratio of the engine's net thrust T and specific fuel consumption, meaning how much thrust does the engine generate at a given fuel weight.

$$I_{sp} = \frac{T}{g\dot{m}_{fuel}} = \frac{U_e}{g} \quad (1.1)$$

Here, g is the gravitational constant. For rockets both fuel and oxidizer mass, which is carried by the rocket or space plane, are included in \dot{m}_{fuel} . Fig. 1.1(b) shows the I_{sp} versus the flight Mach number M_∞ for different propulsion concepts and fuels. Looking at Eqn. 1.1 it is easy to understand, that the airbreathing concepts such as turbojets, ramjets and scramjets have a higher I_{sp} than rockets. For higher flight Mach numbers this figure of merit decreases due to the higher aerodynamic losses. At about $M_\infty = 4$ turbojets cannot be used anymore because of the difficult

interaction of the rotating parts of the engine and the supersonic air flow with strong shock systems. For the higher flight mach number only ram-based engines can be used, whilst at $M_\infty = 6 - 7$ ramjets yield also too high aerodynamic losses. Hydrogen as a fuel has a much higher energy density than hydrocarbon based fuels. Hence the I_{sp} which can be reached are significantly higher. For flight Mach numbers beyond 8 only hydrogen fueled scramjets seem to be feasible.

The term hypersonic flow refers to a flight regime of $M_\infty \gg 1$, typically $M_\infty > 5$ is referred to in literature. Heiser and Pratt (1994) define this more precisely by putting the borderline between supersonic and hypersonic flow where real gas effects in air become important. This happens at a total temperature of $\approx 1700 K$ or at flight Mach numbers of ≈ 6 .

1.1.1 Ramjet Engines

Like a standard turbojet or turbofan engine, ramjets or scramjets also require a compression of the air from the atmosphere, which is used as an oxidizer in the combustion chamber. This ensures efficient combustion processes. To achieve this without a rotating compressor or fan, the deceleration of the high-speed air is used to raise the pressure within the inlet (ram-effect). This is only applicable at high supersonic flight Mach numbers. Up to this point the ramjet cannot be used because not enough air mass-flow per inlet area can be captured. To accelerate the vehicle to these flight speeds, conventional engines such as turbojets and rockets can be used and integrated into the ramjet propulsion system. If a turbo engine is used, this is called a turbo based combined cycle (TBCC). If a rocket engine has been integrated it is denoted as a rocket based combined cycle (RBCC). One advantage of the RBCC is that this propulsion system could also be used once the vehicle has left the part of the atmosphere, where enough oxygen is available to run in ram mode. For sustained hypersonic flight for civil transportation a single stage to orbit (SSTO) concept is sufficient because the flight Mach number and the altitude are comparatively low. To replace current space transportation systems also a second stage might become necessary, which will be propelled by a rocket engine (two stage to orbit - TSTO).

The general function of a scramjet is displayed in Fig. 1.2 (Scheuermann 2010). The air is flowing towards the vehicle at a high Mach number (station 0) and is being decelerated over the forebody of the vehicle and the inlet. Several oblique

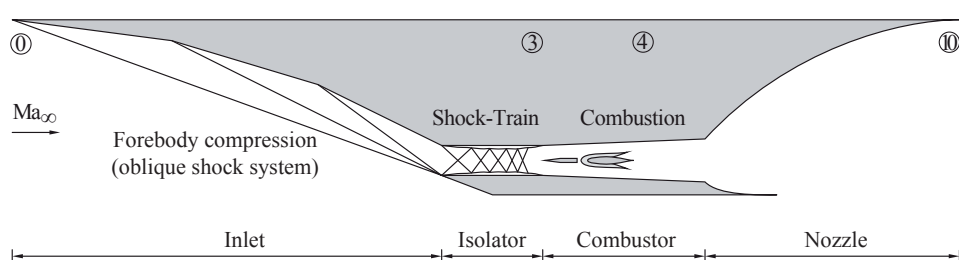


Figure 1.2: Diagram of a possible scramjet propulsion system

1 Introduction

shock waves occur causing substantial total pressure loss which decreases the overall grade of efficiency of the scramjet propulsion system. Therefore, it is important to design the compression in a way that the number of shocks is low and that they are relatively weak. Within the isolator a further compression by a so-called shock train system or pseudo-shock (Matsuo et al. 1999) occurs, which is small compared to the forebody/inlet compression. The isolator is merely used to aerodynamically decouple the combustion chamber from the inlet. Slightly fluctuating pressure ratios between combustor and the inlet can be compensated without causing an operational malfunction (unstart) of the engine. After the isolator (station 3) the fuel is being injected, ignited, and burnt (station 4). This is achieved by using strut injection (see, for example, Scheuermann et al. (2008)), wall injection or both (see, for example, Vellaramkalayil et al. (2009), Vellaramkalayil et al. (2010)). Now, the flow is being accelerated in the nozzle until station 10 is reached. The nozzle can have several shapes depending on the geometry of the ramjet, such as bell or plug nozzles for axis-symmetric engine configuration or a SERN (Single Expansion Ramp Nozzle) which can be used for 2D designs.

1.1.1.1 Ramjet, Scramjet, and Dual-Mode Scramjet Engines

In Fig. 1.3(a) through Fig. 1.3(c) (Scheuermann 2010) the different types of ramjets are shown. The engine of choice for applications up to a flight Mach number of 5 is the ramjet without supersonic combustion (see Fig. 1.3(a)). Here, the deceleration of the flow over the forebody and inlet diffuser and inlet throat is so large that the flow turns subsonic by a normal shock before entering the combustion chamber. The combustion takes place in high static pressure and temperature environment whilst injection, mixing and ignition are not as critical due to the relatively low flow velocities at this location. Afterwards, a convergent-divergent nozzle has to be used to accelerate the flow to supersonic velocities to generate the desired thrust and to convert the internal energy added in the combustion chamber to kinetic energy. Within the combustion chamber high static pressure levels are reached causing high thermal loads on the combustor walls and fuel injectors.

For higher flight velocities of above $M_\infty > 8$ the airflow cannot be decelerated to subsonic velocities in the combustion chamber without tremendous compression losses. Therefore, the flow within the combustion chamber and nozzle is always supersonic, which is the concept of a supersonic combustion ramjet (SCRamjet). No throats, neither in the inlet diffuser nor at the nozzle are present anymore. Problematic is the stable combustion and ignition of the flame within the the high-speed flow. Furthermore, the total temperature levels at $M_\infty > 8$ exceed 3000 K. This causes challenging design issues concerning the the cooling of the propulsion system, leading edges and aircraft skin.

Between flight Mach numbers of 5 and 8 a so-called *dual-mode* scramjet can be used to overcome this flight regime void. At lower flight velocities a shock train appears in the isolator in combination with high combustion chamber pressure,

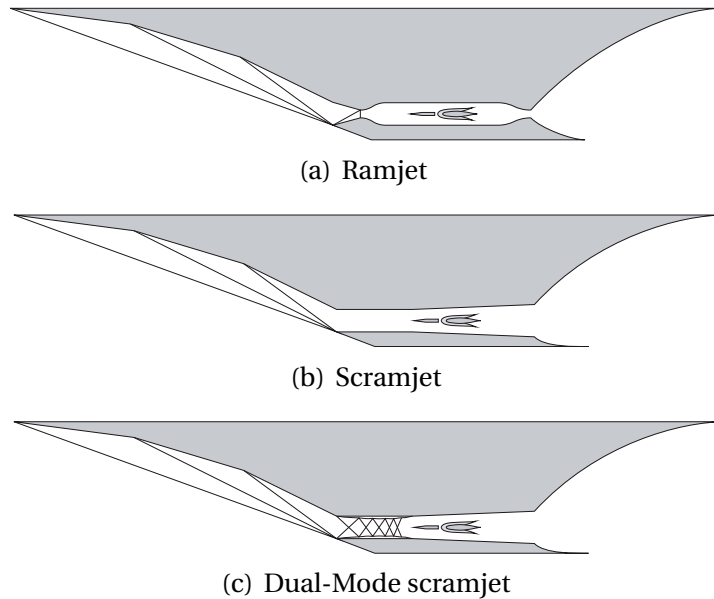


Figure 1.3: Schematic of different ram propulsion systems

which decelerates the flow to subsonic velocities within the combustor. The missing geometrical throat is replaced by a thermal throat. The latter is generated by high heat release in the combustion chamber which increase the static temperature and local speed of sound. From here, the flow can be accelerated again in the diverging geometry. For higher velocities the length of the shock train diminishes and a supersonic core forms (Matsuo et al. 1999). With further acceleration of the vehicle, the shock train will disappear and the engine will work like a regular scramjet. The aerodynamic design of such a propulsion system is extremely challenging, offers in contrast when combined with another cycle (turbo or rocket) the possibility to fly a complete trajectory, from runway start until landing, with one propulsion system. Recent research projects focus or have focussed on such a concept (Serre and Defoort 2009; Novelli and Koschel 2001).

It can be said, that with respect to the system complexity of the propulsion unit ramjets or scramjets do not require a significantly higher design effort than turbojets. Nevertheless, the engine components and the vehicle are highly coupled. Due to the extremely high interaction between the propulsion system and the vehicle fuselage, which acts as the inlet and nozzle which again are aerodynamically coupled with the combustion chamber, a segregated layout is impossible. During the design phase both have to be treated as one integrated system using several design iteration steps in contrast to the layout of podded turbofans for general aviation purposes. These can be engineered and optimized almost as a stand alone unit and installed under different fuselages.

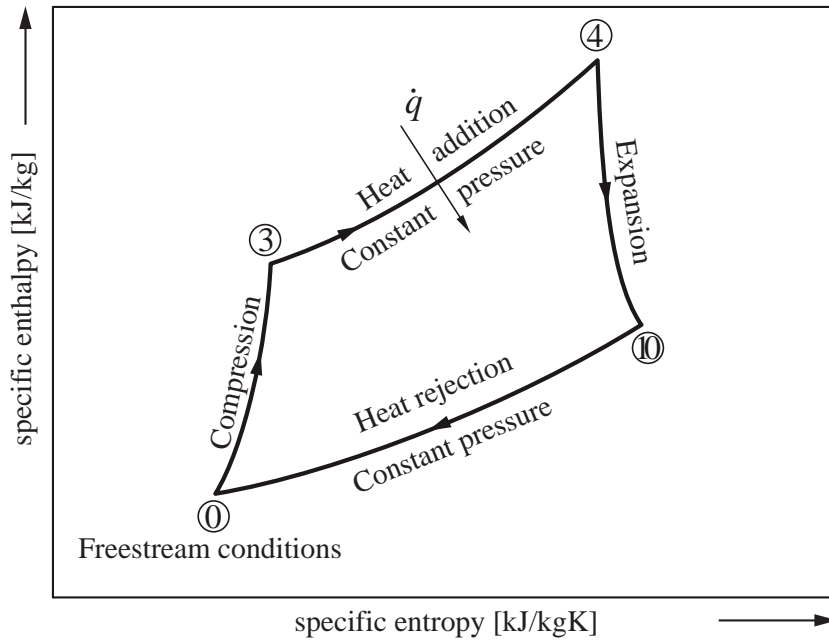


Figure 1.4: Schematic of the Brayton-cycle $h - s$ diagram

1.1.1.2 The Brayton Cycle

The thermodynamic cycle of the ramjet is called *Brayton Cycle*, the simplified schematic is shown in Fig. 1.4, where the specific enthalpy h of the flow is plotted versus the specific entropy s . The nomenclature is related to the turbojet denominations. From station 0 (∞) the air is compressed via an irreversible, polytropic process until the combustor inlet is reached (station 3). The losses are created by friction and the shock waves in the inlet. The combustion heat is added within an isobaric process. The high entropy gain caused by the total pressure loss in the combustion chamber can be seen. From station 4 (exit of combustion chamber) the flow is expanded in the nozzle until its exit (10), due to friction in an irreversible manner. To close the thermodynamic cycle, an isobaric process at ambient pressure connects to the flight condition again (0). This can be seen as a virtual process, where the exhaust plume mixes with the ambient.

1.1.2 Major Technical Challenges

For sustained, hypersonic flight for civil application severe technical hurdles have to be overcome to design a safe and cost-efficient vehicle. First, the adequate plane concept and propulsion system have to be found, which is a highly integrated process. The aerodynamic efficiency has to be sufficiently high so that the maximum thrust produced by the engine is not consumed by the vehicle drag. This is especially important during the transonic acceleration phase, where the lift-over-drag ratio can become very low. By changing the aerodynamic shape of the plane the inlet conditions for the ramjet might change again and therefore different thrust might be available. The same is valid for optimizing the flight trajectory, where flight altitudes

and velocities are altered and the free flight conditions are changed. New propulsion concepts such as combined cycle engines have to be developed and the present design tools have to be enhanced or even established. The multi-use capability of the engines (re-ingitability) has to be ensured to cut maintenance costs and increase safety, similar to modern turbojets. For this, inlet unstart and flame blow-off need to be ruled out, also for off-design conditions.

Not only for the aerodynamic performance, but also for the prediction of the heat flux distribution along the vehicle or the engine inlet it is important to understand laminar-turbulent transition in hypersonic velocity flows (see Schneider (2004)).

Furthermore, $5 \text{ MW}/\text{m}^2$ of wall-heat flux or more than 3000 K wall temperature are possible at a flight Mach number of 8 (Polezhaev 2000)). These loads are especially apparent at the nose, in the leading edge region of the plane's wings, and within the propulsion systems. Here, classical materials like metals or simple ceramics can no longer be used and would thermally and structurally fail. Hence, one is forced to replace these with high-temperature, lightweight components, some of them with active cooling. New porous materials offer in this context very efficient cooling mechanisms such as transpiration cooling and internal cooling within the structure itself. Those materials have to be tested and qualified, which is part of this study. Also, due to different volume distribution of the fuselage and the different flight altitudes compared to modern passenger jets, completely new structures and design philosophies have to be used, for example, for the passenger cabin and tanks.

In addition, there are two more practical hurdles to be overcome. First, is the sonic boom generation of supersonic aircrafts. Nowadays, governments only permit military supersonic aircrafts over land because of the disturbing character of a sonic boom perceived by the population. This is also the reason why the Concorde supersonic aircraft only operated between London or Paris and New York City and Rio de Janeiro because most of the flight trajectory was over the Atlantic ocean. By shaping the aircraft carefully it is possible to modify the pressure level at the ground and therefore the 'loudness' of the sonic boom (Plotkin et al. 2005). Secondly, the limits for environmental pollutants are constantly tightened by authorities. This currently generates additional design issues for the turbojet manufacturers since, for example, NO_x limits are reduced, meaning that the combustion temperature needs to be limited, which again limits the efficiency of the engine. Ramjets are envisaged to have even higher static combustion temperature than turbojets, which increases the difficulties significantly, also because the cruise flight would take place in relatively high altitudes.

1.1.3 Selected Hypersonic Research Programs

Already in the late 1950s and early 1960s, extensive research on a hypersonic test plane at above $M_\infty = 6$, the X-15 (Walker and Weil 1963) was carried out in the United States. Here foundations for the technical challenges in the structural, thermal, propulsive, guidance and control, and piloting field were carried out. This vehicle was still propelled by a rocket motor.

1 Introduction

A further major research project which was launched in the USA in 1986 was the National Aero-Space Plane Program (NASP) (Barthelemy 1989), a manned SSTO concept using a hydrogen fueled scramjet propulsion system. The major research focus was set on the aerothermodynamic design, the development of the propulsion unit and new, advanced, high-temperature materials, by sticking to the SSTO concept. Due to cost reasons this project was terminated in 1993 but some of the know-how was carried over into the Hyper-X programme, which was substantially downsized compared to the NASP.

The first outcome of this project was the X-43A flight demonstrator (Volland et al. 2006), which was the first hydrogen fueled airframe integrated scramjet engine. First, the vehicle was attached to a B-52 airplane, from which it was launched and accelerated by a Pegasus rocket. At a flight Mach number of around 7 the X-43A was separated from the rocket and the scramjet ignited with a hydrogen-silane mixture, whilst afterwards the fuel was switched to pure hydrogen. For about 11 s of the flight a positive thrust was measured. Some scientific highlights of the $M_\infty = 7$ flight data have been summarized by McClinton et al. (2005). The second flight in 2004 at $M_\infty = 9.68$ had an acceleration phase for about 10 s. Here, a higher focus on aerothermal loads at the composite material leading edges was set. A comprehensive overview of the X-43 and the lessons learned from this program have been published by Peebles and Allen (2008).

The X-51 program (Hank et al. 2008) is the direct successor of the X-43 as a scramjet demonstrator, but is sponsored by the Defense Advanced Research Projects Agency (DARPA) of the US government (Department of Defense). Since it is a military project the fuel is a hydrocarbon (JP-7, a US Air Force propellant). The envisaged flight Mach number is 6, but the targeted operation time of the scramjet is around 240 s. The injection of the fuel into the combustion chamber happens at multiple locations and the combustor walls are cooled regeneratively by the fuel. The maiden flight of the X-51 took place on May 26th 2010 whilst a flight Mach number of 4.8 at 140 s of scramjet propulsion could be reached. The demonstrator was launched by similar means as the X-43.

In Europe recent efforts with respect to hypersonic flight research on national level (France, Germany) and also on the European level can be seen. Within the framework of the French research project PREPHA from 1992 until 1998 (Falempin et al. 1998) fundamentals of scramjet propulsion were investigated including the development of large-scale ground testing facilities. In Germany, the TSTO concept *Sänger* was developed during the nineties (Hirschel 1993; Weingartner 1993). Based upon these two projects the German-French JAPHAR project was initiated in 1997 (Novelli and Koschel 2001), combining the experiences available in both countries. During this program, studies concerning the performance of a hydrogen fueled dual-mode ramjet between flight Mach numbers of $M_\infty = 4 - 8$ were carried out. Investigations on supersonic combustion, either with experiments or with the use of computational fluid dynamics (CFD), were emphasized.

More recently within the Long-term Advanced Propulsion Concepts and Technologies (LAPCAT) project co-funded by the European Commission (EC) (Steelant 2008a) considerable research on vehicles for civil hypersonic sustained flight was conducted. It investigated concepts at $M_\infty = 5$ and $M_\infty = 8$. This project was succeeded by LAPCAT II (Serre and Defoort 2009; Steelant 2009b), to further enhance the systems and technologies developed in its predecessor. The intake design and performance, environmentally friendly (low NO_x) combustors, nozzle design and performance, and structural analysis are especially addressed. The engines foreseen for the hypersonic vehicle are combined cycle (sc)ramjets and shall be analyzed and optimized with respect to their cycles and airframe integration. Eventually, a small-scale flight model is supposed to be tested within hypersonic wind-tunnels.

To ensure technology readiness with respect to the available materials and cooling technique once conceptual studies were successful, the project Aerodynamic and Thermal Load Interactions with Lightweight Advanced Materials for High Speed Flight (ATLLAS) (Steelant 2008b) was started in 2006. The design of a $M_\infty = 3$ and $M_\infty = 6$ cruise vehicle was as well part of this study as the enhancement of the available numerical capabilities with respect to the simulation of aerothermodynamics and material interaction problems. Actively cooled ceramic matrix composite (CMC) or ultra high temperature metals were tested in model rocket combustion chambers, hypersonic wind tunnels, and ram-based facilities. Most of the research presented in this thesis was embedded within this project.

Furthermore, the Research Training Group *Aero-Thermodynamic Design of a Scramjet Propulsion System for Future Space Transportation Systems* funded by the German Science Foundation (DFG) (Weigand and Gaisbauer 2009) was founded in 2005. This is a nine-year lasting research project of German universities and the German Aerospace Center (DLR). The goal of this program is to develop a scramjet demonstrator vehicle and perform focused, but interconnected research on the inlet aerodynamics, the combustion processes and the optimization of its efficiency, and the exhaust nozzle. Especially, the strong interaction between the components of such a propulsion system is emphasized.

Another German research project funded by the DFG is the collaborative research center SFB-TRR40 'Technological foundations for the design of thermally and mechanically highly loaded components of future space transportation systems'. Here, novel rocket propulsion technologies are explored focusing on the expansion nozzle, fuel injection and alternative fuels, combustion chamber cooling, and new methods for rocket base-flow control. Amongst others, a subproject focusing on transpiration cooling using CMC materials is installed within this collaborative research center.

1.2 Motivation and Approach

The major part of the research presented in this thesis was embedded within the framework of the ATLLAS project and supported by experiments embedded within

1 Introduction

the SFB-TRR40 project. The goal of this study was to test and qualify CMC materials for the application in rocket or scramjet engines, whilst increasing the thermal efficiency of what is currently possible. Transpiration cooling applied to porous CMC material is a very promising technique to cope with the extremely high heat loads which appear in such engines. Whilst already some literature is available, where, for example, C/C was used as a porous liner in model rocket combustion chamber, more detailed information of the surface temperature distribution, temperature field within the material and cooling efficiency are lacking. With this data, the application of transpiration cooling with CMC material walls can be verified against models from literature, which possibly have to be adjusted. When the physical phenomena within the material are understood, design of actual hardware is eased and results bear more confidence.

At the ITLR a test bench is available which was designed for supersonic combustion experiments. This was used to create a high-temperature supersonic flow in which porous C/C material could be tested whilst applying transpiration cooling to it. Since this facility is continually running, steady state data of the surface temperature of the C/C samples could be acquired by means of infrared thermography and thermocouple measurements for a variety of cooling conditions in a $M = 2.1$ flow. This Mach number corresponds approximately to a value which can be found in a combustion chamber of a scramjet flying at $M_\infty = 5 - 7$. Besides air as a reference coolant, gaseous helium and argon were used to investigate the effect of the coolant's properties on the surface temperature. After the supersonic tests campaigns were completed, investigations using an uncooled channel with a larger cross-section at subsonic flow conditions were carried out to support the findings from the supersonic experiments. This test campaign was embedded in the collaborative research center SFB-TRR40. The test samples were provided by the DLR, Institute of Structures and Design, and were of similar material which has also been used in rocket thrust chamber tests. Therefore, the research was closely related to a possible application in high-pressure environments.

In the following chapter, the state of the technology concerning cooling methods is briefly described, focusing on active cooling techniques. This is followed by a summarization of the theoretical background concerning transpiration cooling and porous walls. Then, the experimental setup featuring the supersonic channel and the uncooled channel is explained including an overview of the measurement methodology. The outflow and through-flow behavior of C/C material was investigated and experimental approach and the results are shown afterwards. These tests were carried out in a separate cold flow setup to understand the flow phenomena in the porous walls in more detail.

Then, the findings from the hot-gas transpiration cooling tests are presented including two-dimensional temperature maps of the cooled surface. The cooling efficiency at different hot-gas conditions using different coolants has been derived and compared to models from literature and amongst each other. From this data, a heat-balance model has been derived which is able to predict the wall temperature

within the investigated parameter range. Furthermore, an equation to calculate the pressure drop over a non-isothermal porous wall subject to transpiration cooling is presented, which was validated against the experimental data. Finally, the transpiration cooling heat-balance model was exemplarily applied to some aerospace applications, including scramjet and rocket combustion chambers using gaseous hydrogen as a coolant. Here a prediction of the needed coolant mass-flow rate and the expected pressure loss over the CMC wall has been derived. The applicability of transpiration cooling for the desired application is shown.

Physical Background

2.1 Cooling Techniques for Aerospace Applications

Cooling of components of spacecrafts and rockets is a common and necessary technology. Especially within the propulsion system cooling techniques are widely applied. Turbine blades, combustors and nozzles have to be kept at a temperature, which is bearable by the material. With, for example, the STS or other reentry vehicles ablative and radiative cooling is used. Here, the high heat fluxes appearing during the ascent from orbit into the atmosphere are dealt with by allowing very high wall temperatures. This enables the hot surface to radiate a fraction of the incident heat flux back to the surroundings. Furthermore, the wall substrates ablates, meaning a phase change from the solid to the liquid and gaseous phase consuming melting and evaporation heat respectively which keeps the wall temperature at the desired limit. Ablation cooling is, for example, also used in the throat section of a rocket thrust chamber because here the highest heat flux appears. The disadvantage is that the ablation process significantly wears down the wall substrate, for example the ceramic tiles used with the STS, which have to be replaced before the vehicle can be flown again. This is costly and cannot be used for reusable vehicles such as space planes which require a short turn-around time. Therefore, active cooling needs to be applied to keep the wall materials at a temperature where no structural damages can appear even though the hot-gas temperature is well above the temperature bearable by the material. This is already the case in current aerospace propulsion systems where convective internal cooling is used for turbine blades (Dailey 2000; Weigand et al. 2001; Ligrani et al. 2003) and the combustion chamber (Valdevit et al. 2006). Rocket nozzles are often regeneratively cooled, where the fuel is the coolant (Mayer 2000; Woschnak and Oschwald 2001). In all cases, the coolant passes the to be cooled component on its backside and absorbs the heat conducted from the hot-gas side through the wall substrate. Turbulators can be used to enhance the heat transfer. For the external protection film cooling (Goldstein 1971) is a widely applied method to protect the hot-gas surface and it can be used in various configuration. Transpiration

2 Physical Background

cooling is a very promising cooling technique that offers very high cooling efficiency, especially because fuel could be used as a coolant, which was already proposed by Kahrs and Corbett in 1967. When using hydrocarbon fuels the limitations are possible coking or soot formation and the resulting blockage of the coolant flow path within the porous wall (Gascoin et al. 2010), especially for long duration missions. For short duration application (military missiles) there is a chance of applicability with hydrocarbons. Furthermore, with the availability of modern porous composite materials and the use in hydrogen fueled propulsion systems it displays a very useful cooling technique, also because of the great heat-sink properties of hydrogen. An introduction into film cooling in supersonic main-flows and transpiration cooling is given in the next sections.

2.1.1 Film Cooling

Both ablation and transpiration cooling are designed to protect the surface where the coolant enters the hot-gas environment. Therefore, both methods are very efficient. Nevertheless, practical problems limit the application of these methods significantly. Ablation cooling can only be used for a single or only a few operations because the wall substrate is being evaporated to achieve adequate cooling. It is often used where heat loads are extremely high and the reusability of the system can be sacrificed or is not of great importance.

The difficulties of transpiration cooling in the past was mainly due to the lack of suitable porous wall material. It has to be sufficiently porous to be able to penetrate enough coolant through it and at the same time be able to cope with the structural loads appearing in the system environment such as combustion chambers. In addition, the pores of the usable wall materials were of small order. This lead to clogging of the pores by soot in hydrocarbon fueled applications.

Hence, film cooling was introduced as a robust and widely used method for the cooling of solid surfaces. It is designed to protect the region downstream of the injection location as opposed to ablation or transpiration cooling. Two main concepts are currently used. First is the slot or 2D film cooling (see Fig. 2.1(a)), where the film is uniformly distributed over the downstream region and is being consumed by mixing with the main-stream flow after a certain distance. The second approach is a single hole jet or an array of inline or staggered film cooling holes, which can be inclined at a certain angle or be perpendicular to the main-flow region (see schematic in Fig. 2.1(b)). The shape of the holes can vary from circular to cross sections of cylinders to more complex geometries. This method is highly three dimensional and the surface temperature distribution is not uniform and strongly dependent on the geometry of the film cooling hole and the cooling parameters. As a coolant normally gases are used in gaseous hot-gas environments.

To describe the effect of the film cooling on the wall temperature a nondimensional temperature ratio, η_{aw} has been defined.

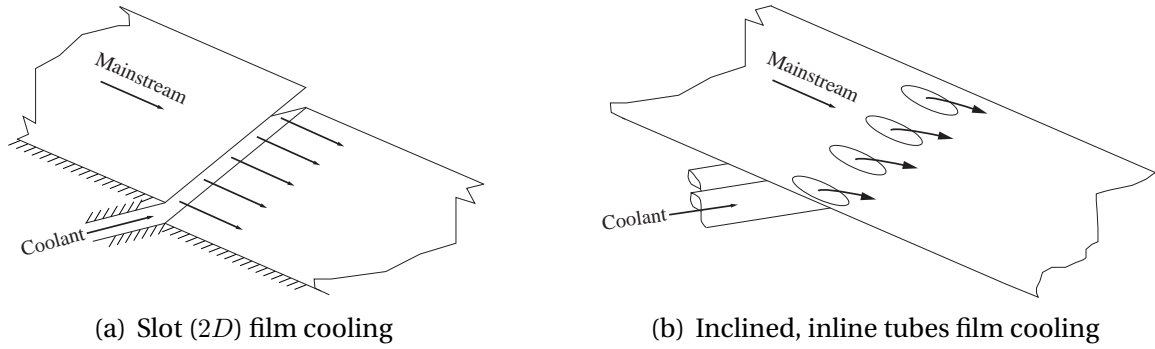


Figure 2.1: Schematic of film cooling configurations

$$\eta_{aw} = \frac{T_{aw} - T_{r,g}}{T_{c,exit} - T_{r,g}} \quad (2.1)$$

Here, $T_{r,g}$ is the recovery temperature (see Section 2.2) of the compressible main-flow. For incompressible flow, this variable collapses into the main-stream total temperature. $T_{c,exit}$ is the temperature of the coolant where it enters the main-flow. The adiabatic wall temperature T_{aw} is the temperature which would be observed, if the heat flux to the wall is zero. In the absence of blowing this value would become the free stream recovery temperature. The actual wall temperature T_w can differ from T_{aw} if for example heat conduction within the wall, internal or backside cooling of the wall is present. Then a heat flux would be present as well, but the adiabatic wall temperature is always larger than the physical wall temperature. To describe the effect of the film and its secondary flow structures on cooling performance, T_{aw} is the major parameter.

Two important parameters are used to describe the film cooling processes. F_{fc} the blowing ratio or mass-flux ratio between coolant and main stream and I the momentum ratio. The last is especially important when dealing with discrete hole film cooling.

$$F_{fc} = \frac{\rho_c v_c}{\rho_g u_g} \quad I = \frac{\rho_c v_c^2}{\rho_g u_g^2} \quad (2.2)$$

Furthermore, the properties of the coolant and the main-stream are of great importance and considered by using the definitions of the density ratio Γ and the temperature ratio Ψ .

$$\Gamma = \frac{\rho_c}{\rho_g} \quad \Psi = \frac{T_c}{T_{r,g}} \quad (2.3)$$

From analytical considerations or experimental studies, correlations for η_{aw} depending on the blowing ratio can be derived. Goldstein (1971) presented a comprehensive study summarizing many correlations and studies on 2D and 3D film cooling in incompressible and compressible main-flow. Typically, most of the considerations are dealing with fully turbulent main-flow because of the relevance for application.

2 Physical Background

In compressible flow the incompressible correlations can often be applied (Goldstein 1971), nevertheless in supersonic flow the influence of compression shocks and expansion fans on the coolant film has to be addressed separately and should be confirmed with additional experiments. Goldstein et al. (1966) presented a study on slot film cooling with supersonic ($M = 3$) main-flow where air and helium were used as a coolant. They carried out tests at different blowing ratios up to $F_{fc} = 0.408$ (air) and $F_{fc} = 0.02$ (helium) and found correlations for blowing with air and blowing with helium. Helium yields better cooling efficiency at the same blowing ratio because of its higher specific heat capacity. At a given blowing rate and step height, the cooling efficiency decreases quadratically with the stream wise distance x (helium and air with $F_{fc} < 0.12$). For higher air blowing rates η_{aw} decreases with $x^{-1.2}$ and is, therefore, higher because the recompression shock at the reattachment zone of the main-flow disappears.

In 1998 Aupoix et al. presented a study for rocket engine cooling investigating supersonic main-flow and film velocities using air and cryogenic nitrogen as coolants. The film was injected through a two dimensional nozzle into the main-flow. It was found that an underexpanded film, which means the film injection static pressure is larger than the main-flow static pressure, yields lower wall temperatures. Supersonic films tend to have a better cooling performance than subsonic ones. Because of their acceleration one can assume a laminar core in the film, which reduces mixing within the boundary layer as opposed to a turbulent film. Further studies on rocket thrust chamber cooling at engine-like conditions were presented by Arnold et al. (2009). The coolant (gaseous hydrogen) was injected through discrete 2D-slots distributed around the injector head of the combustion chamber at blowing rates of $1.61 < F_{fc} < 3.15$. They reported a maximum surface temperature reduction of $\approx 50 K$ and a maximum heat flux reduction by $\approx 45 \%$ at the high blowing rates and close vicinity of the injector head. Generally, heat fluxes and wall temperatures varied greatly in the circumferential direction of the combustion chamber due to the layout of the injector head and film cooling slots. This non-uniformity in the hot-gas high-pressure environment displays a major difficulty in applying this technique. In 1994 Juhany and Hunt investigated a supersonic film of air and helium in a supersonic main flow while the temperature ratio between the film and the mainstream was kept at unity.

More recently, Heufer and Olivier (2006) presented a numerical and experimental study on film cooling for external application in hypersonic flow, for example for inlet cooling. They used perpendicularly to the main-flow inclined film cooling slot up to a blowing ratio of $F_{fc} = 0.11$ and reported a significant reduction (50 %) of the heat transfer up to $x/h \approx 35$. Also, numerical research is currently being carried out by, for example, Konopka et al. (2010). They investigated supersonic film cooling using the LES method under favorable and adverse pressure gradients. They found that under an adverse pressure gradient, which is the case in inlets, isolator and combustion chambers, η_{aw} is substantially reduced.

Finally, it can be stated that film cooling is a potential candidate for the use in hypersonic airbreathing propulsion systems. Nevertheless, its performance can be comparatively low (see Eckert and Livingood (1954) and Laganelli (1970)) because of the rapid mixing of the film by the hot-gas and secondary flow structures induced by the film itself. Transpiration cooling might offer in this context due to its more homogeneous cooling distribution a superior cooling efficiency. In the following section, the transpiration cooling technique is introduced.

2.1.2 Transpiration Cooling

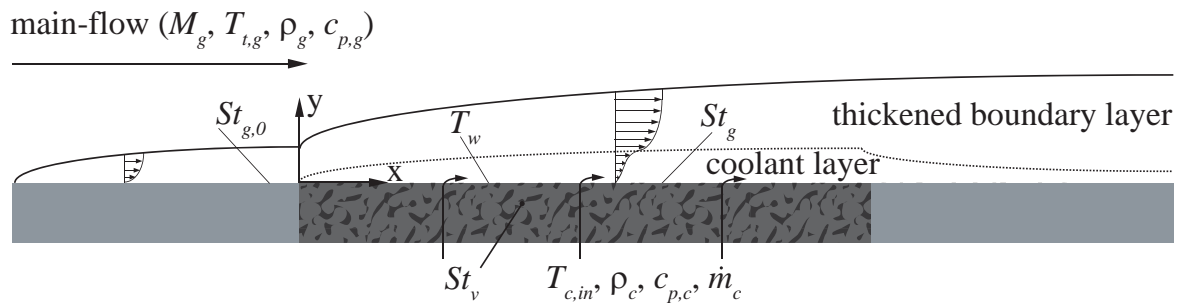


Figure 2.2: Schematic of a transpired boundary layer over a porous wall segment

In Fig. 2.2 the schematic of a transpiration cooling situation is shown where radiation to or from the wall plays a minor role. Within the propulsion system normally a boundary layer of a certain shape is already present, which formed over the forebody/inlet or within the isolator of the engine in case it is uncooled. The main-flow is at the Mach number M_g and has a specific total enthalpy of $c_{p,g}T_{t,g}$. The heat flux to the wall bounding the main-flow, can be described with the Stanton number $St_{g,0}$, whilst the index 0 indicates the state where no blowing is present. Afterwards, the transpiring section above a porous wall is shown. The coolant mass-flow rate \dot{m}_c is injected through the porous material into the boundary layer. Within the porous wall, a very efficient heat exchange between the coolant and the wall material takes place, which can be described by a volumetric Stanton number St_v . Due to the multiple cooling channels with a very small diameter in the porous substrate, this heat transfer can be very large, in extreme thermal equilibrium between the local wall temperature and the local coolant temperature occurs within the porous segment. The specific heat picked up by the coolant and carried back into the main-flow is then defined as $q_v = c_{p,c}(T_w - T_{c,in})$ for constant specific heat capacity of the coolant. Furthermore, the main-flow boundary layer is thickened and the temperature and velocity gradients at the cooled wall are reduced. Therefore the heat transfer and the skin friction is significantly reduced in the presence of blowing ($St_g \ll St_{g,0}$, $C_f \ll C_{f,0}$). This means that by using transpiration cooling not only the heat flux to the wall is significantly lowered but also the total drag of the combustion chamber can be reduced. The most commonly used parameter to describe transpiration

2 Physical Background

cooling processes is the blowing ratio (or blowing parameter) F . It is the mass-flux ratio between the coolant transpired through the wall and the main-flow similar to the blowing ratio used for describing film cooling:

$$F = \frac{\rho_c u_c}{\rho_g u_g} = \frac{\dot{m}_c / A_c}{\dot{m}_g / A_g} = \frac{\text{transpired mass flux}}{\text{hot gas mass flux}} \quad (2.4)$$

The first studies on transpiration cooling for aerospace application were carried out in the late 1940s. Rannie (1947) developed an analytical approach for the porous wall temperature analyzing the laminar, transpired sublayer and compared his theory to experiments. It only fit well for porous substrates of low thermal conductivity due to lateral heat conduction in the samples. Eckert and Livingood (1954) showed in an analytical study the superiority of this cooling technique versus purely convectively cooled and film cooled walls. The investigated Reynolds number range for turbulent flows was from $Re_g = 10^5 \dots 10^9$ and blowing ratios F up to 0.012, which is a similar regime studied in this thesis. For the hot-gas side heat transfer a Stanton number relationship between the case of transpiration cooling and uncooled wall was given. Thereby, thermal equilibrium between the porous wall and the transpiration coolant was assumed and radiation from the surroundings to the wall was neglected. The higher effectiveness of transpiration cooling was again proven in 1970 by Laganelli, who compared this technique to more advanced prediction methods for film cooling.

During the 1950s fundamental analytical (Rubesin 1954), and experimental (Mickley et al. 1954; Mickley and Davis 1957) studies were carried out to investigate and prove the known relationships for the Stanton number and the friction coefficient in the case of transpired boundary layers. Detailed experimental studies on an isothermal, porous wall with transpiration were carried out by Moffat and Kays (1968) and Simpson et al. (1969). These studies proved the equation for $St_g / St_{g,0}$ given by Eckert and Livingood (1954) in a hot-gas Reynolds number range of $Re_g = 10^5 - 2 \cdot 10^6$ and with blowing ratios up to $F = 0.0096$. Generally, it was reported that small blowing ratios of $F < 0.01$ are sufficient for any cooling application (Rannie 1947; Herbertz 2003; Greuel et al. 2004), which was also observed during this study.

Later, it was shown that a porous wall can have a thermal effectiveness of smaller than unity (L'Ecuyer and Colloday 1972), which means thermal non-equilibrium between wall and coolant when the coolant is entering the main-flow. In this case the coolant exits the wall at a lower temperature and is able to pick up more heat from the main-flow close to the wall. A correction factor was introduced, which leads to lower hot-gas side heat transfer coefficients for a not perfectly heat exchanging structure.

To show the use of transpiration cooling for potential supersonic application, Chauvin and Carter carried out a study in 1955 with a transpiration-cooled cone in a $M = 2.05$ free stream at sea level conditions. As coolants, nitrogen, helium, and liquid water were used. Liquid water showed the best cooling performance due to its evaporation enthalpy, whilst the surface temperature reduction using helium was three times higher than with nitrogen. This influence was also shown by Laganelli

(1970). The impact of the coolants specific heat capacity has for example been described by Kays et al. (2005). Bartle and Leadon (1959) conducted an experimental study with a $M = 3.2$ free stream flow on a flat plate, reporting only a minor influence of Re_g on the wall temperature when using transpiration cooling. In 1966 Woodruff and Lorenz presented a study, where foreign gas injection into a hypersonic boundary layer was investigated, confirming previous studies (Rubesin 1954; Bartle and Leadon 1959). These effects of free-stream Mach number and specific heat of the coolant were shown analytically (Dorot and Strelets 1973) as well.

More recent studies of transpiration cooling with foreign gas injection were presented by Meinert et al. (2001). The results were compared to a modified Rannie-equation and to a real application in a high-pressure hydrogen combustion environment similar to the experiments presented by Serbest (2002). With the availability of lightweight, ceramic matrix composites such as carbon/carbon (C/C) (Krenkel 2000) or silicon carbide infiltrated carbon fibers (C/C-SiC) (Heidenreich 2007), transpiration cooling now seems to be a promising technique for combustion chamber cooling for high-speed aerospace applications. Here, continuous heat loads of up to 17 MW/m^2 can appear, where regeneratively cooled walls cannot be used anymore (Kelly and Blosser 1994; Song et al. 2006). The porous nature of these materials combined with the insensitivity to thermal shocks and thermal expansion and its high maximum service temperatures of up to $T_{w,max} = 1800 \text{ K}$ (Bouchez and Beyer 2008) make them ideal candidates for application in supersonic hot-gas environments. System studies showed that using transpiration cooling, for example in rocket thrust chambers, yields much better performance than regeneratively cooled systems (Herbertz 2003; Greuel et al. 2004). Therefore, recent investigations using C/C combustor liners in model rocket combustion chambers were pursued. Serbest et al. (1999) conducted basic hydrogen/oxygen combustion experiments using transpiration cooling. They found a good resistivity of the material with respect to damage and erosion. Several tests concerning transpiration cooling and the through-flow behavior were summarized by Hald et al. (2005). For higher combustion chamber pressure regimes up to $p_{t,g} = 8 \text{ MPa}$ the with gaseous hydrogen transpiration cooled C/C materials worked without major blemishes. An experimental study using air transpiration cooling with C/C for scramjet or ramjet combustion chamber applications was carried out by Langener et al. (2008). The main-flow total temperature ranged up to $T_{t,g} = 750 \text{ K}$ and the surface temperature of several flat plate C/C samples exposed to heated subsonic or supersonic was measured for different blowing ratios. The coolant mass-flow rate was shown to be the most influential parameter on the cooling efficiency compared to the hot-gas Mach number, Reynolds number and sample porosity within the investigated range. Böhrk et al. (2009) presented an analytical design method for the determination of transient wall heat flux to a transpiration-cooled parallel flat plate under laminar or turbulent flow conditions. The SHEFEX II reentry demonstrator using a sounding rocket experiment (Weihs et al. 2008) by the German Aerospace Center is supposed to carry an experiment with a transpiration-cooled CMC wall for reentry application.

2.2 Hot-Gas Heat Transfer without Blowing

When a fluid of a certain velocity flows over an arbitrary surface of a different temperature than the fluid, heat is being exchanged between the surface and the material. Analogous to the velocity boundary layer a temperature boundary layer forms over the surface. Typically, for flat plate flow, channel flow or more complex problems the temperature boundary layer changes with the location. Also the surface can have a temperature distribution. Hence, also the heat flux \dot{q}_w transferred to or from the wall can vary. To simplify this, integral correlation for the heat transfer problem have been developed and are widely used. In Fig. 2.3 a schematic of the thermal situation at a cooled wall exposed to hot compressible flow is shown.

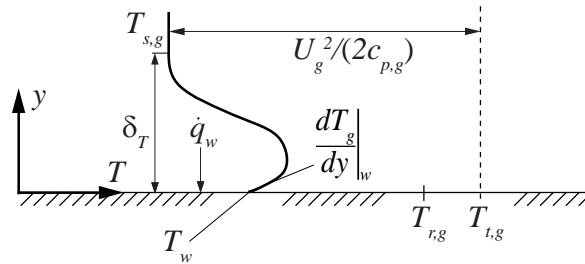


Figure 2.3: Temperature profile and convective heat transfer in compressible flow with a cooled wall

The wall is at a temperature T_w colder than the total temperature of the flow $T_{t,g}$. Due to the high speed flow, the static temperature $T_{s,g}$ needs to be computed using for example isentropic theory (Eqn. 2.5). The difference between these two temperatures is the portion derived from the kinetic energy $U_g^2 / (2c_{p,g})$ whilst U_g is the bulk velocity magnitude of the main-flow.

$$T_{s,g} = \frac{T_{t,g}}{\left(1 + \frac{\gamma-1}{2} M_g^2\right)} \quad (2.5)$$

Within the thermal boundary layer, which height is denoted by δ_T , the flow decelerates towards the wall and therefore the static temperature rises due to recovery of kinetic energy to internal energy. Close to the wall, heat is transferred to the colder wall reducing the temperature until the wall temperature and the fluid temperature are the same. Right at the wall, the temperature profile has a gradient $\left. \frac{dT_g}{dy} \right|_w$ which can be multiplied by the local thermal conductivity of the fluid yielding the wall heat flux $\dot{q}_w = -k_{g,w} \left. \frac{dT_g}{dy} \right|_w$. Basically, \dot{q}_w is the heat flux conducted from the boundary layer into the wall. The temperature gradient at the wall is often difficult to determine. Therefore, the heat transfer coefficient h_g is introduced:

$$h_g = \frac{\dot{q}_w}{T_{r,g} - T_w} = -\frac{k_{g,w} \left. \frac{dT_g}{dy} \right|_w}{T_{r,g} - T_w} \quad (2.6)$$

This can be determined by either measuring the wall heat flux and wall temperature, whilst knowing the recovery temperature $T_{r,g}$ of the main-flow. Also, a manifold

2.3 Turbulent Boundary Layers Subject to Blowing

of correlations for simpler heat transfer problems are available for this quantity (see below). $T_{r,g}$ is the temperature the wall can reach as a maximum in a compressible flow at an adiabatic wall, which is lower than the total temperature (see Fig. 2.3). It is also referred to as adiabatic wall temperature. Due to thermal diffusion within the boundary layer during the deceleration of the flow in the boundary layer, the total temperature cannot be fully recovered for zero velocity, which is the case at a no-slip wall. Therefore, for calculating the heat transfer coefficient in Eqn. 2.6 or heat flux respectively, $T_{r,g}$ is used as a reference temperature. The recovery temperature can be calculated knowing the recovery factor r using the following equation:

$$T_{r,g} = T_{s,g} \left(1 + r \frac{\gamma - 1}{2} M_g^2 \right) \quad (2.7)$$

for a fully turbulent flat plate flow r is determined as:

$$r = \sqrt[3]{Pr_g} \quad (2.8)$$

which equals ≈ 0.9 for air. The Stanton number gives the relationship between the convectively transferred heat to the wall and the internal energy flux in the main-stream:

$$St_g = \frac{h_g}{\rho_g c_{p,g} U_g} = \frac{Nu_g}{Re_g Pr_g} \quad (2.9)$$

As shown in Eqn. 2.9 the Stanton number can also be expressed by other nondimensional quantities, such as the Nusselt number $Nu_g = \frac{h_g L}{k_g}$, the ratio between convection heat transfer to the wall and conduction heat transfer within the fluid at the wall and the Reynolds number $Re_g = \frac{\rho_g U_g L}{\mu_g}$, which represents the ratio of inertia and viscous forces in the flow. L is a characteristic length, for channel flows the hydraulic diameter D is substituted here. The Prandtl number $Pr = \frac{\mu_g c_{p,g}}{k_g}$ is solely dependent on the fluid properties and displays the ratio of heat, which is transported by friction and heat conduction within the fluid. For air Pr equals approximately 0.7. Dittus and Boelter (1985) presented a correlation for the heat transfer of fully developed, turbulent flow in ducts, whilst they differentiated between heating and cooling of the wall. This correlation is given in Eqn. 2.10

$$St_{g,0} = \begin{cases} 0.024 Re_g^{-0.2} Pr_g^{-0.6}, & \text{for heating} \\ 0.026 Re_g^{-0.2} Pr_g^{-0.6}, & \text{for cooling} \end{cases} \quad (2.10)$$

This equation can be used for a wide Prandtl number range and above a Reynolds number of 10000. It is used in this study for finding an estimate of the heat transfer coefficient within the supersonic and subsonic channel flow.

2.3 Turbulent Boundary Layers Subject to Blowing

After the brief introduction into heat transfer from a high-speed flow to a cooled wall, models available from literature describing transpiration cooling are given. All

2 Physical Background

of them feature one dimensional energy balances from the entering of the coolant into the porous wall until it enters the hot-gas boundary layer. They use correlation to model the hot-gas side heat transfer without blowing. All approaches assume thermal equilibrium in the wall, meaning that the coolant is at the same temperature as the wall at every location when it is flowing through it.

2.3.1 Model of Rannie

In 1947 Rannie had already presented a first model dealing with boundary layers subject to wall-normal fluid injection. He assumed fully turbulent pipe flow and neglected the heat conduction in lateral direction within the wall substrate. Then, he set up a heat balance for the laminar sublayer. His model assumption is, that the shape of the viscous sublayer is only changed insignificantly by the wall-normal injection due to its low velocity and momentum. The nondimensional temperature ratio Θ can then be expressed according to Eqn. 2.11.

$$\Theta = \frac{T_{r,g} - T_w}{T_{r,g} - T_{c,in}} = 1 - \frac{e^{-Pr_g \frac{\rho_c \nu_c}{\mu_c} \delta^*}}{1 + \frac{c_{p,c}}{c_{p,g}} \left(\frac{u_g}{u_{g,\delta^*}} - 1 \right) \left(1 - e^{-\frac{\rho_c \nu_c}{\mu_c} \delta^*} \right)} \quad (2.11)$$

The index δ^* indicates the edge of the laminar sublayer, in which thickness can be written as:

$$\delta^* = \frac{\nu_g y^*}{u_g} \sqrt{\frac{2}{C_f}} \quad (2.12)$$

the friction coefficient C_f for turbulent pipe flow without transpiration for a Reynolds number range from $3 \cdot 10^4$ up to 10^6 based on the hydraulic diameter D can be estimated with following equation:

$$C_f = 0.046 Re_D^{-0.2} \quad (2.13)$$

Knowing the height of the laminar sublayer $y^* = 5.6$ (Schlichting and Gersten 2000) one can simplify Eqn. 2.12 with the given definition of C_f to:

$$\delta^* = 36.9 \frac{\mu_g}{\rho_g u_g} Re_D^{0.1} \quad (2.14)$$

Also, the ratio of the velocity at the edge of the laminar sublayer and the free stream velocity is known and can be rearranged:

$$\frac{u_{\delta^*}}{u_g} = y^* \sqrt{\frac{C_f}{2}} = 0.85 Re^{-0.1} \quad (2.15)$$

Now the unknown quantities δ^* and $\frac{u_g}{u_{g,\delta^*}}$ can be replaced in Eqn. 2.11. Furthermore, the ratio of the viscosity of the hot-gas and the coolant is assumed to be unity close to the wall. This yields the final expression for Rannie's approach, which is only

dependent on the blowing ratio F , the specific heat capacity of the coolant $c_{p,c}$ and the free-stream conditions.

$$\Theta = 1 - \frac{e^{-36.9Pr_g Re_D^{0.1} F}}{1 + \frac{c_{p,c}}{c_{p,g}} (1.18 Re_D^{0.1} - 1) (1 - e^{-36.9Pr_g Re_D^{0.1} F})} \quad (2.16)$$

2.3.2 Model of Eckert and Livingood

Eckert and Livingood (1954) presented in a study where they compared the efficiency of different cooling techniques a model for a transpiration-cooled wall. They drew a control volume around a porous wall, neglected lateral heat conduction within the solid and set up an equation for the wall temperature. If one neglects radiation from or to the wall, their model equation can be written as:

$$\Theta = \frac{T_{r,g} - T_w}{T_{r,g} - T_{c,in}} = 1 - \frac{1}{1 + \frac{c_{p,c} \rho_c v_c}{h_{g,0}} \left(\frac{1}{h_g/h_{g,0}} \right)} \quad (2.17)$$

To model the heat transfer coefficient with blowing they proposed a relationship which agreed best with the experimental data available at that time.

$$\frac{h_g}{h_{g,0}} = \frac{\xi \Phi}{e^{\xi \Phi} - 1} \quad (2.18)$$

with ξ being the velocity ratio parallel to the surface at the border of the laminar sublayer and the turbulent part of the boundary layer.

$$\xi = \frac{2.11}{Re_g^{0.1}}$$

The blowing parameter Φ was defined as the ratio between the transpired mass flux multiplied by the specific heat capacity divided by the heat transfer coefficient without blowing, which is the inverse of a Stanton number.

$$\Phi = \frac{c_{p,c} \rho_c v_c}{h_{g,0}}$$

For estimating the hot-gas heat load onto the wall without transpiration cooling, Eckert and Livingood used a correlation for a turbulent boundary layer over a flat plate

$$St_{g,0} = 0.037 Re_g^{-0.2} Pr_g^{-2/3} \quad (2.19)$$

solving for the wanted heat transfer coefficient $h_{g,0}$ yields to:

$$h_{g,0} = c_{p,g} \rho_g u_g St_{g,0} = 0.037 c_{p,g} \rho_g u_g Re_g^{-0.2} Pr_g^{-2/3} \quad (2.20)$$

Now, these model assumptions can be used to eliminate the unknown quantities from Eqn. 2.17. We obtain an expression which only depends on the ratio of specific heats, the free stream conditions and the blowing ratio F .

$$\Theta = 1 - \frac{1}{1 + \frac{Re_g^{0.1}}{2.11} (e^{\xi\Phi} - 1)} \quad (2.21)$$

where

$$\xi\Phi = \frac{c_{p,c}}{c_{p,g}} \frac{2.11}{0.037} Re_g^{0.1} Pr_g^{2/3} F$$

2.3.3 Model of Kays et al.

Kays et al. (2005) assumed that the sublayer thickness in the presence of boundary layer transpiration is significantly affected. From a turbulent Couette flow approximation with a wall normal velocity component v_c they derived a blowing parameter by integrating the governing equation up to the boundary layer edge. It incorporates the blowing ratio F and the friction coefficient C_f . The definition of F has been given in Eqn. 2.4.

$$B_f = \frac{v_c \rho_c / u_g \rho_g}{C_f / 2} = \frac{F}{C_f / 2} \quad (2.22)$$

Now, from the solution of the Couette flow the relationship for the friction coefficient with the presence of blowing can be written as:

$$\frac{C_f / 2}{(C_f / 2)_0} = \frac{\ln(1 + B_f)}{B_f} \quad (2.23)$$

To eliminate the friction coefficient, which is included implicitly in Eqn. 2.23, a new blowing parameter is introduced:

$$b_f = \frac{F}{(C_f / 2)_0} \quad (2.24)$$

which leads to a correlation for the friction coefficient where only $(C_f / 2)_0$ without blowing needs to be known to obtain a value for the transpiration-cooled case.

$$\frac{C_f / 2}{(C_f / 2)_0} = \frac{b_f}{e^{b_f} - 1} \quad (2.25)$$

Analogous to the procedure described above, the derivation can also be made for the heat transfer, where the Stanton number is the analogue to the friction coefficient. Now the parameters are written with the index h to differentiate between heat transfer and skin friction.

$$B_h = \frac{F}{St_g} \quad (2.26)$$

and

$$\frac{St_g}{St_{g,0}} = \frac{\ln(1 + B_h)}{B_h} \quad (2.27)$$

2.3 Turbulent Boundary Layers Subject to Blowing

Again, to eliminate the implicitly appearing Stanton number in Eqn. 2.27 a second blowing parameter was defined:

$$b_h = \frac{F}{St_{g,0}} \quad (2.28)$$

The final equation can be obtained following a few algebraic rearrangements:

$$\frac{St_g}{St_{g,0}} = \frac{b_h}{B_h} = \frac{\ln(1 + B_h)}{B_h} \quad (2.29)$$

$$\Rightarrow b_h = \ln(1 + B_h) \quad (2.30)$$

$$\Rightarrow B_h = e^{b_h} - 1 \quad (2.31)$$

Substituting Eqn. 2.31 into Eqn. 2.27 we obtain the Stanton number correlation for a transpired boundary layer.

$$\frac{St}{St_{g,0}} = \frac{b_h}{e^{b_h} - 1} \quad (2.32)$$

Now, only $St_{g,0}$ has to be known to estimate the heat transfer with blowing. The equation after Dittus and Boelter (see Eqn. 2.10) or Eqn. 2.19 for flat plate flow can, for example, be applied here. When incorporating coolants with a different specific heat capacities into this model, a new blowing parameter needs to be defined:

$$B_{h,for} = \frac{F}{St} \left(\frac{c_{p,c}}{c_{p,g}} \right)^{0.6} \quad (2.33)$$

With keeping the definition of b_h and following again the derivations from Eqns. 2.29-2.31 and substituting into Eqn. 2.27, we obtain a new Stanton number ratio, which incorporates the ratio of the specific heat capacity of the coolant and the main-flow.

$$\frac{St}{St_0} = \frac{b_h \left(\frac{c_{p,c}}{c_{p,g}} \right)^{0.6}}{e^{b_h \left(\frac{c_{p,c}}{c_{p,g}} \right)^{0.6}} - 1} \quad (2.34)$$

To derive a nondimensional wall temperature ratio Θ including this correlation, a heat balance is set up for a control volume around a porous wall neglecting lateral heat conduction within the wall substrate and backside convection heat transfer as previously done by Rannie (1947) and Eckert and Livingood (1954). Then, the heat convectively transferred to the wall is fully picked up by the coolant within the porous segment. Thermal equilibrium is assumed.

$$\underbrace{h_g (T_{r,g} - T_w)}_{\text{convective heat transfer}} = \underbrace{\rho_c c_{p,c} v_c (T_w - T_{c,in})}_{\text{heat picked up by coolant}} \quad (2.35)$$

After rearranging and some modifications, Θ can be written using the correlation for the hot-gas side heat transfer (Eqn. 2.34) as:

$$\Theta = \frac{T_{r,g} - T_w}{T_{r,g} - T_{c,in}} = \left[\frac{c_{p,c}}{c_{p,g}} \left(\frac{b_h^2 \left(\frac{c_{p,c}}{c_{p,g}} \right)^{0.6}}{e^{b_h \left(\frac{c_{p,c}}{c_{p,g}} \right)^{0.6}} - 1} \right) \right] \left[1 + \frac{c_{p,c}}{c_{p,g}} \left(\frac{b_h^2 \left(\frac{c_{p,c}}{c_{p,g}} \right)^{0.6}}{e^{b_h \left(\frac{c_{p,c}}{c_{p,g}} \right)^{0.6}} - 1} \right) \right]^{-1} \quad (2.36)$$

2.4 Thermal Behavior of Porous Structures

This section will give an overview of the thermal situation which can appear at and within a porous wall. The major difference between a solid wall is that within the pores of such a material a second phase such as air or water (or even both) can be present. Now, if the heat transfer between the fluid in the wall and the solid is not perfect, they can be at different temperatures. Therefore, two energy equations are needed to describe the thermal behavior of a porous wall. This is sketched In Fig. 2.4.

The transient energy equation of the coolant fluid (index c) is given in Eqn. 2.37 in temperature form. The changes in temperature are caused by conduction within the fluid, convection of the fluid, and by a source which represents the heat transfer between the solid and the coolant, which is quantified by h_v .

$$\rho_c c_{p,c} \frac{\partial T_c}{\partial t} = \underbrace{k_c \frac{\partial^2 T_c}{\partial x^2}}_{\text{Conduction}} - \underbrace{\rho_c c_{p,c} v_c \frac{\partial T_c}{\partial x}}_{\text{Convection}} + \underbrace{h_v (T_s - T_c)}_{\text{Source}} \quad (2.37)$$

In a similar way the time dependent energy equation of the solid (index s) can be written (Eqn. 2.38). As a matter of fact there is no convective term present and the source has a different sign than in Eqn. 2.37.

$$\rho_s c_{p,s} \frac{\partial T_s}{\partial t} = \underbrace{k_s \frac{\partial^2 T_s}{\partial x^2}}_{\text{Conduction}} + \underbrace{h_v (T_c - T_s)}_{\text{Source}} \quad (2.38)$$

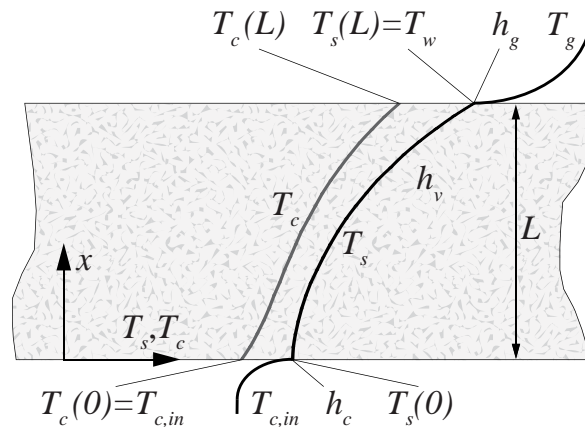


Figure 2.4: Steady thermal situation of a porous wall

The schematic in Fig. 2.4 shows convective boundary conditions at both coolant and hot-gas sides for the solid. Depending on h_v the difference between the coolant temperature distribution and the solid temperature distribution can be greatly affected. For very low volumetric heat transfer the coolant will not pick up significant amounts of heat and exit the porous wall almost at coolant inlet temperature $T_{c,in}$. For $h_v \rightarrow \infty$ at every location within the wall $T_c = T_s$ is valid. In reality the temperature distributions will be somewhere between these extremals because h_v is finite. The coolant is supposed to enter the porous wall always at coolant reservoir (inlet) temperature $T_{c,in}$.

Now, nondimensional quantities are introduced. The Biot number compares the convective heat transfer to the wall with the heat conduction within the solid. As characteristic length the wall thickness L is used.

$$Bi_c = \frac{h_c L}{k_s} \quad Bi_g = \frac{h_g L}{k_s} \quad Bi_v = \frac{h_v L^2}{k_s} \quad (2.39)$$

St_v and Nu_v respectively are calculated with the volumetric heat transfer coefficient. Note, that since h_v is measured in $[W/m^3]$, another length scale is needed in the definition to make the quantity nondimensional. Again, the wall thickness L is used.

$$St_v = \frac{h_v L}{\rho_c c_p c \nu_c} \quad Nu_v = \frac{h_v L^2}{k_c} \quad (2.40)$$

The temperatures of the coolant fluid and the solid can be rewritten using the total (or recovery) temperature of the hot-gas and the coolant inlet temperature.

$$\Theta_c = \frac{T_c - T_{c,in}}{T_g - T_{c,in}} \quad \Theta_s = \frac{T_s - T_{c,in}}{T_g - T_{c,in}} \quad (2.41)$$

Dividing x with the sample thickness L , we obtain the nondimensional wall thickness X :

$$X = \frac{x}{L} \quad (2.42)$$

After these steps, the energy equations Eqn. 2.37 and Eqn. 2.38 can be further simplified for steady state heat transfer by neglecting the time dependent terms and can be written as follows

$$\frac{d\Theta_c}{dX} - \frac{Nu_v}{St_v} \frac{d^2\Theta_c}{dX^2} = St_v (\Theta_s - \Theta_c) \quad (2.43)$$

and

$$\frac{d^2\Theta_s}{dX^2} = Bi_v (\Theta_s - \Theta_c) \quad (2.44)$$

Since in this study only gases are used as coolants, the conduction term within the coolant fluid can be neglected.

$$\frac{d\Theta_c}{dX} = St_v (\Theta_s - \Theta_c) \quad (2.45)$$

2.5 Through-Flow Behavior of Porous Structures

Besides the temperature profiles within the porous wall, it is of great interest how much pressure difference is needed to force a certain coolant mass-flow rate through a porous material. This is important for the system level design as well as for the mechanical layout of the combustion chamber in case transpiration cooling is used. For this, one can state a differential equation (Eqn. 2.46) which is consisting out of two terms, the first being the original Darcy-Equation (Darcy 1856; Innocentini et al. 1999). It represents the viscous forces appearing by penetration of a fluid through a porous solid. For higher through-flow velocities form drag becomes important, which can happen quickly for dense materials due to their small flow cross-section (Innocentini et al. 1999). According to Nield and Bejan (2006) this becomes important if the pore Reynolds number $Re_p = \frac{v_{in} d_p}{\nu}$ is in the range of 1 and 10. The quadratic term which was added to the Darcy-equation is commonly referred to as Forchheimer term. Accordingly, the permeability coefficients are named: K_D is the Darcian permeability coefficient whilst K_F displays the Forchheimer permeability coefficient. With these coefficients all material intrinsic and integral parameters such as porosity, shape of the pores, their surface and the actual material geometry are being described. The Darcy-Forchheimer equation is written as follows:

$$\frac{dp}{dx} = - \left(\underbrace{\frac{\mu}{K_D} v}_{\text{Darcy}} + \underbrace{\frac{\rho}{K_F} v^2}_{\text{Forchheimer}} \right) \quad (2.46)$$

whilst v is the local through-flow velocity depending on the local pressure and the local temperature. Now, the perfect gas law (Eqn. 2.47) for substituting the density in Eqn. 2.46 is used, whilst it is assumed that the temperature throughout the fluid within the wall does not vary in x -direction. The inlet temperature can be used as a constant for the density treatment.

$$\rho = \frac{p}{RT_{in}} \quad (2.47)$$

Furthermore, the dynamic viscosity is assumed to be constant, since it is mostly dependent on the temperature. Now, Eqn. 2.46 is solved. The result is valid for an isothermal, compressible ($\rho = f(p)$) fluid in a porous medium:

$$\frac{\Delta p}{L} = \frac{p_{in}^2 - p_{ex}^2}{2p_{in}L} = \frac{\mu_{in}}{K_D} v_{in} + \frac{\rho_{in}}{K_F} v_{in}^2 \quad (2.48)$$

whilst v_{in} displays the superficial through-flow velocity at inlet conditions and ρ_{in} the inlet density of the coolant:

$$v_{in} = \frac{\dot{m}_c}{\rho_{in} A_c} \quad \rho_{in} = \frac{p_{in}}{RT_{in}} \quad (2.49)$$

A geometrical approach for the permeability coefficients in general porous media was presented by Ergun and Orning (1949). Later, this was specified for a bed of packed spheres by Ergun (1952). The approach was developed for homogeneously distributed beds of packed sphere with high porosity. He proposed correlations for K_D and K_F :

$$K_D = \frac{\varepsilon^3 d_p^2}{150 (1 - \varepsilon)^2} \quad \text{and} \quad K_F = \frac{\varepsilon^3 d_p}{1.75 (1 - \varepsilon)} \quad (2.50)$$

where $\varepsilon = V_{open}/V$ is the volume-averaged porosity of the packed bed and d_p is the effective diameter of the bed particles, a volume averaged surface area of the spheres. For a densest packing of spheres, this parameter collapses into the sphere diameter. With this approach, it is possible to predict the pressure loss in a very wide range of pore Reynolds numbers. According to Nield and Bejan (2006) this range can be divided into the laminar flow regime ($Re_p < 10$), over the transitional ($10 < Re_p < 300$) to the fully turbulent through-flow regime ($300 < Re_p$). Typically, Ergun's approach is valid for highly porous, regular, isotropic media which is not the case for many CMC materials.

2.6 Ceramic Matrix Composite (CMC) Materials

This section is meant to give a brief overview of the materials investigated in this study. In contrast to glass or carbon fiber-reinforced plastic (CFRP) composites, for CMCs the matrix in between the fibers of the finished product is consisting out of a ceramic material. This offers high temperature resistance at low structural weights. Some materials can even be manufactured having a porosity, which makes them ideal candidates for transpiration cooled walls in high-temperature environments. In general the ceramic fibers are wound or pressed to obtain a first shape, then the matrix is infiltrated in several steps depending on the kind of the CMC. In aerospace application the carbon/carbon-silicon carbide (C/C-SiC) (Krenkel and Berndt 2005; Heidenreich 2007) is one of the most popular CMC materials. Due to its high melting temperature and insensitivity to thermal stresses it is not only being used for heat shields or flaps of re-entry vehicles or jet turning vanes, but also in hypersonic research. The leading edges of the nose and control surfaces of the $M_\infty = 10$ X43 flight were made from C/C coated with SiC oxidation protection (Ohlhorst et al. 2005). Glass (2008) presented a study where he summarized the use of CMCs for a various range of aerospace purposes, also with respect to future application including actively cooled parts.

Other CMCs, which were under investigation within the ATLLAS project are WHIPOX (Göring et al. 2003), where the fibers and the matrix are made from aluminium oxide Al_2O_3 . OXIPOL (Heidenreich et al. 2004) is made from oxidic fibers

2 Physical Background

($Al_2O_3 + SiO_2$) and is then infiltrated with a resin which is transformed after the pyrolysis process into $SiOC$ as a matrix in between the fibers.

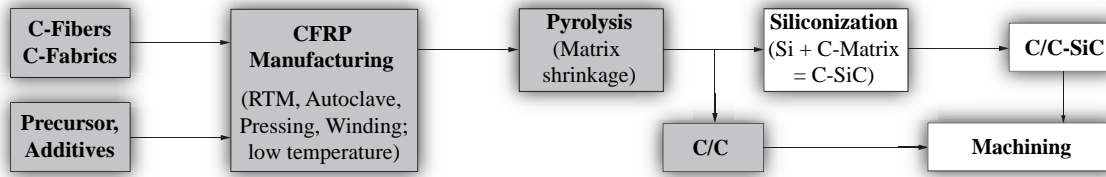


Figure 2.5: DLR C/C and C/C-SiC manufacturing process

In this study C/C samples were used in the experiments. C/C is a byproduct of the C/C-SiC manufacturing process (see Fig. 2.5). At first precursors consisting out of polymers, carbon fibers or if available carbon fabrics and additives are added together to form carbon fiber-reinforced plastics. Here, winding or pressing are the most common techniques and the infiltration usually takes place via resin transfer moulding (RTM) or within an autoclave (Krenkel 2000). Afterwards, the pyrolysis takes place within an inert (usually nitrogen) atmosphere at a temperature above 1200 K . During this process, amorphous carbon forms from the polymers within the matrix in between the carbon fibers. At the same time, the matrix volume shrinks leaving interconnected cracks within it, which constitutes the porosity of the material. The cracking behavior can be adjusted by the pyrolysis temperature and pressure and, therefore, the porosity of the material can be adjusted. Also, the mechanical properties, such as Young's modulus or the interlaminar shear strength (ILSS), which is basically the ability of the matrix to keep the fibers attached, are set this way. Additionally to the pyrolysis process, the properties of the material can also be altered by changing the weave of the fiber fabrics or the orientation of the fiber layers. If the goal is to produce C/C, the process is completed at this point and the plates or tubes can be machined into the desired geometry. An example of a sample tested in the hot-gas tests is shown in Fig. 2.6. Due to the directional reflectance of the fibers, one can clearly see the weave, in this case the fibers are oriented perpendicular to each other.

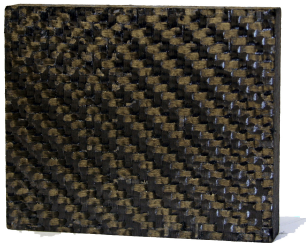


Figure 2.6: Example of C/C sample used in this study

Now, for the production of C/C-SiC the porous C/C material is infiltrated with molten, liquid silicon (LSI process) at around 1900 K and under vacuum conditions, which rapidly fills the gaps in the matrix and leaves the fibers undamaged. The silicon reacts with the carbon in the matrix forming SiC. This greatly reduces the porosity of the material leaving it almost impermeable. This is the main reason why in this study C/C was used, because the pressure drop over such a dense wall material would have been too high to conduct the transpiration cooling test within the desired parameter range.

Experimental Setups and Measurement Techniques for Hot-Gas Tests

In this chapter the two major test setups for the hot-gas tests are described. The first was used for the supersonic hot-gas flow experiments which were the core of this study and is a heavily cooled model combustor. The second channel is an uncooled and thermally insulated stainless steel channel with a converging inlet. Therefore, only subsonic experiments could be carried out which were used to verify and support the findings obtained from the hot-gas tests in the supersonic flow regime. Subsequently, the measurement technique for the determination of the sample temperature is presented. The uncertainty analysis with respect to the used equipment can be found in Appendix A.

3.1 Experimental Facility

The used experimental facility is dedicated to supersonic combustion experiments as described by Scheuermann et al. (2008) or Vellaramkalayil et al. (2009). For this study it was modified and extended to accommodate the transpiration cooling tests. Fig. 3.1 shows the test-bench schematic. The upper portion displays the coolant distribution system while the lower part shows the main-flow path.

The air for the main-flow is being compressed by a staged screw compressor driven by an electrical motor which can deliver flows at 1.05 MPa nominal total pressure and up to 1.45 kg/s of main mass-flow-rate. Additionally, it is possible to use a pebble bed air dehumidifier in order to obtain dry air with a relative humidity in the order of 0.1% with respect to the compressed volume-flow rate. After the screw-compressor two electrical heaters are installed, which are capable of heating the flow convectively using resistively heated metal rods up to 1450 K total temperature. Directly after the heaters the hot-gas plenum can be found. The test section is flanged on at this location. Here, total temperature ($T_{t,g}$, accuracy of 1.1 K) and total pressure ($p_{t,g}$, accuracy 0.008 MPa) are measured and used for determining

3 Experimental Setups and Measurement Techniques for Hot-Gas Tests

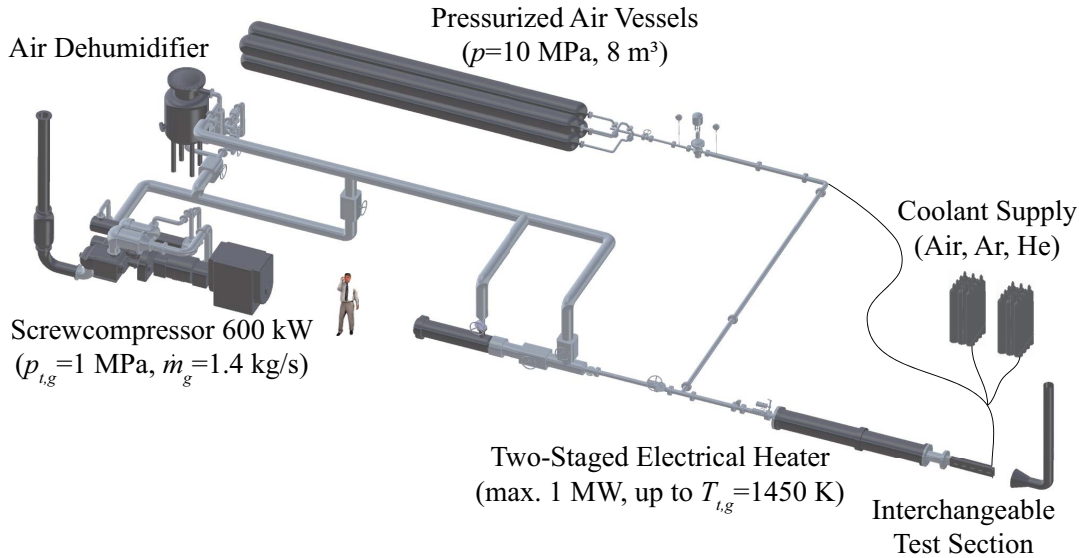


Figure 3.1: ITLR supersonic combustion and hot-gas flow test bench

the flow conditions within the test section. The main volume-flow rate is being measured by an *Endress+Hauser Prowirl PW73* vortex flow meter with an uncertainty of $0.001 \text{ m}^3/\text{s}$ upstream of the heaters. *OMEGA* pressure (0.008 MPa accuracy) and temperature (Type K thermocouple, accuracy of 1.1 K) transducers are installed at the same location to determine the mass-flow rate.

The coolant air is being provided by four pressure tanks of 2 m^3 volume each, which are pressurized at 10 MPa and additionally serve as an emergency supply for the electrical heaters in case of a screw compressor malfunction. In the test chamber the coolant supply pressure is decreased to 1.5 MPa by a pressure reducer and the coolant mass-flow rate is determined and set by a *Teledyne-Hastings HFC-303* thermal mass-flow controller (accuracy $4.8 \cdot 10^{-5} \text{ kg/s}$), which can measure flows up to 0.0108 kg/s . The coolant pressure is read via an *OMEGA* difference pressure transducer with an accuracy of 0.005 MPa . Argon and helium are provided by compressed gas bundles and the mass-flow rate is being set and determined by the same controller as for air using conversion factors.

3.2 Test Setup for Supersonic Experiments

3.2.1 Test Channel

The test section itself (see schematic in Fig. 3.2) is a 1.258 m long, water-cooled copper channel with multiple openings for optical access. The flow enters the channel through a Laval nozzle, that expands the air to $M = 2.1$ with the given nozzle contour. The static pressure can be measured with an accuracy of 100 Pa along the main stream co-ordinate at 71 positions, which can be continuously monitored during the experiments. The height of the test section is 35.4 mm and the width is 40 mm which leads to a cross-sectional area of the copper-channel of 0.001416 m^2 .

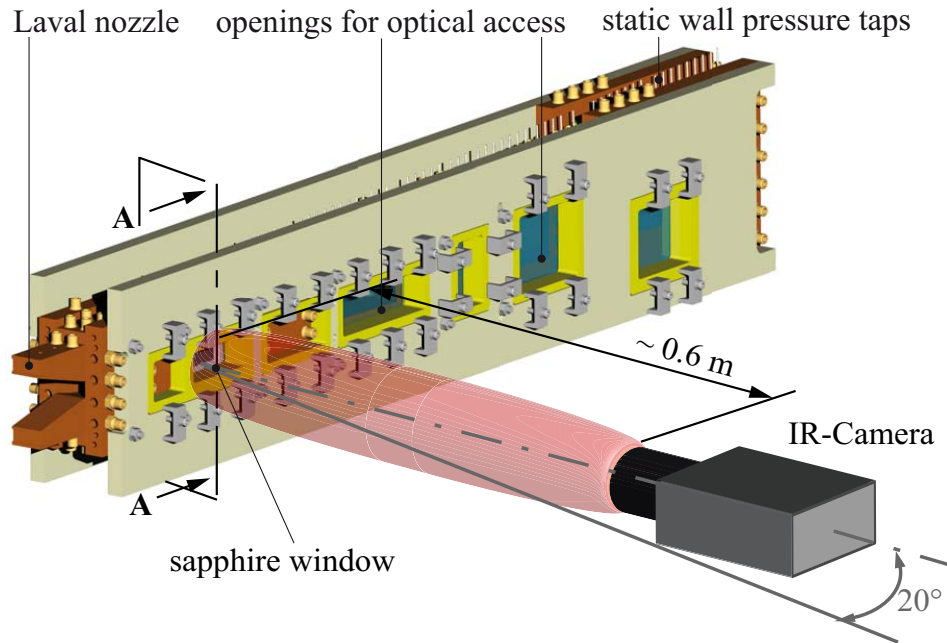


Figure 3.2: Test section with IR-thermography setup

The leading edge of the sample is located at $x = 0.165 \text{ m}$ with respect to the nozzle throat. The optical setup for the IR-measurements is schematically displayed in Fig. 3.2. The surface temperature of the porous wall segment can be monitored through a sapphire window on the opposite wall.

The infrared camera was positioned about 0.6 m away from the sample under an angle of 20° to the sample normal direction. This reduced optical disturbance from the channel and the sapphire window significantly.

3.2.2 Sample Integration Concept

The sample integration concept is shown in Fig. 3.3. The coolant plenum (3) was installed in the constant cross-section isolator part of the supersonic combustion test channel. The porous sample (1) is directly bearing on the water-cooled copper parts (2) of the test channel and being clamped by the coolant plenum (6) from the back. It is embedded for insulation purposes into a *MACOR*-frame (4) and held back by a spacer (5). The *MACOR* ensures with its thermal conductivity of $1.4 \frac{\text{W}}{\text{mK}}$ a good insulation of the sample over the side surfaces. Carbon sealings (6) have been put between the sample, spacer, and coolant plenum. These were customarily machined from *SIGRAFLEXTM* with 2 mm thickness. At the plenum, the coolant is being supplied from the side (7). Its pressure and temperature (8) are being measured at the same position.

From the top, four K-type thermocouples (*OMEGA SuperOMEGACLADTM*, 1.2 K accuracy) are being led through the plenum (6) into the sample, where they are installed tightly and flush with the porous wall's surface. Grounded thermocouples, whose measurement tip has been welded to the shaft have been used. This ensures

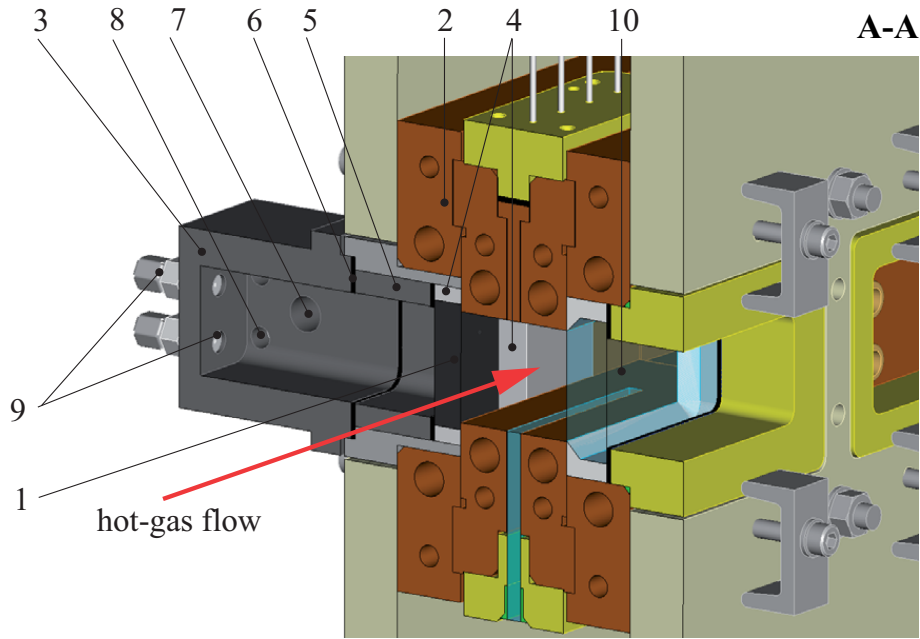


Figure 3.3: Sample integration concept

that the thermocouple reads the temperature as close as possible to the wall whilst not having protruding wires and gaps at the end of the bore holes within the sample. Using thermocouples with smaller diameter proved impractical because of bending whilst installing them flush in the hole. Closer to the hot-gas surface the holes were drilled with a diameter of 1 mm , whilst the rest of it was at 1.1 mm . With this procedure it ensured that the thermocouple, whose diameter were always slightly over size, did not bend during installation, but by pressing it into the end of the bore holes the sealing of the thermocouples was guaranteed. The sapphire window (10) is insulated by a *MACOR*-frame from the water-cooled copper walls as well. Without the frame, the maximum tested total temperature of 1060 K could not be reached without a failure of this window due to thermal stresses in the glass with direct contact to the water-cooled copper walls.

3.2.3 Parameter Range

The supersonic test channel was operated at constant total pressure. Increasing the total temperature means to compensate for the lower density in the channel by setting a lower main mass-flow rate at the screw-compressor to maintain the same total pressure, since the Mach number is fixed by the Laval nozzle. Therefore, the static pressure at the sample location $p_{s,g}$ is nearly constant for both tested temperature levels, but the hot-gas mass-flow rate differs (see Table 3.1)

The Reynolds number Re_g based upon the hydraulic diameter D varied within the tested range from around 270000 up to 460000. Now, the hot-gas Stanton number without blowing can be estimated for our setup using the equation of Dittus and

3.3 Test Setup for Subsonic Experiments

	$M = 2.1, T_{t,g} = 670 \text{ K}$	$M = 2.1, T_{t,g} = 1060 \text{ K}$
$p_{s,g} [\text{bar}]$	0.346	0.346
$\dot{m}_g [\text{kg/s}]$	0.37	0.30
$Re_g [-]$	464358	269737
$St_{g,0} [-]$	0.0028	0.0035
$h_{g,0} [\text{W/m}^2\text{K}]$	615	737

Table 3.1: Supersonic channel flow and heat transfer parameters

Boelter (Eqn. 2.10) for turbulent channel flow, corrected for the not fully developed part up to the position l where the sample is installed (see Baehr and Stephan (2008)).

$$St_{g,0} = 0.024 Re_g^{-0.2} Pr^{-0.7} \left[1 + \left(\frac{D}{l} \right)^{\frac{2}{3}} \right] \quad (3.1)$$

For the tests in the supersonic regime, this number ranged between 0.0028 and 0.0035 which leads to heat transfer coefficients between $h_{g,0} = 615 \frac{\text{W}}{\text{m}^2\text{K}}$ and $737 \frac{\text{W}}{\text{m}^2\text{K}}$. One can see, that that these values differ by $\approx 19 \%$ from each other. In Table 3.2 the parameters for the three different investigated coolants are given. For air and argon the blowing ratio F was set at a maximum of 0.01 in which almost complete cooling could be reached. Due to the volume-flow limitations of the coolant mass-flow controller the blowing ratio for helium was limited to 0.0022 because of its lower molecular weight and density respectively. But this was sufficient to reach the desired wall-temperatures as well. The maximum supply pressure was limited by the test bench to 1.5 MPa , which was only applied for the thicker sample. For the porous specimen with $L = 0.005 \text{ m}$ this value was kept at at maximum of 1.0 MPa for structural reasons.

	Air	Helium	Argon
$\dot{m}_c \cdot 10^3 [\text{kg/s}]$	0 – 2.97	0 – 0.8	0 – 3.7
$F [-]$	0 – 0.01	0 – 0.0022	0 – 0.01

Table 3.2: Coolant parameters in supersonic flow tests

3.3 Test Setup for Subsonic Experiments

Besides the test campaigns using the supersonic channel and data evaluation to model the transpiration cooling efficiency in a non-adiabatic test or operation environment had been performed (see Section 5.3), further tests to prove these findings were carried out. Since the copper-channel was water-cooled it was chosen to use an uncooled, insulated channel to better decouple the porous sample from its surroundings and to generate a near-adiabatic test environment. Additionally, the flow

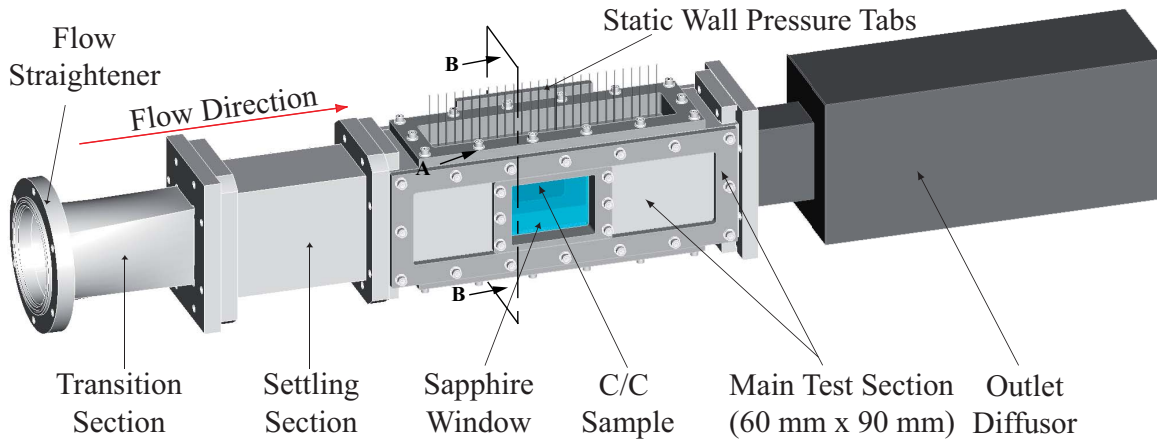


Figure 3.4: Hot-gas channel

cross-section was larger than in the channel described above, which allowed larger material samples and therefore a more detailed instrumentation.

3.3.1 Subsonic Flow Channel and Sample Integration Concept

The test section itself (see schematic in Fig. 3.4) is a 1.32 m long, uncooled stainless steel channel. The flow enters the channel from the test bench through a convergent transition section where a flow straightener is installed into a settling section with the same cross section as the test channel. Afterwards, the actual test section is bolted on. At the end, an outlet diffusor is attached, which decelerates the flow and directs it into the exhaust chimney of the test bench. The static pressure can be measured with an accuracy of 100 Pa along the main stream co-ordinate at 29 positions, which are continuously monitored during the experiments.

The height of the test section is 90 mm and the width is 60 mm leading to a cross-sectional area of 0.0054 m². The leading edge of the porous sample is located at 0.58 m downstream of the transition section after the flow straightener and 0.38 m downstream from the leading edge of the settling section. The surface temperature of the porous wall segment can be monitored via IR-thermography through a sapphire window on the opposite side of the channel similar to the setup for the supersonic flow experiments.

The sample itself is installed into a separate integration setup which can be assembled together with the coolant plenum apart from the test bench and is then bolted to the channel. The cross-section schematic of the integration setup installed at the channel is shown in Fig. 3.5. The C/C sample is bearing on a sample holder made from *TOOLOX*TM (high-strength tool-steel) which is absorbing the forces from the pressurized porous sample. Here, two surface thermocouples are attached as close as possible to the sample to evaluate the heat conduction effects appearing in the setup. The holder itself sits on a *TECAPEEK*TM wall, which is a high-temperature (up to 550 K, limiting value for the total temperature), low thermal conductivity ($k = 0.5 \text{ W/mK}$) plastic. This insulates the sample from the other steel

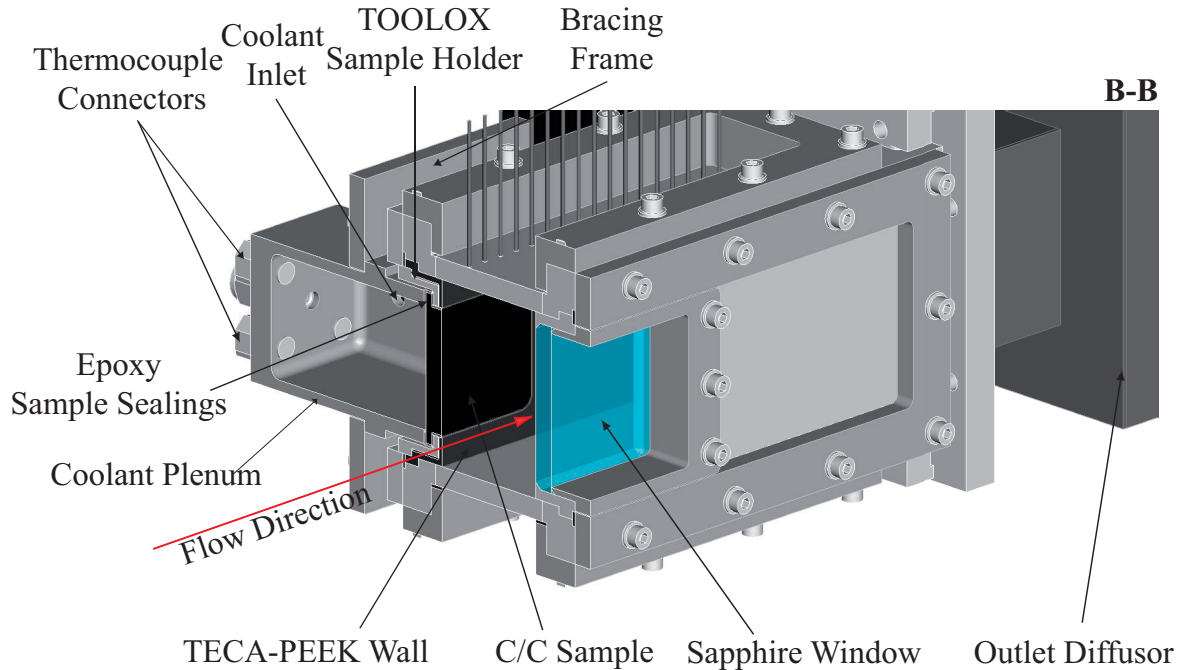


Figure 3.5: Sample integration design

parts of the hot-gas channel and therefore decreases lateral heat conduction. The coolant plenum is pressed onto the sample from the back using a bracing frame, which is bolted to the hot-gas channel. By varying the bolt length, different sample thicknesses can be accommodated.

Eleven grounded thermocouples (*OMEGA SuperOMEGACLADTM* K-type, 1.1 K accuracy) are lead through connectors into the plenum. Four of them were tightly and flush installed with the porous wall's surface for calibration of the IR-images and for measurement of the surface temperature. The bore holes were of the same shape as for the supersonic flow tests. Six thermocouples were installed using carbon glue in different depths within the sample to capture the temperature profile within the porous wall. One sensor for the coolant temperature was centered in the volume of the plenum.

The coolant itself is led into the plenum through another connector, the coolant pressure is read at the same position (0.008 MPa accuracy). The sample is permeable in all coordinate directions, therefore the side surfaces of the porous wall were sealed with an epoxy slurry prior to assembly. Furthermore, *SIGRAFLEXTM* carbon sealings were used to seal the sample between the plenum and the *TOOLOXTM* sample holder and to withstand the temperatures appearing in the setup.

3.3.2 Parameter Range

The maximum achievable Mach number range using the subsonic flow channel is from $M_g = 0.3$ up to $M_g = 0.7$ due to the mass-flow rate limitations of the compressor. In Table 3.3 the six investigated main-flow conditions with their Reynolds number

3 Experimental Setups and Measurement Techniques for Hot-Gas Tests

	M = 0.3, T _{t,g} = 420 K	M = 0.3, T _{t,g} = 540 K
$p_{s,g}$ [bar]	0.957	0.957
\dot{m}_g [kg/s]	0.54	0.50
Re_g [-]	306773	237806
$St_{g,0}$ [-]	0.0032	0.0033
$h_{g,0}$ [W/m ² K]	314	297
	M = 0.5, T _{t,g} = 420 K	M = 0.5, T _{t,g} = 540 K
$p_{s,g}$ [bar]	0.927	0.927
\dot{m}_g [kg/s]	0.87	0.77
Re_g [-]	514000	398446
$St_{g,0}$ [-]	0.0029	0.0030
$h_{g,0}$ [W/m ² K]	465	439
	M = 0.7, T _{t,g} = 420 K	M = 0.7, T _{t,g} = 540 K
$p_{s,g}$ [bar]	0.918	0.918
\dot{m}_g [kg/s]	1.15	1.10
Re_g [-]	751883	582850
$St_{g,0}$ [-]	0.0026	0.0028
$h_{g,0}$ [W/m ² K]	612	576

Table 3.3: Subsonic channel flow and heat transfer parameters

and heat transfer parameters are given. For the estimation of the Stanton number Eqn. 3.1 the inlet length l was taken as the distance of the end of the flow straightener and the sample's leading edge. The parameter range with respect to Re_g and $h_{g,0}$ is wider than what was experienced during the supersonic flow tests. The heat transfer coefficient varies from $297 \frac{W}{m^2K}$ up to $612 \frac{W}{m^2K}$ which is more than 106 %. The hot-gas Reynolds number could even be varied by ≈ 216 %.

Because the porous exit surface for the samples tested here was more than twice as large as the ones investigated under supersonic flow conditions, a higher coolant mass-flow rate was needed to achieve the same blowing ratios as tested before. The maximum \dot{m}_c was determined by the highest supply pressure the porous wall could structurally bear. For all three gases approximately the same surface temperature was measured with the highest blowing ratio. Air ($\dot{m}_{c,max} = 6.6 \cdot 10^3 \frac{kg}{s}$) and argon ($\dot{m}_{c,max} = 7.0 \cdot 10^3 \frac{kg}{s}$) caused comparable pressure drop at the same coolant mass-flow rate, therefore the values of $\dot{m}_{c,max}$ are in the same range. The maximum supply pressure (or coolant plenum pressure) was for all gases limited due to structural reasons to a maximum of 1.3 MPa. Depending on the samples permeability and thickness this value was set even lower.

	Air	Helium	Argon
$\dot{m}_c \cdot 10^3 [kg/s]$	0 – 6.6	0 – 1.3	0 – 7.0
$F [-]$	0 – 0.008	0 – 0.0025	0 – 0.013

Table 3.4: Coolant parameters in subsonic flow tests

3.4 Investigated CMC Samples

Six different C/C samples from three different material charges were investigated. The manufacturing process has been explained in Section 2.6. In this study only samples manufactured via the autoclave technique were used. For the tests with supersonic main-flow the charge PH1732 was investigated. Here, the fabrics are rotated by $\pm 15^\circ$ with respect to each fiber layer. The flow exit area $A_{ex} = 40 \times 40 \text{ mm}^2$ resulted from the geometrical constraints of the model combustor and the nesting of the sample in the *MACOR* frame.

Within the uncooled channel, samples cut from the PH1606 and PH1947 charge were tested. For these, the fibers were oriented perpendicular to each other ($\pm 90^\circ$), whilst the exit flow area is larger than with the PH1732 samples since the cross-section of the subsonic channel is larger and more room for the sample integration was available. For the subsonic tests, it was ensured that one dense (low porosity) charge (PH1606) and one charge with higher porosity (PH1947) was tested. Thereby, the influence of ε onto the cooling behavior of the wall can be investigated in the given range. From all charges, samples with different thicknesses were manufactured, to further determine the impact of this parameter on the cooling efficiency. The raw CMC plate of the material was always thicker than the final samples, therefore the C/C samples were machined to the desired thickness.

	PH1606-1	PH1606-2	PH1732-1	PH1732-2	PH1947-1	PH1947-2
$L \cdot 10^3 [m]$	15	10	10	5	15	10
$\varepsilon [\%]$	11.3	11.3	11	10.7	13.2	13.2
$A_{ex} [mm^2]$	61×61	61×61	40×40	40×40	61×61	61×61

Table 3.5: Investigated sample material

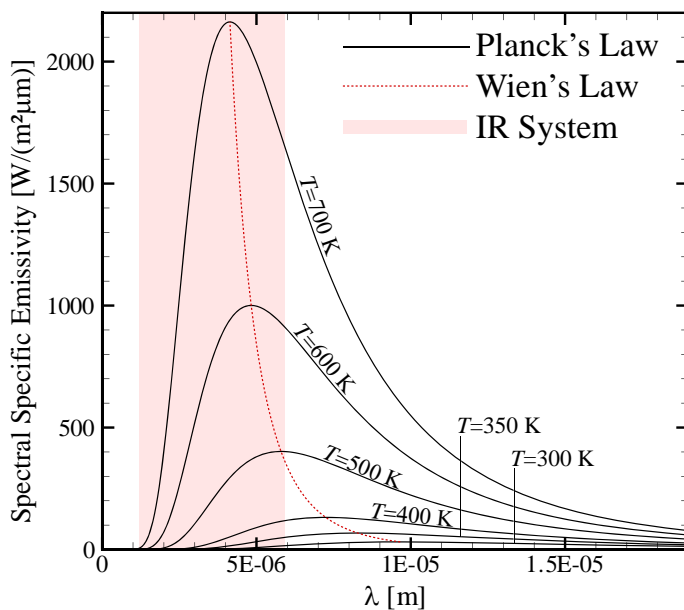
3.5 Infrared Thermography for Quantitative Wall Temperature Measurements

For the determination of the spatial temperature distribution the infrared thermography method was chosen. It is based on the principle that every body which has a temperature greater 0 K irradiates energy distributed over the whole wave length spectrum. Planck’s law (see Eqn. 3.2 (Siegel and Howell 2002)) describes this relationship. Here, λ is the wavelength at which a black body radiates the specific spectral energy i at a temperature T . The Boltzmann constant k and the Planck constant h are given by Siegel and Howell (2002).

$$i = \frac{2hc_0^2}{\lambda^5} \frac{1}{e^{\frac{hc_0}{\lambda k T}} - 1} \tag{3.2}$$

The distribution of i for temperatures from room temperature up to $T = 700 K$, which is the highest value measured with the infrared thermography in this study, is given in Fig. 3.6. For higher T the maxima in the distribution shift to smaller wave lengths according to Wien’s displacement law (Siegel and Howell 2002). The energy contained in the total wavelength spectrum grows with T^4 . For the investigated temperature range, all maxima and also the majority of the spectral energy $\int_0^\infty i d\lambda$ are within the near and medium infrared regime ($0.78 - 14 \mu m$) as displayed in Fig. 3.6. This shows, why infrared thermography is widely used to measure temperatures in this range.

In Table 3.6 the properties of the utilized infrared system are given. It consisted of a *Mitsubishi IR-M700* thermal imager with a detectable wavelength range of $1.2 \mu m - 5.9 \mu m$ which is sketched in Fig. 3.6. One can see, that this system is



T [K]	λ_{max} [μm]
700	4.14
600	4.83
500	5.80
400	7.24
350	8.28
300	9.66

Figure 3.6: Planck’s law and Wien’s law for the investigated temperature range

3.5 Infrared Thermography for Quantitative Wall Temperature Measurements

especially suited for the higher temperature regime since here the radiation intensity is highest, which is beneficial for keeping the relative noise level of the used detector chip low. The data were recorded by the *IRBIS 3.0 Software* by *Infratec GmbH*. The resolution of the camera chip was 720×480 pixel leading to a spatial object resolution with the macro lense of the camera of ca. $10 \text{ px}/\text{mm}$ for this setup. Following the theory from Eqn. 3.2, it seems straightforward to calculate a temperature from a certain radiation value. Unfortunately, the radiation emitted from an object is not only dependent of the temperature, but also on the angle, surface properties, and wavelength. Additionally, the surface might reflect other radiation components from the environment and the optical path could radiate as well. This hardens a quantitative analysis using infrared thermography in technical applications.

Pixelmatrix	720×480
Object resolution (for our setup)	$10 \text{ px}/\text{mm}$
Chip cooling	Stirling cycle cooled
Detectable wavelengths	$1.2 \mu\text{m}$ to $5.9 \mu\text{m}$
Applied lense	100 mm Macro-Lense
Filtering wavelength lense	$3 - 5 \mu\text{m}$

Table 3.6: Main specifications of IR-thermography system

The radiation detected by the camera consists of several components in the described test setup which is sketched in Fig. 3.7. First, the surface to be measured emits radiation I_w at the wanted object temperature T_w . Furthermore, the surroundings within the test channel like, for example, the channel walls is radiating (I_{amb}), which is reflected by the object surface. Furthermore, the hot-gas flow can emit a radiative component, I_g , directly to the camera. All three components propagate through the sapphire window, which has a transmissivity in the detectable wavelength of ≈ 0.88 in this setup and itself is at a temperature T_{win} . Finally, the radiation recorded by the camera is:

$$I_{cam} = I_1 + I_2 + I_3 \quad (3.3)$$

The components can be expressed with the parameters in the optical path:

$$I_1 = \tau_{win}(1 - \varepsilon_w)I_{amb} \quad I_2 = \tau_{win}I_w \quad I_3 = \tau_{win}I_g + I_{win} \quad (3.4)$$

whilst I_{win} can be computed as $I_{win} = \varepsilon_{win}\sigma T_{win}^4$ whilst $\sigma = 5.67 \cdot 10^{-8} \text{ W}/(\text{m}^2\text{K}^4)$. From Eqn. 3.3 and Eqn. 3.4 the object radiation I_{obj} could be calculated and from this the object temperature T_{obj} using the camera system's built-in calibration routine. Eqn. 3.5 gives this relationship, a function similar to Planck's law, whilst R , B and F are calibration constants determined by the IR system manufacturer in a radiation laboratory under clean optical conditions.

$$I_{obj} = \frac{R}{e^{B/T_{obj}} - F} \quad \Rightarrow \quad T_{obj} = \frac{B}{\ln(R/I_{obj} + F)} \quad (3.5)$$

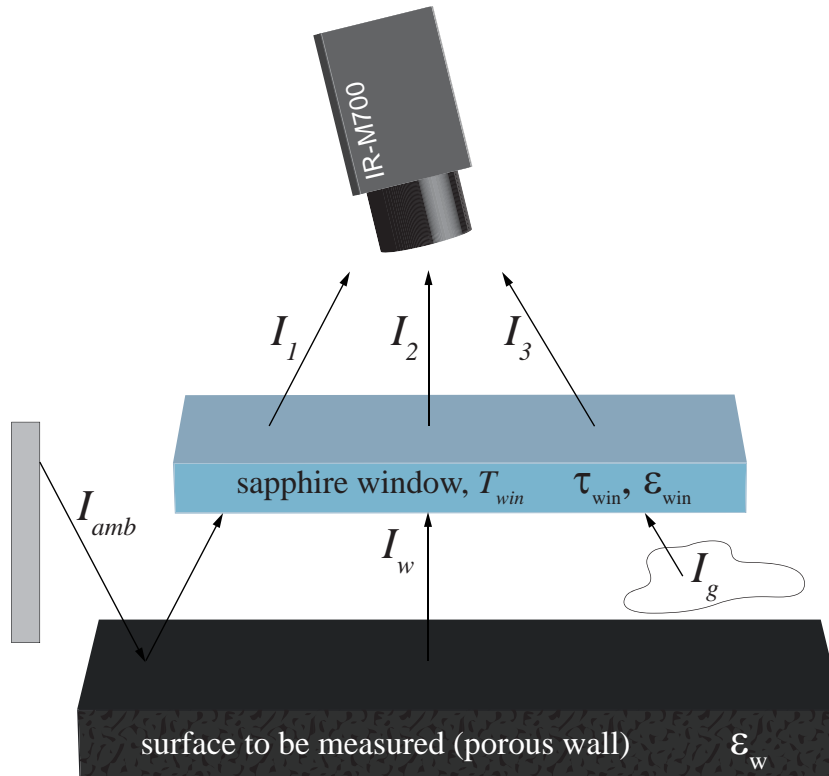


Figure 3.7: Radiation components recorded by the infrared camera

Unfortunately, not all optical parameters are known such as I_{amb} , I_g , ϵ_{win} and even ϵ_{obj} . Especially, the radiation from the window can become quite large compared to the one emitted from the object. Even though its emissivity is quite small ($\epsilon_{win} < 0.12$), from Fig. 3.6 one can see that if the temperature of the window is significantly above the object temperature, I_{win} might become the largest component. This is especially true for the uncooled channel, where the window temperature is close to the hot-gas temperature. Due to these erroneous influences, the software of the infrared system is not able to calculate reasonable temperature values directly from the recorded radiation intensity. Fig. 3.8 shows the data for an actual test case using the built-in calibration and the thermocouple wall temperature measurements versus the recorded radiation intensity. The local radiation data I was averaged from every steady state image within a ring of 1 mm radius around the thermocouple positions. In Fig 3.8, one can see that it is possible to obtain a good match for higher object temperatures between the infrared system and the thermocouple data because the other radiation components are smaller. For lower radiation and object temperatures the discrepancy grows significantly.

Therefore, the IR radiation data was in situ calibrated (Martiny et al. (1996), Schulz (2000), Brauckmann and von Wolfersdorf (2004)). The temperature data (T_{TC}) and the radiation data from around the thermocouples (I_{cam}) was used for a whole set of coolant mass-flow rates ($F = 0$ up to F_{max}) to address the relevant temperature range. These data pairs can be correlated using Eqn. 3.5. This was done using a custom programmed IR image postprocessing *LabView 8.5* software, which uses a

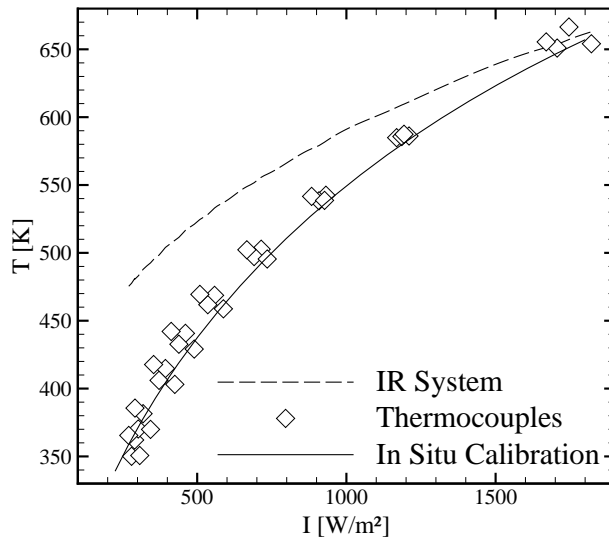


Figure 3.8: Temperature obtained from the infrared system, thermocouple measurements and in situ calibration versus the recorded radiation intensity

script-node to execute *MATLAB* code within *LabView*. The correlation procedure was conducted using the simplex search method of Nelder and Mead (1965) which is part of the *MATLAB* environment. This is a direct search method for multivariate function optimization (I_{cam} and T_{TC} as input; R_{cal} , B_{cal} , and F_{cal} as output of the optimizer), which does not use numerical or analytic gradients. The algorithm proved to be very robust in its convergence behavior (Lagarias et al. 1998) and therefore was preferred over other possibilities. The calibrated relationship between radiation and temperature is also given in Fig. 3.8. One notices that now the temperature values in the lower radiation regime can be determined more accurately. Knowing the parameters R_{cal} , B_{cal} , and F_{cal} from the in situ calibration, the 2D-temperature maps can be calculated from the 2D infrared radiation data omitting any built-in calibration of the camera system:

$$T_{cal} = \frac{B_{cal}}{\ln(R_{cal}/I_{cam} + F_{cal})} \quad (3.6)$$

Brauckmann (2006) presented a study using in situ calibrated infrared data in the field of gas turbine film cooling research and reported an uncertainty in the object temperature of $\delta T_w = 4 K$ after calibration. The same *LabView* software used for the calibration was used to crop the infrared data in a preprocessing step. Since the data were acquired under a viewing angle of 20° the trapezoid distortion of the sample image was also corrected here.

3.6 Measurement and Data Acquisition System

The control and measurement processes of the hot-gas test bench require a complex computer system which uses different interfaces and data communication hardware. The test-bench is operated by a custom designed system control program based upon the *Beckhoff TwinCat* software package. This connects to an *Interbus* bus system to which all test bench equipment such as volume-flow meter, pressure transducers,

3 Experimental Setups and Measurement Techniques for Hot-Gas Tests

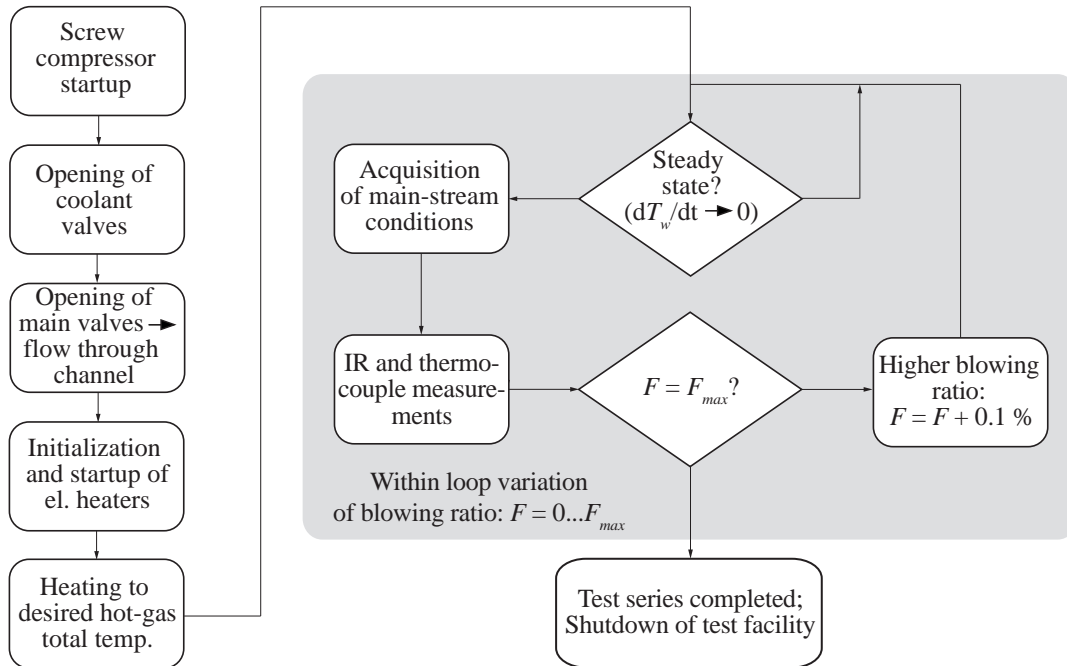


Figure 3.9: Test logic for a hot-gas run measuring several blowing ratios

thermocouples etc. are wired to. At this computer, the hot-gas total temperature, total pressure and mass-flow rate could be set which determines the experimental main-flow parameters. The static pressure along the test-channel is being recorded using a 64-channel *Scanivalve Digital Sensor Array* which is connected to the test facility's ethernet, from where it can be read by the measurement computers.

The test parameters such as hot-gas Mach number, mass-flow rate, and total temperature are set in a *LabView 8.5* software on a second computer and then counterchecked with the state set at the test bench. For the subsonic tests, the static pressure within the test channel at the sample is used for the determination of the local density and the mass-flow rate. This has to match to what is being measured by the control system of the test bench, which is checked in an iterative way. The Mach number cannot be calculated using the isentropic relationship and the measured static and total pressure because the flow straightener at the inlet of the subsonic channel creates a non-negligible pressure loss. For the supersonic experiments, a total pressure above the supercritical pressure was set, which ensures the adequate Mach number within the test section. Here, the isentropic relationship can be employed. The blowing ratio as the determining test parameter can be set as well within this test software. Then, the correct coolant mass-flow rate is calculated according to the geometrical parameters of the channel and the sample and the current flow conditions. This parameter is automatically set at the *Teledyne-Hastings HFC-303* mass-flow controller which is connected via a serial port to the measurement computer.

This *LabView* software also connects to an *Agilent 34970A* datalogger to record and display the surface thermocouple data and the data of any other temperature which

is additionally used and not part of the test bench hardware. To decide whether the steady state is reached, where all of the measurements described in this thesis were performed at, the software routine continually calculates the standard deviation of the thermocouple readings for the data of the past two minutes. If this value is smaller than $0.1 K$ it is assumed that the remaining variation in temperature are only due to random, electrical fluctuations. Now, the data acquisition is started and since the control computer and the measurement computer are synchronized via ethernet all relevant data is read simultaneously. For the temperature data, 20 measurements were taken at a frequency of $\approx 1 Hz$. The infrared data is recorded at the same time manually using a third computer system. All data is available in the ASCII format. For the post-processing of the test-bench and thermocouple data *MATLAB* scripts are used, for the IR data the afore mentioned *LabView* in situ calibration software.

The test logic during the test run is shown as a schematic in Fig. 3.9. On the left hand side, the startup of the test bench and the establishment of the main-flow conditions are shown. The grey box on the right side illustrates the measurement cycle with the incremental variation of the blowing ratio. Important is the criterion of negligible changes in the wall temperature, to record the actual data.

Characterization of Investigated CMC Material

4.1 Introduction

In this chapter techniques to determine the through-flow and the outflow behavior of the investigated C/C samples are presented. In past studies the outflow out of the porous medium was always assumed uniform, meaning that the exiting mass-flow rate is equally distributed over the porous surface. No study was found which showed an investigation to confirm this issue. Therefore, it was decided to setup a test bench to record the outflow-patterns to know if the transpiration cooling models from literature can be applied to the test setup described here. From the outflow tests it could be shown that the flow out of the porous is uniform enough so that the through-flow properties, such as the samples' permeability coefficients can be determined by an integral technique, rather than knowing the local pore distribution and therefore the local permeability distribution. The test setup and the evaluation method for this is based upon the Darcy-Forchheimer equation presented in Section 2.5 which is given thereafter in this chapter.

4.2 Pressure Tank

First, the pressure tank is introduced which was used to test the C/C samples with respect to the through-flow characteristics and pressure requirement but also served as a pressure reservoir for the outflow measurements. In Fig. 4.1 the experimental setup for the stand-alone cold flow tests is displayed. It uses a simple, round pressure tank entirely made from stainless steel, whilst the compressed air is being provided by the coolant-side test-bench as described in section 3.1. The same measurement equipment for the determination of the tank-pressure, the air temperature and the mass-flow rate has been used as well. The custom, plane sealings were cut from a soft carbon material (*SIGRAFLEXTM*) to best seal the slightly rough surface of the ceramic material.

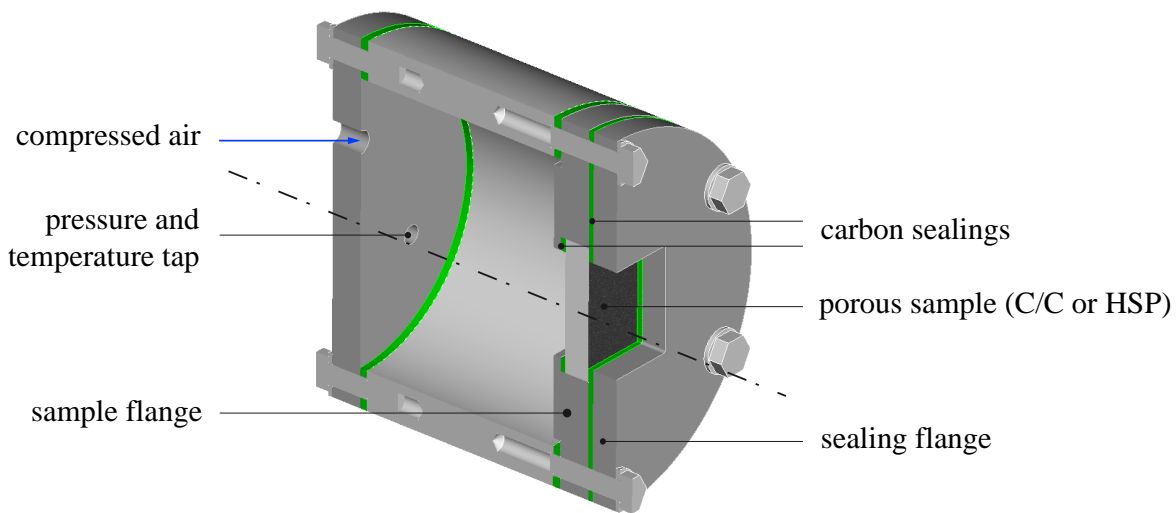


Figure 4.1: Through-flow test rig

On the left hand side, the pressurized air is being connected and the tank pressure is read. The temperature of the test gas is being recorded in the center of the volume of the tank using an *OMEGA H*MT* thermocouple with an accuracy of 1.1 K . The porous material is installed into the sample flange which can accommodate samples with a cross-section of $60 \times 50\text{ mm}^2$. The thickness of the porous material can be varied by using different flanges or spacers. Now, the flat carbon sealing and the sealing flange are put on top of the sample flange and all is bolted tightly to the pressure tank.

4.3 Outflow Measurements

4.3.1 Introduction

For a porous material typically the volumetric porosity ε is known from measurements or geometric calculations. For C/C one can differentiate between the open porosity and the volumetric porosity. First, is normally measured using the Archimedes principle (Selzer et al. 2009) where the sample's underwater weight is measured and then compared to its dry mass. Here, only the pores connected to the surfaces of the sample (fully penetrating through the material) are detected whilst pores surrounded by the C-matrix are neglected. Another unknown quantity is the exit porosity of the material, meaning how much area of the surface exposed to the hot-gas stream is void. This is important for knowing the coolant exit velocity and blowing ration F . Serbest et al. (1999) and Lezuo (1998) assumed that the void area at the sample's exit correlates with the volumetric open porosity: $A_{exit} = \varepsilon A_c$. This is not necessarily true because machining of the C/C material might alter this quantity significantly. Furthermore, inhomogeneities created during the material production process, such as locally increased porosity can change the local permeability

strongly. It can happen that large, single jets emanate from the surface whilst the surrounding area is undersupplied with coolant. Therefore, during this study an approach is presented to determine the exit flow field of porous C/C samples without the presence of the hot-gas flow. From this, qualitatively the integrity of the surface, the pore distribution, and the exit porosity $\varepsilon_{exit} = \frac{A_{exit}}{A_c}$ can be derived.

Wang et al. (2007) presented a photographic technique on how to determine the exit porosity of a porous sintered medium by detecting the penetrating pores. They filled the pores with water and were able to determine the filled pores due to their different reflectance. Due to very small pores of the C/C, which causes problems with adhesion between the water and the pores and spatial resolution of the optical setup this technique could not be applied to the material investigated here. Hall and Hiatt (1994) performed laser doppler velocimetry (LDV) measurements of the outflow profile of highly porous ceramic foams, especially focussing on the outflow velocity patterns and turbulence intensity at this location. They used liquid water sprays as tracer particles, which cannot be used for our C/C material. It would not be possible to inject particles through the low-porosity material. Wharton et al. (2005) also used LDV and hot-wire anemometry to determine the outflow velocity profile out of a highly porous ceramic burner. Titanium dioxide was used as seeder particles for the LDV, which would clog the pores of C/C.

Miniature hot-wire anemometry (Ligrani and Bradshaw 1987) was a possible candidate to measure the outflow profiles. The advantage is that one is able to measure multiple velocity components in high temporal resolution. For the application described here, where one has to measure very close to the porous surface to capture the relatively small jets, the hot-wire anemometry probes proved too fragile. It was decided to use Pitot tube measurements to scan the dynamic pressure of the jets emanating from the surface. With a Pitot tube, the total and static pressure can be determined at the measurement location, and from this the dynamic pressure.

$$p_t - p_s = p_{dyn} = \frac{\rho}{2} v^2 \quad (4.1)$$

In case of free jet condition into ambient, which was assumed at the exit of a pore, and incompressible flow ($M < 0.2$), which is the case for the measured exit velocities, we can substitute for the ambient density in Eqn. 4.1 and the ambient static pressure, so that $p_{dyn} = p_t - p_{amb}$. The outflow velocity can be expressed by the measured dynamic pressure and the ambient conditions.

$$p_{dyn} = \frac{\rho_{amb}}{2} v_{exit}^2 \quad \Rightarrow \quad v_{exit} = \sqrt{\frac{2p_{dyn}}{\rho_{amb}}} = \sqrt{\frac{2p_{dyn} RT_{amb}}{p_{amb}}} \quad (4.2)$$

4.3.2 Experimental Procedure

For the outflow tests the pressure tank test rig described in Section 4.2 was used again to provide a pressure reservoir for the outflow out of the porous material. The whole test setup featuring the measurement equipment is given in Fig. 4.2. The tank

4 Characterization of Investigated CMC Material

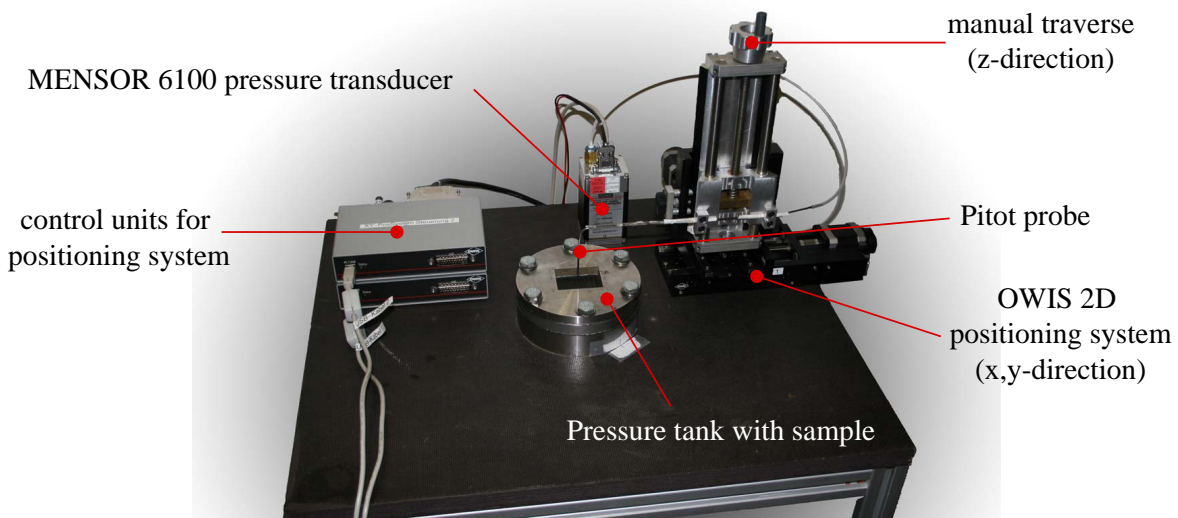


Figure 4.2: Experimental setup for outflow-profile measurements

was equipped with a *OWIS 2D* positioning system to move the probe over the sample. It had a spatial resolution in x and y direction of $5 \mu m$ and a repeatability of $< 15 \mu m$ at $95 mm$ possible adjustment in each direction. For the sample-normal (z) direction a manual traverse was used to adjust the height of the probe over the sample. The Pitot tube was bolted to the traverse for the z direction and aligned properly so it was perpendicular to the porous surface. It was connected to a *MENSOR Series 6100* digital pressure transducer which measures up to $10000 Pa$ difference pressure at an accuracy of $1 Pa$. The pressure transducer was used against ambient and had a data acquisition rate of $50 Hz$. Hence it recorded the dynamic pressure directly given the validity of the free jet condition. To achieve a spatial resolution on the porous material in x and y direction of $0.5 mm$, a commercial Pitot probe from *Airflow LTD* was customary modified with an insert with an inner diameter of $0.25 mm$ and $0.5 mm$ outer diameter, which is the lower limit for Pitot tube measurements.

The *LabView 8.5* software tool *FlowProfile2D* was developed and used to automatically control the positioning system and for DAQ purposes. This software was programmed in a way that it automatically detects a steady state value with respect to the dynamic pressure. During the movement of the Pitot tube it can take quite different time spans until this value is reached due to the physical change in total pressure and due to the dynamic head traveling upstream through the connection tube to the pressure transducer. To optimize the measurement time it was decided to compare a floating average calculated from the current readings to a pressure margin. From every five dynamic pressure reading an average is calculated. If three consecutive averages differ less than the pressure margin from each other, the software starts recording the actual values, which are averaged into one data point afterwards. For these measurements a pressure margin of $1 Pa$ proved to be most reasonable for accuracy and total test time. This procedure is exemplarily shown in Fig. 4.3(a) where the dynamic pressure is plotted versus the number of readings and the measurement

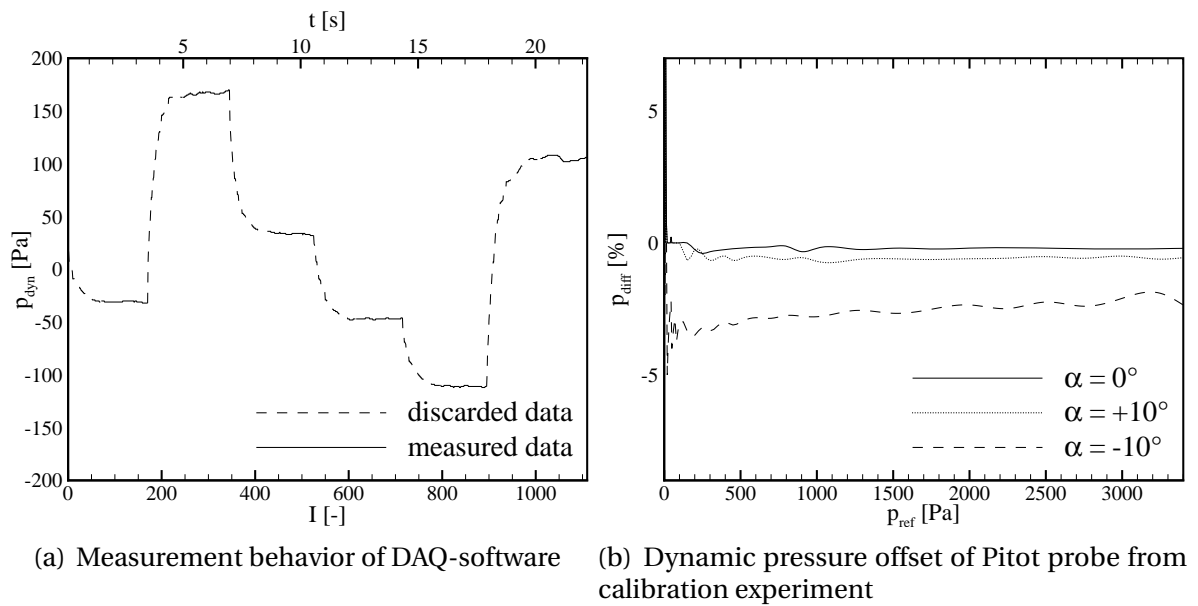


Figure 4.3: Measurement logic of DAQ software and calibration of Pitot tube

time respectively. Here, the rise or fall time after moving the Pitot tube can be seen by looking at the discarded data (dashed line). Once the above explained pressure criterion had been reached, the data is recorded (solid line). Slight fluctuations due to physical transient phenomena such as pulsating or laterally moving jets can still be seen in the data, but are not of large order. Afterwards, the probe is automatically moved to the next position. From this chart one can also see that when using 100 readings to assemble one data point, six data points can take approximately 20 s. The exit flow area of the porous sample in the pressure tank is $50 \text{ mm} \times 40 \text{ mm}$, whereas only $35 \text{ mm} \times 45 \text{ mm}$ can be measured due to geometrical constraints. At the desired spatial resolution this means having $N = 91$ sampling points in x direction and $K = 71$ in y direction, yielding a total of 6461 points per test run. Therefore, one test took around 8 hours to complete. To exclude blockage effects from the sealing flange of the pressure tank, the data at the edge of the measurement region was discarded. For the averaging a rectangle of $30 \text{ mm} \times 40 \text{ mm}$ was used ($N = 81$, $K = 61$). In Fig. 4.4(a) the different areas of the exit surface are sketched.

Then, the Pitot tube was calibrated against an ideal, incompressible nozzle flow. The reference pressure was measured with another *MENSOR Series 6100* digital pressure transducer with an accuracy of 0.25 Pa . Furthermore, the probe was tilted at an angle $\pm 10^\circ$ to investigate the influence of velocity components not aligned with it or the probe being installed slightly off the perpendicular direction of the sample. In Fig. 4.3(b) the difference pressure of the Pitot tube and the reference value in percent is plotted over the reference pressure. One can see that the normal aligned Pitot probe measures the dynamic pressure very accurately. Tilting the probe can yield an error of around 3 % in the range investigated. For larger angles the read dynamic pressure can even become negative.

4 Characterization of Investigated CMC Material

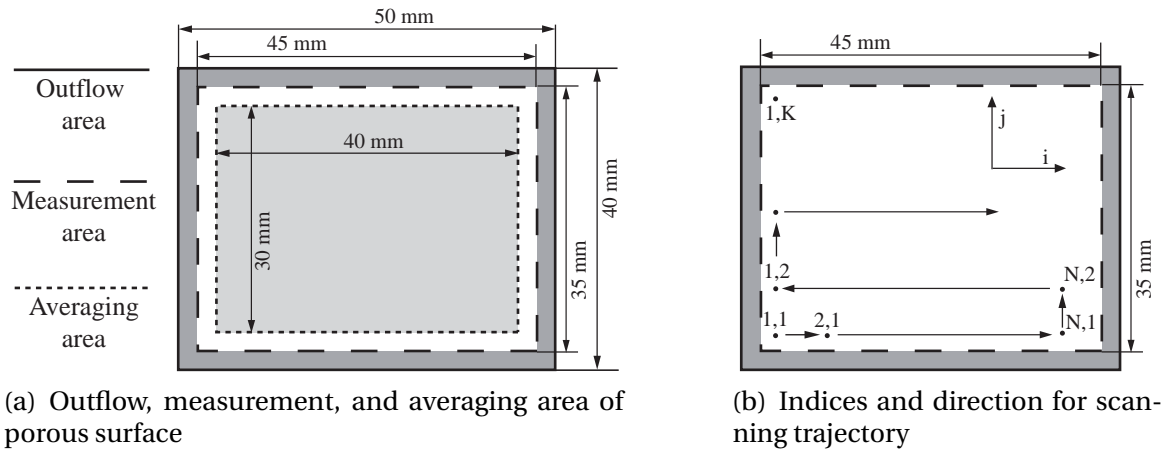


Figure 4.4: Measurement geometry and indices

In case the probe measured a negative value, which was more often the case for the tests with C/C, it was assumed that it is due to a velocity component at a large angle with respect to the probe. This can be caused by flow tangential to the Pitot tube in recirculation regions between the emanating jets. Additionally, jets exiting the porous specimen not normal to the surface can cause this phenomenon. Last is assumed to be true only in rare cases because with the hollow sphere material used for verification the main-flow direction is relatively strict predefined. This is also true for the C/C where the fibres mostly determine the flow path of the coolant exiting the surface. Also the majority of the crack pattern within the matrix points into this direction. Therefore, all negative dynamic pressure data was set to zero (see Eqn. 4.3), which means that it is assumed that no mass-flow is exiting the sample at a location of negative pressure.

$$p_{dyn,ij} = \begin{cases} p_{dyn,ij}, & \text{if } p_{dyn,ij} > 0 \\ 0, & \text{if } p_{dyn,ij} \leq 0 \end{cases} \quad (4.3)$$

With the zeroed pressure distribution one is able to calculate a velocity distribution using Eqn. 4.2. The regions of negative measured dynamic pressure yield following the above explained approach the zero velocity values. To check if the measured exit velocity also yields the set air mass-flow rate in the pressure tank one can calculate the exit mass-flow rate:

$$\dot{m}_{exit} = \rho_{amb} A_{exit} \frac{\sum_{i=1}^N \sum_{j=1}^K v_{exit,ij}}{NK} \quad (4.4)$$

Here, an average of all velocity data over the number of points is calculated and then multiplied by the jet density (ambient) and the exit area ($40 \text{ mm} \times 50 \text{ mm}$). Here a slight uncertainty enters the evaluation, since it is assumed that the averaged velocity of the measured area ($30 \text{ mm} \times 40 \text{ mm}$) equals the average over A_{exit} . Following the uncertainty analysis according to Moffat (1988) applied to Eqn. 4.2 the uncertainty in the exit velocity can be derived as:

$$\left(\frac{\delta v_{exit}}{v_{exit}}\right)^2 = \left(\frac{1}{\sqrt{2}} \frac{\delta p_{dyn}}{p_{dyn}}\right)^2 + \left(\frac{1}{\sqrt{2}} \frac{\delta T_{amb}}{T_{amb}}\right)^2 + \left(\frac{1}{\sqrt{2}} \frac{\delta p_{amb}}{p_{amb}}\right)^2 \quad (4.5)$$

This yields to uncertainties in v_{exit} from 35 % at $v_{exit} = 2 \frac{m}{s}$ down to 0.5% for $v_{exit} > 40 \frac{m}{s}$. The error in the mass-flow rate computed from the average velocity using Eqn. 4.4 is being computed by applying the uncertainty in v_{exit} for every discrete point and multiplying it with the corresponding discrete area ($0.5 \text{ mm} \times 0.5 \text{ mm}$) and ambient density. The uncertainty in the total computed mass-flow rate is up to 4.9 % for $\dot{m} = 4 \text{ g/s}$ and up to 2.2 % for $\dot{m} = 8 \text{ g/s}$ due to the lower uncertainty for higher exit velocities.

To compute the exit porosity two ways are proposed: First, all positive velocities are averaged (\bar{v}_{exit}^+) following the assumption that only positive regions of dynamic pressure represent an outflow of the porous surface. This exit velocity will be higher than \bar{v}_{exit} by the factor of $1/\varepsilon_{exit}$. The second method is to count all points at which a positive dynamic pressure was measured and then compare it to the total number of data points (ε_{exit}^+).

$$\varepsilon_{exit} = \frac{\dot{m}}{\bar{v}_{exit}^+ \rho_{amb} A_c} \quad \text{or} \quad \varepsilon_{exit}^+ = \frac{n^+}{NK} \quad (4.6)$$

4.3.3 Validation

Prior to the actual tests, several influencing factors were investigated using a C/C sample. First, the number of readings per data point was varied. It was tried to find an optimum between accuracy and measurement time. Table 4.1 shows the data measured over a small area of a C/C sample (11×11 data points) for 500 readings per point down to 25 readings. The case with the most readings can be considered a reference case, because at 50 Hz DAQ frequency the measurement time was 10 s and should capture all transient phenomena. The test runs at 100 and 50 readings per data point all resulted in a sufficient agreement with the area averaged dynamic pressure and area averaged velocity (see Table 4.1). The data set with 25 readings per point yielded more inaccurate averaged values. Since the maximum velocity value in the data field was captured better with the 100 readings per data point and the measurement time reduction was not significant, it was chosen to perform all tests with 100 readings per data point (see also in Fig. 4.3(a)).

	$\bar{p}_{dyn} [Pa]$	$v_{exit,max} [m/s]$	$\bar{v}_{exit} [m/s]$
500 Readings	41.9	76.8	6.72
100 Readings	41.8	76.4	6.65
50 Readings	41.6	75.2	6.67
25 Readings	40.8	76.0	6.62

Table 4.1: Effect of variation of readings per data point on outflow data

4 Characterization of Investigated CMC Material

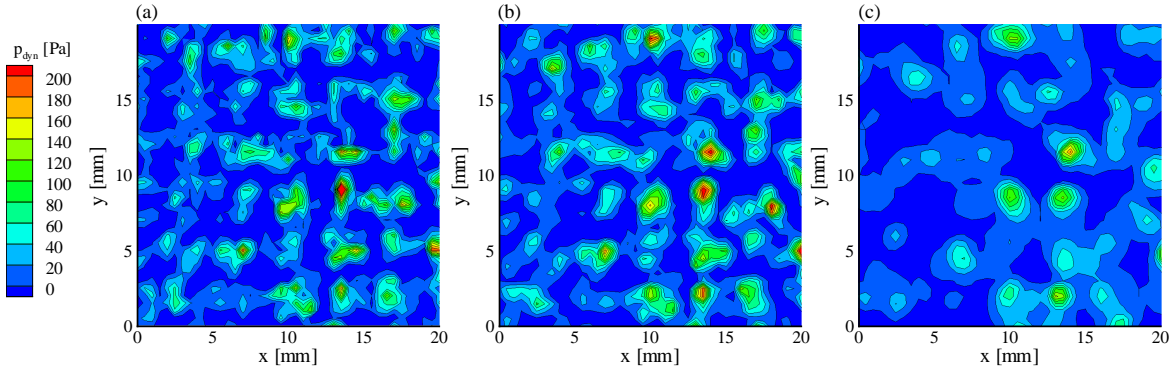


Figure 4.5: Contour plots of dynamic exit pressure for three different Pitot probe heights: a) $H = 0.2 \text{ mm}$, b) $H = 1 \text{ mm}$, c) $H = 3 \text{ mm}$

Another important factor is the height of the Pitot-probe over the surface. If one is measuring too close, a blockage effect will affect the quality of the measurements. If the Pitot probe is positioned too far away, it will be difficult to detect the position of the jet exit because right at the exit the jets will laterally spread and merge with each other. Five tests in the center of a C/C sample were performed in a $20 \text{ mm} \times 20 \text{ mm}$ region. The height above the sample was altered from $H = 0.2 \text{ mm}$ up to $H = 3 \text{ mm}$. It was adjusted by using spacers placed on the sample having the adequate thickness. Then the Pitot tube was moved until it slightly touched the spacer which afterwards was removed. It was ensured, that the positioning system and the sample surface were in plane, so that no changes in height during the test run could occur. In Fig. 4.5 the dynamic pressure contour at the same mass-flow rate at different heights is shown. One can see that very close to the porous surface the high pressure regions are easy to distinguish from the low dynamic pressure regions. The single jets are of high dynamic pressure. At $H = 3 \text{ mm}$ the maxima are lower and the regions of smaller dynamic pressure grew larger, indicating the merging of the jets.

In Table 4.2 the averaged velocity magnitude and the maximum in the velocity field is given. One can notice, similar to Fig. 4.5, that the average velocity stays almost constant up to a height of $H = 1 \text{ mm}$, whilst $v_{exit,max}$ only decreases slightly. To find the best compromise $H = 1 \text{ mm}$ was picked for the measurements. This ensures still a reasonable clarity of the positive pressure regions which are used for the calculation of the exit porosity and the outflow velocity magnitude.

To verify that the Pitot tube measurement technique can be used to determine the outflow flow-field of porous media, first a metallic material was investigated. The

H [mm]	0.2	0.6	1	2.5	3
\bar{v}_{exit} [m/s]	5.51	5.57	5.52	4.48	4.01
$v_{exit,max}$ [m/s]	23.7	22.6	21.2	18.7	17.9

Table 4.2: Pitot probe height variation using C/C as porous material

goal was to match the exiting mass-flow rate with the one set at the test bench with the Pitot tube measurements. The hollow sphere packing, which is introduced in more detail in the following Section 4.4.2, was chosen because of its high porosity and large exit pores, which are in the order of the sphere diameter ($D = 2.5 \text{ mm}$). Therefore, at a spatial step size of 0.5 mm several data points will be taken at one exit pore. The surface of the HSP sample was scanned as complete as possible, meaning an area of $35 \text{ mm} \times 45 \text{ mm}$. This yielded at the above mentioned spatial resolution 6461 data points. The Pitot tube was positioned 1 mm above the porous surface. The thickness of the sample was $L = 10 \text{ mm}$.

The 2D outflow profiles of the HSP material at two different mass-flow rates is shown in Fig. 4.6(a) and Fig. 4.6(b). The air jets emanating from the surface are displayed in the normal co-ordinate direction, whilst the velocity magnitude is being shown by the contour color. One can see from these results that the velocity magnitude scales qualitatively very good with the doubled air mass-flow rate and the distribution of the jets is very uniform.

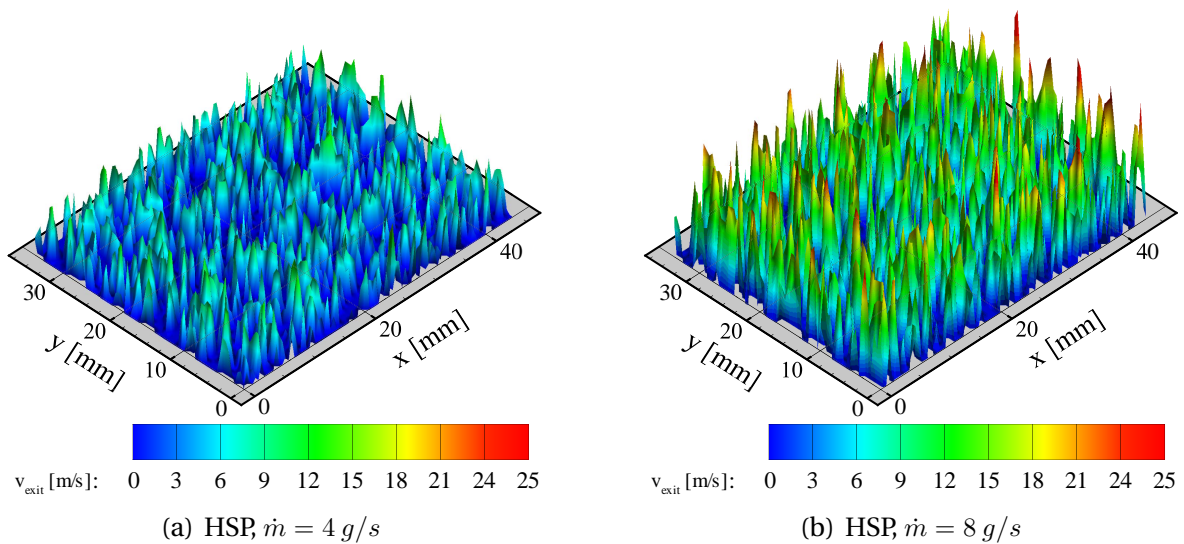


Figure 4.6: Outflow profiles of hollow sphere packings at different air mass-flow rates

To analyze this also quantitatively, the exit mass-flow rate was computed from the averaged velocity (Eqn. 4.4). The maximum offset is at the lower air mass-flow rate of 7.3 % at an uncertainty in the measured mass-flow rate of 4.9 %. This shows, that for a highly porous medium the velocity and mass-flow rate respectively can be measured within a small uncertainty margin considering the assumptions that have been made previously, especially regarding the zeroing of negative dynamic pressure.

From the outflow data the exit porosity of the HSP sample can be computed. Table 4.4 summarizes these values. The measured open (and volumetric) porosity of 37 % for this material is known. From the outflow data lower values for ε_{exit} and ε_{exit}^+ are computed, indicating higher measured outflow velocities. The sample has been

4 Characterization of Investigated CMC Material

Case	\dot{m} [g/s]	\bar{v}_{exit} [m/s]	\dot{m}_{exit} [g/s]	$(\dot{m}_{exit} - \dot{m})/\dot{m}$ [%]	$\frac{\delta\dot{m}_{exit}}{\dot{m}_{exit}}$ [%]
4 g/s	4	1.87	4.29	7.3	4.9
8 g/s	8	3.79	8.48	6.0	2.2

Table 4.3: Outflow characteristics of HSP samples. $\rho_{amb} = 1.148 \text{ kg/m}^3$

cut, i.e. the surface is constituted from sliced hollow spheres (see Fig. 4.10(a)), which means the volumetric porosity value does not represent the porosity at every slice. Furthermore, boundary layers form within the pores of the material which create velocity profiles within the exiting jets. These can not be easily recorded accurately. Given the simplicity of the measurement technique the comparison between volumetric porosity and measured exit porosity are reasonable, the smallest porosity value is -19.5% off, whilst the best comparison is -8.9% smaller.

Case	\bar{v}_{exit}^+ [m/s]	ε [%]	ε_{exit} [%]	ε_{exit}^+ [%]
4 g/s	5.84	37.0	29.8	32.0
8 g/s	10.96	37.0	31.8	33.7

Table 4.4: Exit porosities of HSP samples. $\rho_{amb} = 1.148 \text{ kg/m}^3$

4.3.4 Exit-Flow Profiles of C/C Material

Now, the Pitot tube scanning was applied to two different C/C samples. First, to a sample of the PH1732 charge (randomly oriented fibres $\pm 15^\circ$), which was measured under supersonic hot-gas conditions with transpiration cooling applied. The cooling efficiency of the PH1606, which has a $0/90^\circ$ fibre orientation, was investigated in the subsonic, insulated channel. Both samples had a thickness of 10 mm .

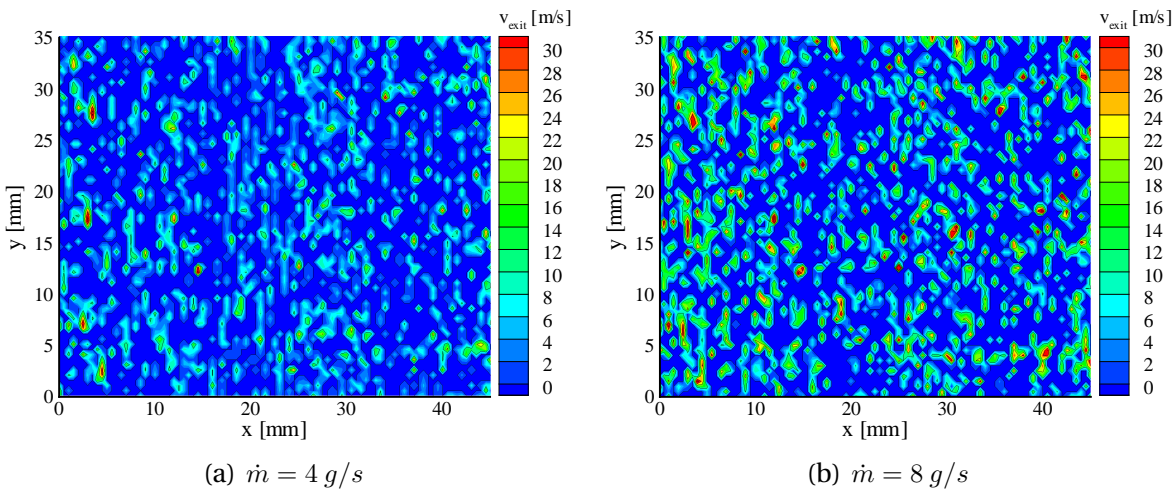


Figure 4.7: Outflow profiles of PH1732 C/C at different air mass-flow rates

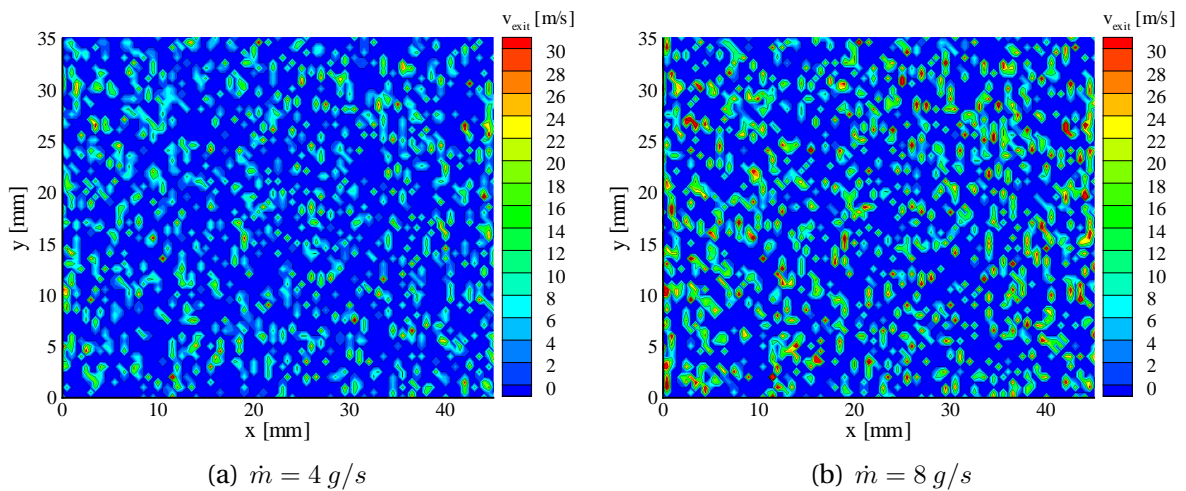


Figure 4.8: Outflow profiles of PH1606 C/C at different air mass-flow rates

Fig. 4.7(a) through Fig. 4.8(b) show the contours of the exit velocity at two air mass-flow rates. Generally one can tell, that when changing the mass-flow rate the velocity pattern stays mostly the same. This indicates, that the actual pores and the jets emanating from them are recorded by the Pitot tube. The pattern shifts into regions of higher velocities and more peak exit velocity values can be seen as compared to the $\dot{m} = 4 \text{ g/s}$ cases. The patterns can be considered homogeneous. No extremely high values can be found nor are heavily undersupplied regions present. Locally, the jets are somewhat distributed differently whilst the regions with zero velocity (negative or zero dynamic pressure) are in total larger than the positive ones. Furthermore, no distinct, repeating pattern which could indicate the weave of the carbon fibres is visible. The tested surfaces in Fig. 4.7(a) through 4.8(b) were all smooth, which is a result of the shaping process of the samples (polishing until desired thickness is reached). The sample PH1606 originally was at $L = 15 \text{ mm}$ thickness, for the outflow tests it had to be cut to $L = 10 \text{ mm}$ which is being done by splitting the sample between the fibres. Therefore, one side of it was unpolished and was scanned as well to see if the surface treatment has a major influence on the outflow pattern. Fig. 4.9(a) and Fig. 4.9(b) show the exit velocity, the contour color indicates its magnitude. The profile of the rough side differs significantly from the smooth side: First, more jets with very high velocity can be observed, which are of smaller diameter. The jets from the rough sides are larger in diameter and lower in velocity magnitude and follow a regular pattern, which coincides with the weave of the composite sample.

Analogous to the HSP outflow data the exit porosity for the tests with C/C has been derived and is summarized in Table 4.5. Quantitatively, the agreement between the set air mass-flow rate set at the test rig and the one derived from the exit velocities is less accurate than for the validation case, and significantly larger than the uncertainty in \dot{m}_{exit} . For the tests at $\dot{m} = 8 \text{ g/s}$ the agreement becomes somewhat better, since the exit velocity does not scale proportional with the air mass-flow rate.

4 Characterization of Investigated CMC Material

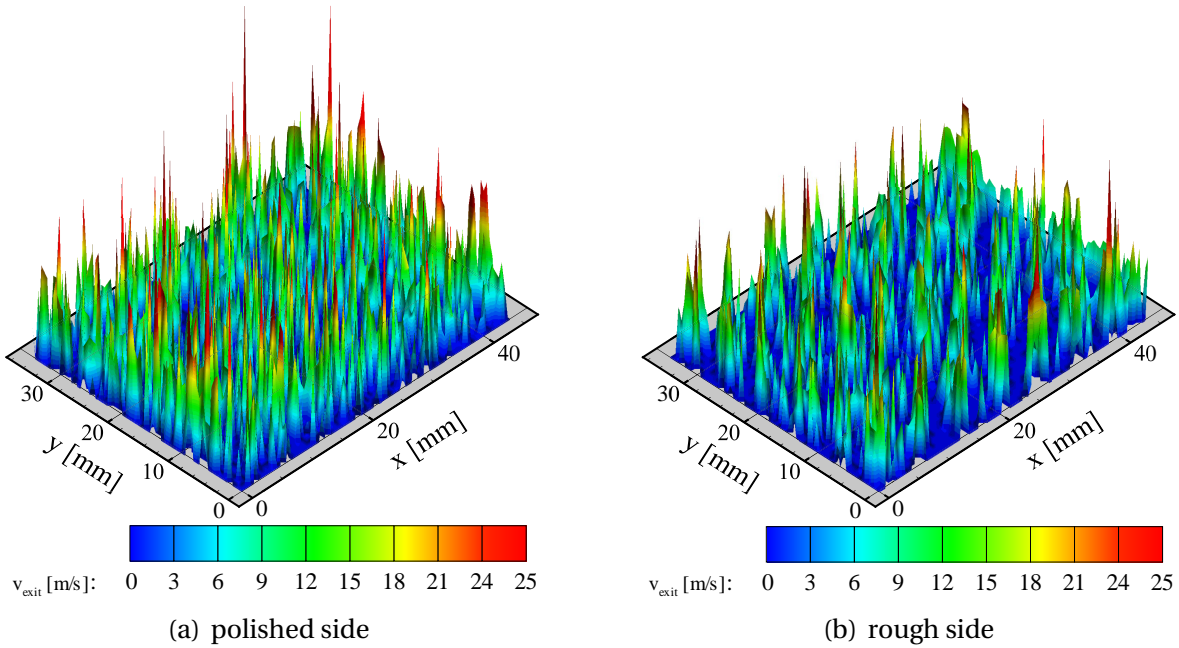


Figure 4.9: Outflow profiles of PH1606 C/C from top (polished side) and bottom (rough side)

Sample	\dot{m} [g/s]	\bar{v}_{exit} [m/s]	\dot{m}_{exit} [g/s]	$\frac{(\dot{m}_{exit}-\dot{m})}{\dot{m}}$ [%]	$\frac{\delta\dot{m}_{exit}}{\dot{m}_{exit}}$ [%]
PH1732	4	2.25	5.18	29.6	3.5
PH1732	8	4.02	9.25	15.6	1.7
PH1606	4	2.62	6.03	50.7	2.3
PH1606	8	4.53	10.42	30.3	1.4
PH1606, rough	4	2.19	5.03	25.7	3.3

Table 4.5: Outflow results for two different C/C samples at different air mass-flow rates. $\rho_{amb} = 1.148 \text{ kg/m}^3$

Now, the exit porosities ε_{exit} and ε_{exit}^+ are given in Table 4.6. Both quantities match less accurately as compared to the HSP validation case. This is because the averaged exit velocity can not be determined at the same precision and is somewhat higher than with the HSP. Nevertheless, ε_{exit}^+ which was computed by counting the positive dynamic pressure data is mostly invariant to the set air mass-flow rate. This again is an indicator that this method is able to capture the pores sufficiently accurate. All measured exit porosity values are significantly higher than the volumetric porosity ε determined by the manufacturer of the C/C material.

4.3.5 Conclusions

The Pitot tube technique is able to detect the exit (connected) pores of the porous C/C material. For quantitatively correct velocity measurements another technique such as miniature hot-wire anemometry can be used. Nonetheless, an exit porosity

4.4 Through-Flow and Permeability Coefficients of C/C

Sample	\dot{m} [g/s]	\bar{v}_{exit}^+ [m/s]	ε [%]	ε_{exit} [%]	ε_{exit}^+ [%]
PH1732	4	7.77	11.1	22.4	30.9
PH1732	8	14.28	11.1	24.4	30.8
PH1606	4	11.14	11.3	15.6	25.1
PH1606	8	17.66	11.3	19.7	27.2
PH1606, rough	4	8.88	11.3	19.6	26.7

Table 4.6: Exit porosities of C/C samples. $\rho_{amb} = 1.148 \text{ kg/m}^3$

can be derived from the dynamic pressure data and outflow velocity data. The best way is counting the values of positive dynamic pressure and comparing it to the total number of measured data points.

For the C/C, ε_{exit}^+ was significantly higher than the open porosity, which proves the assumption that $A_{exit} \neq \varepsilon A_c$. For the sample charge with randomly oriented fibres (PH1732) an exit porosity of $\varepsilon_{exit}^+ \approx 30\%$ was found for the perpendicular oriented C/C (PH1606) a value of $\varepsilon_{exit}^+ \approx 26\%$.

Furthermore, the properties of the surface of the C/C (polished or rough) can have a strong impact on the outflow pattern. The impact on ε_{exit}^+ or the average outflow velocity was small though.

Independent of this, the outflow out of the porous wall sample was very uniform. No significant peaks or large regions with no mass-flow exiting the surface could be seen. For the determination of the permeability coefficients, the through-flow behavior can be described using the one-dimensional Darcy-Forchheimer equation, which incorporates integral values for the permeability coefficients summarizing all pressure losses within the sample. For their determination, the sample size has to be large enough to have enough jets or regions with low mass-flow to give a representative figure for further applications. This is the case for the test setup described in this study as shown in the following section.

4.4 Through-Flow and Permeability Coefficients of C/C

4.4.1 Introduction

For the determination of the permeability coefficients, Innocentini et al. (2000) used a pressure-decay technique, where a tank is being pressurized followed by an blow-off and recording of the transient pressure and mass-flow rate data. The fluid expands over the porous sample and from the pressure loss and mass-flow rate characteristics the permeability coefficients K_D and K_F (see Section 2.5) could be determined. In contrast to this, for the presented research a steady-state measurement technique similar to the one presented by Moreira et al. (2004) was used. Last proved to be more applicable, because during the tests a non-negligible settlement time of the supply pressure in the tank or in the coolant plenum could be observed. This is most likely due to the much higher supply pressure and therefore supply density

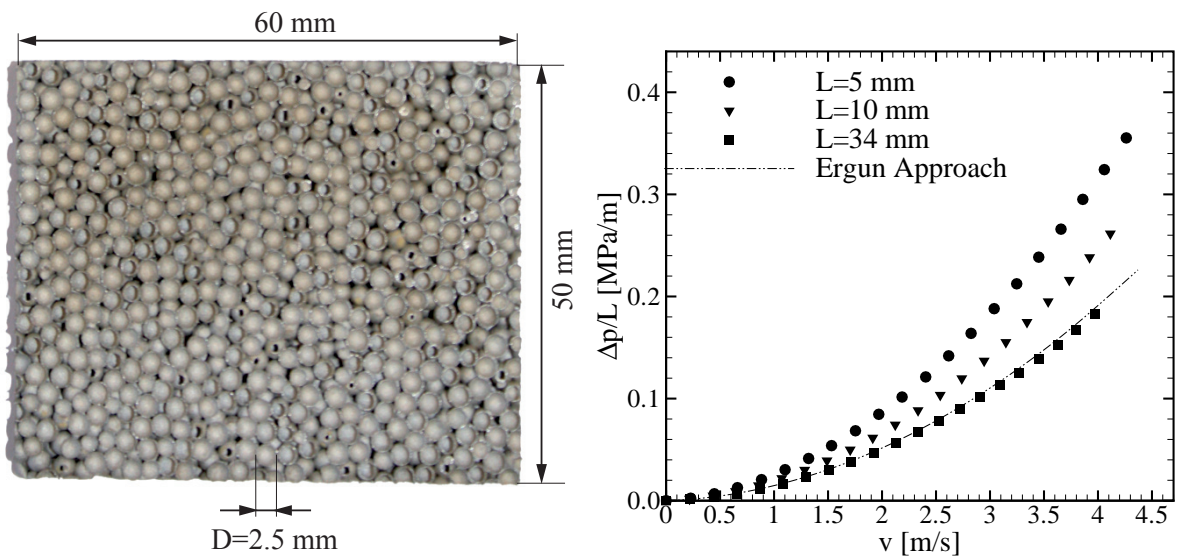
4 Characterization of Investigated CMC Material

in our setup. Furthermore, in the hot-gas tests the coolant temperature needs a substantial amount of time until thermal equilibrium is reached. Hence, using a transient technique would have led to erroneous results. Therefore, the procedure laid out in this section could also be used for the evaluation of the pressure loss data obtained from the transpiration cooling tests (see Section 5.5) at steady state.

4.4.2 Validation of Test-Rig

For the C/C samples no general correlation for the pressure drop and permeability coefficients based upon the internal geometry or porosity is known. Additionally, material intrinsic quantities such as the average pore diameter are also difficult to determine. Therefore, a validation of the test rig had to be conducted using a different porous material. The goal was to be able to record a pressure drop and through-flow velocity relationship, which follows Ergun's approach (see Section 2.5). Therefore, a hollow sphere packing (HSP) was chosen as a test sample because of its known porosity of 37 % and known sphere diameter of $D = 2.5 \text{ mm}$. Since the HSP material is a densest packing of spheres the sphere diameter equals the pore diameter d_p in Ergun's definition. Therefore, this material should follow Ergun's approach which has been developed for a bed of packed spheres and is well established. An image of the sample is given in Fig. 4.10(a). In a study describing the acoustic feature of the HSP material further details on it can be found (Pannert et al. 2009).

The HSP samples were provided by the French Aerospace Lab (ONERA) in three different thicknesses ranging from 5 mm up to 34 mm with an cross-section of $60 \times 50 \text{ mm}^2$ which is the exact same cross-section as for the C/C samples tested in the



(a) Sketch of used hollow sphere sample

(b) Pressure drop per unit length of three different HSP samples compared to Ergun's approach

Figure 4.10: Validation of through-flow test rig

pressure tank. All of them were tested with air as the test gas and the mass-flow rate ranged up to 10.5 g/s . Due to its high porosity the measured pressure loss over the HSP was small in comparison to the C/C samples. Therefore a *MENSOR Series 6100* digital difference pressure transducer with an accuracy of 1 Pa and a maximum range of 10000 Pa could be employed.

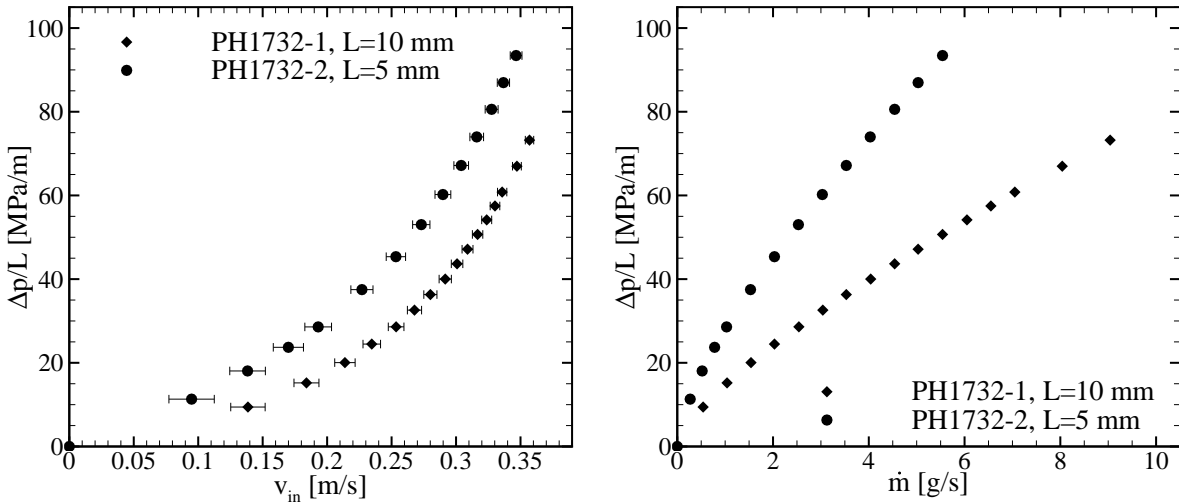
In Fig. 4.10(b) the pressure drop per unit length (see. Eqn. 2.48) has been plotted for all three HSP material samples and for Ergun's approach using a porosity of $\varepsilon = 37 \%$ and a pore diameter of $d_p = 2.5 \text{ mm}$. The samples with $L = 5 \text{ mm}$ and $L = 10 \text{ mm}$ exhibit a higher pressure drop per unit length compared to the other sample and Ergun's approach because of the not fully developed inflow into the HSP material. The flow needs a few sphere layers to have a periodic velocity profile. Theoretically, the thinnest sample only has two layers (twice the sphere diameter equals the thickness) and the $L = 10 \text{ mm}$ one four layers. From the first sphere layer on, the velocity gradients at the sphere walls are steeper than in the periodic flow part and therefore cause higher skin friction and pressure drop respectively as compared to the fully developed part. Since this inflow region only appears in the first few sphere layers, the pressure drop per unit length is higher for the thinner material than for the $L = 34 \text{ mm}$. The inflow effect has here been averaged over a much shorter length (more than thirteen sphere layers for the thick sample). Finally, Ergun's approach, which has been developed for periodic flow within sphere packings, matches the data of the thickest HSP sample very well. Hence, it can be stated that with the present test configuration it is possible to investigate the pressure drop characteristic of highly porous sphere packings. Effects which could be erroneous for the determination of the permeability coefficients of the C/C can be neglected.

4.4.3 Determination of Permeability Coefficients

In this section the technique for the determination of the permeability coefficients of the C/C as it is used in the through-flow tests with the pressure tank and hot-gas experiments is explained. The measurement procedure is the same as for the HSP material samples, but another pressure transducer was used (*OMEGA*, accuracy of 0.005 MPa). Based upon structural failure of the material the pressure for the 5 mm thick samples was limited to 1.0 MPa gauge pressure. For the 10 mm samples the from the test bench available 1.5 MPa gauge pressure could be applied to record the widest data spectrum possible with this test setup.

A typical through-flow data set is shown for the PH1732 C/C material at two thicknesses in Fig. 4.11(a) and Fig. 4.11(b). On the left hand side the pressure drop per unit length is plotted versus the inlet velocity into the porous material, which is calculated according to Eqn. 2.49. For higher v_{in} the curves exhibit a non-linear slope which indicates that the Forchheimer regime representing the drag pressure loss is dominant. Furthermore, the thinner sample yielded a higher pressure drop per unit length than the thicker one. This can be caused by inlet and exit effects of

4 Characterization of Investigated CMC Material



(a) Pressure drop per unit length versus superficial through-flow velocity

(b) Pressure drop per unit length versus air mass-flow rate

Figure 4.11: Through flow characteristics in the pressure tank for the PH1732 sample charge

the fluid entering and leaving the sample causing higher pressure drop here. This effect was not separately investigated in this study. Last, is especially visible for $\Delta p/L$ being plotted versus the air mass-flow rate \dot{m} in Fig 4.11(b).

The pressure loss is according to Eqn. 2.48 depending on the dynamic viscosity of the fluid multiplied with the inlet velocity v_{in} , the term $\rho_{in}v_{in}^2$, and both permeability coefficients, whilst only K_D and K_F are unknowns. All other quantities can be derived from test data. This means, that a multi-variable problem exists. Now, the Darcy-Forchheimer equation can be solved for the permeability coefficients, using the simplex search method of Nelder and Mead (1965) which was previously employed for the in situ calibration of the infrared data in Section 3.5. For the PH1732 samples the values are given in Table 4.7.

Since an analytical uncertainty analysis according to Kline and McClintock (1953) and Moffat (1988) is not possible when using the simplex search method for K_D and K_F , a Monte Carlo method (Hall 2000; Willink 2006) was used to determine these quantities. First, the uncertainty in the input parameters $\Delta p/L$, μv_{in} , and $\rho_{in}v_{in}^2$ has been calculated (see Appendix A). Around every data point which is displayed in for example Fig. 4.11(a) a normal distributed, randomized vector with 100000 components has been computed for $\Delta p/L$, μv_{in} and $\rho_{in}v_{in}^2$. For this, the uncertainty was

	$K_D \cdot 10^{13}$ [m ²]	$K_F \cdot 10^8$ [m]	$\delta K_D/K_D$ [%]	$\delta K_F/K_F$ [%]
PH1732-1	1.63	2.18	4.39	3.81
PH1732-2	1.02	1.17	6.24	7.75

Table 4.7: Darcy and Forchheimer permeability coefficient and their uncertainties obtained from pressure tank test. PH1732 sample material

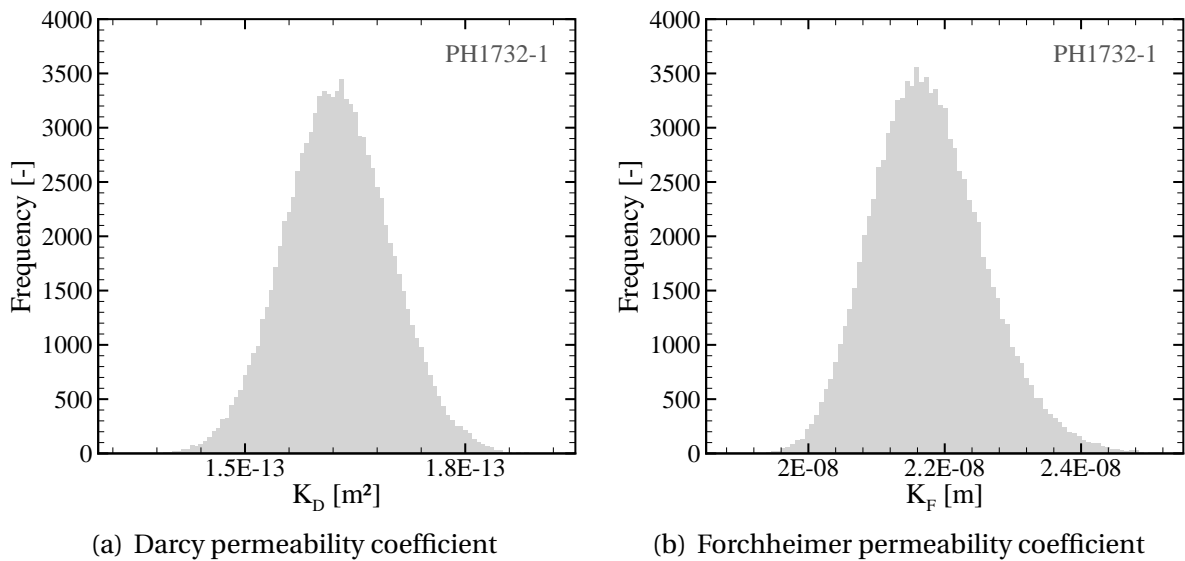


Figure 4.12: Frequency of the permeability coefficients using the Monte Carlo uncertainty determination technique. PH1732-1 sample

taken as the standard deviation for the random number generator. Afterwards, the simplex search method was run for 100000 times as well, so that every combination in the input variables yielded a set of permeability coefficients.

From this data, the mean value was taken as the permeability value which then matched exactly the values obtained from the fitting with the measured data points. This proves the statistical validity of 100000 sampling points. In Fig. 4.12(a) and 4.12(b) exemplarily the frequency of the calculated permeability coefficients is given using the Monte Carlo technique with the data of the PH1732-1 sample. The standard deviation of the data in these plots or in the output vector of K_D and K_F now represents the uncertainty in these quantities given in Table 4.7. These values have a confidence interval of 95.5% since the uncertainty in $\Delta p/L$, μv_{in} , and $\rho_{in} v_{in}^2$ was also given within this range. The uncertainty is always less than ten percent, the Darcian permeability coefficient can be estimated more accurately.

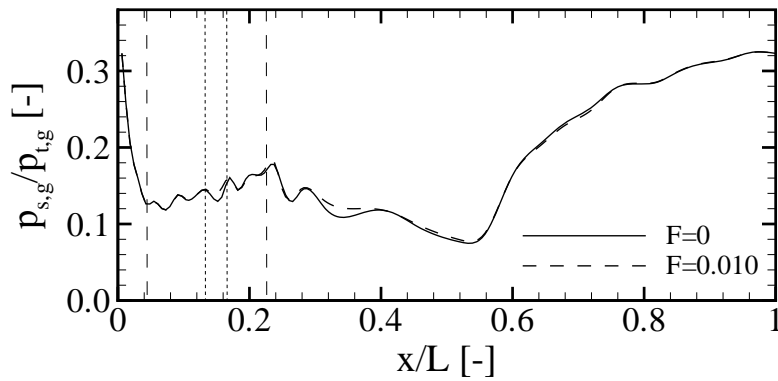
By the validation of the through-flow tank using the HSP material and comparing the data to Ergun's approach and the presented technique for the evaluation of the permeability coefficients in the cold flow pressure tank tests, it is possible to also apply this methodology to the data recorded during the hot-gas tests. Furthermore, these tests showed the maximum pressure drop expected at the mass-flow rates needed for the blowing ratio range to be investigated and hence aided in designing the test facility with respect to pressure and mass-flow rate requirements for air.

Transpiration Cooling of C/C Wall Segments with Different Coolants

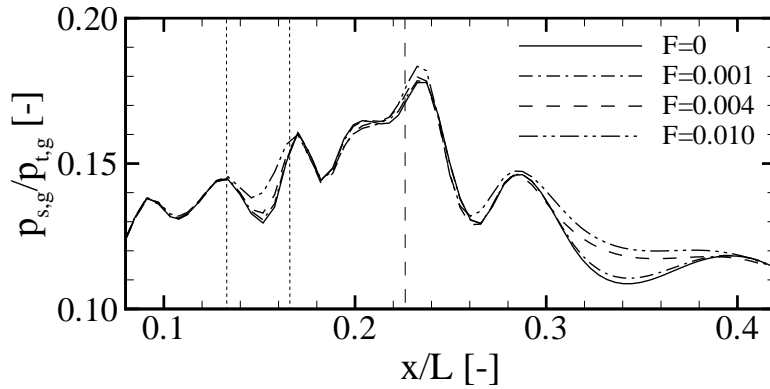
In Chapter 3 the experimental apparatus and the measurement technique for the hot-gas transpiration cooling tests have been described. Here, the results obtained are given. The thermal behavior of the porous C/C wall is being evaluated and models are provided to predict wall temperatures in transpiration cooled setups. In addition, the effect of non-isothermal porous walls on the through-flow behavior was addressed by modifying the Darcy-Forchheimer equation. The experiments using the subsonic flow channel provided data to validate these models. Also, it was possible to analyze the temperature profiles within the porous wall due to the heavier instrumentation in this test configuration.

5.1 Pressure Distribution in the Supersonic Flow Channel

The properties of the flow field within the test channel can be best explained by looking at the wall static pressure distribution. Therefore in Fig. 5.1(a) the normalized static pressure is plotted versus the nondimensional combustor length for the complete channel. First, the flow is expanded by the laval nozzle which is completed at the first perpendicular dashed line. Here, the constant cross-section part of the test section starts (isolator). Weak shocks and expansion fans in form of pressure waves can be seen here, due to the not fully optimized nozzle contour. The location where the sample can be found is indicated by the next two dashed lines. In general, the boundary layer in the isolator grows and therefore the active flow cross-section decreases which means a deceleration and static pressure rise in the supersonic flow regime. Afterwards, the test channel top and bottom wall diverge with an angle of 1° which leads to an acceleration of the flow. Between $x/L = 0.55$ and the end of the combustion chamber a deceleration by a series of shocks (pseudo-shock (Matsuo et al. 1999)) takes place, which adjust the flow static pressure to the ambient pressure



(a) Complete channel



(b) Isolator region

Figure 5.1: Normalized pressure distribution in supersonic flow channel for $M_g = 2.1$, $p_{t,g} = 2.97 \text{ bar}$, $T_{t,g} = 1054 \text{ K}$, coolant: Air

at $p_{s,g}/p_{t,g} \approx 0.32$. In this plot, the pressure distribution for no blowing and the largest blowing ratio tested ($F = 0.010$) are given. The differences in this resolution is small. Hence, a closer view on the pressure distribution in the isolator is given by Fig. 5.1(b) comparing several blowing ratios. The overall influence of blowing is small and no additional major shock or expansion fan structures are triggered by the addition of the transpiration coolant's mass according to the static wall pressure measurements. Nevertheless, directly over the sample (in between the first perpendicular dashed lines) a small pressure rise can be noticed due to the added mass. Further downstream in the diverging part of the test section also an influence on the flow expansion leading to higher static wall pressure can be found.

5.2 Surface Temperature Distribution

To get extended information of the thermal behavior of the transpiration cooled porous C/C wall segment, which means to quantify the influence of the gases' specific heat capacity on the boundary layer and internal heat transfer, experiments

5.2 Surface Temperature Distribution

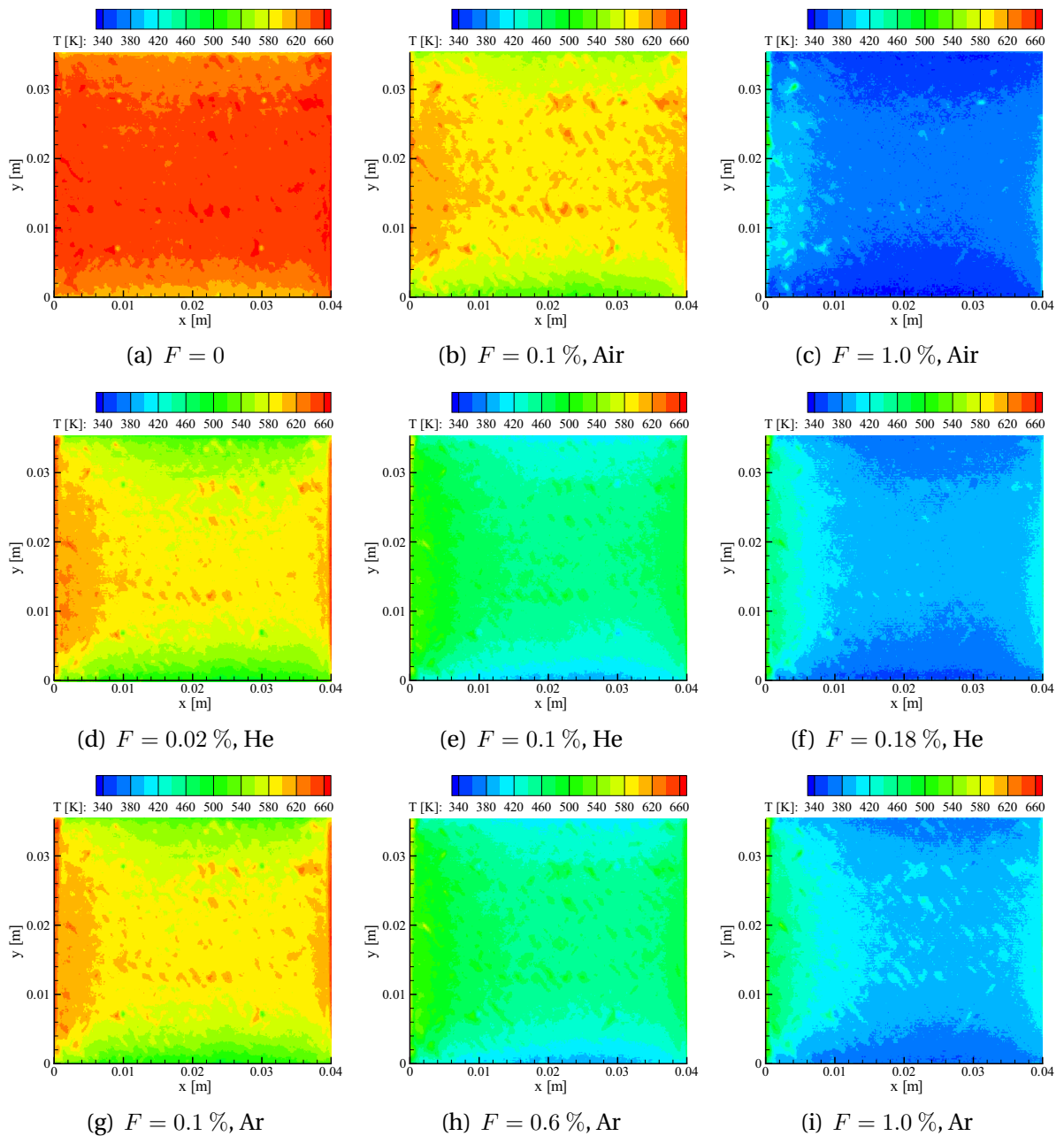


Figure 5.2: Surface temperature distributions of C/C PH1732-1 sample for different blowing ratios. Top: Air as a coolant, middle: Helium as a coolant, bottom: Argon as a coolant. Main-flow conditions: $M_g = 2.1$, $p_{t,g} = 2.97 \text{ bar}$, $T_{t,g} = 1039 - 1060 \text{ K}$

with different coolant gases were conducted. In addition to the reference case where air is used as a coolant, tests using argon and helium were carried out.

In Fig. 5.2(a) through Fig. 5.2(i) surface temperature distributions obtained with the infrared camera system are displayed. The complete infrared data sets for the supersonic flow experiments using air, argon and helium as coolant are given in Appendix B.1. In Fig. 5.2(a) the uncooled case is given. On top and bottom of the sample one can see the influence of the lateral heat conduction due to the water

cooled environment the wall segment is embedded in. Due to this, the recovery temperature (Eqn. 2.7) at the wall is not reached for the case without transpiration. The maximum measured wall temperature was at $T_{w,max} \approx 670 \text{ K}$. Additionally, the structure of the C/C is somewhat visible, because of non-uniform optical parameters on the surface and fibres. Also, the tips of the wall thermocouples can be distinguished from the porous wall due to the differing emission coefficient of their steel sheaths.

With increasing blowing ratio F the surface temperature decreases significantly. Very small blowing ratios of $F = 0.001$, corresponding to 0.1 % coolant mass-flux in relation to the hot-gas mass-flux, lead to a temperature reduction of $\approx 90 \text{ K}$ (air). For comparison, in Fig. 5.2(d) through Fig. 5.2(i) the surface temperature with foreign gas injection (helium and argon) is given. At a very low blowing ratio of $F = 0.0002$ with helium (Fig. 5.2(d)) approximately the surface temperature level obtained at $F = 0.001$ with air as a coolant (Fig. 5.2(c)) is reached. The factor of five in F for the same wall temperature corresponds roughly to the ratio in specific heat capacity for helium and air. Furthermore, the temperature maps of the argon cooled sample show in comparison to the helium cooled case that the relationship between wall temperature and coolant specific heat capacity is not linear. The factor in F ranges between 5 and 6 whilst the ratio of $c_{p,c}$ is approximately 10. For very high blowing ratios the surface temperature decreases further. In Fig. 5.2(c) with air as coolant at $F = 0.010$ almost coolant temperature is reached. At the same blowing ratio the argon cooled case yields a surface temperature which is approximately 25 K higher. From the infrared data, one is able to tell, that transpiration cooling applied to C/C is a very efficient process and that the cooling is nearly homogeneous over the sample's surface. Additionally, it is strongly dependent on the gases' specific heat capacity.

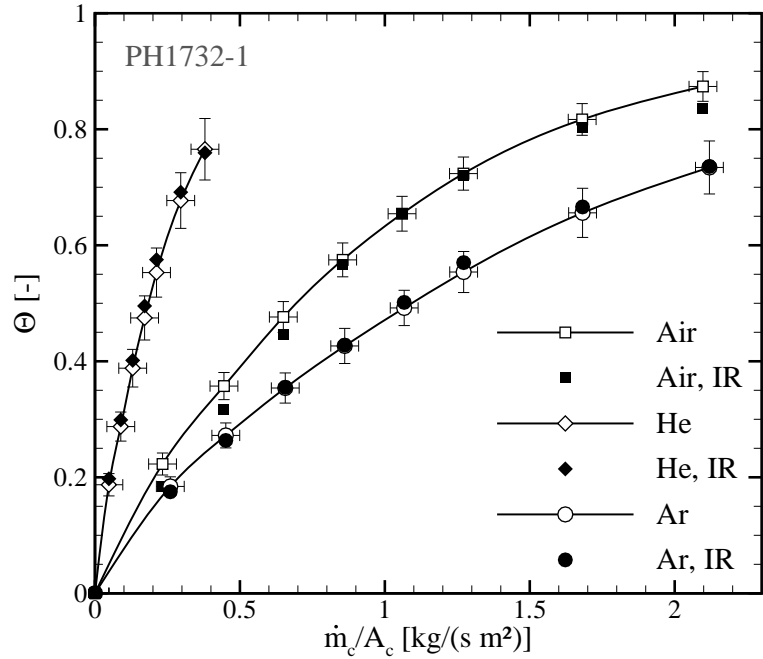
5.3 Cooling Efficiency of the Porous Wall

Due to the significant heat conduction effects in the water-cooled test channel described above, Langener et al. (2008) suggested a nondimensional temperature ratio to describe the cooling efficiency of the transpiration cooled porous wall. It aims to reduce the influence of the lateral heat conduction effects in such a situation and data interpretation by referring to the non-transpiration cooled case. It ranges from zero (no transpiration cooling) to unity (complete cooling). With this definition, one is able to compare tests with for example different coolants and different sample materials amongst each other. The wall temperature data has been averaged from the four wall thermocouples.

$$\Theta = \frac{\bar{T}_{w,0} - \bar{T}_w}{\bar{T}_{w,0} - T_c} \quad (5.1)$$

In Fig. 5.3 and Fig. 5.4 the cooling efficiency (Eq. 5.1) is being plotted versus the coolant mass-flow rate per cooled area. In Fig. 5.3 the influence of the different coolants using the PH1732-1 sample is shown. The impact of the gases' specific heat

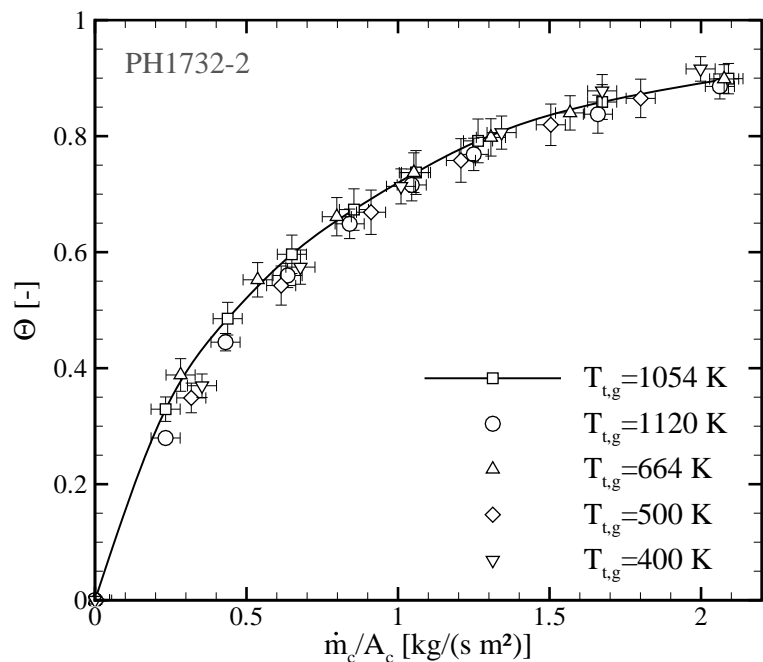
Figure 5.3: Nondimensional temperature Θ versus coolant mass-flux \dot{m}_c/A_c for sample PH1732-1: Different coolant gases. Comparison of thermocouple to infrared data. $T_{t,g} = 1037 - 1060 K$



capacity is clear. With the same amount of coolant mass-flow rate helium cools the wall segment much better than air, whilst the cooling efficiency with argon is inferior due to its smaller $c_{p,c}$.

Furthermore, the cooling efficiency obtained from the infrared data is given in Fig. 5.3 as solid symbols. The data for $\bar{T}_{w,0}$ and \bar{T}_w have been obtained in this case by averaging the complete surface area, including the warmer and colder parts of the porous wall. The agreement with the thermocouple data (blank symbols) is very good, which shows that the thermocouples are installed in locations representing the cooling efficiency for the whole sample.

Figure 5.4: Nondimensional temperature Θ versus coolant mass-flux \dot{m}_c/A_c for sample PH1732-2: Different total temperatures for air as coolant



5 Transpiration Cooling of C/C Wall Segments with Different Coolants

In the following, only the thermocouple data is used for Θ . The cooling efficiency of Sample 2 at different hot-gas total temperature ranging from $T_{t,g} = 400\text{ K}$ up to $T_{t,g} = 1120\text{ K}$ is shown in Fig. 5.4. One notices, that the nondimensional temperature ratio Θ is fairly independent from the hot-gas total temperature at the same Mach number and coolant mass-flow rate. For further evaluation only the data at a hot-gas total temperature of $T_{t,g} \approx 1060\text{ K}$ will be discussed.

To investigate the effect of the coolants in more detail, the experimental data was compared to different approaches in literature. All models follow a 1D heat balance approach with semi-empirical assumptions for the heat transfer coefficients for the cooled and uncooled cases, neglecting lateral heat conduction. Eckert and Livingood (1954) use a correlation for flat plate heat transfer, whilst Kays et al. (2005) and Rannie (1947) use a relationship for fully developed channel flow. The models are explained in detail in Section 2.3.

In Fig. 5.5 cooling efficiency predictions using the models of Rannie and Eckert and Livingood are shown. Typically, the model of Rannie overestimates the cooling efficiency measured in our test setup. Eckert and Livingood's model fits well for argon as a coolant, and overestimates Θ for higher coolant $c_{p,c}$ (air and helium). Both approaches incorporate the ratio of specific heat capacities between the main-flow and the coolant as a proportional factor.

In Fig. 5.6 the model of Kays et al. is compared to the experimental data with a hot-gas Stanton number without blowing of $St_{g,0} = 0.0044$ used for the calculation of the model curves. This value has been chosen to achieve best agreement of the curves with the test data and to point out that this model is able to correctly calculate the trend of varying coolant specific heat capacities. For our test setup typical empirical correlations yield much lower $St_{g,0}$ than used for the calculation for Fig. 5.6. This mean that for more realistic values of the hot-gas Stanton number the model of Kays

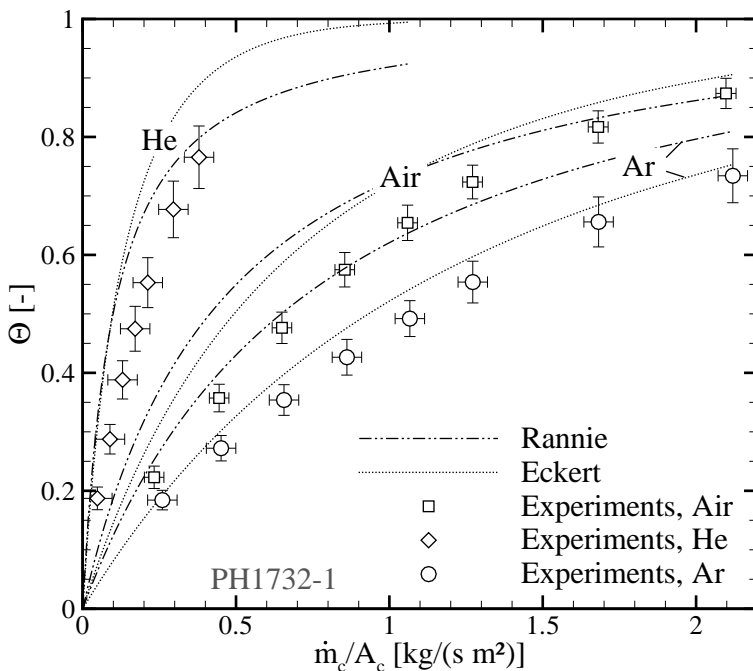
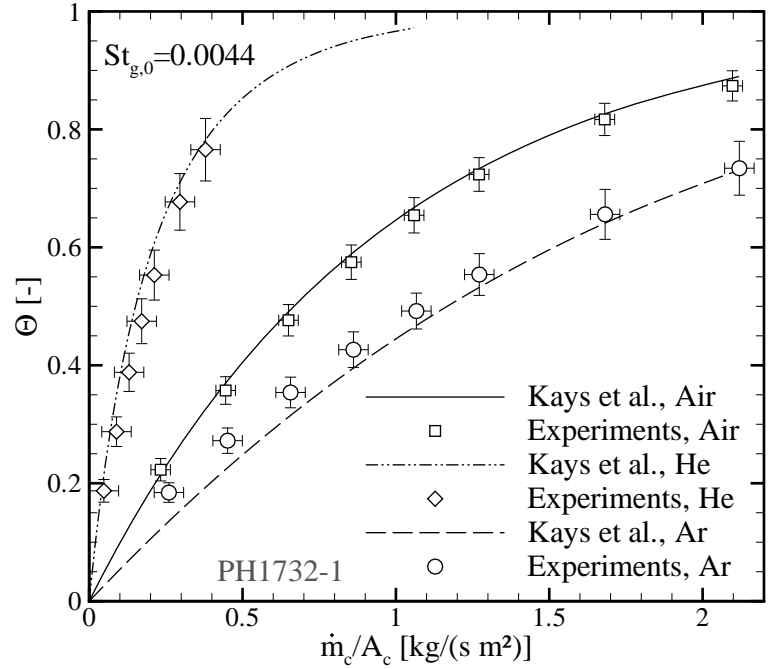


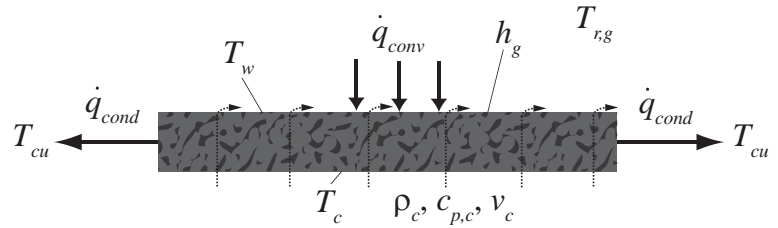
Figure 5.5: Comparison of test data versus the models of Rannie and Eckert and Livingood. Main-flow conditions: $M_g = 2.1$, $T_{t,g} = 1039 - 1060\text{ K}$, $p_{t,g} = 2.97\text{ bar}$

Figure 5.6: Comparison of test data versus the model from Kays et al. using an arbitrary hot-gas Stanton number. Main-flow conditions: $M_g = 2.1$, $T_{t,g} = 1039 - 1060 K$, $p_{t,g} = 2.97 bar$



et al. would yield too optimistic results. Due to its good agreement with the test data with respect to the foreign gas effect, the Kays et al. model was used and a modified modeling approach to take the lateral heat conduction effects appearing in our setup into account was developed in order to explain the overall thermal situation.

Figure 5.7: Schematic of the heat transfer situation according to the heat balance model



To capture this effect, a simplified heat balance for the ITLR test arrangement in Eqn. 5.2 was set up. The schematic of the thermal situation is shown in Fig. 5.7. It contains the convective heat transfer onto the porous wall, the heat picked up by the coolant within the wall and the heat conduction losses towards the water cooled copper parts of the test channel at a temperature of T_{cu} . The heat conduction term leads to less heat which has to be removed by the transpiration cooling mechanisms (internal and external). Therefore, the cooling efficiency will be lower, when including lateral heat conduction in our model. Additionally, thermal equilibrium between the coolant and the porous wall and negligible coolant side heat transfer has been considered.

$$\underbrace{h_g (T_{r,g} - T_w)}_{\text{convective heat transfer}} = \underbrace{\rho_c c_{p,c} v_c (T_w - T_c)}_{\text{internal cooling}} + \underbrace{B (T_w - T_{cu})}_{\text{heat conduction losses}} \quad (5.2)$$

The coefficient B accounts for the thermal resistance from the porous surface to the water cooled copper parts in steady state. These heat losses appear over the side

5 Transpiration Cooling of C/C Wall Segments with Different Coolants

surfaces as well as the regions where the copper parts and the sample are in contact. B is assumed to be constant for all blowing ratios. It can be determined from a heat balance of the uncooled case, were the heat convected onto the wall is only being laterally conducted into the copper parts:

$$\underbrace{h_{g,0} (T_{r,g} - T_{w,0})}_{\text{convective heat transfer}} = \underbrace{B (T_{w,0} - T_{cu})}_{\text{heat conduction losses}} \Rightarrow B = \frac{h_{g,0} (T_{r,g} - T_{w,0})}{(T_{w,0} - T_{cu})} \quad (5.3)$$

Using Eqn. 5.2 and Eqn. 5.3 one can solve for the expected wall temperature T_w in case of transpiration cooling:

$$T_w = \frac{aT_c + T_{r,g} + \frac{h_{g,0}}{h_g} T_{cu} \frac{T_{r,g} - T_{w,0}}{T_{w,0} - T_{cu}}}{1 + a + \frac{h_{g,0}}{h_g} \frac{T_{r,g} - T_{w,0}}{T_{w,0} - T_{cu}}} \quad (5.4)$$

Here a is a parameter describing the change in heat transfer towards the cooled wall, the effect of the specific heat capacity of the coolant $c_{p,c}$, and the blowing ratio F compared to the uncooled case.

$$a = \frac{F}{St_{g,0}} \frac{c_{p,c}}{c_{p,g}} \frac{St_{g,0}}{St_g} \quad (5.5)$$

For $\frac{St_g}{St_{g,0}}$ the model approach after Kays et al. (2005) for a transpired boundary layer with foreign gas injection was used which is given in more detail in Section 2.3.3.

$$\frac{St_g}{St_{g,0}} = \frac{b_h}{e^{b_h} - 1} \quad b_h = \frac{F}{St_{g,0}} \left(\frac{c_{p,c}}{c_{p,g}} \right)^{0.6} \quad St_{g,0} = \frac{h_{g,0}}{\rho_g u_g c_{p,g}} \quad (5.6)$$

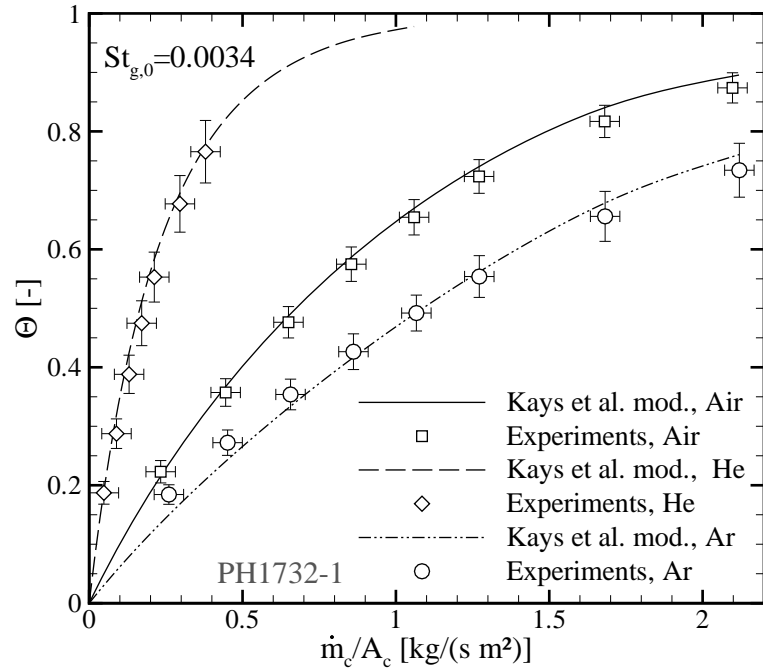
The hot-gas heat transfer coefficient $h_{g,0}$ or Stanton number $St_{g,0}$ respectively are the only parameters left, which have to be given. All other values can either be measured or obtained from tables. The hot-gas Stanton number can be estimated for our setup using the equation of Dittus and Boelter (1985) presented in Section 3.2.3. Here, the actual values for $h_{g,0}$ and $St_{g,0}$ are given for the investigated test conditions.

Using Eqn. 3.1 leads to $St_{g,0} = 0.0034$ for the $M_g = 2.1$ and $T_{t,g} = 1039-1060 \text{ K}$ test conditions. Knowing the main-flow parameters and the properties of the coolants (see Table 5.1), we can solve for T_w from Eqn. 5.4 and obtain a prediction of the porous wall temperature. With this value, we can calculate the cooling efficiency as used and compare it to the measured values.

$$\Theta = \frac{\overbrace{T_{w,F=0}}^{\text{measured}} - \overbrace{T_w}^{\text{from model}}}{\underbrace{T_{w,F=0}}_{\text{measured}} - \underbrace{T_c}_{\text{measured}}} \quad (5.7)$$

This data has been compared to the experimental results in Fig. 5.8. Within the margin of errors it is possible to predict the transpiration cooling efficiency of C/C

Figure 5.8: Lateral heat conduction modified approach of Kays et al. using a realistic hot-gas Stanton number. $M_g = 2.1$, $T_{t,g} = 1039\text{-}1060\text{ K}$, $p_{t,g} = 2.97\text{ bar}$: Comparison to experimental results with different coolants



Name	Symbol	Value
hot-gas total temperature (meas.)	$T_{t,g}$ [K]	1039 – 1060
porous wall temperature without blowing (meas.)	$T_{w,0}$ [K]	644
copper temperature (meas.)	T_{cu} [K]	317
specific heat capacity hot-gas	$c_{p,g}$ [J/(kgK)]	1024
specific heat capacity coolant: air	$c_{p,c}$ [J/(kgK)]	1010
specific heat capacity coolant: Ar	$c_{p,c}$ [J/(kgK)]	525
specific heat capacity coolant: He	$c_{p,c}$ [J/(kgK)]	5193
coolant temperature (meas.) $f(F)$	T_c [K]	309 – 395
hot-gas bulk velocity	u_g [m/s]	979 – 989
hot-gas density	ρ_g [kg/m ³]	0.210 – 0.214
Reynolds number	Re_g [–]	269737 – 276293
Prandtl number	Pr [–]	0.686

Table 5.1: Parameters for modified Kays et al. model with heat conduction losses

within our test setup using a reasonable value for $St_{g,0}$. The influence of the different coolants can be captured quite well. This again underlines that the approach of Kays et al. (2005) predicts the transpiration cooling mechanisms very well, with respect to foreign gas injection.

In Fig. 5.9(a) the Stanton number change with blowing obtained from the analytical model incorporating the transpiration cooling model of Kays et al. (2005) is plotted versus the blowing ratio for the case displayed in Fig. 5.8. One can see the strong decrease in St_g for all three coolant gases. The effect of the coolant's specific heat capacity following Eqn. 5.6 is clear. The Stanton number decreases slower when

5 Transpiration Cooling of C/C Wall Segments with Different Coolants

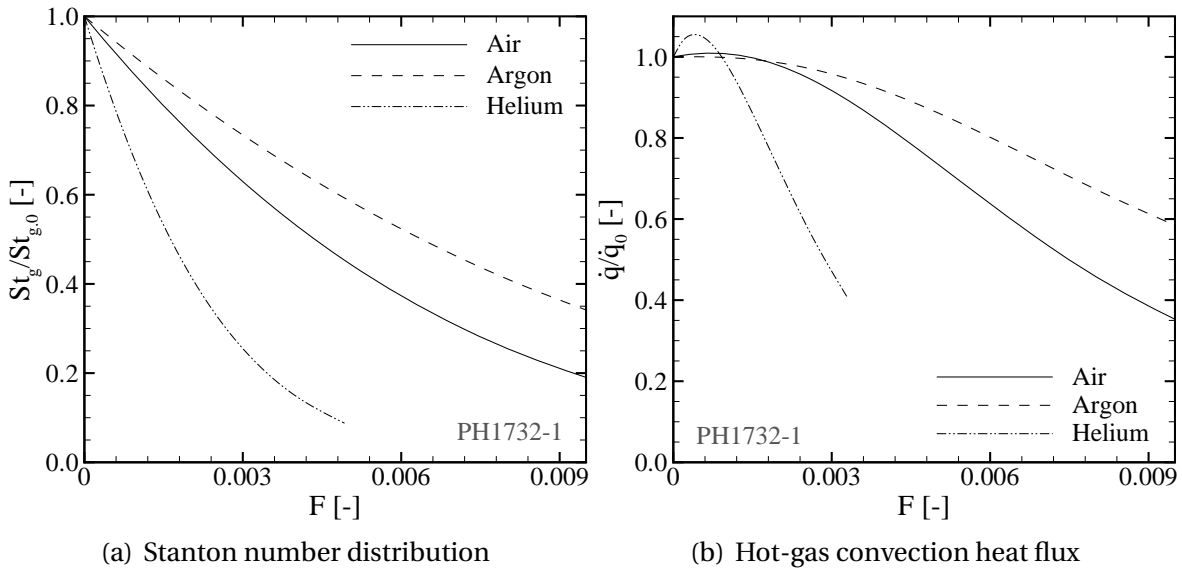


Figure 5.9: Normalized convective heat flux from the transpiration cooling model for different coolant gases. $T_{t,g} = 1039 - 1060$ K, PH1732-1 sample

using argon, whilst with helium it is significantly faster than with air. The influence is not linear with the ratio of the specific heat capacity, which is also contained in Eqn. 5.6. The convective heat flux has been normalized with the heat flux to the sample at no blowing \dot{q}_0 (the sample is at a lower wall temperature than the recovery temperature of the hot-gas flow) and are plotted in Fig. 5.9(b). The values for \dot{q}_0 are summarized in Table 5.2. The heat flux decreases with higher F significantly. For small blowing ratios a slight increase could be observed. This is due to the higher

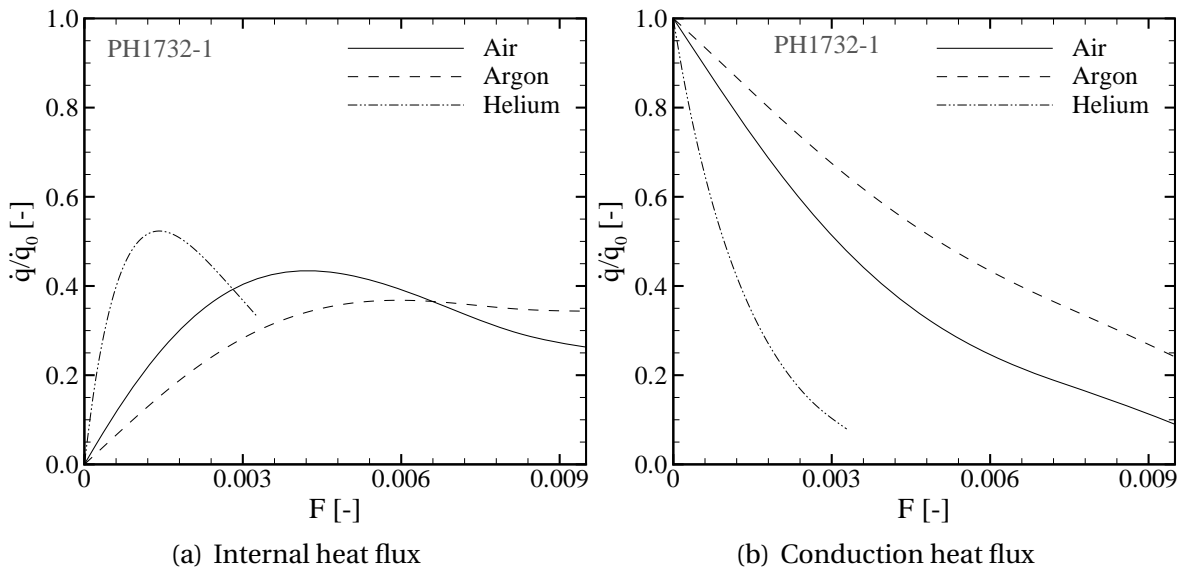


Figure 5.10: Normalized internal and conduction heat flux from the transpiration cooling model for different coolant gases. $T_{t,g} = 1039 - 1060$ K, PH1732-1 sample

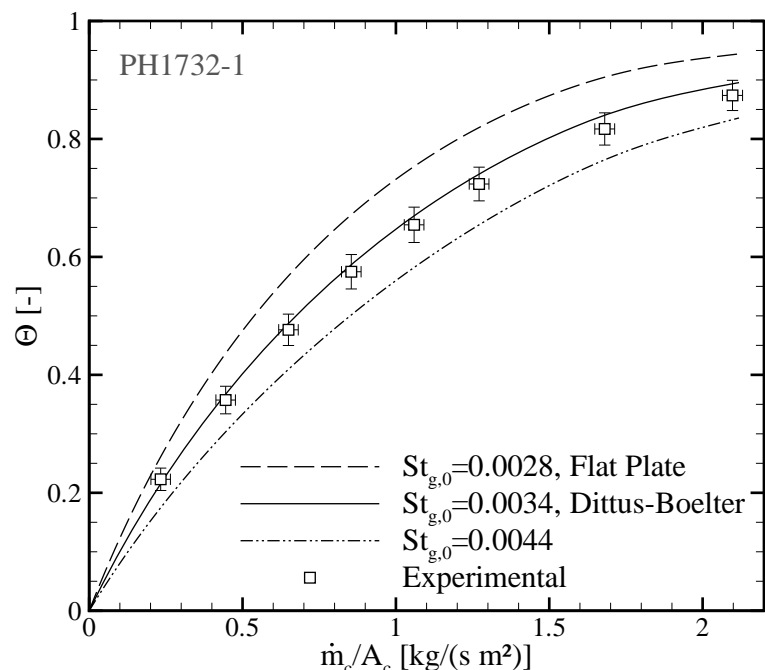
increase in temperature difference than decrease in Stanton number for this blowing regime due to the very strong internal heat transfer within the porous wall.

The evolution of the terms on the right side of Eqn. 5.2 versus the blowing ratio is plotted in Fig. 5.10(a) and Fig. 5.10(b). The internal heat flux (heat pick up by the coolant) is given on the left side normalized with the heat flux to the wall at no blowing. First, this term steadily grows for all gases, because of the higher coolant mass-flow rate and possibility of enthalpy gain. For higher blowing, this value decreases again, because of the reduced heat transfer from the external flow. Test cases using gases with higher $c_{p,c}$ experience this maximum at lower blowing ratio due to their ability to pick up more heat within the porous material for the given conditions. The actual value of \dot{q}/\dot{q}_0 is also higher for these coolants, because the conduction portion of the overall heat balance is in relation to the other positions of the maxima the lowest for gases with lower $c_{p,c}$. Therefore, more heat has to be picked up internally. The conduction heat transfer from the sample towards the cooled parts of the hot-gas channel (see Fig. 5.10(b)) depends on the copper temperature T_{cu} which is fixed and the porous wall temperature. Since the wall temperature reduces more slowly for coolants with lower specific heat capacity, more heat is being conducted away from the sample for these test cases at the same blowing ratio.

The sensitivity of the model towards the channel heat transfer without blowing is shown in Fig. 5.11. The originally assumed Stanton number of 0.0044 in Fig. 5.6 over estimates the hot-gas side heat transfer of about 29 %. A Stanton number correlation for turbulent flat plate flow (see Eqn. 5.8, which is about 18 % lower than the modified Dittus and Boelter’s correlation), has been compared as well.

$$St_{g,0} = 0.037 Re_x^{-0.2} Pr^{-\frac{2}{3}} \quad (5.8)$$

Figure 5.11: Lateral heat conduction modified approach of Kays et al. $M_g = 2.1$, $T_{t,g} = 1060 \text{ K}$, $p_{t,g} = 2.97 \text{ bar}$, Air as coolant: effect of the variation of the hot-gas side heat transfer coefficient without cooling $h_{g,0}$



The hot-gas side heat transfer estimation has a non-negligible effect on the cooling efficiency prediction. Altering $St_{0,g}$ in the margins given above, leads to a maximum error in the cooling efficiency of 23 %, which appears at very low coolant mass-flow rates. For higher coolant mass-flow rates the impact of the heat transfer without blowing on Θ decreases.

5.4 Thermal Behavior of the Porous C/C Wall in Subsonic Flow Experiments

5.4.1 Pressure Distribution in Subsonic Flow Regime

The tests in the uncooled, subsonic flow channel were conducted at three Mach numbers. Therefore, three different wall static pressure distributions exist. In Fig. 5.12 the normalized static pressure is given versus the nondimensional downstream distance x/L . Here, L is the length of the test channel section with constant cross-section, beginning after the convergent part and ranging up to the outlet diffuser. The location of the porous wall segment is indicated by perpendicular dashed lines. The flow at a high Mach number leads to lower measured static pressure distributions than for the one at $M_g = 0.3$ which is following the compressible flow theory. Furthermore, the pressure loss from left to the right of the measurement section is relatively small. Nevertheless, the flow at higher Mach number exhibits a steeper slope in the pressure distribution due to higher wall skin friction causing higher total pressure loss at high flow velocities.

The pressure distribution for several blowing ratios F is given in Fig. 5.13 at a main-flow Mach number of $M_g = 0.3$. The influence of the transpiration cooling mass addition is very low and in the order of the accuracy of the measurement device, even for the highest F of 0.015. In the supersonic flow regime the effect of blowing was more visible.

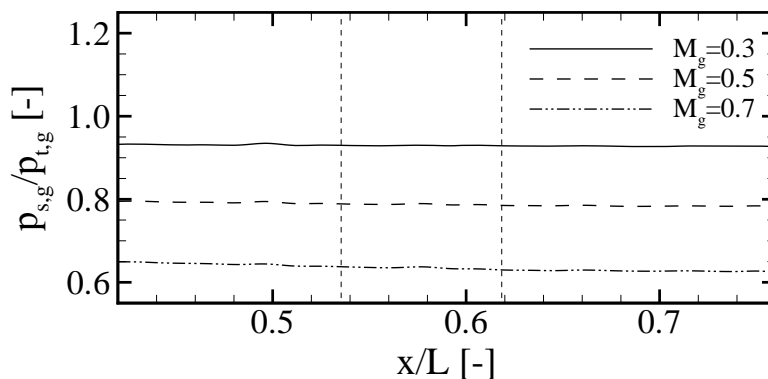


Figure 5.12: Normalized pressure distribution of subsonic flow regime in the uncooled channel for $T_{t,g} = 523 \text{ K}$, coolant: Air

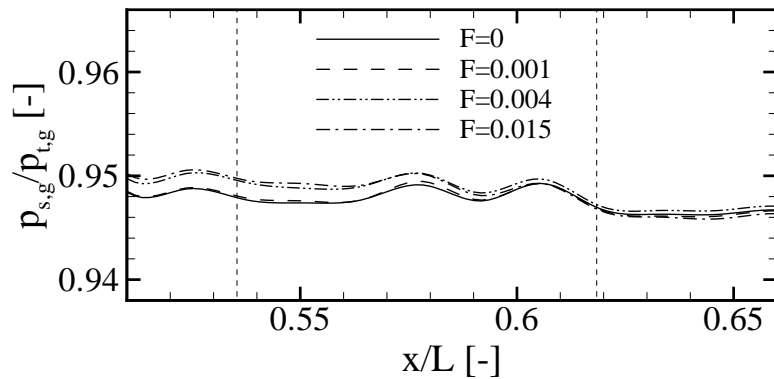


Figure 5.13: Normalized pressure distribution of subsonic flow regime in the uncooled channel at the sample location for $T_{t,g} = 523 K$, coolant: Air

5.4.2 Wall Temperature Distribution

To validate the model presented in the previous section and to obtain extended information of the thermal behavior of the transpiration cooled porous C/C wall segment, the experiments using the subsonic flow channel were conducted. The standard test case was again cooled with air, whilst argon and helium were used too.

In Fig. 5.14(a) through Fig. 5.14(i) surface temperature distributions obtained with the infrared camera system are displayed for steady conditions. The complete infrared data sets for the subsonic flow experiments using air, argon and helium as coolant at $M_g = 0.5$ are given in Appendix B.2. In Fig. 5.14(a) the uncooled case is given. On the leading edge of the sample one can see minor influence of the lateral heat conduction to the *TOOLOX* sample holder and to the backside environment of the porous specimen. Due to this, the recovery temperature of the hot-gas flow ($T_{r,g} \approx 520 K$) at the wall is not reached for the case without transpiration. The maximum measured wall temperature was at $T_{w,max} \approx 480 K$. This difference between both temperatures is in relation to the experiments within the water-cooled channel much smaller meaning that the lateral heat conduction effects decreased substantially.

Furthermore, at the edges of the sample typically a higher temperature is measured. This is due to two effects: First, the epoxy sealing could have penetrated the pores within the C/C and locally decreased the permeability, which possibly reduces the coolant mass-flow rate here. Secondly, heat conduction from the surrounding mount into the sample can occur at higher blowing ratios, when the channel walls are warmer than the sample itself. This is an adverse heat conduction effect compared to the supersonic flow experiments. One can also see, that the leading edge region is slightly warmer than the trailing edge part because of the in flow direction developing transpiration cooling film.

With increasing blowing ratio F the surface temperature decreases significantly. Relatively small blowing ratios of $F = 0.002$, corresponding to 0.2 % coolant mass-flux in relation to the hot-gas mass-flux, lead to a temperature reduction of $\approx 60 K$

5 Transpiration Cooling of C/C Wall Segments with Different Coolants

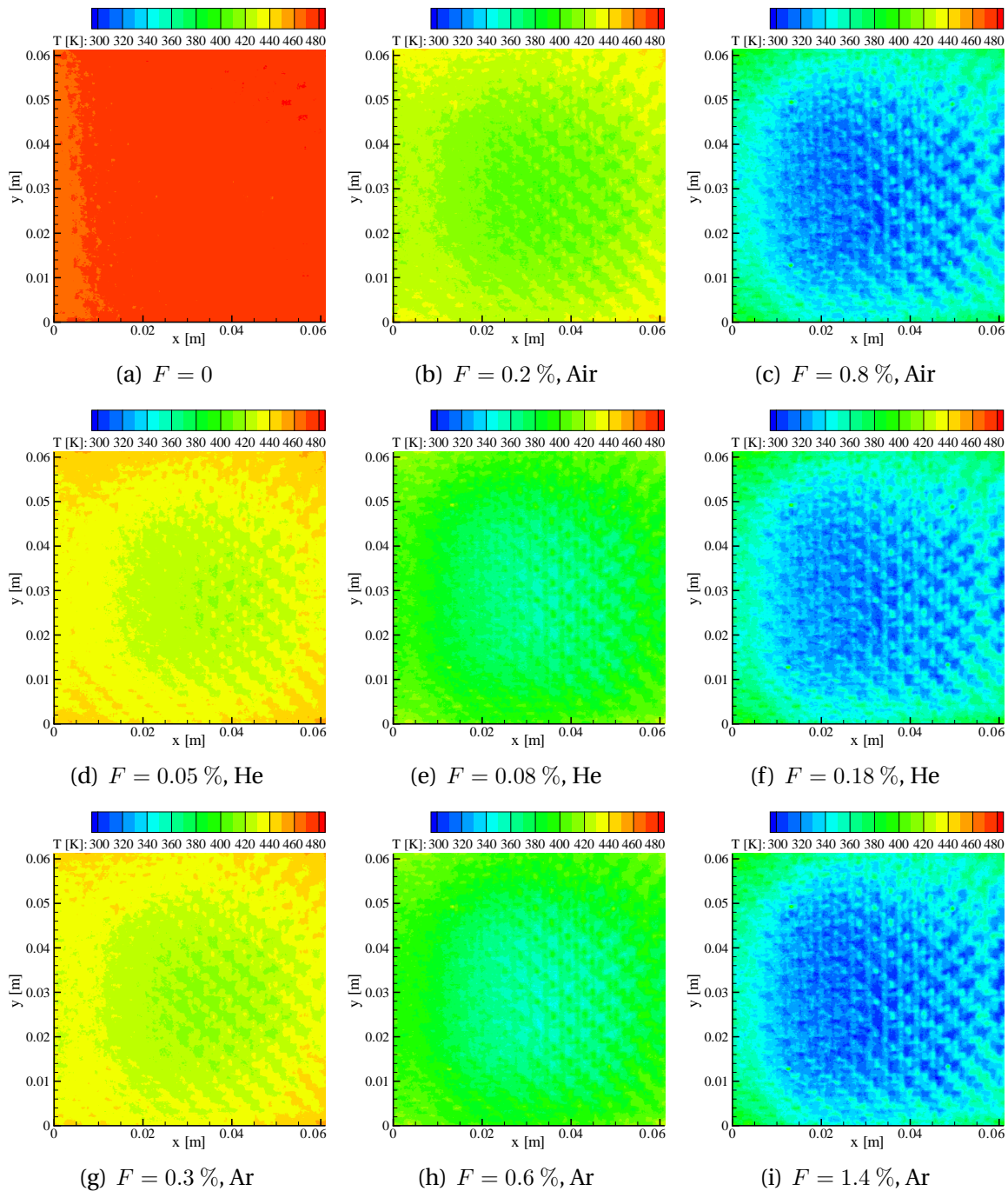


Figure 5.14: Surface temperature distributions of PH1606-1 sample ($L = 15\text{ mm}$) for different blowing ratios. Top: Air as a coolant, middle: Helium as a coolant, bottom: Argon as a coolant. Main-flow conditions: $M_g = 0.5$, $T_{t,g} = 523\text{ K}$

(air). For comparison, in Fig. 5.14(d) through Fig. 5.14(i) the surface temperature with foreign gas injection (helium and argon) is given. At a very low blowing ratio of $F = 0.0005$ with helium (Fig. 5.14(d)) approximately the surface temperature level obtained at $F = 0.002$ with air as a coolant (Fig. 5.14(b)) is reached. Furthermore, the temperature maps of the argon cooled sample show in comparison to the helium cooled case that the relationship between wall temperature and coolant's specific heat capacity is not linear. With different blowing ratios, almost exactly the same surface temperature is obtained. The factor in F ranges between 6 and 7.5 whilst the ratio of $c_{p,c}$ is approximately 10 (helium versus argon). For very high blowing ratios the surface temperature decreases further. In Fig. 5.14(c) with air as a coolant at $F = 0.008$ almost coolant temperature is reached. At a much higher blowing ratio of $F = 0.014$ the argon cooled case (Fig. 5.14(i)) yields a similar surface temperature whilst this is the case for helium with only $F = 0.0018$ (see Fig. 5.14(f)). To summarize, basically the same effects as experienced in the first test campaign with the foreign gas injection could be observed here as well. In contrast the heat conduction influence is very different. Whilst the cooling of the sample was increased by the water-cooling of the supersonic channel, in this case the warmer parts of the subsonic flow test section lead to a heating of the sample when it is subject to blowing.

5.4.3 Wall Cooling Efficiency

In Fig. 5.15(a) to Fig. 5.15(d) the cooling efficiency of different samples at different main-flow conditions is plotted versus the coolant mass-flow rate normalized by the sample surface. Here, the definition is the same as in Eqn. 5.1 and also the same measured quantities are used for the subsonic flow tests.

The main-flow Mach number and total temperature has been varied in Fig. 5.15(a) using the PH1606-2 sample at 10 mm thickness. In the nondimensional notation of Θ the total temperature does not influence the cooling efficiency. In contrary, a higher Mach number decreases the cooling efficiency which can be explained by the higher main-stream mass-flow rate and therefore higher heat load onto the sample (see Table 3.3 for an overview of the Stanton number without blowing). Fig. 5.15(b) compares the same sample material (PH1606) at $L = 10$ mm and $L = 15$ mm at different main-flow conditions. It is evident, that the sample thickness, at least within the range it was varied, does not have a significant influence on the cooling efficiency, which means that nearly the same surface temperatures are measured at the same main-flow conditions. Afterwards, Θ for the two investigated C/C materials has been compared at different M_g and at $T_{t,g} = 523$ K (Fig. 5.15(c)). Again, the material and the porosity respectively do not show a significant impact on the cooling efficiency. The porosity of PH1947 is 16.8 % (relative) higher than the one of PH1606. This is an indicator of thermal equilibrium within the sample, because the porosity does mainly influence the internal, volumetric heat transfer coefficient.

5 Transpiration Cooling of C/C Wall Segments with Different Coolants

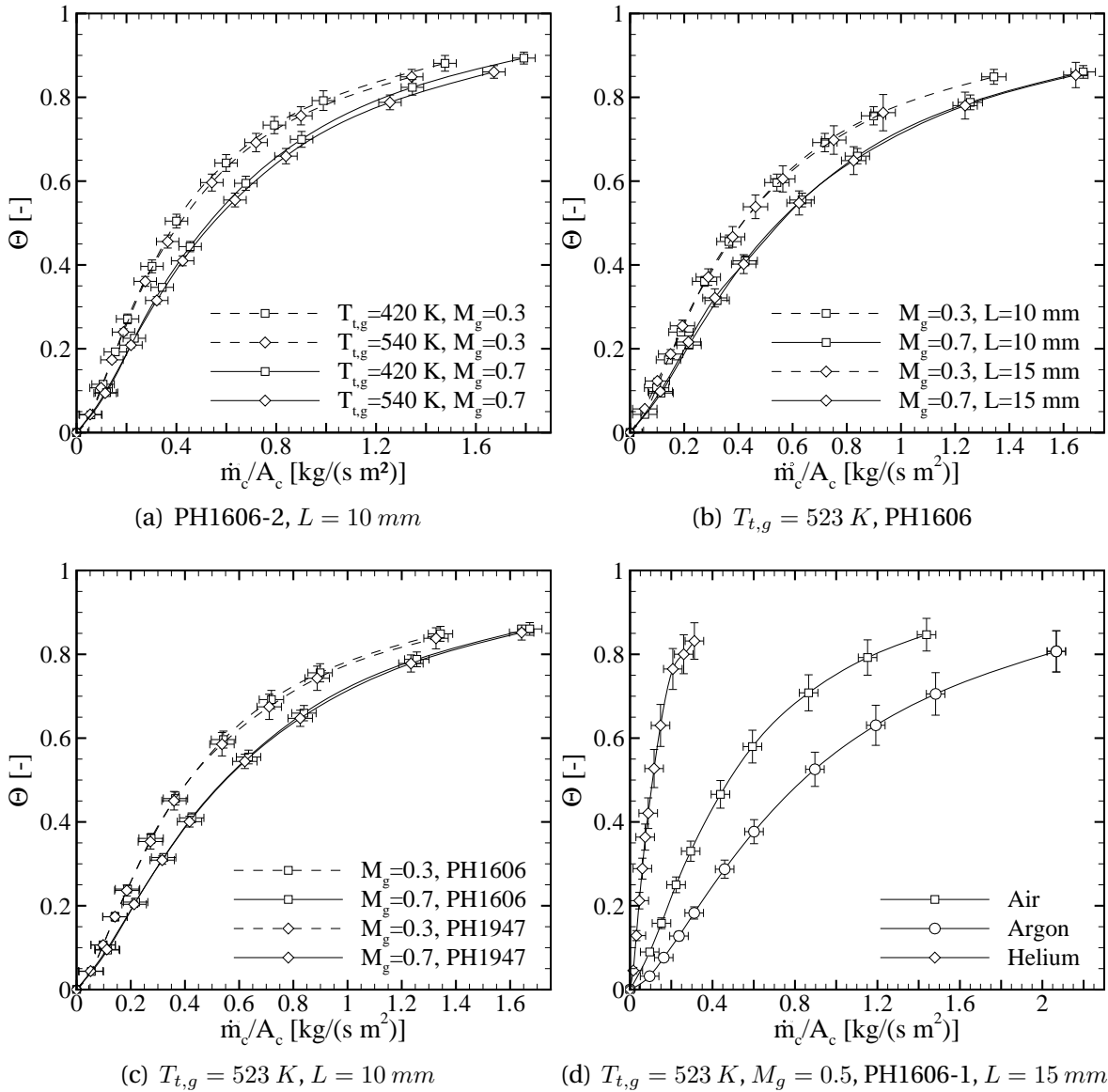


Figure 5.15: Cooling efficiency of C/C samples: (a) Influence of total temperature, (b) Influence of thickness, (c) Influence of sample charge, (d) Influence of coolant

If this would have been changed in local thermal non-equilibrium, a somewhat different wall temperature for both material samples would have been measured.

For the tests summarized in Fig. 5.15(d) the coolant was varied whilst the main-stream conditions were kept constant ($M_g = 0.5$, $T_{t,g} = 523 \text{ K}$). Here, a clear impact is observed. The tests using a coolant with a high specific heat capacity (helium) yield a much better cooling efficiency than with a small $c_{p,c}$ (argon) as compared to the reference case using air. Here, one can again see, that Θ does not scale linearly with the ratio of the coolants specific heat capacity. This factor would be ≈ 5 between helium and air, and ≈ 2 between air and argon. The cooling efficiency curves do not

5.4 Thermal Behavior of the Porous C/C Wall in Subsonic Flow Experiments

scale with these factors when looking at the measured points. These effects are the same as for the tests with supersonic flow.

To compare the cooling behavior obtained by the measurements in both flow regimes, Θ is plotted versus the coolant mass-flow rate divided by the cooled area in Fig. 5.16(a) and Fig. 5.16(b). On the left side the coolant is air. Here, the cooling efficiency of the PH1732-1 material exposed to the $M_g = 2.1$ flow is lower than for both subsonic flow tests. This is because of the higher heat load onto the sample, which is given in Table 3.1 and Table 3.3. The convective heat flux \dot{q}_0 onto the porous wall in case of no blowing can be computed by knowing the hot-gas heat transfer coefficient and the temperature difference between uncooled wall and the hot-gas. Both were measured during the tests. Table 5.2 gives the values for \dot{q}_0 and the heat load for the supersonic flow tests is one order of magnitude above the ones for the subsonic flow regime. This can be explained by the higher heat transfer coefficient and substantially greater temperature difference of $\approx 400\text{ K}$ versus $\approx 40\text{ K}$ experienced using the uncooled channel. This also explains the cooling efficiency behavior, even though the PH1732 sample experiences a heat-loss towards the copper channel.

	$M_g = 2.1\ T_{t,g} = 1054\text{ K}$	$M_g = 0.3$	$M_g = 0.5$	$M_g = 0.7$
$\dot{q}_0\ [W/m^2]$	257320	18343	21083	23681

Table 5.2: Convective wall heat flux without blowing for several main-flow conditions. Subsonic regime all at $T_{t,g} = 523\text{ K}$

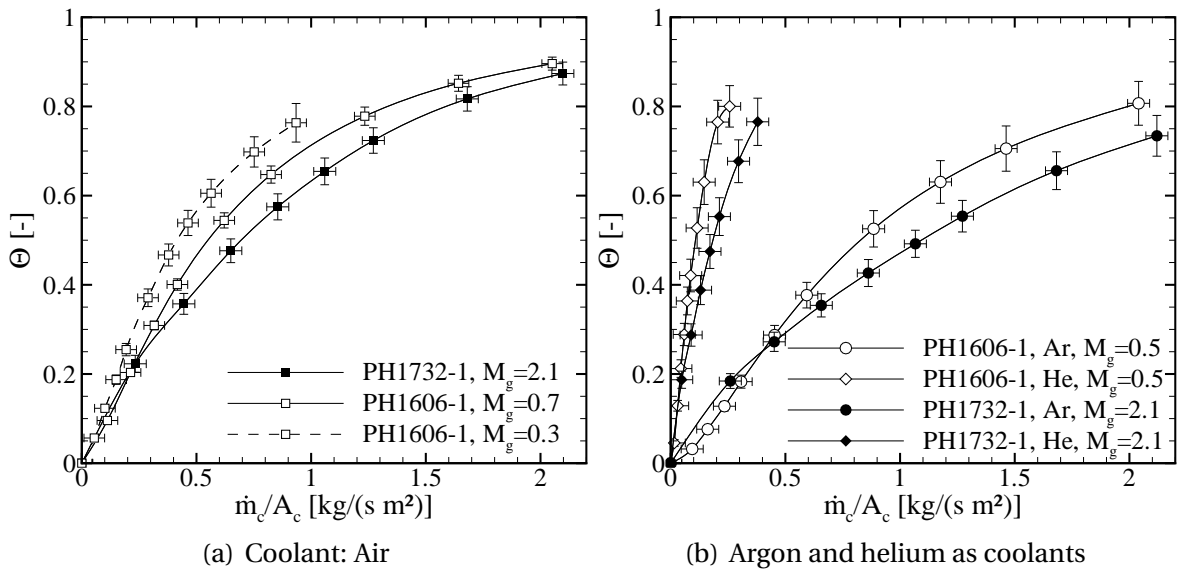


Figure 5.16: Cooling efficiency comparing both flow regimes: $T_{t,g} = 1039 - 1060\text{ K}$ and $M_g = 2.1$ with the PH1732-1 sample versus $T_{t,g} = 523\text{ K}$ and $M_g = 0.3 - 0.7$ with the PH1606-1 porous wall material

5.4.4 Cooling Efficiency Model

The model derived in Section 5.3 to predict the porous wall temperature and the cooling efficiency respectively in non-adiabatic test environments is also used to calculate Θ from the current flow conditions. To apply the model, the surface temperature without blowing, which has been taken from the thermocouple data at no blowing and the sink temperature for the heat conduction has to be known. For the last, the temperature measured at the *TOOLOX* frame has been used for estimating the heat conduction at the sample similar to the copper temperature T_{cu} of the water-cooled channel. This temperature T_{sink} varies slightly with the coolant mass-flow rate because it cannot be avoided that heat is being conducted from the frame and test setup into the sample and the coolant respectively. The direction of the conduction heat transfer and the heat load variations are the major thermal differences in this test setup. The parameters for the model are given in Table 5.3.

In Fig. 5.17(a) the cooling efficiency for a test with the PH1606-1 sample at different Mach numbers is given. In addition, the results of the in this thesis derived model are shown using lines. Within the margin of error, the model is able to accurately predict the cooling efficiency for different main-flow Mach numbers and thus at different heat loads. The heat transfer coefficient $h_{g,0}$ varies for the shown test cases from $297 \frac{W}{m^2K}$ up to $576 \frac{W}{m^2K}$ for $M_g = 0.7$ meaning that the heat load almost doubles.

The experimental results for the foreign gas injection have been compared to the ones from the analytical model 5.3 (see Fig. 5.17(b)). Here, the data from a test at $M_g = 0.5$ and $T_{t,g} = 520 K$ has been used. The foreign gas effect can be described quite accurate as well.

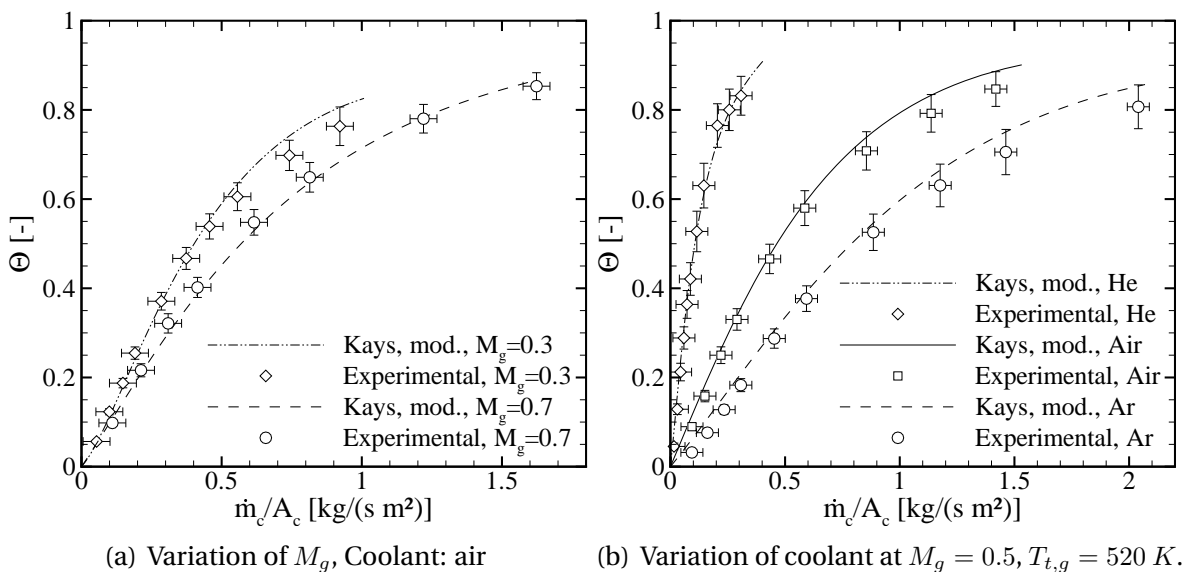


Figure 5.17: Comparison of heat-balance cooling efficiency approach to experiments in subsonic flow regime. PH1606-1

5.4 Thermal Behavior of the Porous C/C Wall in Subsonic Flow Experiments

Name	Symbol	Value
hot-gas total temperature (meas.)	$T_{t,g}$ [K]	520 – 525
porous wall temperature without blowing (meas.)	$T_{w,0}$ [K]	473 – 481
sink temperature (meas.) $f(F)$	T_{sink} [K]	407 – 460
specific heat capacity hot-gas	$c_{p,g}$ [J/(kgK)]	1010
specific heat capacity coolant: air	$c_{p,c}$ [J/(kgK)]	1010
specific heat capacity coolant: Ar	$c_{p,c}$ [J/(kgK)]	525
specific heat capacity coolant: He	$c_{p,c}$ [J/(kgK)]	5193
coolant temperature (meas.) $f(F)$	T_c [K]	302 – 386
hot-gas bulk velocity	u_g [m/s]	160 – 306
hot-gas density	ρ_g [kg/m ³]	0.64 – 0.67
Reynolds number	Re_g [–]	237806 – 582850
Prandtl number	Pr [–]	0.68

Table 5.3: Parameters for modified Kays et al. model applied to the subsonic flow transpiration cooling tests

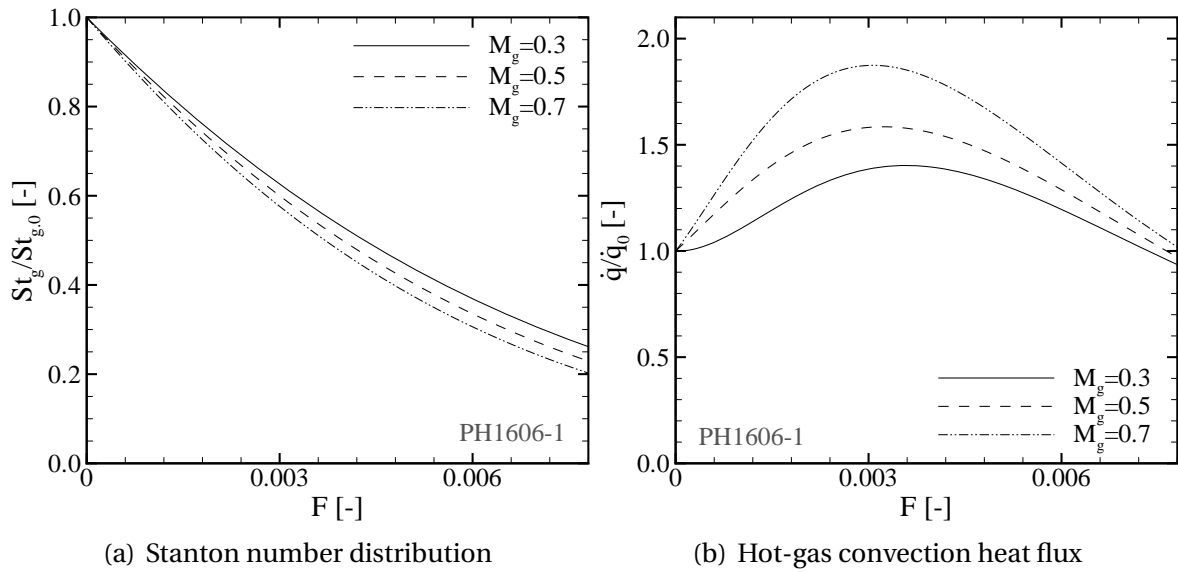


Figure 5.18: Normalized convective heat flux from the transpiration cooling model for different hot-gas Mach number. $T_{t,g} = 520$ K, PH1606-1 sample

By conducting the subsonic flow tests it could be shown, that the model derived from the experiments conducted in a high temperature and supersonic flow environment can also be applied for quite different flow regimes and other thermal situations including foreign gas transpiration cooling.

The thermal behavior of the samples exposed to subsonic flow conditions can also be further analyzed by evaluating the heat flux components based upon the model calculations. Fig. 5.18(a), Fig. 5.18(b), Fig. 5.19(a), and Fig. 5.19(b) show the Stanton number and normalized heat flux data versus the blowing ratio. The heat flux without blowing is given in Table 5.2. Within the range of the tested subsonic

5 Transpiration Cooling of C/C Wall Segments with Different Coolants

Mach numbers the Stanton number distribution is very similar. The convective heat flux to the wall (see 5.18(b)) shows a quite different behavior: First, the heat flux reaches a maximum at moderate blowing ratios. This is caused by the rapid decrease of the wall temperature for low blowing ratios, whilst the decrease in Stanton number due to effects on the external boundary layer is not as strong. For the test case at $M_g = 0.7$ the increase in the heat flux is highest, because the wall temperature is mainly a function of the coolant mass-flow rate. For a higher hot-gas Mach number at the same blowing ratio, this value is higher than for tests with lower hot-gas Mach numbers and mass-flow rates respectively. Therefore, the heat flux reduction from the transpired boundary layer is not as strong as compared to the increase in temperature difference in relation to lower hot-gas Mach numbers for the same F . For the high blowing ratios the wall heat flux decreases again, but reaches the value at no blowing for the range investigated.

The heat picked up by the coolant increases steadily up to a blowing ratio of approximately 0.004 where at the maximum circa twice the heat as convected to the porous wall at now blowing is reached. For higher blowing ratios this heat flux component decreases again, but never becomes less than $\dot{q}/\dot{q}_0 = 1.5$. This is because of the conduction heat transfer which is displayed in Fig. 5.19(b). First, this component decreases significantly, because the difference between the sample and the sink temperature, which is the temperature measured at the sample holder. At $F \approx 0.002$ zero conduction heat flux is reached (temperature difference close to zero) and for higher blowing this component becomes negative, since the porous wall temperature is colder than the surrounding channel parts of the uncooled test section. This is the largest difference in comparison with the tests using the

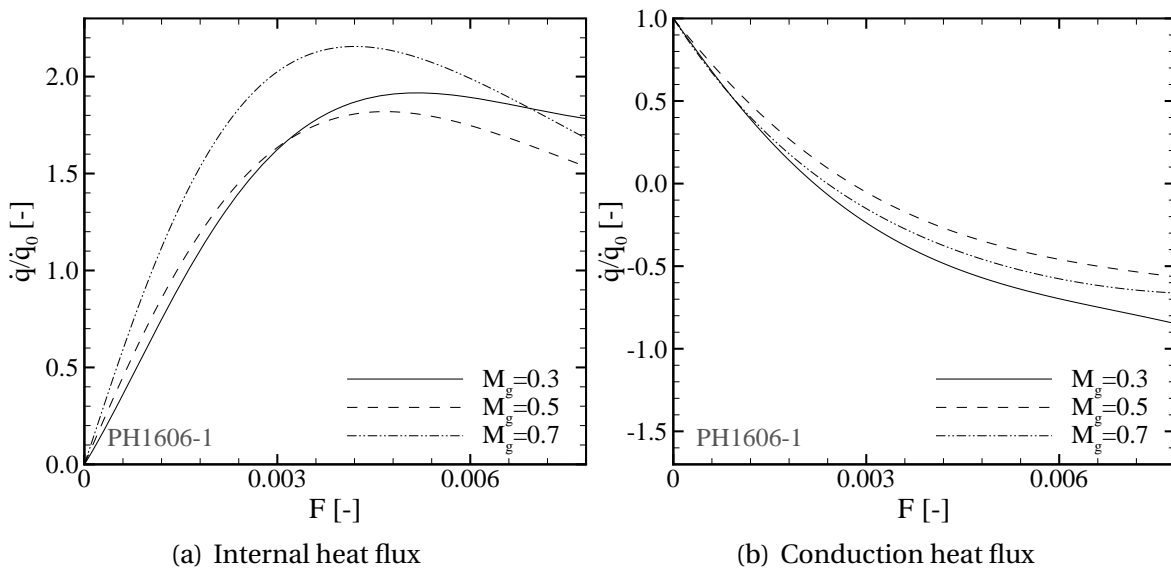


Figure 5.19: Normalized conduction and internal heat flux from the transpiration cooling model for different hot-gas Mach number. $T_{t,g} = 520 \text{ K}$, PH1606-1 sample

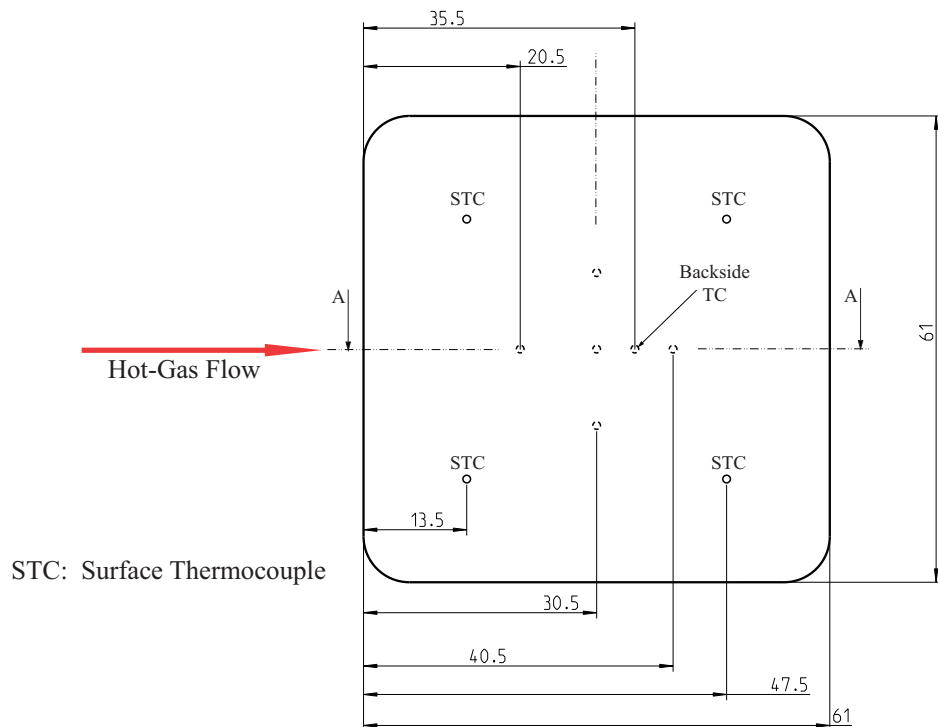
5.4 Thermal Behavior of the Porous C/C Wall in Subsonic Flow Experiments

supersonic flow channel. Here, the conduction heat flux was always directed from the sample towards the water-cooled copper test section walls.

In analogy to the data given in Section 5.3 and in this section, the normalized heat flux components for the subsonic flow test at $T_{t,g} = 523\text{ K}$ using the PH1606-1 sample are given in the Appendix. The model data for the foreign gas injections tests are given in Fig. C.1(a), Fig. C.1(b), Fig. C.2(a), and Fig. C.2(b).

5.4.5 Internal Temperature Profile of C/C Wall Segment

Figure 5.20: Location of thermocouples on and within the porous wall samples. Dashed circles: In-sample thermocouples



To gain more information about the thermal behavior of the porous CMC samples, it is important to also know the temperature profile within the sample where the heat is being transferred from the solid structure to the coolant. Therefore, the samples were equipped with several thermocouples (see Section 3.3.1) to assess these distributions. Measurements of temperature profiles in porous media are always difficult, because of the two intermixing media (solid and coolant) with potentially two different temperatures. Furthermore the installed thermocouples can slightly disturb the temperature field as well as the coolant flow field. The thermocouple has been glued with the tip to the C/C wall. Therefore, it is assumed to be not in contact with the gaseous phase and the influence of the coolant if local thermal non-equilibrium is present should be small. The installation pattern of the thermocouples within the porous wall is sketched in Fig. 5.20. One can see that all thermocouples used to measure the temperature profile in the C/C wall are located in the region with the most homogeneous temperature (compare to the infrared surface temperature data in Figs. 5.14(a) through 5.14(i)).

5 Transpiration Cooling of C/C Wall Segments with Different Coolants

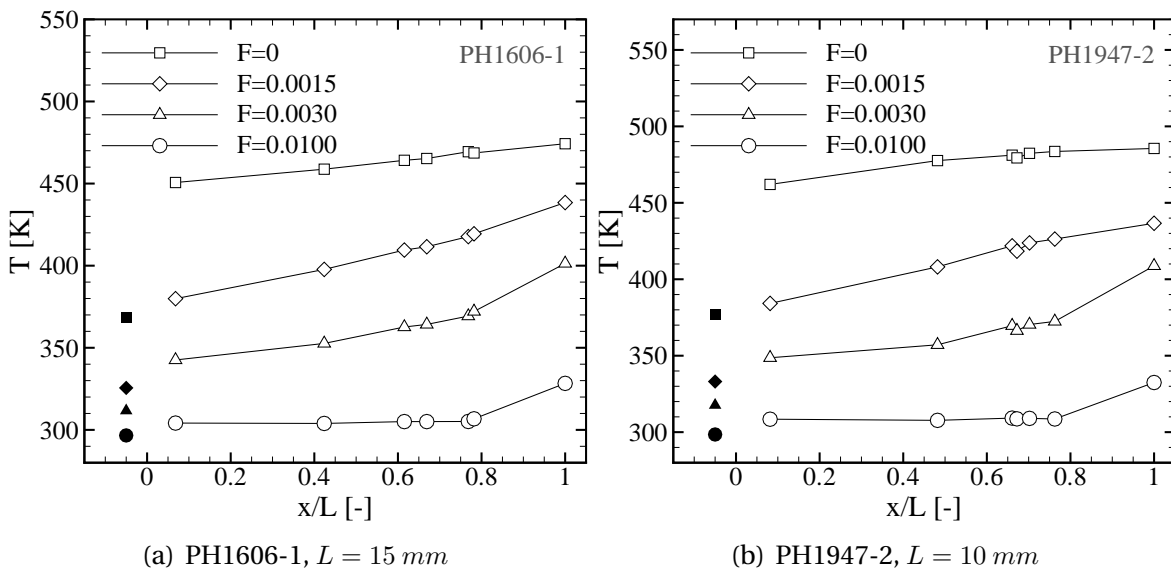


Figure 5.21: Temperature profile of different C/C samples over nondimensional wall thickness, $T_{t,g} = 525 \text{ K}$, $M_g = 0.5$. Solid symbols represent the coolant temperature in the coolant plenum

In Fig. 5.21(a) and 5.21(b) temperature profiles within a PH1606 sample and a PH1947 sample at $T_{t,g} = 525 \text{ K}$ and $M_g = 0.5$ for different blowing ratios are shown. The readings of the thermocouples are displayed with blank symbols over the nondimensional thickness of the porous wall. This installation depth of the thermocouples varies from sample to sample, because the bore holes could not be reproduced accurately and the carbon glue thickness varies. The actual depth has been measured after the tests and after ultrasound cleaning of the holes. The solid symbols give the temperature of the coolant in the plenum. With zero blowing, this is the temperature of the resting gas within the reservoir. For all blowing ratios the backside of the sample stays warmer than the gas temperature in the plenum. Therefore, natural convection and radiation heat transfer plays a significant role at this location. At $x/L = 1$ the values of the averaged surface thermocouple data is given, which was also discussed in the previous sections.

For zero blowing the temperature profile is nearly linear for both samples. This indicates that besides hot-gas and cold-gas side heat convection, only heat conduction within the sample is present. Increasing the blowing ratio, this shape turns into a slightly non-linear curve which could be described by an exponential function. This has also been suggested in literature (see for example von Wolfersdorf (2005)). For the highest blowing ratio $F = 0.010$ the temperature profile is almost flat, except for the portion close to the hot-gas surface, where still heat is being convected to the sample. Due to the heat transfer reduction by the transpired boundary layer and the high coolant mass-flow rate a higher temperature than the coolant temperature does not penetrate far into the sample.

5.4.6 1D-Approach for Wall-Temperature Profile Prediction

In this section an equation for the temperature distribution within the porous wall is being derived. This shall be used to better understand the experimental findings presented in Section 5.4.5. For this, thermal equilibrium between the coolant and the solid is assumed, which was previously the case for the transpiration cooling model from Section 5.3. At the hot-gas side, a constant wall temperature boundary condition will be set, whilst at the plenum side of the sample a convective boundary condition is assumed to represent the radiation and natural convection appearing here. The constant wall temperature will be later provided by measurements of the porous surface temperature using the thermocouples. The free stream temperature for the coolant side convective boundary conditions is the coolant temperature measured in the plenum.

First the one-dimensional, steady energy equation for the porous wall can be given (Eqn. 5.9), which consists out of the convective part of the coolant (conduction for the coolant gas can be neglected). In the solid only conduction is considered.

$$\underbrace{\rho_c c_{p,c} v_c \frac{dT}{dx}}_{\text{Convection of Coolant}} = \underbrace{k_s \frac{d^2 T_c}{dx^2}}_{\text{Conduction in Solid}} \quad (5.9)$$

Now, this equation can be written in a nondimensional form :

$$\frac{d\Theta}{dX} = \frac{1}{C} \frac{d^2 \Theta}{dX^2} \quad (5.10)$$

Here, Θ is the temperature ratio with reference to the wall temperature at the hot-gas side ($X = 1$) and the coolant temperature. The nondimensional wall thickness is given as X .

$$\Theta = \frac{T - T_c}{T_w - T_c} \quad \text{and} \quad X = \frac{x}{L}$$

The coefficient C is defined as shown in Eqn. 5.4.6 and represents the wall material properties and coolant mass-flow rate.

$$C = \frac{\rho_c c_{p,c} v_c L}{k_s}$$

The solution of the differential equation follows an exponential behavior for Θ :

$$\Theta = \alpha_1 e^{AX} + \alpha_2 \quad (5.11)$$

Inserting this approach into the original differential equation 5.10 we obtain that $A = C$. Now, we state a convective boundary conditions to include natural convection and effective radiation heat transfer at the cold side of the porous wall:

$$x = 0 : \quad k_s \left. \frac{dT}{dx} \right|_{x=0} = h_c (T - T_c) \quad (5.12)$$

5 Transpiration Cooling of C/C Wall Segments with Different Coolants

or in nondimensional form:

$$X = 0 : \quad \left. \frac{d\Theta}{dX} \right|_{X=0} = Bi_c \Theta \quad (5.13)$$

At the hot-gas side, we first assume a constant wall temperature which can be provided by separate measurements or from model calculations.

$$x = L : \quad T = T_w \quad \text{or} \quad X = 1 : \quad \Theta = 1 \quad (5.14)$$

Now, using the boundary conditions and the approach for Θ the coefficients α_1 and α_2 can be calculated.

$$\alpha_1 = \frac{Bi_c}{C - Bi_c} \left(\frac{1}{1 + \frac{Bi_c e^C}{C - Bi_c}} \right) \quad (5.15)$$

and

$$\alpha_2 = \frac{1}{1 + \frac{Bi_c e^C}{C - Bi_c}} \quad (5.16)$$

The coolant side heat transfer coefficient h_c can be calculated assuming mixed boundary conditions of natural convection at the backside of the sample and radiation to the coolant plenum. For the estimation of the first, the Grashof number Gr_L for a vertical flat plate has to be known (Merker and Eiglmeier 1999).

$$Gr_L = \frac{|T_c - T_b| g H^3}{T_c \nu_m^2} \quad (5.17)$$

Here, g is the gravitational constant, H the height of the sample and ν_m the kinematic viscosity at the average between both temperatures. Using this quantity, a correlation for the natural convection Nusselt number can be given (Merker and Eiglmeier 1999):

$$Nu_n = \frac{4}{3} 0.508 Pr^{1/2} \frac{Gr_L^{1/4}}{(0.952 + Pr)^{1/4}} \quad (5.18)$$

Using this equation, the natural convection heat transfer coefficient h_n can be calculated. From the radiation heat flux from the backside to the coolant plenum an effective heat transfer coefficient can be calculated:

$$h_{rad} = \frac{\dot{q}_{rad}}{(T_b - T_{pl})} = \frac{\sigma (\varepsilon_b T_b^4 - \varepsilon_{pl} T_{pl}^4)}{(T_b - T_{pl})} \quad (5.19)$$

Now, the coolant side heat transfer coefficient is assumed to be the sum of h_n and h_{rad} . From this the coolant side Biot number can be computed. Now, all parameters for the calculation of the analytical temperature profile are known and are summarized in Table 5.4.

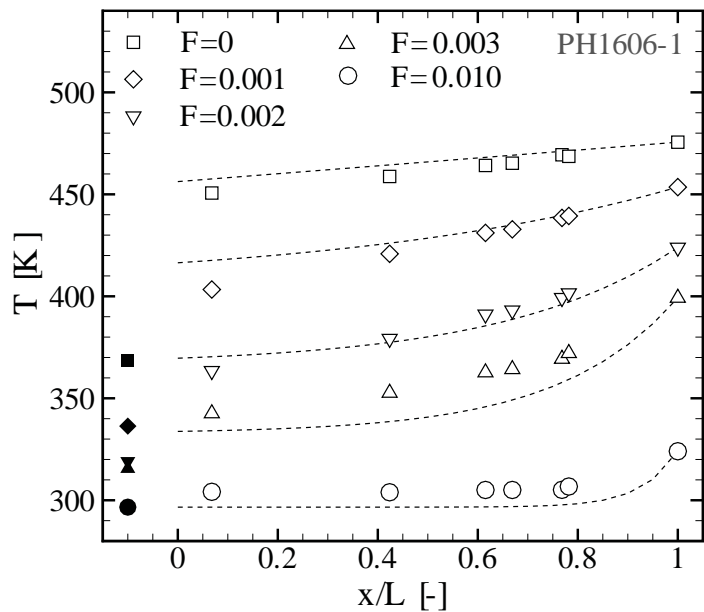
5.4 Thermal Behavior of the Porous C/C Wall in Subsonic Flow Experiments

Name	Symbol	Value
through-flow velocity	v [m/s]	0 – 0.16
coolant inlet density	ρ [kg/m ³]	0.88 – 12.8
specific heat capacity coolant (air)	$c_{p,g}$ [J/(kgK)]	1010
wall thermal conductivity	k_s [W/(mK)]	1.4
wall temperature	T_w [K]	319 – 488
coolant temperature	T_c [K]	304 – 362
sample backside temperature	T_b [K]	298 – 377
plenum wall temperature	T_{pl} [K]	300 – 352
sample thickness	L [m]	0.01 – 0.015

Table 5.4: Parameters for analytical calculation of temperature profile in porous wall

The solution obtained from Eqn. 5.11 with the coefficients α_1 and α_2 can be rearranged for the wall temperature profile using the via thermocouples measured values for T_w and T_c . These distributions are shown in Figs. 5.22 and 5.23 as dashed lines in comparison to the thermocouple measurements of the porous wall temperature versus the nondimensional sample thickness. The coolant temperature is indicated by a solid symbol. For no blowing or small blowing ratios the agreement between the analytical solution and the experimental data is quite good, especially closer to the hot-gas surface and. With higher F the temperature profiles shape becomes less linear and the exponential shape prescribed by the solution Eqn. 5.11 can be seen. Furthermore, the model somewhat under predicts the wall temperature levels measured in this F -regime. Since the analytical solution is a simplified one-dimensional approach, no effects of the lateral heat conduction are included. For lower blowing ratios there is a small heat flux from the sample into the non-adiabatic test environment. Once the sample becomes colder (see Section 5.4.4) the direction of the

Figure 5.22: Temperature profile within the porous sample compared to the analytical, one-dimensional, thermal equilibrium solution (dashed lines). $T_{t,g} = 525$ K, $M_g = 0.5$. PH1606-1



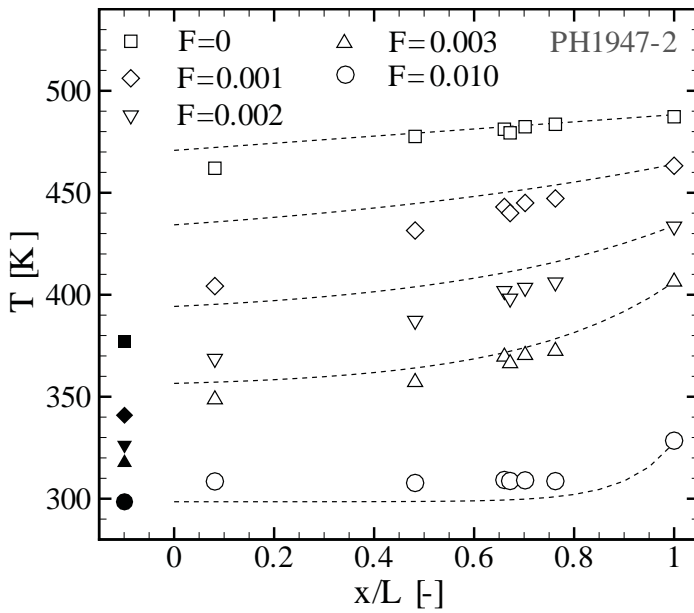


Figure 5.23: Temperature profile within the porous sample compared to the analytical, one-dimensional, thermal equilibrium solution (dashed lines). $T_{t,g} = 525 \text{ K}$, $M_g = 0.5$. PH1947-2

lateral heat flux changes and heats the wall specimen. Furthermore, the coolant side heat transfer has been approximated. These influences can be seen in the measured profiles but not in the computed ones.

If the fluid and the solid within the wall were not at thermal equilibrium, the solid temperature distribution would be higher than shown in Fig. 5.22 and 5.23. The coolant would not be able to extract as much heat from the wall structure. Since the curves obtained from the 1D thermal equilibrium computation are mostly over estimating the measured temperature in the wall, it is unlikely that significant local thermal non-equilibrium is present here. Especially for the lower blowing ratio regime the non-equilibrium effect would be more pronounced, because of the low through-flow velocity leading to a small volumetric heat transfer coefficient, the low coolant mass-flow rate, and the still relatively high hot-gas side heat flux.

These results show, that the assumption of thermal equilibrium used when setting up the model for the through-flow behavior (see Section 5.5.1) and the model for the wall temperature estimation (see Section 5.3) is valid. Even if small local thermal non-equilibrium was present, these effects would not be captured with the current test setup and the impact on for example coolant viscosity or density would be comparatively low, since the integral value of the pressure drop was investigated.

5.5 Through-Flow Behavior of Porous Materials in Hot-Gas Tests

5.5.1 Modified Darcy-Forchheimer Equation for Non-Isothermal Porous Media

To obtain through-flow data of the samples integrated within the test setups for the transpiration cooling experiments, cold flow tests were performed. These were

5.5 Through-Flow Behavior of Porous Materials in Hot-Gas Tests

carried out similar to the pressure tank tests as described in Section 4.2. Air and when tested under hot-gas conditions also argon and helium were employed. From these data, the permeability coefficients K_D and K_F can be determined by curve-fitting the Darcy-Forchheimer equation (Eqn. 2.48) to them. Table 5.5 gives these coefficient within the test setup and the uncertainty computed from the measurements using the Monte Carlo method. One notices, that for the PH1732 material charge K_D and K_F are somewhat smaller than what was acquired from the pressure tank tests. This is caused by the different installation, smaller sample geometry in the actual tests and sealing of the samples within the Macor frame. For the further evaluation always the coefficients from Table 5.5 are used to ensure the comparability between cold flow tests and hot-gas foreign gas experiments.

During the hot-gas transpiration cooling, the coolant supply pressure was measured at equilibrium with respect to the coolant temperature and pressure for every blowing ratio. With the coolant mass-flow rate for a certain blowing ratio the pressure drop can be expressed in terms of through-flow velocity. In previous studies (Innocentini et al. 2000; Moreira et al. 2004; Langener et al. 2008) and for the pressure tank tests described in this study, the fluid properties were always assumed at isothermal conditions throughout the porous specimen, while the density was considered a function of pressure using the perfect gas law.

	$K_D \cdot 10^{13} \text{ [m}^2\text{]}$	$K_F \cdot 10^8 \text{ [m]}$	$\delta K_D / K_D \text{ [%]}$	$\delta K_F / K_F \text{ [%]}$
PH1732-1	1.12	1.43	6.75	15.24
PH1732-2	0.86	0.97	6.91	12.50
PH1606-1	1.25	0.88	5.28	5.55
PH1606-2	1.21	0.84	5.72	6.45
PH1947-1	1.77	1.21	5.18	4.82
PH1947-2	1.84	1.46	4.68	4.26

Table 5.5: Permeability coefficients and their uncertainties for all tested materials obtained from cold flow tests with the sample integrated in the hot-gas setups

In case of non-isothermal through-flow, which is related to transpiration cooling applications, the temperature dependency of the viscosity and the density needs to be considered. Therefore, an extended Darcy-Forchheimer equation is derived assuming thermal equilibrium within the sample for a one-dimensional situation. This will be developed from the test data acquired using the supersonic channel and air as a coolant and later verified with the experiments in the subsonic flow regime and by using different coolant gases. The nondimensional energy equation for this case is given by Eqn. 5.20:

$$\frac{d\Theta}{dX} = \frac{1}{C} \frac{d^2\Theta}{dX^2} \quad (5.20)$$

5 Transpiration Cooling of C/C Wall Segments with Different Coolants

in which the quantities are defined as:

$$\Theta = \frac{T - T_{in}}{T_w - T_{in}} \quad X = \frac{x}{L} \quad C = \frac{\rho c_{p,c} v_{in} L}{k_s}$$

At the hot-gas side ($X = 1$) a constant temperature ($\Theta = 1$) is used, which later can be provided by the measurements (T_w) or separate model predictions. The coolant side ($X = 0$) is assumed to be at coolant inlet temperature ($\Theta = 0$), leading to the solution:

$$\Theta = \frac{e^{CX} - 1}{e^C - 1} \quad (5.21)$$

For the investigated through-flow velocities and the given coolant and sample properties the parameter C is relatively small ($0 \leq C \leq 1.5$). This means that the temperature distribution within the CMC wall can be approximated for simplicity by a linear function. This allows for an analytical solution of the differential equation Eqn. 2.46, which is important for obtaining an engineering equation for future design estimates of transpiration cooled systems.

$$T = T_{in} + (T_w - T_{in}) \frac{x}{L} = T_{in} + b \frac{x}{L} \quad (5.22)$$

Eqn. 5.22 is used to locally determine the coolant viscosity incorporating a general power-law (Eqn. 5.23). Last uses reference data at 300 K. In Table 5.6 these reference quantities which were taken from the NIST fluid property database *REFPROP* (Lemmon et al. 2007) are given for the investigated coolants.

$$\mu = \mu_{ref} \left(\frac{T}{T_{ref}} \right)^n = \mu_{ref} \left(\frac{T_{in} + b \frac{x}{L}}{T_{ref}} \right)^n; \quad T_{ref} = 300 \text{ K} \quad (5.23)$$

The Darcy-Forchheimer Equation in differential form is given in Eqn. 2.46 in Section 2.5. First, the the superficial through-flow velocity $v = \dot{m}_c \rho A_c$ and the perfect gas law for the density $\rho = p/RT$ are substituted together with Eqn. 5.22 and Eqn. 5.23. A_c here depicts the actively cooled surface, or porous flow cross-section. After separation of variables this yields to:

$$p dp = -R \left\{ \frac{\dot{m}_c}{K_D A_c} T_{in} \mu_{in} \left(1 + \frac{b}{T_{in}} \frac{x}{L} \right)^{n+1} + \frac{\dot{m}_c^2}{K_F A_c^2} T_{in} \left(1 + \frac{b}{T_{in}} \frac{x}{L} \right) \right\} dx \quad (5.24)$$

Coolant	μ_{ref} [kg/(m s)]	n [-]
air	18.38E-6	0.70
argon	22.67E-6	0.77
helium	19.93E-6	0.69

Table 5.6: Reference dynamic viscosity quantities for used coolants (@ 300 K)

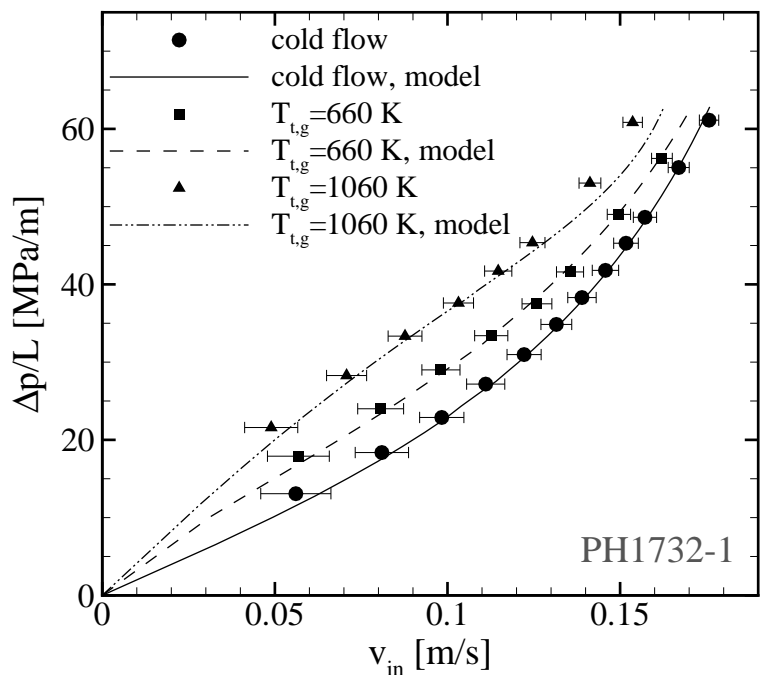
After integration from inlet (*in*) to outlet (*ex*) conditions, an extended form of the Darcy-Forchheimer equation with $v_{in} = \dot{m}_c \rho_{in} A_c$ is being obtained. The inlet quantities can be determined from the reservoir conditions, for the experiments here, this is the coolant plenum condition.

$$\frac{p_{in}^2 - p_{ex}^2}{2p_{in}L} = \frac{\mu_{in} v_{in}}{K_D} \frac{1}{\frac{b}{T_{in}}(n+2)} \left[\left(1 + \frac{b}{T_{in}}\right)^{n+2} - 1 \right] + \frac{\rho_{in} v_{in}^2}{K_F} \left(1 + \frac{b}{2T_{in}}\right) \quad (5.25)$$

For isothermal conditions, which means $T_{in} = T_{ex}$ or $b = 0$, Eqn. 5.25 collapses into the compressible definition (Eqn. 2.48). In Figs. 5.24 and 5.25 this analytical approach has been compared to the experimental data from the supersonic main-flow tests using the K_D and K_F from the cold flow tests. One can see a very good agreement between the predictions from Eqn. 5.25 with the experimental pressure loss data of both investigated samples at different test temperatures. The data for the through-flow test at ambient conditions with no main-flow is shown as circles and solid line respectively. This data matches the best, since the permeability coefficients used for the calculations were derived from it. For the model results at the higher total temperature level these coefficients were used as well (see Table 5.5).

The largest impact of the non-isothermal sample conditions can be seen at low or moderate mass-flow rates and through-flow velocities respectively. Here, the pressure drop can be twice as high as compared to the cold flow tests. For higher coolant mass-flow rate the curves almost collapse again, since the temperature within the sample approaches again isothermal conditions at coolant inlet temperature. This is due to the high cooling efficiency of the porous wall at high coolant mass-flow rates (see Section 5.3). This shows that the evaluated permeability coefficients from cold flow experiments can well be used to predict the pressure loss under thermal

Figure 5.24: Normalized pressure loss versus superficial through-flow velocity showing the temperature effect: Comparison of through-flow model with experimental data at $M_g = 2.1$. PH1732-1, Coolant: Air



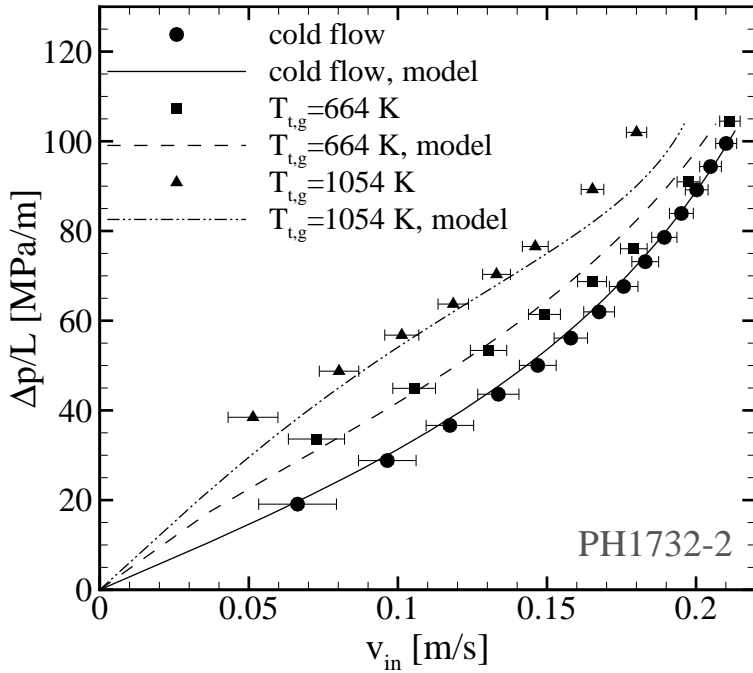


Figure 5.25: Normalized pressure loss versus superficial through-flow velocity showing the temperature effect: Comparison of through-flow model with experimental data at $M_g = 2.1$. PH1732-2, Coolant: Air

loadings when taking the temperature dependency of the coolants properties adequately into account. For the present calculations, the porous wall temperature measured via the thermocouples was used as T_w to calculate b and the pressure drop respectively.

5.5.2 Prediction of the Pressure Loss Using the Wall Temperature Model for Different Coolants

For the layout of a transpiration cooled system the expected wall temperature of the porous material T_w normally is not known prior to test or without more advanced design tools such as computational fluid dynamics. For the model of the through-flow behavior of the C/C at higher test temperatures, this value had to be given at a certain coolant mass-flow rate (Section 5.5.1). With the availability of the wall temperature model developed prior in this study (Section 5.3), this value can be provided for different coolants knowing the main-flow parameters and for given coolant mass-flow rates. In this section both models are coupled and then the calculated pressure drop is compared to the obtained experimental data for both the subsonic as well as the supersonic flow tests.

First, the permeability coefficients for all test gases at ambient conditions using cold flow tests without main-flow were again evaluated by the curve-fitting technique. These parameters are plotted in Fig. 5.26 for the PH1732-1 sample, and in Fig. 5.27(a) and 5.27(b) for the PH1606 sample charge. The uncertainties in K_D and K_F were determined by the Monte Carlo method with 100000 randomly distributed data pairs and curve fits using the uncertainties in the parameters $\mu_{in}v_{in}$ and $\rho_{in}v_{in}^2$ (see Section 4.4). The mean values, i.e. the values for the permeability coefficients obtained by applying this method, differ for the different test gases due to the different coolant

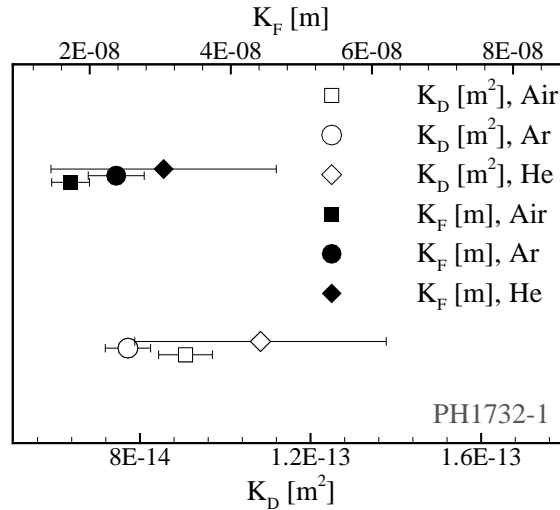


Figure 5.26: Permeability coefficients K_D and K_F from the cold flow tests for different coolants including uncertainties from Monte Carlo analysis. PH1732-1 sample

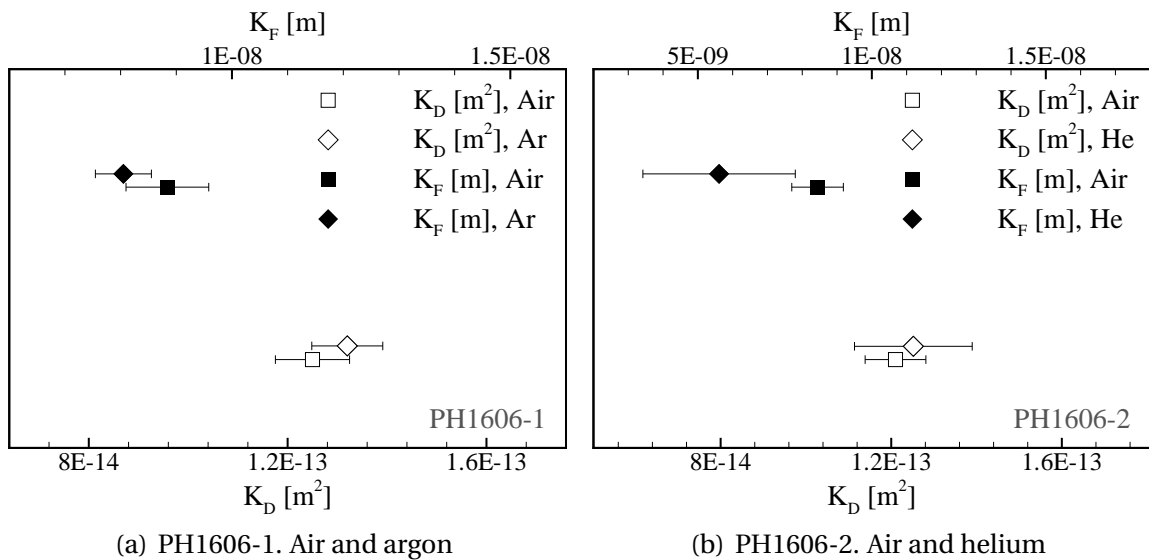


Figure 5.27: Permeability coefficients K_D and K_F from the cold flow tests for different coolants including uncertainties from Monte Carlo analysis. PH1606 material

mass-flow rate regimes and the same test equipment used. This shows, that within the margin of errors, all cold flow tests yield similar permeability coefficients. This is because these parameters are material intrinsic values and should not depend on fluid properties or temperature. The high uncertainty of K_D and K_F for helium can be explained by the the very low coolant mass-flow rates investigated with this gas. For the PH1606-2 sample this value is somewhat smaller, because the coolant mass-flow rate was higher using this material due to the larger actively cooled surface. Using these coefficients and applying the through-flow model coupled with the wall temperature model, one is able to compute the pressure drop for different coolants

5 Transpiration Cooling of C/C Wall Segments with Different Coolants

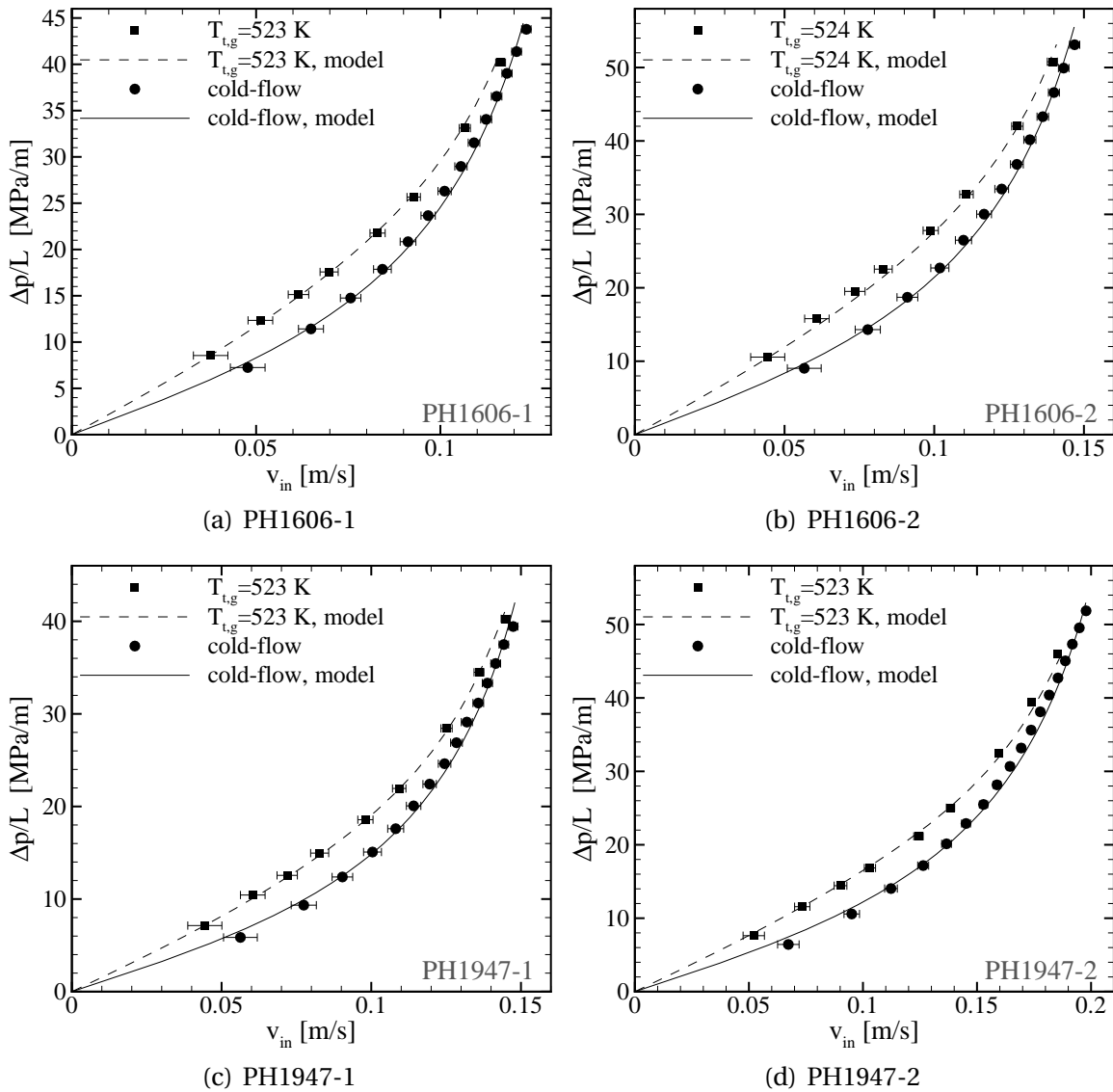


Figure 5.28: Normalized pressure loss versus superficial through-flow velocity: experimental data compared to coupled approach for the pressure loss using the cold flow test permeability coefficients. $M_g = 0.7$, $T_{t,g} = 523 - 524 \text{ K}$

and conditions with thermal loads. This model has to be solved iteratively, because the pressure drop is a function of the density of the coolant which again depends on the inlet pressure.

As a first validation step, the pressure drop calculated from the coupled model has been plotted for several samples versus the superficial through-flow velocity v_{in} in Fig. 5.28(a) through 5.28(d). The results have been taken from the tests in the subsonic channel whilst the main-flow condition were: $M_g = 0.7$ and $T_{t,g} = 523 - 524 \text{ K}$ and for the cold flow checks. All other parameters for the wall-temperature model can be found in Table 5.3. The uncertainties in v_{in} are low, because air as a coolant and high coolant mass-flow rates were used. Nevertheless, the coupled model including the prediction of the hot-gas wall temperature T_w match the test data accurately. The

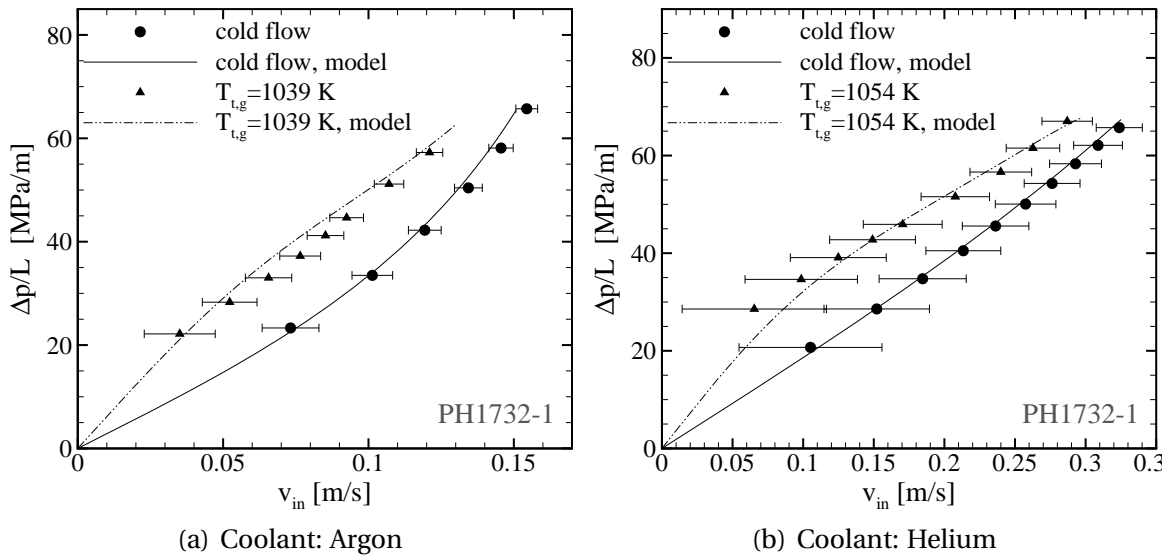


Figure 5.29: Normalized pressure loss versus superficial through-flow velocity: Experimental data compared to coupled approach for the pressure loss using the cold flow test permeability coefficients. PH1732-1 sample. $M_g = 2.1$, $T_{t,g} = 1039 - 1054$ K

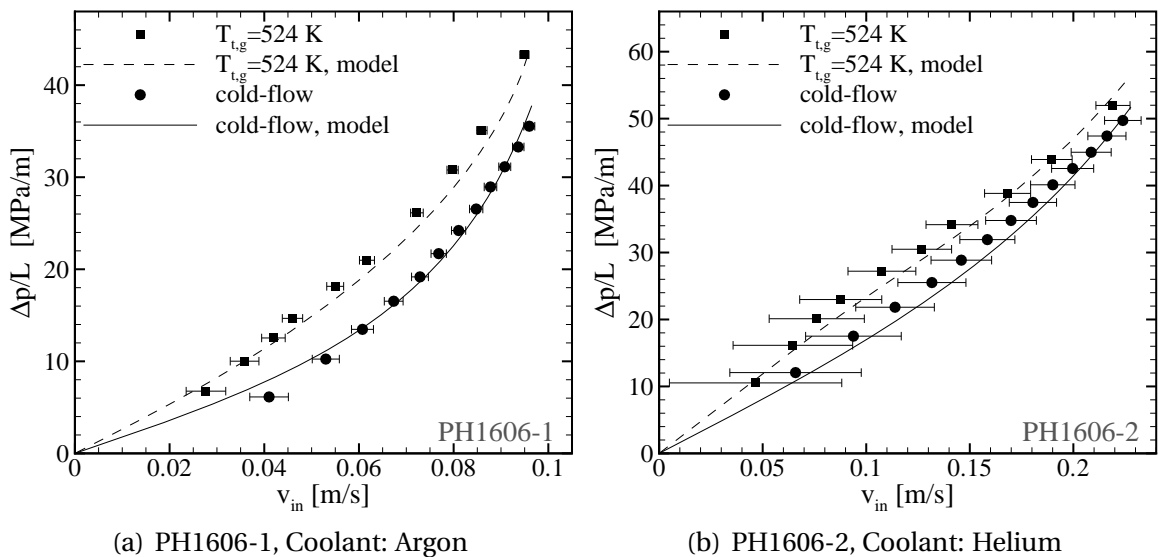


Figure 5.30: Normalized pressure loss versus superficial through-flow velocity: Experimental data compared to coupled approach for the pressure loss using the cold flow test permeability coefficients. $M_g = 0.5$, $T_{t,g} = 524$ K

difference in pressure drop for the medium blowing cases (medium values in v_{in}) can be remodeled as well as the merging of the curves for the highest coolant mass-flow rates. This works for all samples investigated under these main-flow conditions.

To further prove the validity of the coupling of both models, the pressure loss data for the tests conducted with argon and helium were investigated. Fig. 5.29(a), Fig. 5.29(b), Fig. 5.30(a), and 5.30(b) show these results compared to the experimental

ambient and hot-gas conditions for both flow regimes. The agreement is very good. This means the effects of the non-isothermal porous wall, i.e. the temperature dependency of the dynamic viscosity and the through-flow velocity, can also be predicted well for different gases and different flow conditions. The uncertainty in the helium tests is higher than for the ones with argon. The permeability coefficients were taken from the through-flow tests at ambient temperature such as displayed in Fig. 5.26. To validate the developed model with the experimental results, the coefficients from the tests with the different test gases have been used. This ensures comparability to the measured pressure loss data and allows to examine the effect of the non-isothermal coolant on the pressure drop for all gases used.

This model using the modified Darcy-Forchheimer equation including the predictions for the transpiration cooled wall temperature can therefore be used to predict the pressure drop of a porous composite material for scramjet combustion chamber application under thermal loading. For this, the coolant mass-flow rate and the heat transfer coefficient without blowing has to be given. The permeability coefficients from through-flow tests at ambient cold flow check conditions without any hot-gas flow need to be given. These coefficients have to be determined accurately for the coolant to be applied using adequate test equipment to be able to obtain a good prediction of the real pressure loss. In addition, the hot-gas side Stanton number without blowing has to be known properly and the test or application specific conduction situations have to be addressed.

5.6 Conclusions

In this chapter, transpiration cooling tests with $M = 2.1$ flow at total temperatures $T_{t,g}$ of up to 1120 K have been described using air, argon and helium as coolants. 2D surface temperature maps of the C/C sample were recorded by IR-Thermography and calibrated with wall thermocouple measurements. From this data, the cooling efficiency Θ of the porous wall was presented. The main influencing parameters for Θ are the coolants' specific heat capacity and the coolant mass-flow rate. To validate this effect, a one-dimensional heat balance model, taking the lateral heat conduction within the experimental setup into account, was developed. This model showed good agreement with the experimental data. The approach of Kays et al. (Kays et al. 2005) was shown to adequately describe the transpiration cooling effects for foreign gas injection if the test setup's specific thermal situation is taken into account. The developed model was then verified by transpiration cooling experiments using a thermally insulated channel in a subsonic flow regime with quite different thermal loads and thermal situation.

Furthermore, the pressure drop over the porous C/C wall was measured in the hot-gas tests and the influence of the sample's temperature distribution on the through-flow behavior was determined. Higher temperature levels within the porous wall lead to higher pressure-drops. For this reason, the Darcy-Forchheimer equation was

modified to capture this effect. The analytical data fit well to the measured pressure drop. With this analysis, it is possible to predict the pressure loss over a porous wall, for thermally loaded situations knowing the hot-gas side wall temperature T_w for the different coolant mass-flow rates and different coolant gases. This model was coupled to the transpiration cooling model eliminating the wall temperature T_w . Now, the pressure drop of transpiration cooled systems using porous CMCs can be estimated using the permeability coefficients of the porous wall evaluated from cold flow experiments and the expected heat transfer without blowing for different coolant gases. In the following chapter, these models are applied for aerospace application using realistic combustion chamber data to give an estimate of the needed mass-flow rate for cooling and of the pressure drop which would appear in the propulsion system using transpiration cooling.

Estimates for Transpiration Cooling Applied to Aerospace Structures

In the previous chapters a model for the prediction of the wall temperature and cooling efficiency of porous composite material subject to transpiration cooling was presented along with the measurement of transpiration cooled wall segments. This model had been customary modified with respect to our test setup. In this chapter the general feasibility of the application of transpiration cooled walls in aerospace application, mostly for the use in combustion chambers is shown. The only coolant which has been tested here and would be available on an hypersonic aircraft is air. Unfortunately, it yields a relative low effectiveness due to its low specific heat capacity. Furthermore, at high flight Mach numbers, the air which is being extracted from the ambient would be at a high stagnation enthalpy. This would require additional heat exchanger equipment and would impose thermal challenges to the coolant ducting. Therefore, using the fuel available on the hypersonic vehicle which is carried either at sealevel ambient temperature or even cryogenic, i.e. at extremely low temperatures, provides a great option. Using another coolant system for example for helium would not make sense because of structural weight reasons. Thus, calculations with gaseous hydrogen as a cooling fluid are presented in this section.

The injected hydrogen in the low-speed, high static temperature boundary layer would combust close to the cooled wall. Such tests were not performed in this study. Nevertheless, extensive research on boundary layer combustion with hydrogen and the effect on the skin friction coefficient and Stanton number has been carried out in the past. Stalker (2005) presented an analytical approach to predict these variables in a hypersonic boundary layer on a flat plate for a mainstream temperature of 1500 K and a wall temperature of 300 K . The hydrogen is injected into the boundary layer at a discrete location and burns in the downstream part of the boundary layer with respect to the injection location until it has been consumed. It is shown, that the Stanton number with boundary layer combustion is not differing significantly from the one which was computed for hydrogen injection without combustion. Last can

also be computed with the model presented in this study. This can be explained by the low density of hydrogen and the increased static temperature in the boundary layer by the combustion heat addition, which decreases the density and therefore reduces skin friction coefficient and the Stanton number. Further downstream in the boundary layer the Stanton number approaches asymptotically the value for no hydrogen injection, because the burning film has mixed with the main-stream. The analytical distributions were compared to experimental results obtained in a shock tunnel (Goynes et al. 2000) and to numerical simulations (Brescianini and Morgan 1993) at the same flow conditions. The analytical model was found to match these studies within a margin of $\approx 10\%$.

Furthermore, Kirchhartz et al. (2008) presented an experimental study in which they investigated the skin friction drag in a combustor at around $M = 4.5$ and high enthalpy free stream conditions. The gaseous hydrogen was injected via slits into the incoming main-stream. They found that despite the pressure increases significantly within the test section with hydrogen combustion, the drag of the combustor did not grow as compared to a non-reacting test run. This is because the skin friction with combustion was nearly the same as without reaction in the boundary layer. The values were compared to Stalker's theory and the measured drag of the combustor showed very good agreement.

Based upon these studies, it was decided that the effect of boundary layer combustion on the cooling efficiency derived by the heat-conduction modified model (Section 5.3) or the standard model of Kays et al. (Section 2.3.3) is small. Therefore, the calculations in this chapter can be performed with a reasonable uncertainty.

6.1 Exemplary Thermal Prediction of Application Related Combustors with Hydrogen as a Coolant

The experimental findings along with the simple 1D-analytical model can now be used to demonstrate if a real combustion chamber can be cooled by means of transpiration cooling and with the used CMCs. This is more to show a general feasibility than an exact prediction of coolant mass-flow rates or wall temperatures appearing under real conditions. Here, the equivalence ratio of the cooling needs to be well below unity to guarantee efficient combustion by other injection concepts.

In an aerospace application, the thermal situation in which the composite combustion chamber is embedded will differ from the one in which the porous samples in this study were tested. The combustor will be fairly long, therefore the effect of lateral heat conduction will be smaller. The hot-gas Biot number which compares the convective heat transfer to the cooled wall and the heat conduction within the wall is shown in Fig. 6.1 versus the blowing ratio. The data has been calculated for the applications explained later in this section and the combustion chamber length was taken as a length scale. The lateral heat conductivity of the porous wall was $k_w = 14 \text{ W/mK}$. One can clearly see that for the scramjet, ramjet, and scramjet

6.1 Exemplary Thermal Prediction of Application Related Combustors with Hydrogen as a Coolant

demonstrator combustion chamber Bi_g is very large, also for strong blowing. This indicates the small influence of lateral heat conduction in the setups. In contrast, the tested configuration exhibits for helium transpiration cooling a Biot number of around unity and smaller. Therefore, the estimates of transpiration cooling for application related combustors were carried out with the non-conduction modified model of Kays et al. (Section 2.3.3), because of its superiority to describe the foreign gas effect compared to other models.

The combustion chamber conditions were taken from the scramjet propulsion system investigated in the LAPCAT project. Two flight Mach numbers of $M_\infty = 7$ and $M_\infty = 8$ were under investigation. In Table D.1 the conditions with the elliptical combustion chamber and the used model parameters are given. Next, the ramjet

Figure 6.1: Biot number of the combustion chamber heat transfer as a function of the blowing ratio for different combustion chamber conditions

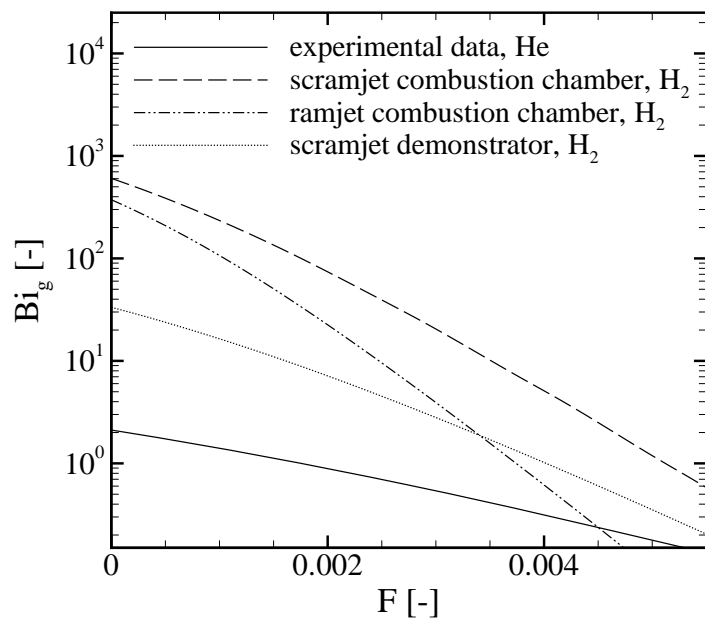
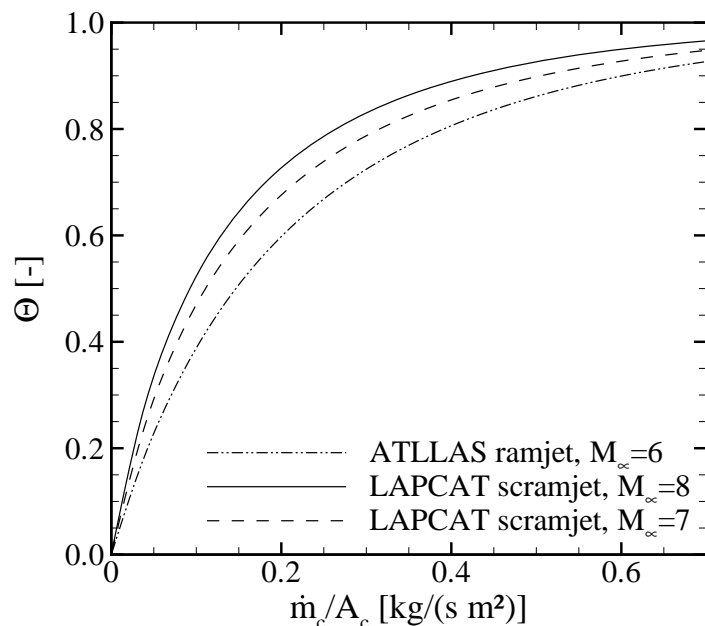


Figure 6.2: Cooling efficiency using hydrogen as a coolant as a function of the coolant mass-flow rate per cooled area: LAPCAT and ATLLAS flight configurations



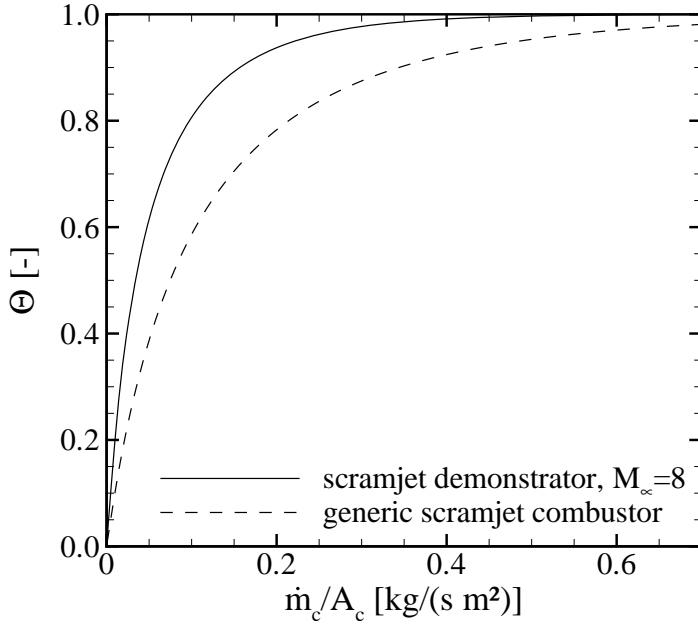


Figure 6.3: Cooling efficiency using hydrogen as a coolant as a function of the coolant mass-flow rate per cooled area: Scramjet demonstrator and generic scramjet geometry

propulsion concept studied in the ATLLAS project at a flight Mach number of $M_\infty = 6$ has been used as a hot-gas condition for the transpiration cooling. Table D.2 summarizes these parameters, the combustor is circular in this case. Finally, a scramjet demonstrator combustor with rectangular cross-section described by Fuhrmann (2009) has been used as a reference for the transpiration cooling estimates (see Table D.3).

In Fig. 6.2 the prediction of the cooling efficiency of the hydrogen cooled combustor wall for the above mentioned LAPCAT scramjet and ATLLAS ramjet concept has been plotted versus the coolant mass-flow rate per unit wall surface area. The cooling efficiency for the ramjet combustor is the lowest, because of its high static combustion chamber pressure and therefore very high heat load onto the cooled wall. Nevertheless, with small coolant mass-flow rates per wall surface area a high Θ can be reached due to the high specific heat capacity of hydrogen.

The estimated transpiration cooling efficiency for the use in the scramjet demonstrator is shown in Fig. 6.3. In this case, Θ is relatively high due to the high-speed and low static pressure flow within this combustor. Furthermore, the cooling efficiency of a generic hydrogen cooled combustor is shown. Last will be discussed in Section 6.2.

For one data set the calculation of the cooling equivalence ratio ϕ_{cool} is exemplarily given according to the LAPCAT concept at $M_\infty = 8$: Assuming a bearable wall temperature of $T_{w,max} = 1000 \text{ K}$, a total temperature of $T_{t,g} = 2400 \text{ K}$ in the combustion chamber and estimating that the hydrogen as a coolant is available at $T_c = 500 \text{ K}$ we can calculate Θ for our point of operation. We find according to Eqn. (5.1):

$$\Theta = \frac{T_{r,g} - T_{w,max}}{T_{r,g} - T_c} = \frac{2349 \text{ K} - 1000 \text{ K}}{2349 \text{ K} - 500 \text{ K}} = 0.72 \quad (6.1)$$

6.1 Exemplary Thermal Prediction of Application Related Combustors with Hydrogen as a Coolant

From Fig. 6.2 we can read at a value of $\Theta = 0.72$ a normalized coolant mass-flow rate of $\dot{m}_c/A_c = 0.20 \text{ kg}/\text{m}^2\text{s}$.

Knowing the wall surface area of this elliptical combustion chamber (see Table D.1) we can calculate the hydrogen coolant mass-flow rate:

$$\dot{m}_c = 7.22 \frac{\text{kg}}{\text{s}} \quad (6.2)$$

The intake air mass-flow rate can be calculated using the known values from Table D.1. With an equivalence ratio of unity (stoichiometric hydrogen combustion) the maximum hydrogen mass-flow rate which can be burnt in air is $\dot{m}_{H_2,stoich} = \dot{m}_g/34.3 = 47.47 \text{ kg}/\text{s}$. Therefore the cooling equivalence ratio, i.e. the hydrogen mass-flow rate used for the transpiration cooling compared to stoichiometric one is:

$$\phi_{cool} = \frac{\dot{m}_c}{\dot{m}_{H_2,stoich}} = 0.15 \quad (6.3)$$

One obtains from this example a value well below unity, indicating that in theory transpiration cooling could be used as an active cooling technique for these combustion chamber walls. For the LAPCAT configuration the total equivalence ratio envisaged for the operation was $\phi_{tot} = 0.6$, this means this cooling technique can be applied here as well. Additionally, an equivalence ratio of 0.15 would allow different hydrogen injection concepts such as strut injection to increase the energy converted in the center of the combustion chamber.

	(a) $T_{w,max} = 1600 \text{ K}$		(b) $T_{w,max} = 1000 \text{ K}$	
	$M_\infty = 7$	$M_\infty = 8$	$M_\infty = 7$	$M_\infty = 8$
$\Theta_{max} [-]$	0.41	0.38	0.73	0.72
$\dot{m}_c/A_c [\text{kg}/(\text{s} \cdot \text{m}^2)]$	0.08	0.06	0.24	0.20
$\dot{m}_c [\text{kg}/\text{s}]$	2.89	2.16	8.77	7.22
$F \cdot 10^3 [-]$	0.12	0.09	0.37	0.31
$\phi_{cool} [-]$	0.05	0.05	0.16	0.15

Table 6.1: Coolant mass-flow rate, blowing ratio, and equivalence ratio for the LAPCAT scramjet at two flight Mach numbers

Furthermore, this prediction can be carried out for a bearable wall temperature of $T_w = 1600 \text{ K}$ which is the upper limit of the available CMC materials and for the second possible flight Mach number of the LAPCAT scramjet. Table 6.1(a) and Table 6.2(a) show the results for the needed coolant mass-flow rate, the to be set blowing ratio, and the needed coolant equivalence ratio for the cases calculated. From this data, one can see that for the different parameters the equivalence ratio always stays well below unity (or 0.6) and the blowing ratios for these cases are very low.

The coolant data for the ATLLAS ramjet concept is given in Table 6.2(a) and Table 6.2(b). Here, the same applies as for the scramjet discussed above. The equivalence ratio for the cooling is very low. The coolant mass-flow rate is smaller than before,

(a) $T_{w,max} = 1600\text{ K}$		(b) $T_{w,max} = 1000\text{ K}$	
	$M_\infty = 6$		$M_\infty = 6$
Θ_{max} [-]	0.56	Θ_{max} [-]	0.80
\dot{m}_c/A_c [$kg/(s \cdot m^2)$]	0.18	\dot{m}_c/A_c [$kg/(s \cdot m^2)$]	0.39
\dot{m}_c [kg/s]	1.00	\dot{m}_c [kg/s]	2.16
$F \cdot 10^3$ [-]	0.25	$F \cdot 10^3$ [-]	0.53
ϕ_{cool} [-]	0.08	ϕ_{cool} [-]	0.17

Table 6.2: Coolant mass-flow rate, blowing ratio, and equivalence ratio for the ATLLAS ramjet

due to the smaller engine dimensions in this case. Table 6.3(a) and Table 6.3(b) summarize the data for the scramjet demonstrator. The values for ϕ_{cool} are very high, because the aspect ratio of the inlet and the length of the rectangular combustion chamber are large. Because of this, the cooled wall surface area is compared to the inlet area much bigger in comparison to the flight concepts of the LAPCAT and ATLLAS project. Therefore, less air can be captured and less hydrogen can be burnt leading to a smaller total equivalence ratio.

(a) $T_{w,max} = 1600\text{ K}$		(b) $T_{w,max} = 1000\text{ K}$	
	$M_\infty = 8$		$M_\infty = 8$
Θ_{max} [-]	0.53	Θ_{max} [-]	0.76
\dot{m}_c/A_c [$kg/(s \cdot m^2)$]	0.05	\dot{m}_c/A_c [$kg/(s \cdot m^2)$]	0.09
\dot{m}_c [kg/s]	0.07	\dot{m}_c [kg/s]	0.12
$F \cdot 10^3$ [-]	0.50	$F \cdot 10^3$ [-]	0.90
ϕ_{cool} [-]	0.45	ϕ_{cool} [-]	0.80

Table 6.3: Coolant mass-flow rate, blowing ratio, and equivalence ratio for the scramjet demonstrator

6.2 Application of the Transpiration Cooling Model to a Generic Combustor of Varying Geometry

In this section a generic combustion chamber related to a flight concept was investigated. The hot-gas parameters can be found in Table D.4 and the related cooling efficiency curve in Fig. 6.3. The inlet geometry and the length L of this combustion chamber was varied, whilst a rectangular and an elliptical cross-section was analyzed for different aspect ratios W/H (W : combustor width, H : combustor height). The coolant equivalence ratio has been plotted on a logarithmic scale versus the combustion chamber width for aspect ratios ranging from 1 up to 8 in Fig. 6.4(a) through Fig. 6.4(d). For $W/H = 1$ no difference between the rectangular geometry and the

6.2 Application of the Transpiration Cooling Model to a Generic Combustor of Varying Geometry

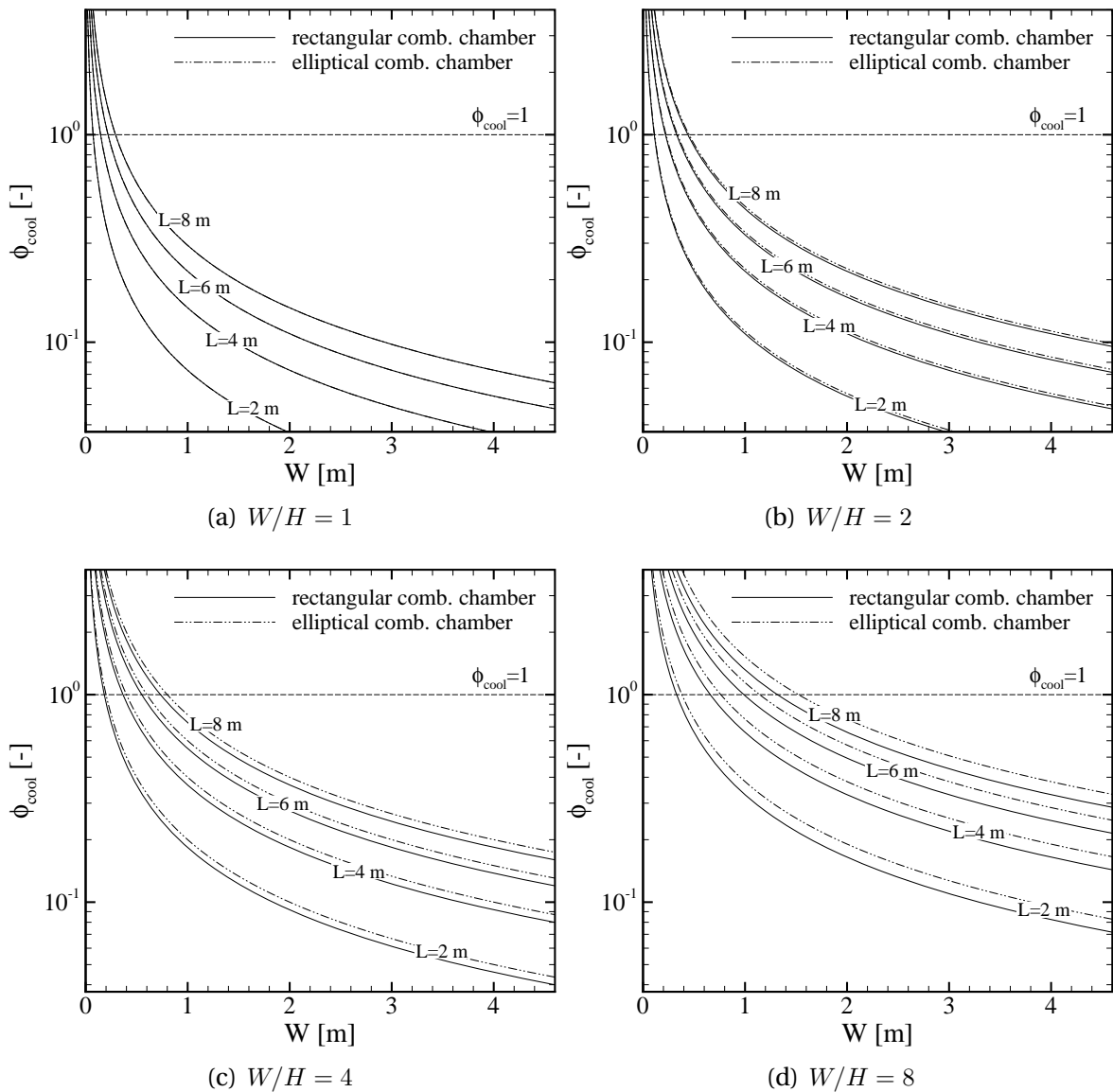


Figure 6.4: Equivalence ratio of the coolant (hydrogen) for the generic combustor geometry versus the combustion chamber width. Variation of the aspect ratio W/H

elliptical geometry can be seen, because of the similar geometrical relationships of a circle and a square. For bigger L more coolant is needed and ϕ_{cool} increases. A larger combustion chamber (bigger W) requires less hydrogen cooling equivalence ratio (but more coolant mass-flow rate) because of the decreasing ratio of cooled wall surface area and inlet capture area.

For aspects ratio greater unity, a difference between a rectangular and elliptical cross-section can be seen in ϕ_{cool} . This is caused by the larger circumference and area ratio for an ellipse causing a bigger cooled wall area as compared to the rectangular shape. For very wide combustion chambers the required coolant equivalence ratio is generally higher than more narrow ones. This effect can be seen for the scramjet

demonstrator concept where very high ϕ_{cool} were calculated and should be taken into account when designing the propulsion unit.

6.3 Estimates of the Pressure Drop for Hydrogen Transpiration Cooled Porous Combustion Chambers

Finally, it is important to know the needed coolant supply pressure of the hydrogen to achieve the above described cooling of the combustion chamber. Therewith, it can be shown if keeping the combustor wall at the desired wall temperature is feasible given the material parameters. In Section 5.5.2 the model for the prediction of the cooling efficiency was coupled with the through-flow model for non-isothermal porous media (see Section 5.5.1). This can be used to calculate the pressure drop for the application related cooling situations. The reference dynamic viscosity of hydrogen is given in Table 6.4(a). As generic combustor materials for the estimates a well permeable composite and a highly dense generic C/C-SiC was chosen. The order of magnitude of the permeability coefficients as shown in Table 6.4(b) was chosen similar to the ones of the C/C investigated in this study (permeable material) or to the C/C-SiC material studied by Gascoin et al. (2010). C/C-SiC provides normally very low permeability coefficients due to the infiltration of the C/C with silicon which decreases the porosity of the wall material significantly. In contrast, this enables the material to bear very high surface temperatures.

(a) Dynamic viscosity data		(b) Permeability coefficients	
μ_{ref} [kg/(m s)]	n [-]	K_D [m ²]	K_F [m]
8.96E-6	0.68	$1 \cdot 10^{-13}$	$2 \cdot 10^{-8}$
		$1 \cdot 10^{-16}$	$8 \cdot 10^{-11}$

Table 6.4: Reference properties of hydrogen for the through-flow model obtained from *REFPROP* (@ 300 K) and generic permeability coefficients

The results of the coupled computations for the coolant supply pressure for the LAPCAT $M_\infty = 7$ combustion chamber configuration are shown in Fig. 6.5(a) and Fig. 6.5(b). In the left plot, the bearable wall temperature was set to 1600 K whilst the generic permeable CMC could be loaded with 1000 K. The needed coolant supply pressure is given as a function of the wall thickness L for both calculations. It is evident, that the combustor made from the C/C-SiC material would need an extremely high p_c due to its low permeable structure. For sufficient cooling and a wall thickness of $L = 2.5$ mm a supply pressure of $p_c = 19.14$ MPa would be needed, for $L = 10$ mm even $p_c = 38.3$ MPa. One can see, that it would be difficult to use transpiration cooling as the only cooling technique with such a combustor material. First, for structural reasons and secondly from a system level point of view, where every pressure loss is a penalty for the overall efficiency of the engine, especially in the order of magnitude it presents itself here. Even though the more permeable material

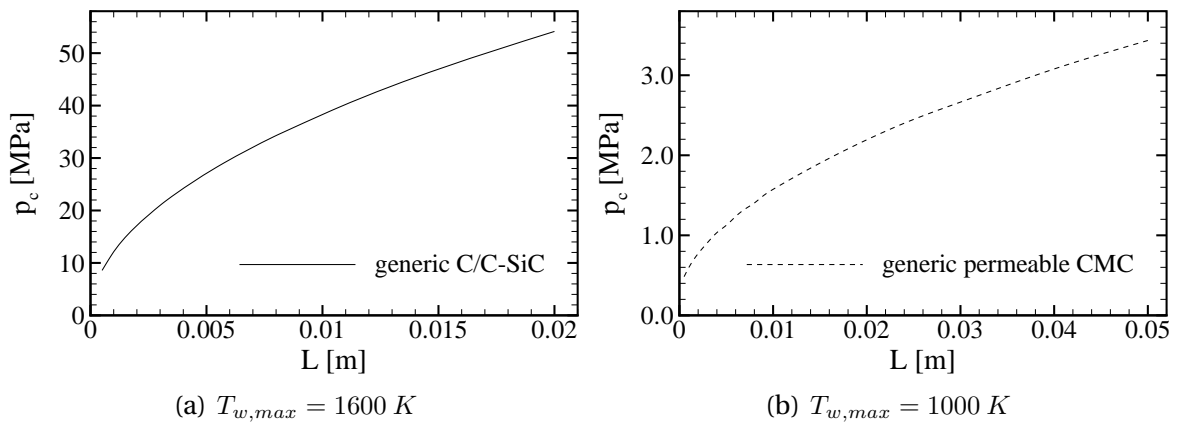


Figure 6.5: Pressure drop for different generic wall material for the cooling situations described in Table D.1 ($M_\infty = 7$). Hot-gas conditions see Table D.2

requires higher coolant mass-flow rates to keep it at a low wall temperature, the coolant supply pressure level is significantly lower than for the C/C-SiC. Due to its better through-flow properties, the pressure drop of a $L = 2.5 \text{ mm}$ thick combustor wall would be 0.84 MPa , for $L = 10 \text{ mm}$, $p_c = 1.57 \text{ MPa}$, and for $L = 20 \text{ mm}$, $p_c = 2.19 \text{ MPa}$ at the given combustion chamber pressure. The computed pressure losses for the generic permeable CMC are feasible on an engine level and do not bear too high structural loads onto the combustor.

Overall this shows that for the configurations described in this section the permeability of the material is the most limiting parameter, since the coolant equivalence ratio was well below unity for all concepts investigated. Therefore, materials with high bearable wall temperature but also high permeability coefficients have to be available to efficiently use transpiration cooling of combustors for the discussed applications.

6.4 Conclusions

The models developed in the previous chapters for the wall temperature of a transpiration cooled system and for the pressure drop over a porous wall were used to compute these values for real combustor conditions. First, it was shown that transpiration cooling for the selected aerospace application is feasible when using hydrogen as a coolant. The needed coolant equivalence ratio was in most cases well below unity. Only for combustors with very high aspect ratios (width over height) this cooling method become problematic in terms of coolant constraints due to the geometrical relations between circumference and wall area.

Thereafter, the pressure drop using two generic CMC materials was computed. For the more porous wall material, a pressure drop which can be coped with on system level could be found. For a very dense wall with extremely low permeability, as for example C/C-SiC, this technique seems to be very difficult to apply because of the large supply pressure requirements and resulting structural issues.

Summary and Outlook

For the cost efficient access to space or hypersonic civil aviation, scramjet propulsion systems offer a great potential. Many challenges are to be overcome until technical readiness is reached. Amongst other, the thermal loads within the propulsion system impose difficulties on design, safety, and life cycle issues. To cope with these, transpiration cooling applied to composite wall material, which is discussed in this thesis, is a promising technique. The goal of this work was to qualify and analyze the thermal processes when using this technique in an application related test environment with carbon/carbon as a representative wall material.

First, this material had to be qualified with respect to its through-flow and outflow behavior. A Pitot tube technique was used to measure the outflow velocity pattern. By using this technique, the exit porosity of the material could be determined, which differed significantly from the volumetric porosity. It could further be shown that single jets were exiting the surface emanating from the connected pores within the porous material. The distribution of the jets and, therefore, the outflow out of the porous material was very uniform. No significant peaks or large undersupplied regions could be seen. This means that for the characterization of the through-flow behavior or pressure loss of the porous wall, a one-dimensional integral description by using the Darcy-Forchheimer equation is sufficient. To apply this technique, the porous wall sample has to be large enough to give a representative figure for further application. All samples tested in this study followed this assumption.

Now, the transpiration cooling efficiency of several porous wall segments was determined in hot-gas experiments. At first, the C/C samples were exposed to a supersonic flow ($M = 2.1$) with total temperatures up to $T_{t,g} = 1120 \text{ K}$ using gaseous air, argon, and helium as coolants. The surface temperature of the material was measured by in situ calibrated infrared thermography and wall thermocouples to obtain quantitative and qualitative results for the following analysis. From this data the cooling efficiency was derived and it was shown that the main influencing parameters in our setup were the coolant's specific heat capacity and the coolant mass-flow rate. To validate this, a one-dimensional heat balance model was developed assuming thermal equilibrium between the porous material and the coolant within the

7 Summary and Outlook

wall and taking the strong lateral heat conduction in our setup into account. This model showed good agreement with the experimental data. The approach of Kays et al. (Kays et al. 2005) was shown to adequately predict the transpiration cooling effect, also when taking the foreign gas injection effect into account. For this, the thermal situation of the test setup or application has to be included in the model. These findings were verified by using a thermally insulated channel in a subsonic flow regime with quite different thermal loads and thermal situation.

In addition, during the above mentioned experiments the pressure loss of the porous C/C wall was measured in the hot-gas test and the influence of the sample's temperature distribution on the through-flow behavior was identified by modifying the Darcy-Forchheimer equation. This analytical approach fit the measured data well. Now it is possible to predict the pressure drop of over a non-isothermal porous wall for a given coolant mass-flow rate and for different coolant gases by knowing the hot-gas side wall temperature. To eliminate this, the transpiration cooling model was coupled to the through-flow approach. Now, it is possible to estimate the pressure drop of a transpiration cooled system using porous CMC walls when the hot-gas side heat transfer coefficient and pressure are given.

This model can now be applied to aerospace related application such as scram-jet or ramjet combustion chambers. First, it was shown that it is possible to use transpiration cooling applied to composite wall materials when using hydrogen as a coolant due to its very high cooling efficiency. The needed coolant equivalence ratio was for all investigated cases well below unity. Afterwards, the pressure loss using generic wall material was estimated. Pressure losses, which are that high that they cannot be dealt with on system level anymore were found for a CMC related to C/C-SiC. Therefore, it is important to ensure the availability of a suitable wall material, if one desires to use transpiration cooling in such high pressure and high heat-load applications.

To further qualify the described cooling technique and achieve readiness for its application in aerospace propulsion systems, it is important that additional tests with hydrogen as a coolant are carried out. These should be conducted in high-pressure and high-heat load environments similar to those investigated at the end of this thesis. Additionally, it is crucial to further develop CMC materials to ensure structural integrity and stiffness at high permeability to keep the pressure loss over the porous wall at a manageable level.

Bibliography

- Arnold, R., D. Suslov, and O. Haidn (2009). Circumferential film cooling effectiveness in a LOX/H₂ subscale combustion chamber. *Journal of Propulsion and Power* 25(3), 760–770.
- Aupoix, B., A. Mignosi, S. Viala, F. Bouvier, and R. Gaillard (1998). Experimental and numerical study of supersonic film cooling. *AIAA Journal* 36(6), 915–923.
- Baehr, H. and K. Stephan (2008). *Wärme- und Stoffübertragung*. Springer.
- Barthelemy, R. (1989). The national aero-space plane program. In *Symposium on the Maintainability of Aerospace Systems*, Anaheim, CA. AIAA 1989-5053.
- Bartle, E. and M. Leadon (1959). Experimental evaluation of heat transfer with transpiration cooling in a turbulent boundary layer at M=3.2. *Journal of the Aerospace Sciences* 26, 78–80.
- Böhrk, H., O. Piol, and M. Kuhn (2009). Heat balance of a transpiration-cooled heat shield. In *Proceedings of the 16th AIAA/DLR/DGLR International Space Planes and Hypersonic Systems and Technologies Conference*, Bremen. AIAA 2009-7273.
- Bouchez, M. and S. Beyer (2008). PTAH-SOCAR fuel-cooled composite material structure. In *Proceedings of the 15th AIAA International Space Planes and Hypersonic Systems and Technologies Conference*, Dayton, OH. AIAA 2008-2626.
- Brauckmann, D. (2006). *Experimentelle Untersuchungen von Filmkühlungsvorgängen an konturierten Bohrungen*. Ph. D. thesis, Universität Stuttgart.
- Brauckmann, D. and J. von Wolfersdorf (2004). Infrared thermography with in-situ calibration using thermochromic liquid crystals applied to film cooling. In *Proceedings of ASME Turbo Expo 2004*, Volume GT2004-53855, Vienna. ASME.
- Brescianini, C. and R. Morgan (1993). Numerical modeling of wall-injected scramjet experiments. *Journal of Propulsion and Power* 9(2), 169–175.
- Chauvin, L. and H. Carter (1955). Exploratory tests of transpiration cooling on a porous 8° cone at M=2.05 using nitrogen gas, helium gas, and water as the

BIBLIOGRAPHY

- coolants. Technical Report RM L55C29, NACA, Langley Aeronautical Laboratory, Langley Field, VA.
- Dailey, G. (2000). Aero-thermal performance of internal cooling systems in turbomachines. Technical report, von Karman Institute for Fluid Dynamics - Lecture Series, Rhode-Saint-Genése, Belgium.
- Darcy, H. (1856). *Les Fontaines Publiques de La Ville de Dijon*. Paris: Victor Dalmont.
- Dittus, P. W. and L. M. K. Boelter (1985). Heat transfer in automobile radiators of the tubular type. *International Communications in Heat Mass Transfer* 12, 3–22.
- Dorot, V. and M. Strelets (1973). Transpiration cooling in a supersonic boundary layer. *Translated from Teplofizika Vysokikh Temperatur* 11(3), 64–68.
- Eckert, E. and J. Livingood (1954). Comparison of effectiveness of convection-, transpiration-, and film-cooling methods with air as coolant. Technical Report 1182, NACA, Lewis Flight Propulsion Laboratory, Cleveland, OH.
- Ergun, S. (1952). Fluid flow through packed columns. *Chemical Engineering Progress* 48, 89–94.
- Ergun, S. and A. Orning (1949). Fluid flow through randomly packed columns and fluidized beds. *Industrial Engineering and Chemistry* 41(6), 1179–1184.
- Falempin, F., D. Scherrer, G. Laruelle, P. Rostand, and J. Schultz (1998). French hypersonic propulsion program PREPHA - results, lessons and perspectives. In *Proceedings of the 8th AIAA International Space Planes and Hypersonic Systems and Technologies Conference*, Norfolk, VA. AIAA-1998-1565.
- Fuhrmann, T. (2009). *Auslegung und Betriebsverhalten von SCRamjet-Antriebssystemen für Raumtransporter-Hyperschallflugzeuge*. Ph. D. thesis, Technische Universität München.
- Gascoin, N., G. Fau, J. Bioud, and P. Gillard (2010). Permeation of inert and supercritical reactive fluids through metallic and composite media. In *Proceedings of the 46th AIAA/ASME/SAE/ASEE Joint Propulsion Conference & Exhibit*, Nashville, TN. AIAA 2010-6551.
- Glass, D. (2008). Ceramic matrix composite (CMC) thermal protection systems (TPS) and hot structures for hypersonic vehicles. In *Proceedings of the 15th AIAA International Space Planes and Hypersonic Systems and Technologies Conference*, Dayton, OH. AIAA 2008-2682.
- Goldstein, R. (1971). Film cooling. *Advances in Heat Transfer* 7, 321–379.
- Goldstein, R., E. Eckert, F. Tsou, and A. Haji-Sheikh (1966). Film cooling with air and helium injection through a rearward-facing slot into a supersonic air flow. *AIAA Journal* 4(6), 981–985.

- Göring, J., B. Kanka, M. Schmücker, and H. Schneider (2003). A potential oxide/oxide ceramic matrix composite for gas turbine applications. In *Proceedings of the ASME Turbo Expo 2003*, Atlanta, GA. ASME.
- Goyne, C., R. Stalker, A. Paull, and C. Brescianini (2000). Hypervelocity skin-friction reduction by boundary-layer combustion of hydrogen. *Journal of Spacecraft and Rockets* 37(6), 740–746.
- Greuel, D., A. Herbertz, O. Haidn, M. Ortelt, and H. Hald (2004). Transpiration cooling applied to C/C liners of cryogenic liquid rocket engines. In *Proceedings of the 40th AIAA/ASME/SAE/ASEE Joint Propulsion Conference and Exhibit*, Fort Lauderdale, FL. AIAA 2004-3682.
- Hald, H., M. Ortelt, I. Fischer, D. Greuel, and O. Haidn (2005). Effusion cooled CMC rocket combustion chamber. In *Proceedings of the AIAA/CIRA 13th International Space Planes and Hypersonics Systems and Technologies Conference*, Capua, Italy. AIAA 2005-3229.
- Hall, B. (2000). Computer modelling of uncertainty calculations with finite degrees of freedom. *Meas. Sci. Technol.* 11, 1335–1341.
- Hall, M. and J. Hiatt (1994). Exit flows from highly porous media. *Physics in Fluids* 6(2), 469–479.
- Hank, J., J. Murphy, and R. Mutzman (2008). The X-51A scramjet engine flight demonstration program. In *Proceedings of the 15th AIAA International Space Planes and Hypersonic Systems and Technologies Conference*, Dayton, OH. AIAA 2008-2540.
- Heidenreich, B. (2007). Carbon fibre reinforced SiC materials based on melt infiltration. In *Proceedings of the 6th International Conference on High Temperature Ceramic Matrix Composites*, New Delhi, India.
- Heidenreich, B., W. Krenkel, M. Frieß, and H. Gedon (2004). Net shape manufacturing of fabric reinforced Oxide/Oxide components via resin transfer moulding. In *Proceedings of the 28th International Cocoa Beach Conference on Advanced Ceramics and Composites*, Cocoa Beach, FL.
- Heiser, W. and D. Pratt (1994). *Hypersonic Airbreathing Propulsion*. American Institute of Aeronautics and Astronautics, Inc.
- Herbertz, A. (2003). Numerische Leistungsanalyse von Triebwerksauslegungen mit transpirativ gekühlter keramischer Raketenbrennkammer. In *Proceedings of the DGLR Deutscher Luft- und Raumfahrtkongress*, Munich, Germany. DGLR.
- Heufer, K. and H. Olivier (2006). Film cooling of an inclined flat plate in hypersonic flow. In *Proceedings of the 14th AIAA/AHI Space Planes and Hypersonic Systems and Technologies Conference*, Canberra, Australia. AIAA 2006-8067.
- Hirschel, E. (1993). The hypersonics technology development and verification strategy of the german hypersonics technology programme. In *Proceedings of*

BIBLIOGRAPHY

- the AIAA/DGLR 5th International Aerospace Planes and Hypersonics Technologies Conference*, Munich, Germany. AIAA 1993-5072.
- Innocentini, M., A. Pardo, and V. Pandolfelli (2000). Modified pressure-decay technique for evaluating the permeability of highly dense refractories. *Journal of the American Ceramic Society* 83(1), 220–222.
- Innocentini, M., A. Pardo, V. Salvini, and V. Pandolfelli (1999). How accurate is Darcy's law for refractories. *The American Ceramic Society Bulletin* 78, 64–68.
- Innocentini, M., V. Salvini, V. Pandolfelli, and J. Coury (1999). The permeability of ceramic foams. *The American Ceramic Society Bulletin* 78, 78–84.
- Juhany, K. and M. Hunt (1994). Flowfield measurements in supersonic film cooling including the effect of shock-wave interaction. *AIAA Journal* 32(3), 578–585.
- Kahrs, J. and A. Corbett (1967). Propellant injection through porous media. In *Proceedings of the AIAA 3rd Propulsion Joint Specialist Conference*, Washington D.C. AIAA 67-463.
- Kays, W., M. Crawford, and B. Weigand (2005). *Convective Heat and Mass Transfer* (4th ed.). McGraw-Hill.
- Kelly, H. and M. Blosser (1994). Active cooling from the sixties to NASP. Technical Report NASA-TM-109079, NASA, Langley Research Center, Hampton, VA.
- Kirchhartz, R., D. Mee, and R. Stalker (2008). Skin friction drag with boundary layer combustion in a circular combustor. In *15th AIAA International Space Planes and Hypersonic Systems and Technologies Conference*, Dayton, OH. AIAA 2008-2589.
- Kline, S. and F. McClintock (1953). Describing the uncertainties in single sample experiments. *Mechanical Engineering* 1, 3–8.
- Konopka, M., M. Meinke, and W. Schröder (2010). Large-eddy simulation of supersonic film cooling. In *Proceedings of the 46th AIAA/ASME/SAE/ASEE Joint Propulsion Conference & Exhibit*, Nashville, TN. AIAA 2010-6792.
- Krenkel, W. (2000). Entwicklung eines kostengünstigen Verfahrens zur Herstellung von Bauteilen aus keramischen Verbundwerkstoffen. Technical report, German Aerospace Center (DLR), Stuttgart, Germany.
- Krenkel, W. and F. Berndt (2005). C/C-SiC composites for space applications and advanced friction systems. *Materials Science and Engineering A* 412, 177–181.
- Laganelli, A. (1970). A comparison between film cooling and transpiration cooling system in high speed flow. In *Proceedings of the AIAA 8th Aerospace Sciences Meeting*, New York, NY. AIAA 1970-153.
- Lagarias, J., J. Reeds, M. Wright, and P. Wright (1998). Convergence properties of the Nelder-Mead simplex method in low dimensions. *SIAM Journal of Optimization* 9(1), 112–147.

- Langener, T., J. von Wolfersdorf, T. Laux, and J. Steelant (2008). Experimental investigation of transpiration cooling with subsonic and supersonic flows at moderate temperature levels. In *Proceedings of the 44th AIAA/ASME/SAE/ASEE Joint Propulsion Conference & Exhibit*, Hartford, CT. AIAA 2008-5174.
- L'Ecuyer, M. and R. Colloday (1972). Influence of porous-wall thermal effectiveness on turbulent-boundary-layer heat transfer. Technical Report TN D-6837, NASA, Lewis Research Center, Cleveland, OH.
- Lemmon, E., M. Huber, and M. McLinden (2007). *REFPROP - Reference Fluid Thermodynamic and Transport Properties*. NIST Standard Reference Database 23, Version 8.0.
- Lezu, M. (1998). *Wärmetransport in H₂-transpirativ gekühlten Brennkammerkomponenten*. Ph. D. thesis, RWTH Aachen.
- Ligrani, P. and P. Bradshaw (1987). Subminiature hot-wire sensors: Development and use. *Journal of Physics E: Scientific Instruments* 20, 323–332.
- Ligrani, P., M. Oliveira, and T. Blaskovich (2003). Comparison of heat transfer augmentation techniques. *AIAA Journal* 41(3), 337–362.
- Martiny, M., R. Schiele, M. Gritsch, A. Schulz, and S. Wittig (1996). In situ calibration for quantitative infrared thermography. In *Proceedings of the Eurotherm Seminar No. 50*, Stuttgart, Germany.
- Matsuo, K., Y. Miyazato, and H. Kim (1999). Shock train in pseudo-shock phenomena in internal gas flows. *Progress in Aerospace Science* 35, 33–100.
- Mayer, W. (2000). TEKAN - research on cryogenic rocket engines at DLR Lampoldshausen. In *Proceedings of the 36th AIAA/ASME/ASEE Joint Propulsion Conference and Exhibit*, Huntsville, AL. AIAA 2000-3219k.
- McClinton, C., V. Rausch, L. Nguyen, and J. Sitz (2005). Preliminary X-43 flight test results. *Acta Astronautica* 57, 266–276.
- Meinert, J., J. Huhn, E. Serbest, and O. Haidn (2001). Turbulent boundary layers with foreign gas transpiration. *Journal of Spacecrafts and Rockets* 38, 191–198.
- Merker, G. and C. Eiglmeier (1999). *Fluid- und Wärmetransport; Wärmeübertragung*. B.G. Teubner.
- Mickley, H., R. Ross, A. Squyers, and W. Stewart (1954). Heat, mass, and momentum transfer for flow over a flat plate with blowing or suction. Technical Report TN 3208, NACA, Massachusetts Institute of Technology, Cambridge, MA.
- Mickley, H. S. and R. S. Davis (1957). Momentum transfer for flow over a flat plate with blowing. Technical Report TN 4017, NACA, Massachusetts Institute of Technology, Cambridge, MA.
- Moffat, R. (1988). Describing the uncertainties in experimental results. *Experimental Thermal and Fluid Science* 1(1), 3–17.

BIBLIOGRAPHY

- Moffat, R. and W. Kays (1968). The turbulent boundary layer on a porous plate: Experimental heat transfer with uniform blowing and suction. *International Journal of Heat and Mass Transfer* 11, 1547–1566.
- Moreira, E., M. Innocentini, and J. Coury (2004). Permeability of ceramic foams to compressible and incompressible flow. *Journal of the European Ceramic Society* 24, 3209–3218.
- Nelder, J. and R. Mead (1965). A simplex method for function minimization. *Computer Journal* 7(4), 308–313.
- Nield, D. and A. Bejan (2006). *Convection in Porous Media* (3rd ed.). Springer, Berlin.
- Novelli, P. and W. Koschel (2001). Progress of the JAPHAR cooperation between ONERA and DLR on hypersonic airbreathing propulsion. In *Proceedings of the AIAA/NAL/NASDA/ISAS - 10th International Space Planes and Hypersonic Systems and Technologies Conference*, Kyoto, Japan. AIAA 2001-1870.
- Ohlhorst, C., D. Glass, W. Bruce, M. Lindell, W. Vaughn, R. Smith, R. Dirling, P. Hogenson, J. Nichols, N. Risner, D. Thompson, W. Kowbel, B. Sullivan, and J. Koenig (2005). Development of X-43A Mach 10 leading edges. In *Proceedings of the 56th International Astronautical Congress*, Fukuoka, Japan. IAS.
- Pannert, W., R. Winkler, and M. Merkel (2009). On the acoustical properties of metallic hollow sphere structures (MHSS). *Material Letters* 63, 1121–1124.
- Peebles, C. and N. Allen (2008). *Road to Mach 10 - Lessons Learned from the X-43A Flight Research Program*. AIAA.
- Plotkin, K., E. Haering, J. Murray, D. Maglieri, J. Salamone, B. Sullivan, and D. Schein (2005). Ground data collection of shaped sonic boom experiment aircraft pressure signatures. In *Proceedings of the 43rd AIAA Aerospace Sciences Meeting and Exhibit*, Reno, NV. AIAA 2005-0010.
- Polezhaev, Y. (2000). Will there or will there not be a hypersonic airplane. *Journal of Engineering Physics and Thermophysics* 73(1), 3–8.
- Rannie, W. (1947). A simplified theory of porous wall cooling. Technical report, Jet Propulsion Laboratory, Pasadena, CA.
- Rubesin, M. (1954). An analytical estimation of the effect of transpiration cooling on the heat-transfer and skin-friction characteristics of a compressible, turbulent boundary layer. Technical Report TN 3341, NACA, Ames Aeronautical Laboratory, Moffett Field, CA.
- Scheuermann, T. (2010). *Untersuchungen zur Verbrennung in einer SCRamjet-Brennkammer*. Ph. D. thesis, Universität Stuttgart.
- Scheuermann, T., J. Chun, and J. von Wolfersdorf (2008). Experimental investigation of scramjet combustor characteristics. In *15th AIAA International Space*

- Planes and Hypersonic Systems and Technologies Conference*, Dayton, OH. AIAA 2008-2552.
- Schlichting, H. and K. Gersten (2000). *Boundary Layer Theory* (8th ed.). Berlin: Springer.
- Schneider, S. (2004). Hypersonic laminar-turbulent transition on circular cones and scramjet forebodies. *Progress in Aerospace Sciences* 40, 1–50.
- Schulz, A. (2000). Infrared thermography as applied to film cooling of gas turbine components. *Measurement Science and Technology* 11, 948–956.
- Selzer, M., T. Langener, H. Hald, and J. von Wolfersdorf (2009). Production and characterization of porous C/C material. *Sonderforschungsbereich/Transregio 40, Annual Report 1*, 75–85.
- Serbest, E. (2002). *Untersuchungen zur Anwendung der Effusionskühlung bei Raketenbrennkammern*. Ph. D. thesis, RWTH Aachen, Germany.
- Serbest, E., O. Haidn, H. Hald, G. Korger, and P. Winkelmann (1999). Effusion cooling in rocket combustors applying fiber reinforced ceramics. In *Proceedings of the 35th AIAA/ASME/SAE/ASEE Joint Propulsion Conference and Exhibit*, Los Angeles, CA. AIAA 1999-2911.
- Serre, L. and S. Defoort (2009). LAPCAT II: towards a Mach 8 civil aircraft concept, using advanced rocket/dual-mode ramjet propulsion system. In *Proceedings of the 16th AIAA/DLR/DGLR International Space Planes and Hypersonic Systems and Technologies Conference*, Bremen, Germany. AIAA 2009-7328.
- Siegel, R. and J. Howell (2002). *Thermal Radiation Heat Transfer*. Francis & Taylor.
- Simpson, R., R. Moffat, and W. Kays (1969). The turbulent boundary layer on a porous plate: Experimental skin friction with variable injection and suction. *International Journal of Heat and Mass Transfer* 12(7), 771–789.
- Song, K., S. Choi, and S. Scotti (2006). Transpiration cooling experiment for scramjet engine combustion chamber by high heat fluxes. *Journal of Propulsion and Power* 22(1), 96–102.
- Stalker, R. (2005). Control of hypersonic turbulent skin friction by boundary-layer combustion of hydrogen. *Journal of Spacecrafts and Rockets* 42(4), 577–587.
- Steelant, J. (2008a). Achievements obtained for sustained hypersonic flight within the LAPCAT project. In *Proceedings of the 15th AIAA/DLR/DGLR International Space Planes and Hypersonic Systems and Technologies Conference*, Dayton, OH. AIAA 2008-2578.
- Steelant, J. (2008b). ATLLAS: Aero-thermal loaded material investigations for high-speed vehicles. In *Proceedings of the 15th AIAA/DLR/DGLR International Space Planes and Hypersonic Systems and Technologies Conference*, Dayton, OH. AIAA 2008-2582.

BIBLIOGRAPHY

- Steelant, J. (2009a). Achievements obtained on aero-thermal loaded materials for high-speed atmospheric vehicles within ATLLAS. In *Proceedings of the 16th AIAA/DLR/DGLR International Space Planes and Hypersonic Systems and Technologies Conference*, Bremen, Germany. AIAA 2009-7225.
- Steelant, J. (2009b). Sustained hypersonic flight in Europe: Technology drivers for LAPCAT II. In *Proceedings of the 16th AIAA/DLR/DGLR International Space Planes and Hypersonic Systems and Technologies Conference*, Bremen, Germany. AIAA 2009-7240.
- Valdevit, L., N. Vermaak, K. Hsu, F. W. Zok, and A. Evans (2006). Design of actively cooled panels for scramjets. In *Proceedings of the 14th AIAA/AHI Space Planes and Hypersonic Systems and Technologies Conference*, Canberra, Australia. AIAA 2006-8069.
- Vellaramkalayil, J., T. Scheuermann, and J. von Wolfersdorf (2009). Numerical and experimental investigation of a two-staged supersonic combustion chamber. In *Proceedings of the 16th AIAA/DLR/DGLR International Space Planes and Hypersonic Systems and Technologies Conference*, Bremen, Germany. AIAA 2009-7363.
- Vellaramkalayil, J., T. Scheuermann, S. Winkler, J. von Wolfersdorf, and M. Banica (2010). Experimental and numerical study of a supersonic combustion chamber with different two-staged injection concepts. In *Proceedings of the 46th AIAA/ASME/SAE/ASEE Joint Propulsion Conference & Exhibit*, Nashville, TN. AIAA 2010-6647.
- Voland, R., L. Huebner, and C. McClinton (2006). X-43A hypersonic vehicle technology development. *Acta Astronautica* 59, 181–191.
- von Wolfersdorf, J. (2005). Effect of coolant side heat transfer on transpiration cooling. *Heat Mass Transfer* 41, 327–337.
- Walker, J. and J. Weil (1963). The X-15 program. In *Proceedings of the 2nd Manned Space Flight Meeting*, Dallas, TX. AIAA 1963-1440.
- Wang, J., M. Gan, and J. Shi (2007). Detection and characterization of penetrating pores in porous materials. *Materials Characterization* 58, 8–12.
- Weigand, B. and U. Gaisbauer (2009). An overview on the structure and work of the DFG research training group GRK 1095: Aero-Thermodynamic Design of a SCRamjet Propulsion System. In *Proceedings of the 16th AIAA/DLR/DGLR International Space Planes and Hypersonic Systems and Technologies Conference*, Bremen, Germany. AIAA 2009-7276.
- Weigand, B., K. Semmler, and J. von Wolfersdorf (2001). Heat transfer technology for internal passages of air-cooled blades for heavy duty gas turbines. *Annals of the New York Academy of Sciences* 934, 179–193.
- Weih, H., J. Longo, and J. Turner (2008). The sharp edge flight experiment SHEFEX II, a mission overview and status. In *Proceedings of the 15th AIAA/DLR/DGLR In-*

- ternational Space Planes and Hypersonic Systems and Technologies Conference*, Dayton, OH. AIAA 2008-2542.
- Weingartner, S. (1993). SÄNGER-The reference concept of the german hypersonics technology program. In *Proceedings of the AIAA/DGLR 5th International Aerospace Planes and Hypersonics Technologies Conference*, Munich, Germany. AIAA 1993-5161.
- Wharton, J., J. Ellzey, and D. Bogard (2005). An experimental study of turbulence intensities and non-uniformities in the exit flow from a porous combustor. *Experiments in Fluids* 38, 701–707.
- Willink, R. (2006). On using the Monte Carlo method to calculate uncertainty intervals. *Metrologia* 43, L39–L42.
- Woodruff, L. and G. Lorenz (1966). Hypersonic turbulent transpiration cooling including downstream effects. *AIAA Journal* 4(7), 969–975.
- Woschnak, A. and M. Oswald (2001). Thermo- and fluidmechanical analysis of high aspect ratio cooling channels. In *Proceedings of the 37th AIAA/ASME/SAE/ASEE/ Joint Propulsion Conference and Exhibit*, Salt Lake City, UT. AIAA 2001-3404.

Uncertainty Analysis

For the reliability of the presented results it is indispensable to give an accurate estimate of the uncertainty margin for each test parameter and for the resulting quantities. For testing in aerospace engineering it is often impossible to repeat an experiment in a statistically sufficient frequency, so that the uncertainty could be given based upon the double standard deviation (2σ) of the obtained results. This corresponds to a confidence interval of 95.5 % of the presented data. For single sample experiments Kline and McClintock (1953) and Moffat (1988) presented a methodology where based upon the accuracy of the measurement equipment, the uncertainty for the computed experimental parameters can be estimated, even though only one single test has been carried out. The results will also suffice the confidence interval of 95.5 % because the accuracy of the equipment has to be given in 2σ . For this, the Gaussian root sum square (RSS) method is used.

$$(\delta R)^2 = \sum_{i=1}^N \left(\frac{\partial R}{\partial x_i} \right)^2 \delta x_i^2 \quad (\text{A.1})$$

Here, x_i displays the measurand with its uncertainty δx_i , which has to be given in 2σ . R is the variable which is a function of x_i . In Table A.1 the accuracies of the relevant measurands in the transpiration cooling experiments are given. For the wall temperature measured by thermocouple an accuracy of 1.1...1.9 K based upon the actual reading is given by the manufacturer. The coolant mass-flow controller was calibrated in the factory which leads to a uncertainty of 0.048 g/s in the reading which is lower than given in the specifications. By calibrating devices against more accurate sensors, the accuracy in these measurands can be improved.

Now, with knowing the accuracy of each measured quantity the uncertainty in the variable can be computed using the RSS method from Eqn. A.1. The blowing ratio consists out of many different variables:

$$F = \frac{\dot{m}_c R T_g A_g}{\dot{V}_g p_g A_c} \quad (\text{A.2})$$

hence

A Uncertainty Analysis

	Symbol	Measurement Range	Accuracy δx_i
sample thermocouples	T_w	300...700 K	1.1...1.9 K
coolant mass-flow rate	\dot{m}_c	0...7 g/s	0.048 g/s
main-stream volume-flow rate	\dot{V}_g	0...0.55 m ³ /s	0.001...0.0055 m ³ /s
main-stream supply pressure	p_g	0...4 bar	0.08 bar
main-stream supply temperature	T_g	280...400 K	1.1 K
hot-gas total pressure	$p_{t,g}$	0...3 bar	0.05 bar
hot-gas total temperature	$T_{t,g}$	420...1060 K	1.1 K...3.9 K
coolant inlet temperature	$T_{c,in}$	280...400 K	1.1 K
typical length	B, H, L	5...90 mm	0.1 mm
ambient pressure	p_{amb}	0...2 bar	0.001 bar
static chamber pressure	p_s	0...2 bar	0.001 bar
coolant pressure	p_c	0...250 bar	0.05 bar

Table A.1: Overview of the most important error sources in the measurement equipment

$$\begin{aligned} \left(\frac{\delta F}{F}\right)^2 &= \left(\frac{\delta \dot{m}_c}{\dot{m}_c}\right)^2 + \left(\frac{\delta \dot{V}_g}{\dot{V}_g}\right)^2 + \left(\frac{\delta p_g}{p_g}\right)^2 + \left(\frac{\delta T_g}{T_g}\right)^2 + \\ &\quad \left(\frac{\delta B_g}{B_g}\right)^2 + \left(\frac{\delta H_g}{H_g}\right)^2 + \left(\frac{\delta B_c}{B_c}\right)^2 + \left(\frac{\delta H_c}{H_c}\right)^2 \end{aligned} \quad (\text{A.3})$$

The cooling efficiency Θ , as explained in Chapter 5 is calculated from three values, the temperature at no blowing $T_{w,0}$, the wall temperature for the current blowing case T_w and the coolant temperature T_c .

$$\Theta = \frac{T_{w,0} - T_w}{T_{w,0} - T_c} \quad (\text{A.4})$$

The equation to calculate the associated uncertainty is given in Eqn. A.5 and the theoretical values range from 1 % up to 15 %.

$$\left(\frac{\delta \Theta}{\Theta}\right)^2 = \frac{1}{(T_{w,0} - T_w)^2 (T_{w,0} - T_c)^2} \left[(T_w - T_c)^2 \delta T_{w,=0}^2 + \right. \quad (\text{A.5})$$

$$\left. (T_c - T_{w,=0})^2 \delta T_w^2 + (T_{w,0} - T_w)^2 \delta T_c^2 \right] \quad (\text{A.6})$$

Since the wall temperatures used in the equation for the cooling efficiency Θ are being averaged from four thermocouple values one also has to consider the effect of averaging on the value given for Θ besides the uncertainties originating from the measurement equipment. Since for four thermocouple it is not possible to conduct a statistical analysis (not enough sample positions to be normal distributed), we have to compare the cooling efficiency computed for every thermocouple to the average

cooling efficiency calculated from an average wall temperature. The difference here will be our uncertainty in Θ for a certain blowing ratio.

$$\Theta_i = \frac{T_{w,(F=0),i} - T_{w,i}}{T_{w,(F=0),i} - T_c}, \text{ for } i = 1 \dots 4 \quad (\text{A.7})$$

whilst i is the number of the thermocouple. With $\bar{\Theta}$ being the cooling efficiency computed with the average of all thermocouples, the uncertainty in Θ is defined as:

$$\frac{\delta\Theta}{\Theta} = \max \left\{ \frac{\Theta_i - \bar{\Theta}}{\bar{\Theta}} \right\} \quad (\text{A.8})$$

If a sample's surface is being cooled homogeneously, i.e. the thermocouple readings are relatively close to each other, the uncertainty will be low. For samples with varying surface temperature the thermocouples will physically read different temperatures. This method has been applied for the results of every single test run.

The Mach number in the supersonic channel can be determined via the isentropic relationship.

$$\frac{p_{t,g}}{p_{s,g}} = \left(1 + \frac{\gamma - 1}{2} M_g^2 \right)^{\frac{\gamma}{\gamma - 1}} \Leftrightarrow M_g = \sqrt{\frac{2}{\gamma - 1} \left(\frac{p_{t,g}}{p_{s,g}} \right)^{\frac{\gamma - 1}{\gamma}}} \quad (\text{A.9})$$

Using the differentiation technique from the RSS method, this yields to following formula for the uncertainty of the Mach number:

$$\left(\frac{\delta M_g}{M_g} \right)^2 = \left(\frac{\kappa - 1}{4\kappa} \right)^2 \left(\frac{1}{p_{t,g}} \right)^2 \left[\delta p_{t,g}^2 + \frac{p_{t,g}^2}{p_{s,g}^2} \delta p_{s,g}^2 \right] \quad (\text{A.10})$$

For the uncooled channel the flow is not isentropic between the position where the hot-gas plenum is situated and the sample location. Therefore the Mach number has to be determined using the measured hot-gas mass-flow rate, the hot-gas total temperature and the static pressure at the sample location.

$$M_g = \sqrt{\sqrt{\frac{1}{\gamma - 1} + \frac{2}{\gamma - 1} C} - \frac{1}{\gamma - 1}} \quad (\text{A.11})$$

with $C = \frac{\dot{m}_g^2 R T_{t,g}}{p_{s,g}^2 A_g^2 \gamma} = \frac{\dot{V}_g^2 p_g T_{t,g}}{R T_g p_{s,g}^2 B_g^2 H_g^2 \gamma}$

The uncertainty in the hot-gas Mach number for the subsonic experiments can be determined to:

$$\left(\frac{\delta M_g}{M_g} \right)^2 = \frac{\sqrt{10}}{\left(2\sqrt{\sqrt{5(4C + 5)}}\sqrt{4C + 5} \right)^2} \delta C^2 \quad (\text{A.12})$$

with the uncertainty in the test parameter C :

$$\begin{aligned} \left(\frac{\delta C}{C}\right)^2 &= \left(2\frac{\delta \dot{V}_g}{\dot{V}_g}\right)^2 + \left(2\frac{\delta p_g}{p_g}\right)^2 + \left(2\frac{\delta T_g}{T_g}\right)^2 + \\ &\quad \left(2\frac{\delta p_{s,g}}{p_{s,g}}\right)^2 + \left(\frac{\delta T_{t,g}}{T_{t,g}}\right)^2 + \left(2\frac{\delta B_g}{B_g}\right)^2 + \left(2\frac{\delta H_g}{H_g}\right)^2 \end{aligned} \quad (\text{A.13})$$

The through-flow velocity through the porous material is being defined at the inlet of the wall as described in Section 2.5 (Eqn. 2.49). Its uncertainty can be estimated using following equation:

$$\left(\frac{\delta v_{in}}{v_{in}}\right)^2 = \left(\frac{\delta \dot{m}_c}{\dot{m}_c}\right)^2 + \left(\frac{\delta p_c}{p_c}\right)^2 + \left(\frac{\delta T_c}{T_c}\right)^2 + \left(\frac{\delta B_c}{B_c}\right)^2 + \left(\frac{\delta H_c}{H_c}\right)^2 \quad (\text{A.14})$$

To determine the permeability coefficients in the through-flow test or in the hot-gas experiment, the parameter $\rho_{c,in}v_{in}^2$ is used and its uncertainty is computed as:

$$\left(\frac{\delta \rho_{in}v_{in}^2}{\rho_{in}v_{in}^2}\right)^2 = \left(2\frac{\delta \dot{m}_c}{\dot{m}_c}\right)^2 + \left(\frac{\delta p_c}{p_c}\right)^2 + \left(\frac{\delta T_c}{T_c}\right)^2 + \left(2\frac{\delta B_c}{B_c}\right)^2 + \left(2\frac{\delta H_c}{H_c}\right)^2 \quad (\text{A.15})$$

The normalized pressure-drop per unit length as used in the Darcy-Forchheimer equation $\Delta p/L$ (Eqn. 2.48) is also used during the above mentioned routine. Its uncertainty is given as follows:

$$\begin{aligned} \left(\frac{\delta(\Delta p/L)}{(\Delta p/L)}\right)^2 &= \frac{1}{4p_{in}^2 L^2 (p_{in}^2 - p_{ex}^2)^2} \left[(2p_{in}^2 L + 2p_{ex}^2 L)^2 \delta p_{in}^2 + \right. \\ &\quad \left. (4p_{in}p_{ex}L)^2 \delta p_{ex}^2 + (2p_{in}(p_{in}^2 - p_{ex}^2))^2 \delta L^2 \right] \end{aligned} \quad (\text{A.16})$$

The maximum and minimum values of the uncertainty in the experimental parameters experienced during the test data analysis are summarized in Table A.2 through Table A.4. When the results are presented in the following chapters, typically the uncertainty will be displayed in the according plot. In the supersonic channel, the Mach number can be calculated very accurately, because the pressure sensors offer good accuracy. Since the blowing ratio F is computed from several quantities δF can be as high as 16 %. The uncertainty in the cooling efficiency Θ can reach up to 17 % whilst for these values Eqn. A.8 was used. For most of the results this value was between 4 % and 10 %.

The parameters for the through-flow analysis such as the determination of the permeability coefficients exhibit similar uncertainty values as the blowing ratio, because they are computed using almost the same measurands. Again, the pressure can be determined quite accurately.

For the uncooled subsonic channel experiments the value differ slightly from what has been displayed in Table A.2, especially for M_g . The uncertainty in the blowing

Name	Symbol x_i	Uncertainty $\delta x_i/x_i$
Blowing ratio	F	ca. 2 %- 16 %
Cooling efficiency	Θ	ca. 1 %- 17 %
Hot-gas Mach number	M_g	ca. 0.5 %

Table A.2: Estimated uncertainties in supersonic tests

Name	Symbol x_i	Uncertainty $\delta x_i/x_i$
Normalized Pressure Drop	$\Delta p/L$	ca. 1.0 %- 6.0 %
Through-Flow velocity	v_{in}	ca. 0.8 %- 10.8 %
Curve-Fit Parameter	$\rho_{in} v_{in}^2$	ca. 1.3 %- 19.9 %

Table A.3: Overview of uncertainties in through-flow analysis for air as a test gas

Name	Symbol x_i	Uncertainty $\delta x_i/x_i$
Blowing Ratio	F	ca. 2 %- 24 %
Cooling Efficiency	Θ	ca. 1 %- 10 %
Mach Number	M_g	ca. 1.5 %- 15 %

Table A.4: Estimated uncertainties in experiments using the uncooled, subsonic channel

ratio can be up to 24 % for the lowest values and at the lowest Mach number due to the accuracy of the mass-flow meter and main-flow mass-flow rate determination. Typically though, this value ranges between 6 – 8 %. The lowest hot-gas Mach number of $M_g = 0.3$ can be set with an accuracy of 15 % due to the low main-stream supply pressure and the low volume flow rate of the main-stream. For the higher Mach number this value decreases significantly, so that at $M_g = 0.7$ it is as low as 1.5 %.

B

2D Surface Temperature Maps

B.1 Supersonic Flow Regime

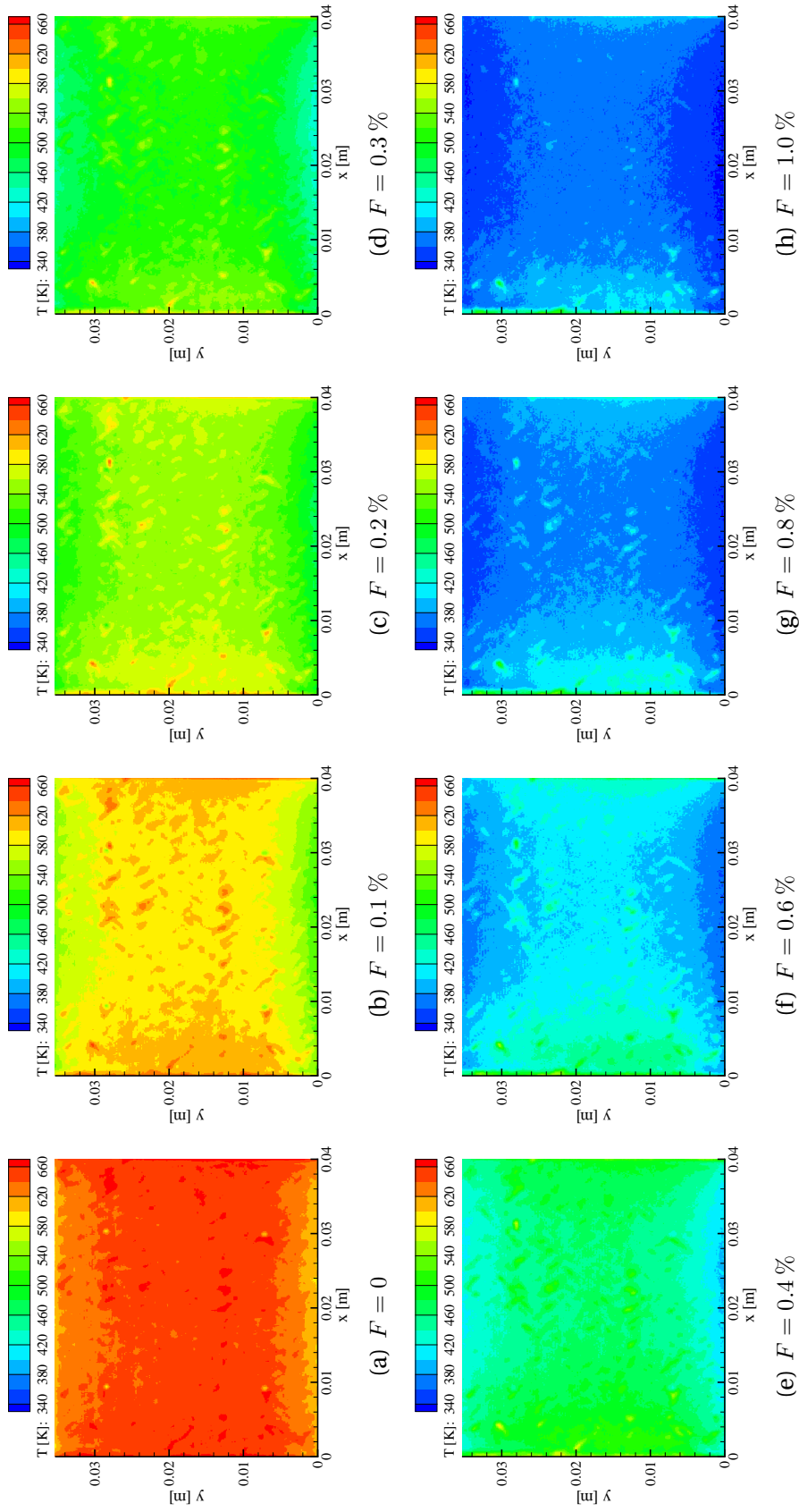


Figure B.1: Surface temperature distributions of the PH1732-1 sample ($L = 10 \text{ mm}$) for different blowing ratios. Air as a coolant. Main-flow conditions: $M_g = 2.1$, $T_{t,g} = 1060 \text{ K}$

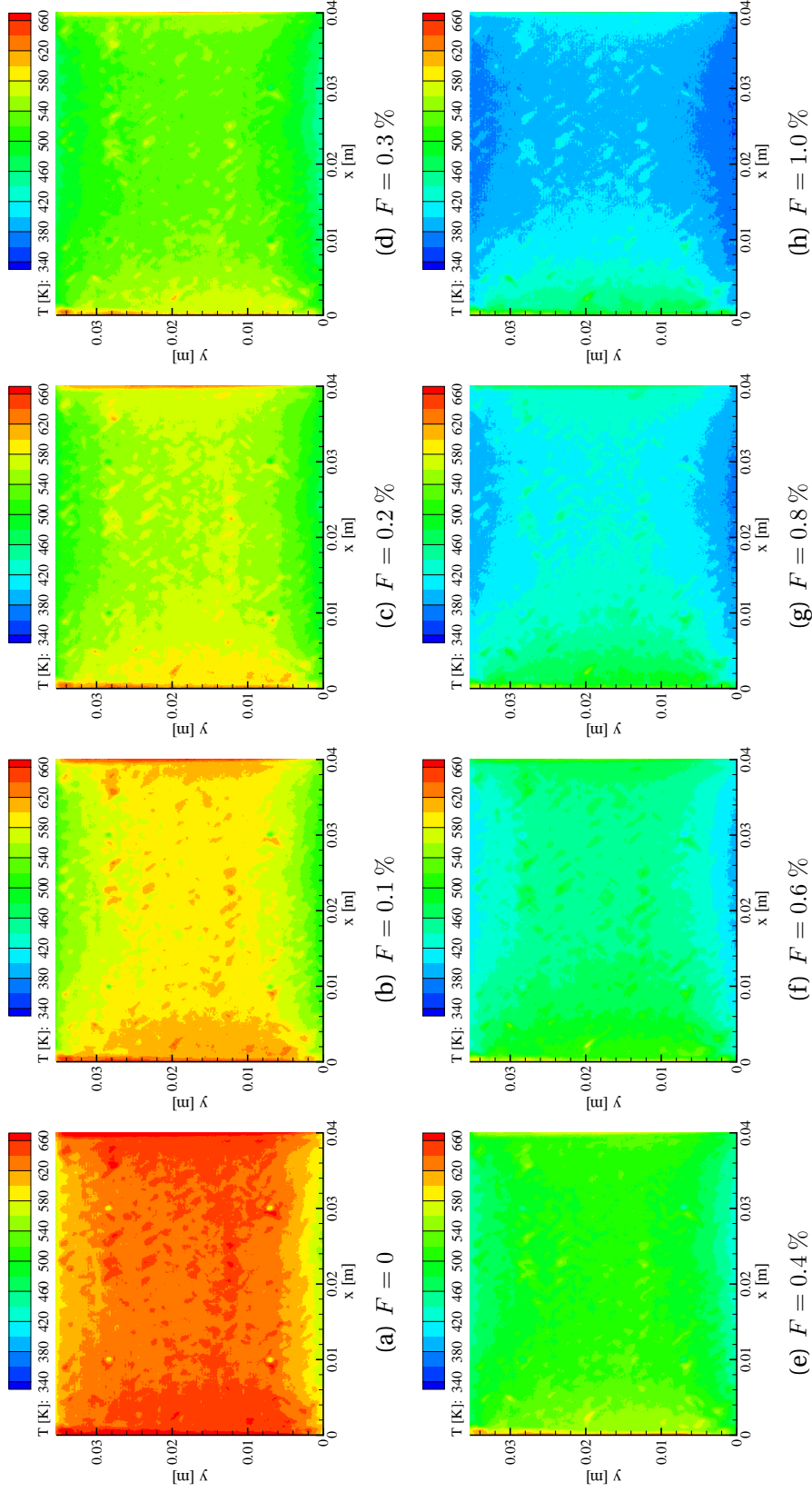


Figure B.2: Surface temperature distributions of the PH1732-1 sample ($L = 10 \text{ mm}$) for different blowing ratios. Argon as a coolant. Main-flow conditions: $M_g = 2.1$, $T_{t,g} = 1039 \text{ K}$

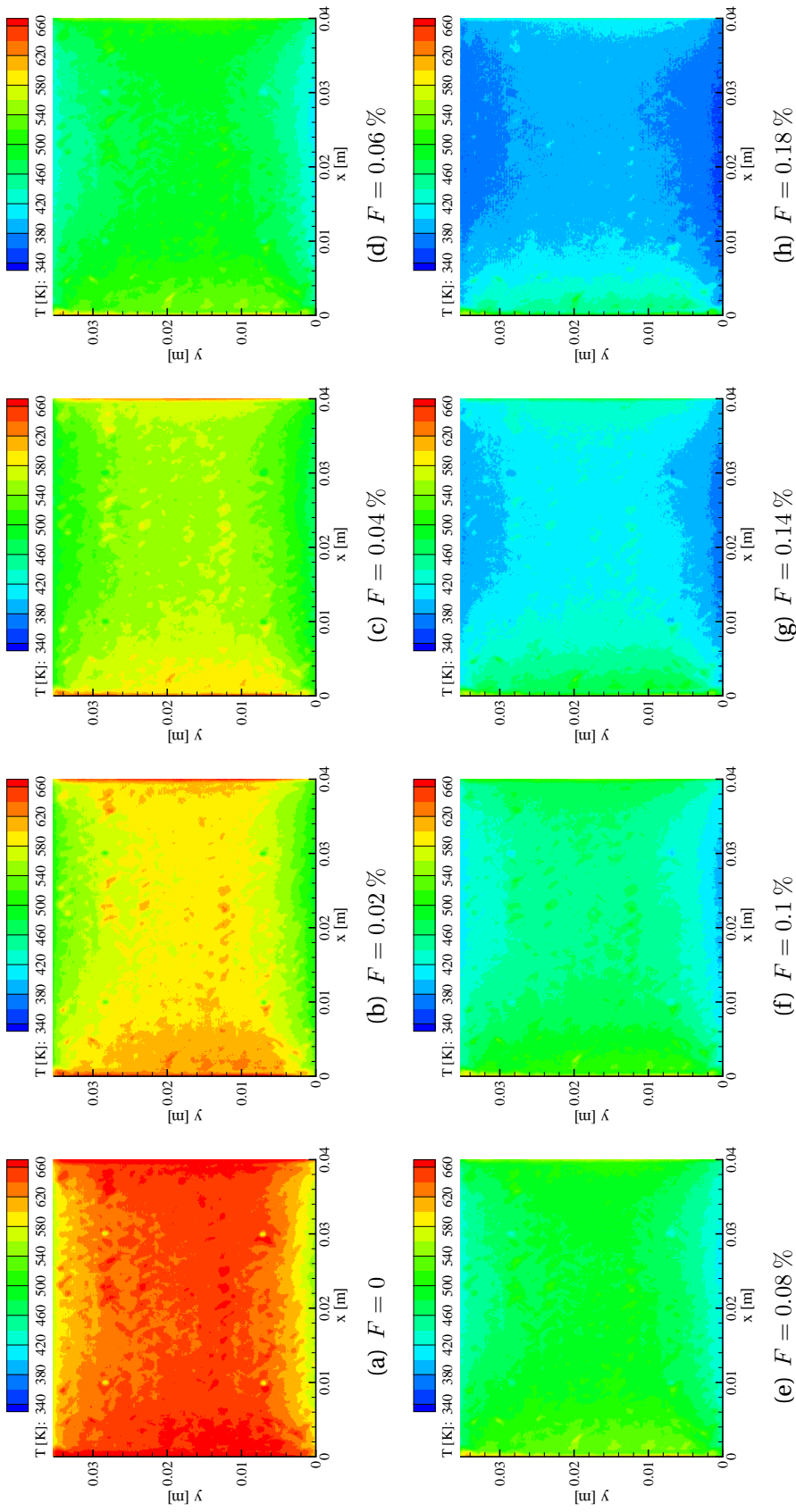


Figure B.3: Surface temperature distributions of the PHI732-1 sample ($L = 10\text{ mm}$) for different blowing ratios. Helium as a coolant. Main-flow conditions: $M_g = 2.1$, $T_{t,g} = 1054\text{ K}$

B.2 Subsonic Flow Regime Using the Uncooled Channel

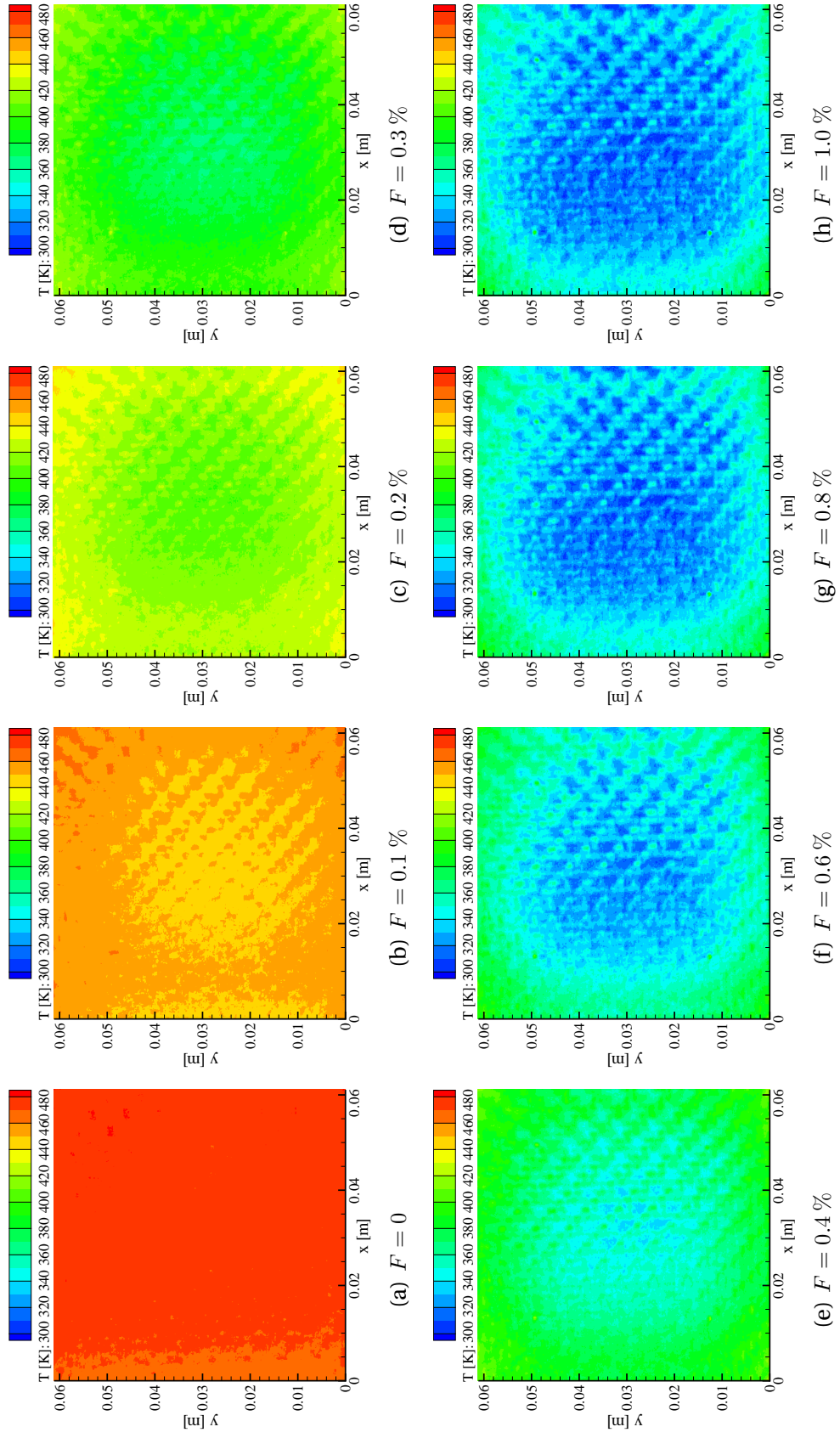


Figure B.4: Surface temperature distributions of the PH1606 sample ($L = 15 \text{ mm}$) for different blowing ratios. Air as a coolant. Main-flow conditions: $M_g = 0.5$, $T_{t,g} = 521 \text{ K}$

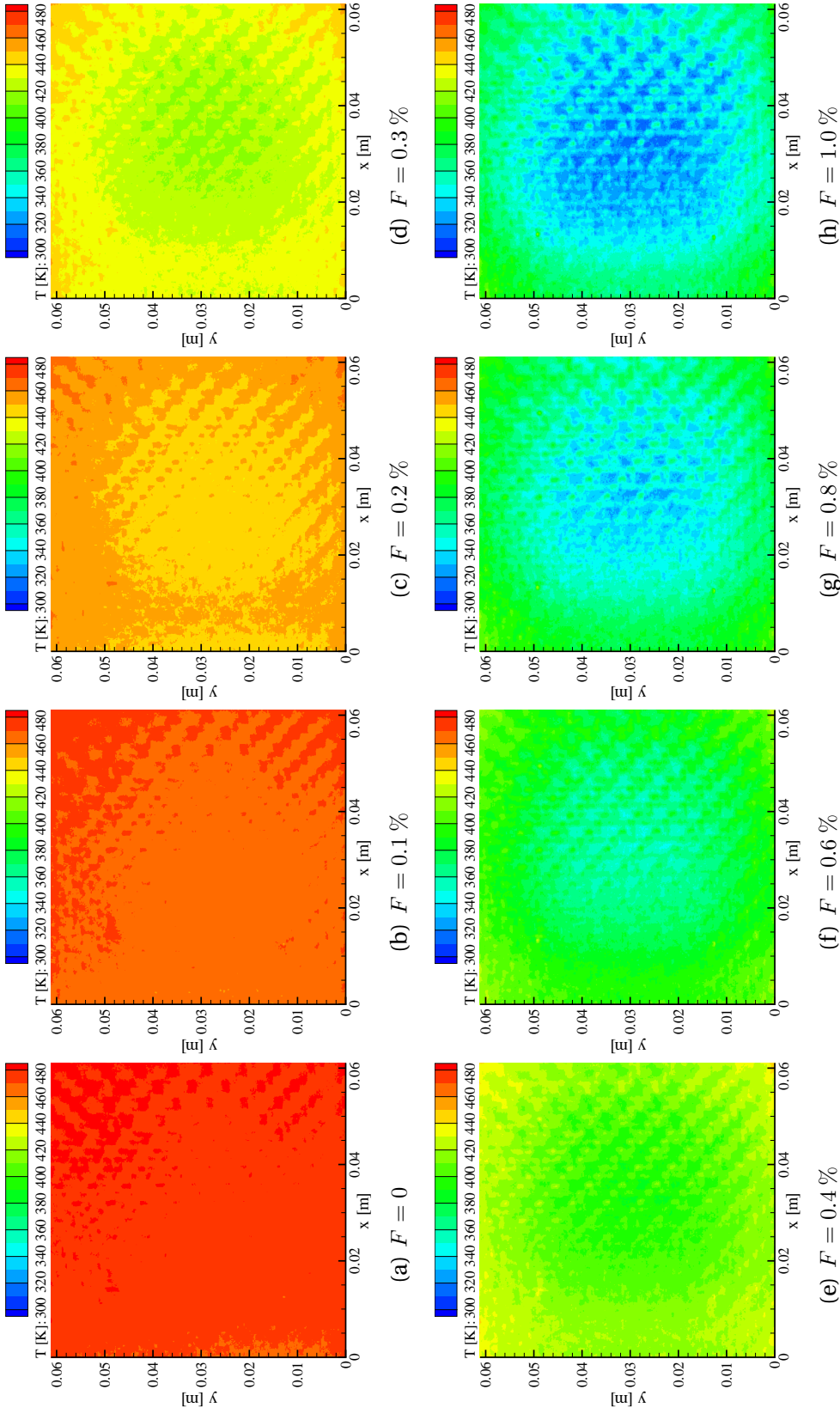


Figure B.5: Surface temperature distributions of the PH1606 sample ($L = 15\text{ mm}$) for different blowing ratios. Argon as a coolant. Main-flow conditions: $M_g = 0.5$, $T_{t,g} = 525\text{ K}$

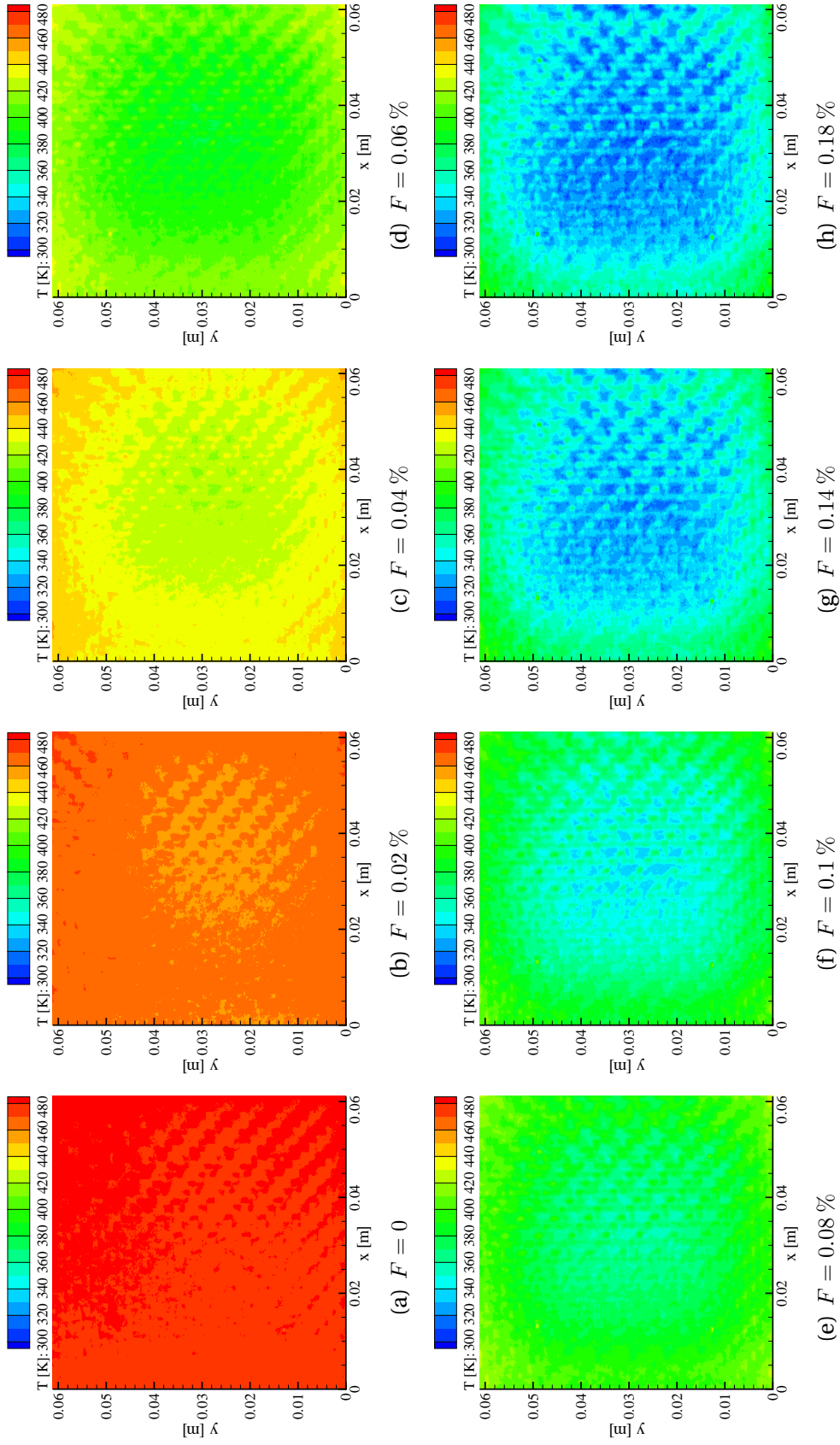


Figure B.6: Surface temperature distributions of the PHI1606 sample ($L = 15\text{ mm}$) for different blowing ratios. Helium as a coolant. Main-flow conditions: $M_g = 0.5$, $T_{t,g} = 525\text{ K}$

Heat Flux Components

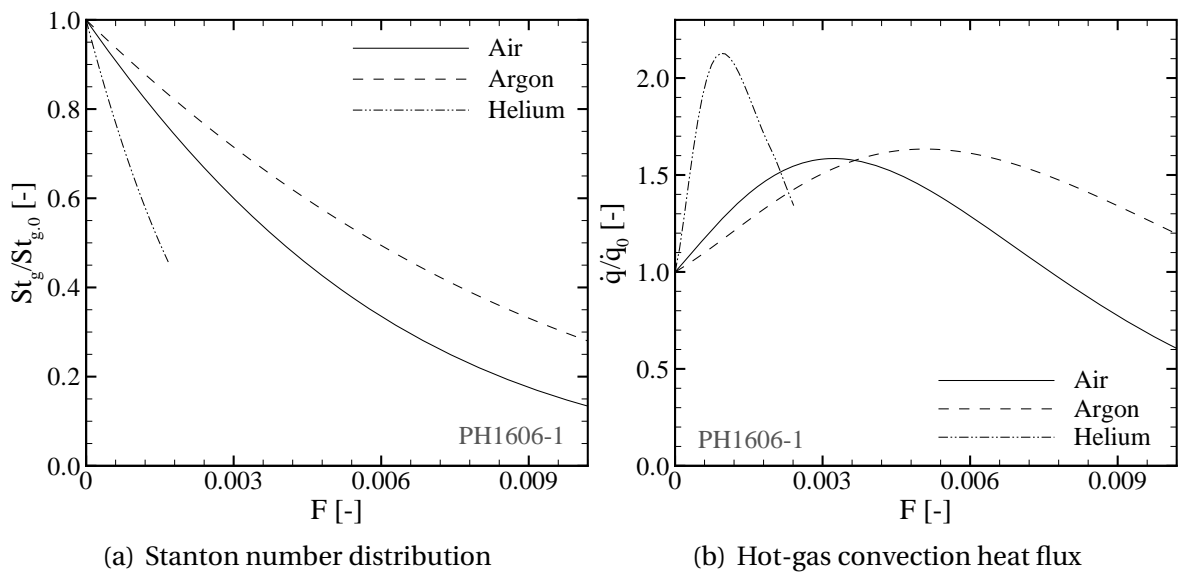


Figure C.1: Normalized convective heat flux from the transpiration cooling model for different coolant gases. $T_{t,g} = 520$ K, PH1606-1 sample

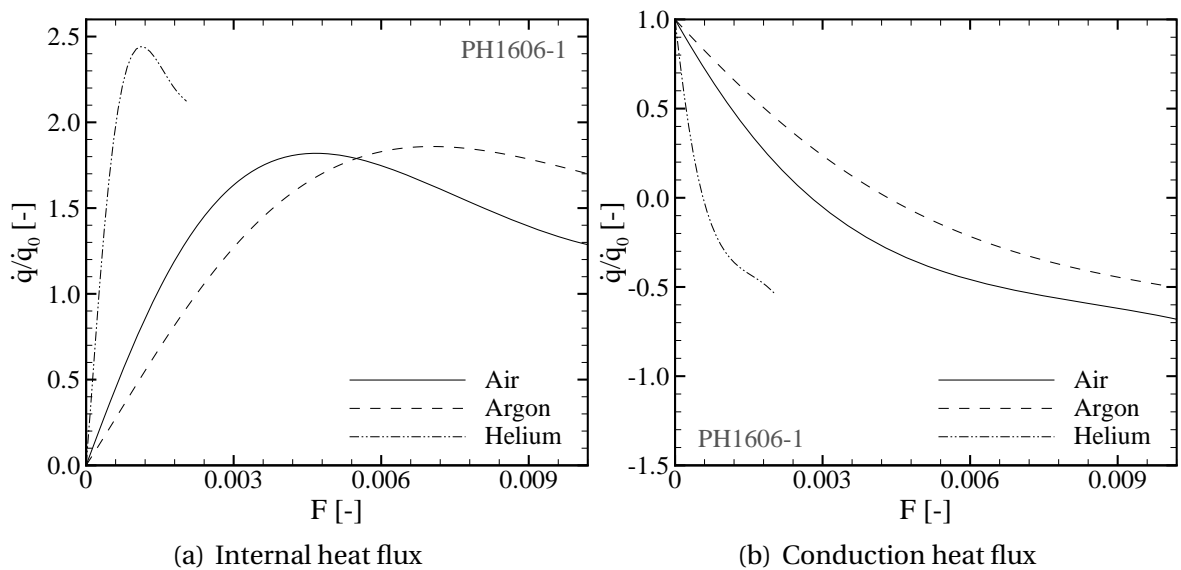


Figure C.2: Normalized conduction and internal heat flux from the transpiration cooling model for different coolant gases. $T_{t,g} = 520$ K, PH1606-1 sample

Combustion Chamber Conditions of Selected Aerospace Application

Name	Symbol	$M_\infty = 7$	$M_\infty = 8$
hot-gas Mach number	$M_g [-]$	1.28	1.81
hot-gas total temperature	$T_{t,g} [K]$	2404	2349
hot-gas static pressure	$p_{s,g} [bar]$	3.43	2.06
combustion chamber air mass-flow rate	$\dot{m}_g [kg/s]$	1889	1627
heat transfer coefficient without blowing	$h_{g,0} [W/(m^2K)]$	1879	1561
specific heat capacity hot-gas	$c_{p,g} [J/(kgK)]$	1388	1317
assumed wall temperature without blowing	$T_{w,0} [K]$	2359	2275
specific heat capacity coolant: hydrogen	$c_{p,c} [J/(kgK)]$	14304	14304
hydrogen supply (coolant) temperature	$T_c [K]$	500	500
stoichiometric mass-flow rate ratio air/H2	$\dot{m}_g/\dot{m}_{H2} [-]$	34.3	34.3
isentropic exponent in combustion chamber	$\kappa [-]$	1.28	1.28
combustion chamber semimajor axis	$W [m]$	1.8	1.8
combustion chamber semiminor axis	$H [m]$	0.6	0.6
combustion chamber length	$L [m]$	4.5	4.5
combustion chamber wall surface area	$A_w [m^2]$	36.08	36.08
combustion chamber cross section area	$A_{CC} [m^2]$	3.39	3.39

Table D.1: Average parameters for exemplary elliptical combustion chamber calculation with hydrogen as a coolant. LAPCAT hypersonic vehicle concept with scramjet propulsion system at two flight Mach numbers

D Combustion Chamber Conditions of Selected Aerospace Application

Name	Symbol	$M_\infty = 6$
hot-gas Mach number	$M_g [-]$	0.3
hot-gas total temperature	$T_{t,g} [K]$	2984
hot-gas static pressure	$p_{s,g} [bar]$	25
combustion chamber air mass-flow rate	$\dot{m}_g [kg/s]$	444.2
heat transfer coefficient without blowing	$h_{g,0} [W/(m^2K)]$	2616
specific heat capacity hot-gas	$c_{p,g} [J/(kgK)]$	3003
specific heat capacity coolant: hydrogen	$c_{p,c} [J/(kgK)]$	14304
hydrogen supply (coolant) temperature	$T_c [K]$	500
stoichiometric mass-flow rate ratio air/H ₂	$\dot{m}_g/\dot{m}_{H_2} [-]$	34.3
isentropic exponent in combustion chamber	$\kappa [-]$	1.17
combustion chamber diameter	$D_{CC} [m]$	0.88
combustion chamber length	$L [m]$	2
combustion chamber wall surface area	$A_w [m^2]$	5.53
combustion chamber cross section area	$A_{CC} [m^2]$	0.61

Table D.2: Assumed average parameters for exemplary circular combustion chamber calculation with hydrogen as a coolant. ATLLAS hypersonic vehicle concept with ramjet propulsion system at $M_\infty = 6$

Name	Symbol	$M_\infty = 8$
hot-gas Mach number	$M_g [-]$	2.58
hot-gas total temperature	$T_{t,g} [K]$	2496
hot-gas static pressure	$p_{s,g} [bar]$	0.6
combustion chamber air mass-flow rate	$\dot{m}_g [kg/s]$	5.3
heat transfer coefficient without blowing	$h_{g,0} [W/(m^2K)]$	574
specific heat capacity hot-gas	$c_{p,g} [J/(kgK)]$	1279
specific heat capacity coolant: hydrogen	$c_{p,c} [J/(kgK)]$	14304
hydrogen supply (coolant) temperature	$T_c [K]$	500
stoichiometric mass-flow rate ratio air/H ₂	$\dot{m}_g/\dot{m}_{H_2} [-]$	34.3
isentropic exponent in combustion chamber	$\kappa [-]$	1.17
combustion chamber height	$H [m]$	0.038 – 0.134
combustion chamber height	$W [m]$	0.66
combustion chamber length	$L [m]$	0.95
combustion chamber wall surface area	$A_w [m^2]$	1.38
combustion chamber inlet cross section area	$A_{CC} [m^2]$	0.025

Table D.3: Averaged parameters between inlet and outlet for rectangular combustion chamber calculation with hydrogen as a coolant. Scramjet demonstrator concept at $M_\infty = 8$. See Fuhrmann (2009)

Name	Symbol	Generic
hot-gas Mach number	$M_g [-]$	2.1
hot-gas total temperature	$T_{t,g} [K]$	2500
hot-gas static pressure	$p_{s,g} [bar]$	1.3
combustion chamber air mass-flow rate	$\dot{m}_g [kg/s]$	0.09 – 9359
heat transfer coefficient without blowing	$h_{g,0} [W/(m^2K)]$	1263
specific heat capacity hot-gas	$c_{p,g} [J/(kgK)]$	1304
specific heat capacity coolant: hydrogen	$c_{p,c} [J/(kgK)]$	14304
maximum wall temperature	$T_{w,max} [K]$	1500
hydrogen supply (coolant) temperature	$T_c [K]$	500
stoichiometric mass-flow rate ratio air/H2	$\dot{m}_g/\dot{m}_{H2} [-]$	34.3
isentropic exponent in combustion chamber	$\kappa [-]$	1.28
combustion chamber height /semiminor axis	$H [m]$	0.006 – 5
combustion chamber height /semimajor axis	$W [m]$	0.05 – 5
combustion chamber length	$L [m]$	2 – 8
combustion chamber wall surface area	$A_w [m^2]$	0.205 – 31.4
combustion chamber inlet cross section area	$A_{CC} [m^2]$	0.00025 – 25

Table D.4: Averaged parameters for generic combustion chamber calculation with hydrogen as a coolant

Finis Coronat Opus.

Curriculum Vitae

Tobias Langener



Personal Data

Date and place of birth July 20th, 1980, in Haltern am See, Germany
Nationality German
Marital Status single

Education:

08/2005-07/2006 Rensselaer Polytechnic Institute (RPI), Troy, NY, USA
Exchange student
09/2000-08/2006 Universität Stuttgart, Stuttgart, Germany
Student, Aerospace Engineering
Graduation with the degree: Dipl.-Ing.
07/1991-06/2000 Clemens-Brentano-Gymnasium, Dülmen, Germany
Abitur

Practical experience:

10/2010-present European Space Agency (ESA) at the European Space
Research and Technology Center (ESTEC), Noordwijk,
The Netherlands:
Propulsion Aerothermodynamics and Jet Interaction
Engineer; Employed by AOES B.V.
09/2006-09/2010 Universität Stuttgart, Stuttgart, Germany:
Research associate at ITLR
02/2005-07/2005 ESA-ESTEC, Noordwijk, The Netherlands:
Intern, Aerothermodynamics and Propulsion Analysis
Section (TEC-MPA)
11/2002-03/2003 German Aerospace Center (DLR), Lampoldshausen,
Germany:
Intern, Institute of Space Propulsion

